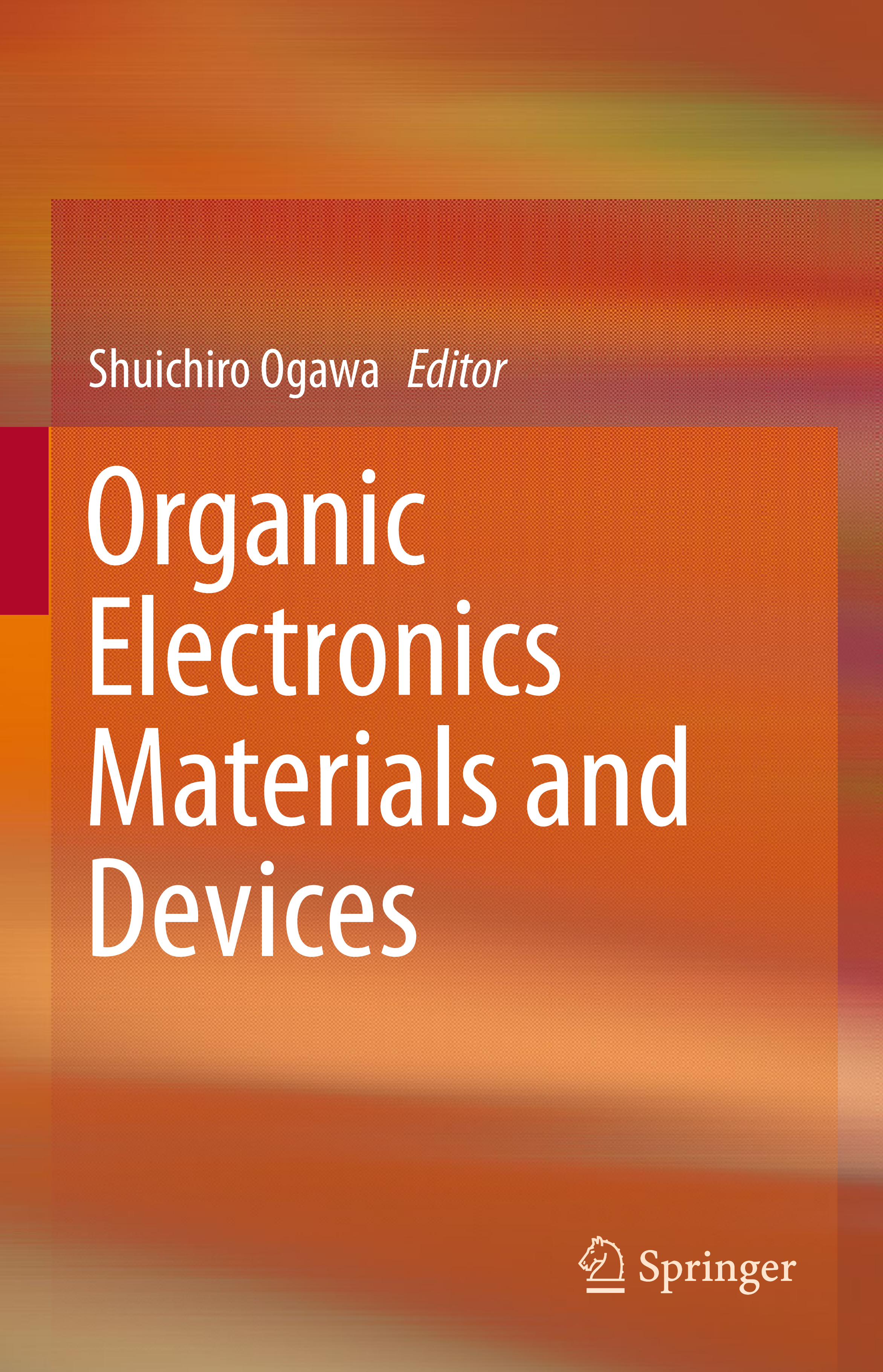

Shuichiro Ogawa *Editor*

Organic Electronics Materials and Devices

Springer

Organic Electronics Materials and Devices

Shuichiro Ogawa
Editor

Organic Electronics Materials and Devices

Springer

Editor
Shuichiro Ogawa
Asahi Kasei Corporation
Fuji, Japan

ISBN 978-4-431-55653-4 ISBN 978-4-431-55654-1 (eBook)
DOI 10.1007/978-4-431-55654-1

Library of Congress Control Number: 2015946780

Springer Tokyo Heidelberg New York Dordrecht London

Printed on acid-free paper

Springer Japan KK is part of Springer Science+Business Media (www.springer.com)

Collaborators

Prof. Jun Mizuno
Waseda University
Tokyo, Japan

Prof. Toshiyuki Watanabe
Tokyo University of Agriculture and Technology
Tokyo, Japan

Satoru Toguchi
NEC Corporation
Tokyo, Japan

Dr. Kazuaki Furukawa
NTT Basic Research Laboratories of the NTT Corporation
Tokyo, Japan

Preface

The Japanese Research Association for Organic Electronics Materials (JOEM) was established as an independent nonprofit organization in 1984. At that time, the electronics industry had been growing rapidly, and companies and their researchers were searching for the technologies and science of not only silicon and compound semiconductor materials but also organic semiconductor materials and organic conductive materials. Dr. Yoshio Taniguchi, who was working for Hitachi Ltd. then, had recognized that organic substances were promising materials in the field of electronics, and with his colleagues he coined the terms "organic electronics" and "organic electronics materials." Dr. Taniguchi and his colleagues founded the JOEM in order to stimulate the research activities of organic electronics materials among academia, governmental institutes, and industries by providing the opportunities for communication and discussion.

For the past 30 years, a large number of researchers in academia and industry have been studying and developing organic electronics. There are many unsolved obstacles, but there have been significant advances such as the development of organic light-emitting diodes (LED), organic thin-film transistors (TFT), and organic photovoltaic modules (PV). Notably, organic electronics technologies have attracted attention from the printing industries for application in flexible devices, wearable devices, and others, which may be commercialized in the near future.

The future of organic electronics is promising and growing, but there are still many challenges facing commercialization, such as material degradation involving oxygen, moisture, heat, process inadaptability, and cost. In order to solve these problems, there must be further advancement in our understanding of organic electronics, particularly in the basic sciences. We are concerned that researchers in industry who are involved in developing organic electronics may not be sufficiently educated in the basic principles and sciences of organic electronics materials and devices. This is an unfortunate result of a highly competitive global environment in industry, where most of the researchers and engineers have to focus so much on product development and commercialization. In order to avoid such misfortune, we started an educational course called the “JOEM Academy” in 2011 for younger researchers and engineers, to promote better understanding of basic principles and sciences of organic electronics. Every year, eight to ten professors of organic electronics in Japan from the top universities are invited as lecturers at the JOEM Academy for 4–5 days. The number of participants is kept small (about 10 people) to encourage free discussion, which we believe to be the key to enhancing the understanding of basic principles and sciences. After the lectures, laboratory tours are held, where participants have the opportunity to see the latest research and facilities. We hope that participants have a valuable time with the lecturers and other participants. In 2014, Springer Japan contacted us concerning publishing some proceedings of the JOEM Academy, and we decided to compile this book.

This work is intended to be a resource and reference book for graduate students and researchers in the industry who are new to organic electronics materials, devices, and their applications. The book focuses primarily on the fundamental principles and theories behind organic electronics materials and devices, but also highlights state-of-the-art technologies, applications, and future prospects. For example, physics for organic transistors, structure control technologies of polymer semiconductors, nanotube electronics, organic solar cells, organic electroluminescence, and many other topics are included. In the first three chapters, the fundamental principles and sciences of organic electronics materials and devices are discussed. These include the physics and chemistry of organic electronics materials, organic light-emitting diodes, and organic solar cells. The following six chapters focus on practical knowledge essential for research and development and commercialization.

I am profoundly grateful to the members of the JOEM Academy committee who are also coeditors of this book: Prof. Jun Mizuno at Waseda University, Prof. Toshiyuki Watanabe at the Tokyo University of Agriculture and Technology, Mr. Satoru Toguchi at the NEC Corporation, and Dr. Kazuaki Furukawa at the NTT Basic Research Laboratories of the NTT Corporation. The production of this book would not have been possible without their enthusiasm for publication and stimulating discussion. I am also thankful to Emeritus Prof. Yoshio Taniguchi of Shinshu University, who is the emeritus chairman of JOEM; Dr. Hiroyuki Suzuki, who is the president of JOEM; and the executive directors Mr. Kei Fujinami and Dr. Ryuichi Nakamura for their help and encouragement. I am particularly indebted to Ms. Miyuki Kitamura, a secretary at JOEM, for her long hours of office work in communication with the authors and formatting manuscripts. I am also thankful to Dr. Shin’ichi Koizumi and Ms. Mihoko Kumazawa at Springer Japan, the publisher, for their help.

Some mistakes certainly remain because of my inability to amend and correct them. Nevertheless, I hope that this book will give a reasonable picture of what organic electronics materials and devices are and that readers will understand the importance of organic electronics in creating a new future. I also hope that some readers will become researchers and engineers who lead the field of organic electronics and make a significant contribution to our society.

Fuji, Shizuoka, Japan
Spring, 2015

Shuichiro Ogawa

Contents

Chapter 1
Physics of Organic Field-Effect Transistors and the Materials

Tatsuo Hasegawa

Abstract Organic semiconductors that were discovered more than half century ago in Japan (H. Inokuchi, Org. Electron. **7**, 62 (2006)) are now transfigured into the practicable electronic materials by the recent concentrated studies of the materials, thin-film processing, and device fabrication technologies. In this chapter, we first present and discuss fundamental aspects of electronic phenomena in organic semiconductors as the bases to understand and study the organic electronics technologies. Then we discuss how to understand the charge-carrier transport in organic field-effect transistors (or more frequently refferd as organic thin-film transistors, or OTFTs). Finally we introduce recent studies to fabricate OTFTs by print production technologies.

Keywords Organic thin-film transistor • Organic semiconductor • π-electron • Carrier dynamics • Printed electronics

1.1 Fundamentals for Crystalline Organic Semiconductors

1.1.1 Semiconductors with Hierarchical Structure

Organic semiconductors are a class of semiconducting organic materials composed mainly of carbon elements. The rigorous definition of semiconductors – i.e., the filled electronic states and the empty electronic states are divided energetically by a moderate width of forbidden band or energy gap – is naturally satisfied by all the organic semiconductors, as is similar to other inorganic semiconducting materials. In fact, the most basic (or crude) characteristics of the materials and the devices based on the organic semiconductors are typical of semiconductors, whereas they exhibit specific characteristics unique to this whole class of the materials.

T. Hasegawa (✉)
Department of Applied Physics, The University of Tokyo, 7-3-1 Hongo,
Bunkyo-ku, 113-8656 Tokyo, Japan

National Institute of Advanced Industrial Science and Technology (AIST),
AIST Central 4, 1-1-1 Higashi, Tsukuba, 305-8562 Ibaraki, Japan
e-mail: t-hasegawa@ap.t.u-tokyo.ac.jp; t-hasegawa@aist.go.jp

S. Ogawa (ed.), *Organic Electronics Materials and Devices*,
DOI 10.1007/978-4-431-55654-1_1

The organic semiconductors may be defined, for a rather practical reason, as the semiconductors composed of organic molecules that are synthesized by the techniques of organic synthetic chemistry. Along with this feature, however, the organic semiconductors are quite unique in that the whole solid-state properties are ascribed to a hierarchical nature of [atom–molecule–solid], where the molecules are composed of atoms held together by covalent bonds, and the solids are formed by discrete molecules held together by van der Waals interactions. The key player to bridge this hierarchy is the π-electrons that are the source for all the functional electronic properties of the organic semiconductors. In this section, we outline the electronic structure and the origin of fundamental and specific characteristics of the organic semiconductors, with specially focusing on the roles of the π-electrons. Then we briefly outline the basic architecture of the organic field-effect transistors.

1.1.2 π-Electrons as Source of Mobile Carriers

A major source for an enormous number of organic materials is the unique nature of carbon that can form chains, rings, or branches by stable covalent σ- or π-bonds. The σ-bonds are formed by the 2s–2p hybrid orbitals (sp^1, sp^2, or sp^3) between the adjacent atoms, whereas the π-bonds are formed by the overlap between 2p orbitals of adjacent atoms that do not participate in the formation of σ-bonds (Fig. 1.1). The terms of σ and π are originally associated with the symmetry of the bonds with respect to the rotation along the inter-atomic axes, although the term of π is now frequently utilized to refer to the electrons in the π-bonds. The σ-bonds are relatively strong and the electrons in the σ-bonds are likely to be localized. In contrast, the π-electrons are widely delocalized when the 2p orbitals of respective atoms along the connected linear chains or rings are all aligned in parallel, as presented in Fig. 1.1.

The effect of the delocalized π-electrons most obviously appears in the color of the materials. The usual organic or plastic materials that are formed only by the σ-bonds do not have colors or are transparent. This is because the σ-bonds are so strong that the electronic excitation energy becomes high and the optical gap energy is much larger than the visible photon energy range (1.6–3.3 eV). In contrast, when the π-electrons are delocalized over the molecule, the electronic excitation energy considerably decreases, and the materials become colored. Figure 1.2 presents the optical gap energies of polyacenes (and polyenes), plotted as a function of the number of fused benzene rings and double bonds. When the molecules become larger and the

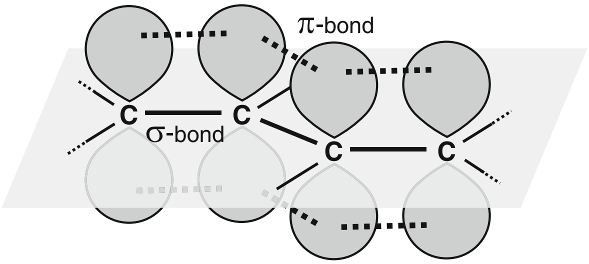

Fig. 1.1 Schematic for a linear chain of carbon connected with σ and π bonds

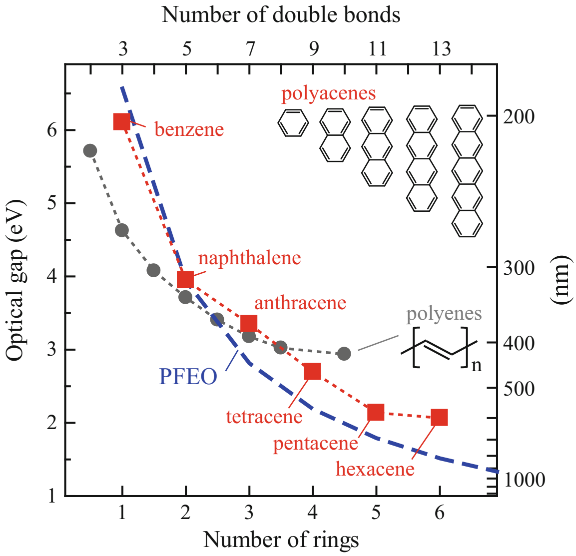

Fig. 1.2 Optical gap energy of polyacenes as a function of number of fused rings or double bonds (*red squares*); Values calculated by PFEO model (*blue dashed line*); Optical gap energy in polyenes as a function of double bonds (*gray circles*)

delocalized π-electrons are more extended, the excitation energy becomes considerably lowered and becomes colored due to the absorption of visible light.

In both the polyenes and polyacenes, each carbon has one π-electron along the alternating sequence of single and double bonds in the chemical notation. Actually, however, these π-electrons do not belong to each double bond but rather to a group of atoms along the alternating sequence of single and double bonds. The sequence is often called as conjugated double bonds, which allow a delocalization of π-electrons across all the adjacent aligned p-orbitals.

Here we present the most intuitive picture for the delocalized π electrons of polyacene by a perimeter-free electron orbital (PFEO) model [1]. We assume naphthalene, composed of two fused benzene rings as an example, that has 10 delocalized π-electrons along the circle, as presented in Fig. 1.3. For the simplicity, it is considered that the 10 π-electrons can move freely ($V = 0$) along the circle with a length L but infinite potential ($V = \infty$) outside the circle. The wave function ϕ^{PFEO} is the simple plane wave as a free electron, and the energy E can be written as a solution of the Schrödinger equation by the following form:

$$\phi_q^{\mathrm{PFEO}} = \frac{1}{\sqrt{L}} \exp\left[-i\left(\frac{E_q}{\hbar}t - \frac{2\pi q}{L}x\right)\right], \tag{1.1}$$

$$E_q = \frac{\hbar^2 k^2}{2m} = \frac{\hbar^2}{2m}\left(\frac{2\pi}{L}\right)^2 q^2. \tag{1.2}$$

Here, $\hbar$ is the Planck constant, k is the wave number, and $q(=0, \pm 1, \pm 2)$ is the quantum number. The energy depends on the number of nodes in the wave

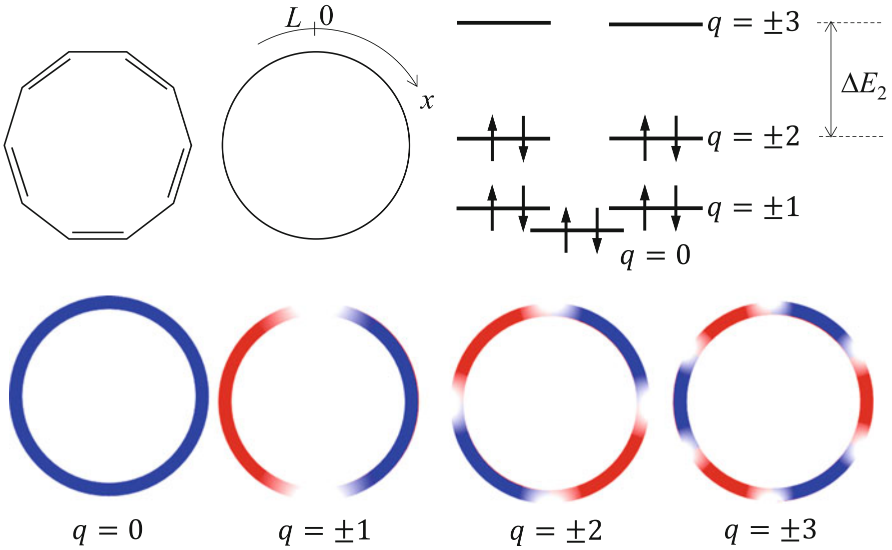

Fig. 1.3 Energy levels and wave functions in perimeter-free electron orbital (PFEO) model

functions, which is equal to $2q$. The energy diagram of the systems is depicted in Fig. 1.3. The circle length can be represented as: $L = Na = (4n + 2)a$, where N is the number of atoms ($N = 10$ in the case of naphthalene), a is the inter-atom distance, and n is the ring number ($n = 2$ in the case of naphthalene). As two electrons are filled at each level, the highest filled level will have $q = n$, and the lowest unfilled level have $q = n + 1$, so that the energy difference between the levels can be written (with using typical interatomic distance value of $a = 0.138$ nm) as

$$\Delta E_n = \frac{\pi^2 \hbar^2}{2ma^2} \frac{1}{2n + 1} = \frac{19.7 \text{ eV}}{2n + 1}. \tag{1.3}$$

The dashed line in Fig. 1.2 presents the result of the calculation. In spite of such simplicity, it is surprising to find the overall consistency as to the trend and rough values. Another important result is also obtained in terms of the stability of the molecules. As the electrons are filled from the lower levels, these ringlike molecules become stable, if there are $(4n + 2)$ π-electrons per molecule (one from each carbon atom). This is the origin of the stability of aromatic compounds and is often called as Hückel's rule. These features demonstrate that the delocalized nature of the π-electrons where the weak linkage between the 2p orbitals can form the nearly free electrons within the molecules. The unique nature of organic molecular materials is the designability of materials in terms of the shape and size of such free electron system within the molecules.

1.1.3 Molecular Orbitals

The molecular orbital (MO) theory is used to determine the π-electronic states in the molecules [2]. The MO theory is based on the concept that the electrons are not assigned to the individual bonds between atoms but to the molecular orbital that is extended to the whole molecule. This concept is in contrast to the valence bond (VB) or Heitler–London theory. The simplest model is based on linear combinations of atomic orbitals (LCAO) to present the molecular orbital ϕ^m as follows:

$$\phi^m = \frac{1}{\sqrt{N}} \sum_{n=1}^{N} c_n^a \chi_n^a, \tag{1.4}$$

where N is the number of atoms and c_n^a and χ_n^a are the coefficient and atomic orbitals of the nth atom, respectively. The linear combination should compose the eigenfunction of one-electron molecular Hamiltonian h with eigen energy ε as

$$h\phi^m = \varepsilon\phi^m. \tag{1.5}$$

By multiplying $\chi_{n'}^a{}^*$ (complex conjugate of $\chi_{n'}^a$) and integrating both sides as $\int \chi_{n'}^a{}^* h\phi^m \mathrm{d}\tau = \varepsilon \int \chi_{n'}^a{}^* \phi^m \mathrm{d}\tau$, and by substituting (1.4) into (1.5), simultaneous equations for coefficients c_n^a are obtained. In the Hückel theory for π-electrons, the following simplifications are assumed:

$$h_{nn'} = \int \chi_{n'}^a{}^* h \chi_n^a \mathrm{d}\tau = \begin{cases} \alpha \ (n' = n) \\ \beta \ (n' = n+1) \\ 0 \ (n' \neq n,\ n+1) \end{cases}, \tag{1.6}$$

$$s_{ij} = \int \chi_i^a{}^* \chi_j^a \mathrm{d}\tau = \begin{cases} 1 \ (i = j) \\ 0 \ (i \neq j) \end{cases}. \tag{1.7}$$

Here α and β are called as Coulomb integral and resonance integral, respectively. The s_{ij} is called as overlap integral. For example, the simultaneous equations in the case of benzene ($i = 1, 2, \ldots, 6$) can be simply represented by the matrix formula as

$$\begin{pmatrix} \alpha-\epsilon & \beta & 0 & 0 & 0 & \beta \\ \beta & \alpha-\epsilon & \beta & 0 & 0 & 0 \\ 0 & \beta & \alpha-\epsilon & \beta & 0 & 0 \\ 0 & 0 & \beta & \alpha-\epsilon & \beta & 0 \\ 0 & 0 & 0 & \beta & \alpha-\epsilon & \beta \\ \beta & 0 & 0 & 0 & \beta & \alpha-\epsilon \end{pmatrix} \begin{pmatrix} c_1^a \\ c_2^a \\ c_3^a \\ c_4^a \\ c_5^a \\ c_6^a \end{pmatrix} = 0. \tag{1.8}$$

By solving the equation, eigen energy and eigenfunction can be obtained. The eigen energy is obtained as $\epsilon = \alpha - 2\beta, \alpha - \beta, \alpha + \beta, \alpha + 2\beta$, as presented in Fig. 1.4.

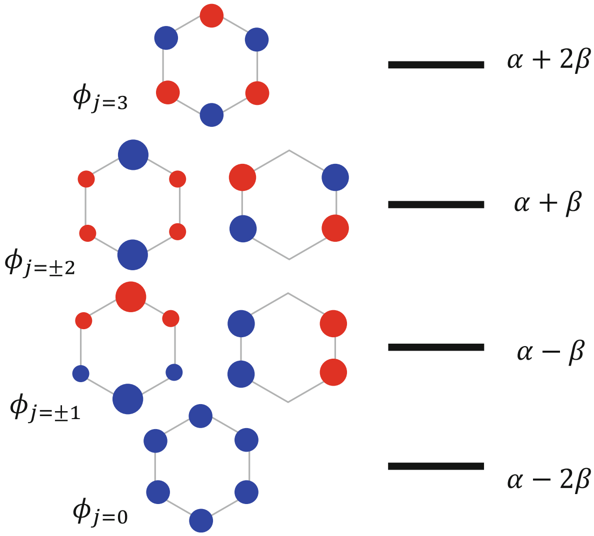

Fig. 1.4 Molecular orbital and energy diagram of benzene

It is also important to understand, for solving the equation, that the coefficients c_n^a obey some relations due to the molecular symmetry. In the case of benzene, the π/3 rotation of the eigenfunction as to the axis perpendicular to the molecular plane at the center of the molecule still affords the eigenfunction with the same eigen energy. It means that the $\phi^m = c\phi^{m'}$, where c is complex number with absolute value 1 and $\phi^{m'}$ is the molecular orbital after the rotation. Furthermore, the 6 times repetition of the π/3 rotation should give it back to the original eigenfunction. Therefore, the eigenfunction of benzene can be represented as

$$\phi^m = \frac{1}{\sqrt{6}}\sum_{n=1}^{6} e^{i\frac{2\pi n}{6}j}\chi_n^a \; (j = 0, \pm 1, \pm 2, \pm 3). \tag{1.9}$$

The wave functions of molecular orbitals of benzene are depicted in Fig. 1.4.

The cyclic compounds can also include non-carbon elements within the cycles (which are called as heteroatoms). For example, 5-membered ring becomes stable due to the Hückel's rule ($N = 4n + 2$), in case that one sulfur atom is included, because two electrons in the lone pair of 3p orbitals contribute to the molecular orbitals. In particular, the thiophene ring is known to be an extremely important unit to obtain high-performance organic semiconductors. This is associated with the characteristics of the 3p orbitals of sulfur, which is more extended outside the molecules than 2p orbitals of carbon, and is effective to increase the intermolecular interactions when the semiconducting molecular crystals are formed.

In the simplest MO calculations, empirical values are used for α and β to describe the one electronic states in the molecules. Electrons in the molecules fill the states from lower levels with satisfying the Pauli principle. Ground states of the molecules that are formed by many electrons are approximated by using the Slater

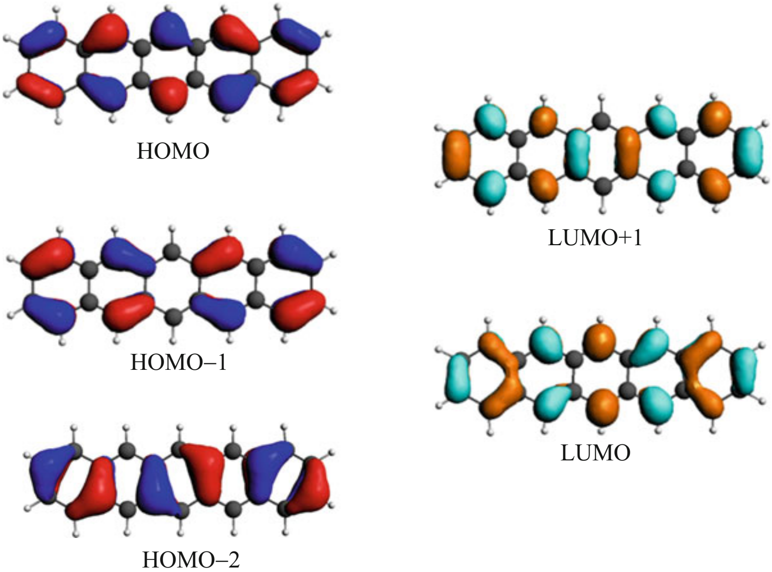

Fig. 1.5 Wave functions of molecular orbitals in a pentacene molecule calculated by ADF program [5]

determinant, the treatment of which is called as the Hartree–Fock approximation. The detailed calculations for the many-electron system are conducted by ab initio (or first principles) calculations. In the states of many electrons, Coulomb and exchange interactions between electrons should be considered and are treated by configuration interactions that hybridize many excited electronic states to minimize the total energy and to obtain the more reasonable ground states of the molecule.

Recently, calculations using density functional theory (DFT) is more frequently used to calculate ground states of many-electron system; the method is based on the calculation of distribution function of electron density, $n(r)$, and the effective potential. These methods are now familiarized, owing to the rapid development of programs and calculation speed of the computers. Today, DFT applications such as B3LYP (Becke, Lee, Yang, and Parr) [3] or ADF (Amsterdam density function) [4] calculations are commercially available and are used by using laptop computers with standard configuration. Figure 1.5 illustrates the wave function of molecular orbitals of pentacene as obtained by the ADF calculations [5].

1.1.4 Electronic Band Formation

When same kinds of organic molecules are gathered, they are self-organized to form crystals, if the molecular shapes have relatively high symmetry and the molecules can be packed densely without opening within the molecular arrangement that holds the translational symmetry. In the crystals composed of densely packed molecules, molecular orbitals of π-electrons, composed of such as spatially extended carbon 2p orbitals, are overlapped and interacted with those of the adjacent molecules. Thus, the electronic states of the π-electrons are extended widely over the crystals. In the crystals, the intermolecular interactions between the combination of adjacent molecules should become equivalent with others between a crystallographically equivalent combinations. Such a formation of crystals that have translational symmetry is essentially important for the (translational) charge-carrier motion in the semiconductors.

Here we discuss the electronic wave function in the crystals with certain intermolecular interactions. In the case of organic semiconductors in which the molecules are bound by relatively weak van der Waals interactions, it is quite effective, as a first approximation, to use the tight-binding model in which the wave function is formulated by linear combination of molecular orbitals for obtaining wave functions in solids. This is analogous to the LCAO for the formation of molecular orbitals by the linear combination of atomic orbitals. The wave function is represented by the following form [6]:

$$\varphi^s(\mathbf{r}) = \frac{1}{\sqrt{N}} \sum_{n=1}^{N} c_n^m \phi_n^m(\mathbf{r} - \mathbf{R}_n). \tag{1.10}$$

where N is the number of molecules and c_n^m and $\phi_n^m(\mathbf{r} - \mathbf{R}_n)$ are the coefficient and molecular orbitals of the nth molecule at the position $\mathbf{R}_n$, respectively. Because of the translational symmetry of the crystals, the wave function can be represented by the following form (by obtaining the same procedure as (1.9)):

$$\varphi_{\mathbf{k}}^s = \frac{1}{\sqrt{N}} \sum_{n=1}^{N} \exp(i\mathbf{k} \cdot \mathbf{R}_n) \phi_n^m(\mathbf{r} - \mathbf{R}_n). \tag{1.11}$$

This kind of formula is called as the Bloch function and satisfies the Bloch's theorem.

Electronic energy, $E(k)$, which is plotted as a function of wave number k is the electronic band structure. The tight-binding method affords the trigonometric function (or called as "cosine" band). Because the intermolecular interaction is relatively weak in organic semiconductors, the highest occupied valence band (HOVB) is mainly composed of HOMOs of the molecules, and the lowest unoccupied conduction band (LUCB) is mainly composed of LUMOs of the molecules. Therefore, the solids composed of closed-shell molecules should be the semiconductors (each band is filled) and are divided by the energy gap. Effective mass of each band is approximated by the following equations:

$$\frac{1}{m^*} = \frac{1}{\hbar^2} \frac{\partial^2 E(k)}{\partial k^2}. \tag{1.12}$$

Thus the effective mass m^* is inversely proportional to the intermolecular transfer integrals. Band transport usually means the free-carrier motion with the effective mass as is determined by the band curvature. Under an electric field, free carriers are not infinitely accelerated but are frequently scattered such as by phonons in the crystals at finite temperature, so that they have average velocity. In other words, the mean free path of free carriers is finite at room temperature in the crystals, so that the transport of charge carriers becomes “diffusive” motion. In the diffusive motion, the average velocity of diffusive drift motion under an electric field carrier is proportional to the applied electric field, whose proportional coefficient is defined as the drift mobility (or simply mobility) μ of carriers as

$$v = \mu E. \tag{1.13}$$

By using the mobility, the electrical conductivity σ is described by the following equation:

$$\sigma = ne\mu. \tag{1.14}$$

Here n is number of carriers per unit volume and e is the elementary charge. In the diffusive motions of carriers, the following Einstein relation generally holds with assuming the diffusion constant D (defined as the coefficient in diffusion equation):

$$D = \frac{\mu k_B T}{e}. \tag{1.15}$$

Intrinsic mobility in the semiconductor single crystals should be determined by such a mechanism.

For achieving efficient carrier transport in organic semiconductors, it is necessary to design organic molecules which can form highly crystalline solids with large intermolecular interactions and translational symmetry. The molecular orbital calculations using the DFT are also utilized to calculate intermolecular interactions between the molecules by using the atomic coordinates as is obtained by the crystal structure analysis. Figure 1.6 shows a result of the intermolecular interactions in pentacene calculated by the ADF method. The pentacene is known to crystallize layered-crystal structures where the molecules packed by herringbone-type motif, as presented in Fig. 1.7. It is empirically known that a number of materials with this type of packing motif afford high-performance OTFTs.

Crystal structure analysis [7] is an indispensable tool for investigating the molecular packing. The structure analysis is done by irradiating monochromatic x-ray beam on single crystals and collecting data of a number of Bragg reflections of respective indexes. By the Fourier transformation of the intensity distributions of each index, distribution of electron density in the unit cells can be obtained. As is different from inorganic materials, it is difficult to conduct the crystal structure analysis of organic semiconductors by means of x-ray analysis for polycrystalline films or powders, because the materials are composed of many atoms in the unit cell. So it is indispensable to use the full x-ray single-crystal structure analysis to obtain the reliable crystal structures.

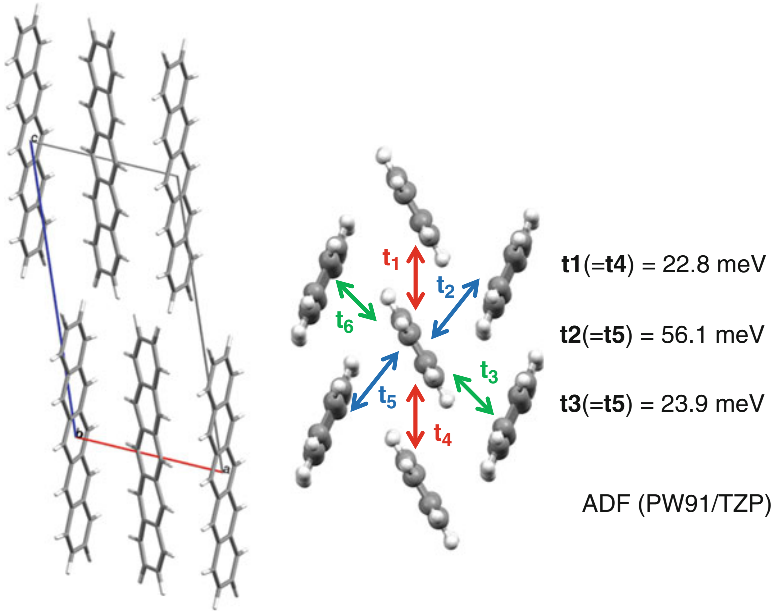

Fig. 1.6 Crystal structure and intra-layer transfer integrals of thin-film pentacene [5]

Fig. 1.7 Herringbone-type molecular packing and atomic contacts in pentacene crystals

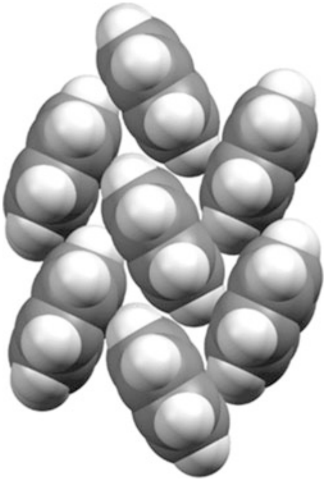

So far it is actually difficult to predict what kind of crystal structure can be formed by a molecule before it is synthesized and crystallized. For the development of materials, it is actually necessary to obtain the materials and to conduct the crystal structure analyses. Probably from many actual examples, we could empirically predict what kind of crystal structures can be obtained in the designed molecules. Nonetheless, the stability of molecular packing in the crystals are also studied, based on molecular dynamics (MD) simulations that can simulate the motion of respective atoms and molecules classically with assuming an interatomic potential. By the technique, the stability and origin of actual crystal structures are confirmed by the MD calculations for some typical organic semiconductors [8].

1.1.5 Architecture of Organic Field-Effect Transistors

Figure 1.8 shows typical device structure of OTFTs. The device is composed of semiconductor layer, gate dielectric, and gate/source/drain electrodes. In the device, drain current flows between source and drain electrodes, by applying drain voltage between the source and the drain electrodes. The drain current can be controlled by the gate voltage which is applied between the source and the gate electrodes. Nominally, there should be no current through the gate dielectric layer. Carriers are accumulated both at the gate electrode and semiconductor layer as like a capacitor. These accumulated charges contribute to the drain current as a drift current.

The channel semiconductors are usually composed of intrinsic organic semiconductors without intentional doping. This feature of the device is much different from that of conventional field-effect transistors composed of inorganic semiconductors like covalent-bonded crystals of silicon [9]. The first reason of this feature is that the intentional doping in organic semiconductors is difficult, because the crystal lattice in which molecules are densely packed without opening and are bound by weak intermolecular interaction is very easily broken by the introduction of molecular dopants with different shapes. The second is a rather positive reason that the surface states due to dangling bonds in covalent-bonded crystals are not formed in organic semiconductors, so that the carrier injection is possible without intentional doping.

Due to the feature of the OTFTs as presented above, a type of the device is rather close to the enhancement-type Si-MOSFET. Carriers are injected into the organic semiconductor layer, if the Fermi level of metal for source/drain electrode coincides with the band energy of semiconductors. Therefore, the organic semiconductors with higher HOVB energy (i.e., lower work function) usually show *p*-type

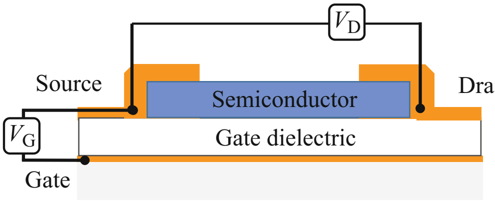

Fig. 1.8 Schematic for organic thin-film transistors

operation, while those with lower LUCB energy (i.e., higher work function) usually show *n*-type operation. Indeed, even if the small number of charge carriers with different types (hole for *n*-type operation or electron for *p*-type operation) could be injected into the semiconductor layer by the direct semiconductor-metal junctions, they are usually trapped in some trap agents within the semiconductor layers and do not contribute to the drain current. We note that if the carriers are not accumulated under the application of the gate voltage, gate electric field should be penetrated into the channel semiconductor layers.

We give the expression for the drain current I_D as a function of gate voltage V_G and drain voltage V_D [10]. When V_D is smaller than V_G, the charge accumulation covers the whole channel region between the source and drain electrodes. In this case, I_D is proportional to $(V_G - V_T)$(V_T is the threshold voltage), which is called as the linear regime and can be described by the following equation:

$$I_D \cong \frac{Z}{L}\mu C_0 (V_G - V_T) V_D, \tag{1.16}$$

where Z is channel widith, L is channel length, and C_0 is capacitance of the gate dielectric layer per unit area. The threshold voltage is associated with the number of traps within the semiconductor layer. When $V_D$is larger than V_G, the charge accumulation does not cover the whole channel region but is limited in the region close to the source electrodes. The location where the charge accumulation is depleted is called as the pinch-off point. In this case, I_D is proportional to $(V_G - V_T)^2$, and becomes independent of V_D. This is called as the saturation regime and can be described by the following equation:

$$I_D^\mathrm{sat} \cong \left(\frac{Z\mu C_0}{2L}\right)(V_G - V_T)^2. \tag{1.17}$$

These equations are used to evaluate the mobility of the semiconductor layers in the experiment.

From the architecture of the field-effect transistors, layered-crystalline organic semiconductors are quite suitable to afford high-performance OTFTs. It has been demonstrated that a high degree of layered crystallinity is essential for the production of single-crystalline or uniaxially oriented polycrystalline thin films in which high-mobility carrier transport occurs along the film planes. We give some typical examples of materials that show high-performance OTFTs in Fig. 1.9.

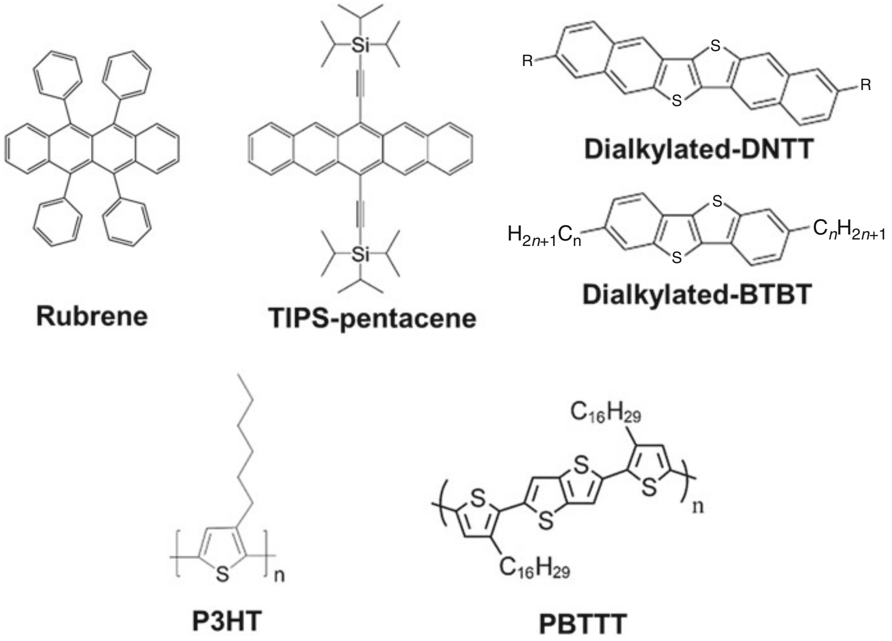

Fig. 1.9 Some important materials for high-performance organic semiconductors

1.2 Charge-Carrier Dynamics in Organic Field-Effect Transistors

1.2.1 Overview

In the Sect. 1.1, we discussed that the electronic band structures with relatively narrow bandwidths are formed in crystalline organic semiconductors that feature periodic crystal lattices. This picture provides a primary fundamental basis for understanding the charge-carrier transport in organic semiconductor thin films of OTFTs. However, we also have to know that the charge-carrier dynamics in actual OTFTs is not that simple as is determined by the "free motion" of charge carrier with an effective mass that is prescribed by the electronic band structure. As a clue to address this issue, temperature dependence of carrier mobility (or conductivity) is frequently utilized to characterize the carrier transport in real devices as either "metallic type" or "activation type." Figure 1.10 presents an example of current–voltage characteristics of a pentacene OTFT at various temperatures (gate voltage is fixed). When assuming free-carrier (i.e., metallic-type) transport, the mobility is expected to gradually increase by lowering the temperature due to the reduction of phonon scattering. In reality, however, almost all the OTFTs including single-crystalline organic field-effect transistors present activation-type characteristics at least at low temperature, even if the "metallic-type" behavior is observed at relatively high temperature [11–13]. In this

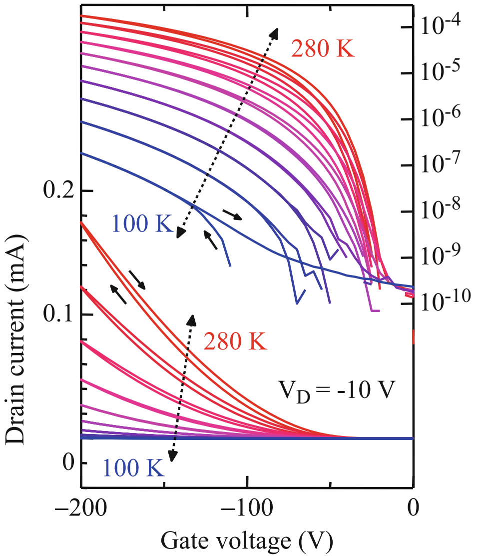

Fig. 1.10 Transfer characteristics of pentacene OTFT at various temperatures

respect, the charge transport has an intermediate character between the band transport and the charge localization at finite temperature.

Here we have to comment that the use of the "hopping" theory should not be justified in crystalline organic semiconductors that show relatively high carrier mobility, even if the activation-type characteristics are observed. In the hopping model, it is assumed that the charge transport is based on a hopping process between diabatic molecular states, where the molecules are energetically relaxed to localize the hopped charge on the respective molecule. The hopping frequency, k_{hopping}, is simply given by [14–16]

$$k_{\text{hopping}} = \frac{t^2}{\hbar}\left(\frac{\pi}{\lambda k_B T}\right)^{1/2} \exp\left(-\frac{\lambda}{4 k_B T}\right), \tag{1.18}$$

where t is transfer integral, $\hbar$ is Planck constant, λ is reorganization energy, k_B is Boltzmann constant, and T is temperature. The hopping model makes a basic assumption that the nuclear motion that "reorganizes" the molecular structure via ionization is much faster than the charge hopping rate between molecules. However, it is difficult to apply this picture into the crystalline organic semiconductors that involve strong intermolecular interactions in the range of 0.01–0.1 eV; the energy is comparable to the calculated reorganization energy for isolated molecules which is limited by a fast intramolecular vibrational mode, such as C=C bond stretching, and is less than 0.2 eV at most. Thus, the hopping picture may be only applicable to the disordered amorphous organic semiconductors whose intermolecular hopping rate is very small due to the small intermolecular electronic coupling less than 1 meV. It was also pointed out that the hopping transport between the neighboring molecules is improbable by the Hall effect measurements for some OTFTs [17].

We also briefly note here that it has been demonstrated that carrier transport becomes apparently “metallic type” in the similar but different type of π-conjugated organic molecular solids, if the number of carriers becomes large enough [18]: two-component organic charge-transfer (CT) compounds composed of similar π-conjugated molecules have high enough carrier density (typically one carrier per two molecules) and show metallic behavior down to the lowest temperature [19]. Particularly, the effective nature of electronic band structure has been preponderantly demonstrated in the single crystals of these compounds; the coincidence of Fermi surface topology between the theory and experiments is investigated by the carrier transport studies under high magnetic field and at low temperature.

Back to the discussion on the temperature dependence of carrier mobility in OTFTs, it is most probable that the thermally activated behavior should be ascribed to the existence of local potential (with either intrinsic or extrinsic origin) that disturbs the translational symmetry or lattice periodicity, and forms carrier trap states within the semiconductor channel layers. This effect should be essentially important in the OTFTs whose device operation is carried by a limited number of charge carriers: the number of carriers induced by gate voltages in the OTFTs is roughly estimated as small as 10^{-12} cm^{-2} at most, which roughly corresponds to “one carrier per one thousand molecules,” if we assume that the charges are accumulated at the surface of conventional organic semiconductor crystals. Such a tiny amount of charge carriers should be directly affected by the disordered potential in the crystals or in the gate dielectric layers. In other words, carrier transport in OTFTs should be dominated by shallow or deep trap states that are formed in the vicinity of the bandedge states. The distribution of these trap states is also quite important in understanding the device operation of OTFTs especially at the subthreshold regions.

Many theoretical studies have been also reported, so far, to identify the origin of charge localization in organic semiconductors. Role of thermal fluctuation [20–22], vibration coupling [23, 24], and fluctuation in gate dielectric layer [25] have been discussed so far, as associated with the unique nature of organic semiconductors. A number of experimental studies have been also reported so far to investigate trap density of states in organic semiconductors, mainly on the basis of electrical device-characteristic measurements [26]. In spite of these works, the real picture has not been established due to the limited number of microscopic experimental studies. This is also related to the fact that the number of charge carriers is strictly limited in OTFTs, which make it difficult to conduct these studies. In this section, we especially focus on microscopic charge-carrier transport in OTFTs by providing experimental results by field-induced electron spin resonance (FESR) measurements. It is shown that the measurements can exceptionally probe microscopic motion of charge carriers accumulated in OTFTs by gate voltages, which is quite useful to investigate the charge-carrier dynamics in OTFTs.

1.2.2 Field-Induced Electron Spin Resonance

1.2.2.1 Electron Spin Resonance

Figure 1.11 presents a schematic for the principle of electron spin resonance (ESR) technique. When holes (electrons) are accumulated in the OTFTs by negative (positive) gate voltages, they are accommodated at the HOMO (LUMO) levels and can move from molecule to molecule through the intermolecular interactions or the electronic band states. When we view the carrier states in terms of electronic spins, only charge carriers are unpaired and have finite magnetic moments with spin quantum number $S = 1/2$. The ESR technique probes the response of electronic magnetic moment in terms of the magnetic resonance absorption of microwaves under static magnetic field [27].

In the presence of an external static magnetic field, the electronic magnetic moment aligns itself either parallel ($m_s = -1/2$) or antiparallel ($m_s = +1/2$) to the field. They have different magnetic energies whose separation is called as Zeeman splitting, as shown in Fig. 1.11. The split is proportional to the applied static magnetic field strength B and is given by $g\mu_B B$. Here g is a dimensionless constant called as g factor, and μ_B ($=9.3 \times 10^{-24}$ J/T) is the Bohr magneton. When we irradiate the spin system with microwave at frequency ν, magnetic resonant absorption takes place at the resonance condition:

$$h\nu = g\mu_B B, \tag{1.19}$$

by which the spin direction is converted between the parallel and antiparallel alignment. In usual cases, the ESR signal cannot be detected with the channel organic semiconductors under no gate bias due to the intrinsic semiconductor

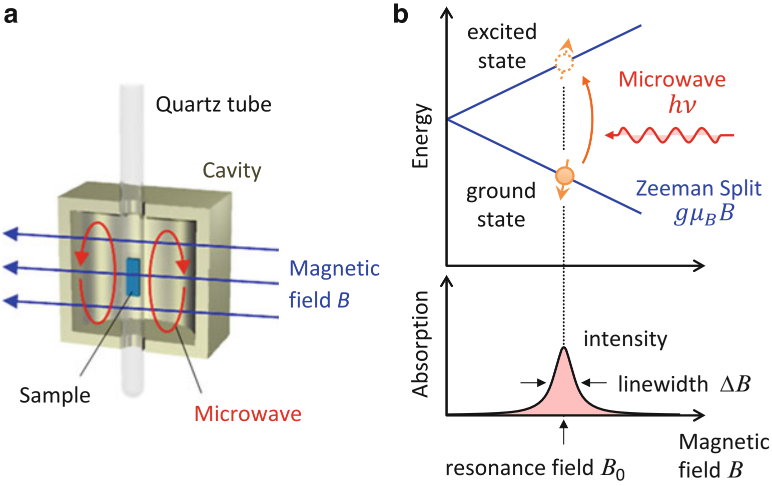

Fig. 1.11 Schematic of electron spin resonance measurement

nature. So the ESR measurements allow us to probe, sensitively and selectively, the carriers that are accumulated at the semiconductor–insulator interface in the OTFTs by the gate voltages.

Because of the simple and general features of ESR measurements as presented above, it is expected that similar experiments should be possible for the devices based on inorganic semiconductors. However, there are no examples, except for the OTFTs, to detect the charge carriers in field-effect transistors by ESR experiments. This may be due to the fact that the number of carriers induced by the gate voltages is considerably limited in the device, whose detection is not feasible. Nonetheless, extremely highly sensitive detection of electronic spins in the OTFTs is possible, because the relaxation time of excited spin state is fairly long in organic materials due to the small spin–orbit interactions of light atomic elements, so that much narrow ESR spectrum is observed.

ESR measurements of field-induced carriers in OTFTs are first reported by Marumoto and Kuroda in 2004 [28]. They successfully demonstrated that the detected FESR signal from the OTFTs is proportional to the applied gate voltages and is surely ascribable to the charges accumulated at the organic semiconductor interfaces. They also claimed that the carrier states are spatially extended over several molecules in pentacene OTFTs by the fact that the observed FESR linewidth is narrower than that of the isolated cationic molecule in solution [29]. Then Matsui and Hasegawa observed the so-called motional narrowing effect in the FESR spectra of OTFTs, from which the various aspects of charge-carrier dynamics that are directly connected to the device operations can be extracted [30].

1.2.2.2 Field-Induced Electron Spin Resonance Technique

The FESR measurements could be done with conventional X-band ESR apparatus equipped with a cavity with high Q value (4000–6000 in TE_{011} mode). Figure 1.12a schematically illustrates the device structure of an OTFT as used for the FESR measurements. A 100-μm-thick poly(ethylene naphthalate) film was used as the nonmagnetic substrate, and an 800-nm-thick parylene C film was used as the gate dielectric layer. The capacitance C_i is estimated at 4.5 nF cm^{-2} by AC method at 1 mHz. The semiconductor layer of pentacene was fabricated by vacuum deposition to form a total area of 2.5 mm × 20 mm and a thickness of 50 nm on top of the gate dielectric layer. As the gate, source, and drain electrodes, vacuum-deposited gold films with a thickness of 30 nm were used. The thickness is much smaller than the skin depth of gold at the X-band microwave. By using these devices, it is possible to eliminate the ESR signals from the device components. It is also useful to use a stack of sheet devices for the high-precision FESR measurements.

The ESR experiment detects magnetic resonance absorption at the condition: $B = h\nu/g\mu_B$, by sweeping static magnetic field at a constant microwave frequency. The spectrum is obtained in the form of a first derivative curve of the resonance absorption as a function of magnetic field due to the use of lock-in detection technique. An example of the FESR spectrum is presented in Fig. 1.12c for the

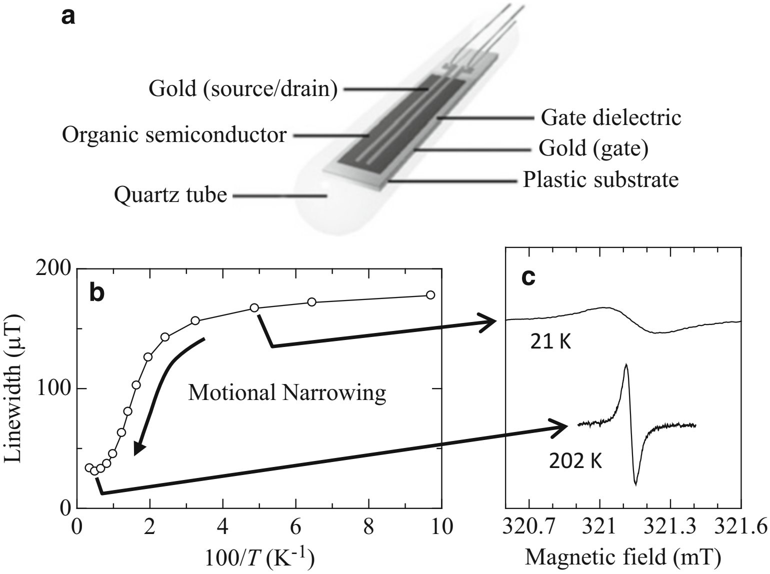

Fig. 1.12 (**a**) Schematic of device structure of OTFT for FESR measurement, (**b**) temperature dependence of FESR linewidth, (**c**) typical FESR spectrum [30]

pentacene OTFTs. The spectra usually exhibit symmetric, single-shaped, and very narrow resonance absorption line with width of ten to several hundred μT. The resonance field allows to evaluate the *g* factor which is usually close to that of free electron (=2.002319) in organic semiconductors. The *g* factor depends on the direction of applied static magnetic field as to the semiconductor crystals to afford anisotropic *g* tensor, which is mainly originated from the anisotropy of spin–orbit interaction of the component molecules.

1.2.2.3 Motional Narrowing Effects

Here the "motional narrowing effect" is briefly outlined as a core concept to analyze the FESR experiments [31, 32]. First we presume that charge carriers with electronic spins do not move and continue to stay at respective sites. In this case, the origin of finite linewidth in the ESR spectrum is classified into two fundamentally different cases. The one comes from a decay of the excited spin state, i.e., lifetime width, which leads to the Lorentzian line shape. This effect becomes more crucial at higher temperature because of the increased phonon scattering. The other is a result of inhomogeneity in local magnetic field, $\Delta B_{\mathrm{local}}$, at respective sites, i.e., inhomogeneous width. Especially, an important origin of the $\Delta B_{\mathrm{local}}$ is the interaction of electronic spins with nuclear spins which is known as hyperfine interaction. The hyperfine interaction with proton nuclear spin in π-conjugated molecules reaches as high as 0.1–1 mT. As a result of the independent nature of respective nuclear spin

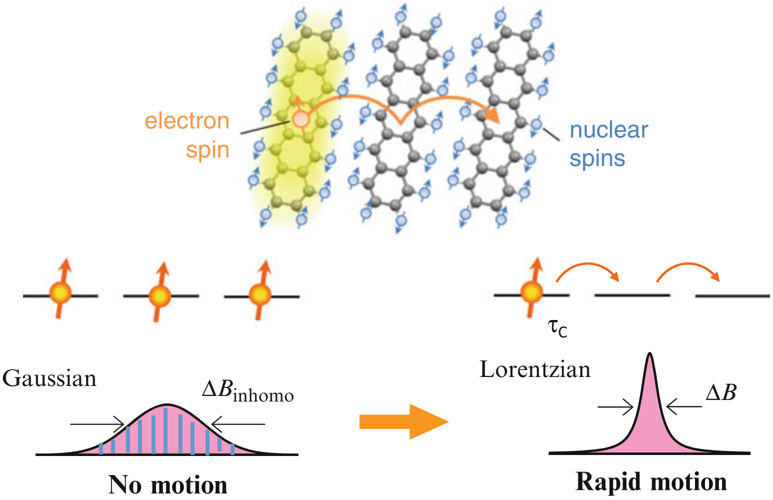

Fig. 1.13 An electron spin moving through randomly oriented nuclear spins

orientations, the ESR spectrum is inhomogeneously spread, as schematically shown in Fig. 1.13, where the resonance condition by sweeping static magnetic field at a constant microwave frequency reflects the probability distribution of nuclear spin moments as given by

$$B = h\nu/g\mu_B - \Delta B_{\mathrm{local}}. \tag{1.20}$$

The motional narrowing takes place in the latter case. Let us assume that the electronic spins of charge carriers move rapidly within the space that involves nonuniform distribution of $\Delta B_{\mathrm{local}}$. The electronic spins should feel the $\Delta B_{\mathrm{local}}$ that rapidly varies with time, but they effectively feel the average magnetic field within a certain period of time, in terms of the magnetic resonance absorption. Because the fluctuation width of the averaged magnetic field, $\Delta B_{\mathrm{local}}$, is smaller than that of local magnetic field, the spectral width of the obtained ESR spectrum becomes narrower than that of the ESR spectrum without motion (see Fig. 1.13). This is the motional narrowing effect. The motional narrowing is observed only when the motion velocity exceeds over a threshold value. If we define k as the motion frequency between sites per unit time, the condition is given by the relation

$$k > \gamma\left(\Delta B_{\mathrm{local}}{}^2\right)^{1/2}, \tag{1.21}$$

where $\gamma = 1.8 \times 10^{11}\ \mathrm{T}^{-1}\ \mathrm{s}^{-1}$ is the gyromagnetic ratio. Considering that the $\Delta B_{\mathrm{local}}$ is in the range of 0.1–1 mT, the threshold motion frequency is estimated at about 10^7–$10^8\ \mathrm{s}^{-1}$. Motional narrowing does not appear when the motion frequency is lower than the threshold value. The ESR spectrum begins to be narrowed when the motion frequency becomes higher than the threshold value and the linewidth is inversely proportional to k (see Eq. (1.22)). Therefore, the motion frequency of charge carriers can be estimated by the measurement of motionally narrowed linewidth.

1.2.3 Carrier Transport Inside Microcrystal Domains

Based on the backgrounds as presented in the preceding subsections, we focus on various aspects of microscopic charge-carrier dynamics in OTFTs as experimentally revealed by the FESR measurements in the subsequent three subsections. The first two are based on the experiments where the static magnetic field is applied perpendicular to the plane of polycrystalline organic semiconductor thin films. In the OTFTs showing relatively high mobility, polycrystalline films are usually composed of layered microcrystals (as discussed in Sect. 1.1) that are uniaxially oriented with the layer parallel to the substrate plane. Therefore, the obtained FESR spectra are equal for all the microcrystals in terms of the measured direction of g tensor, where the magnetic field is applied parallel to the crystal axes perpendicular to the layer. In contrast, the last subsection is based on the experiment where the static magnetic field is applied parallel to the film plane.

Figure 1.14 presents the temperature dependence of the ESR linewidth for four kinds of OTFTs (pentacene, DNTT, PBTTT, and PNDTBT) measured at the magnetic field perpendicular to the film plane [33]. The plots present unique temperature variation which can be commonly divided into the three regions for all the OTFTs: (1) low-temperature range where the linewidth is independent of temperature, (2) mid-temperature range where the linewidth decreases with increasing temperature, and (3) high-temperature range where the linewidth increases with increasing temperature.

The OTFTs do not operate in the low-temperature range (see Fig. 1.10). It means that the motion of charge carriers should be “frozen,” which is consistent with the temperature-independent nature of the ESR linewidth where no motional narrowing is observed. In sharp contrast, the temperature-dependent feature in the mid-temperature range should be attributed to the motional narrowing effect, where the carriers are thermally detrapped (or released) from the trap sites and begin to move in the crystals. This interpretation of the temperature dependence is also demonstrated by the dependence of the ESR linewidth on the input microwave power at various temperatures; the results indicate that the spectrum in the low-temperature range is inhomogeneous, while the spectrum character becomes more homogeneous with the increase of temperature in the mid-temperature range. In the high-temperature range, the linewidth turns to increase with the increase of temperature, where the temperature dependence should be dominated by the fast spin–lattice relaxation. Actually, this feature becomes more apparent in DNTT than in pentacene, most probably because the DNTT are composed of a larger element of sulfur, leading to the larger spin–orbit coupling.

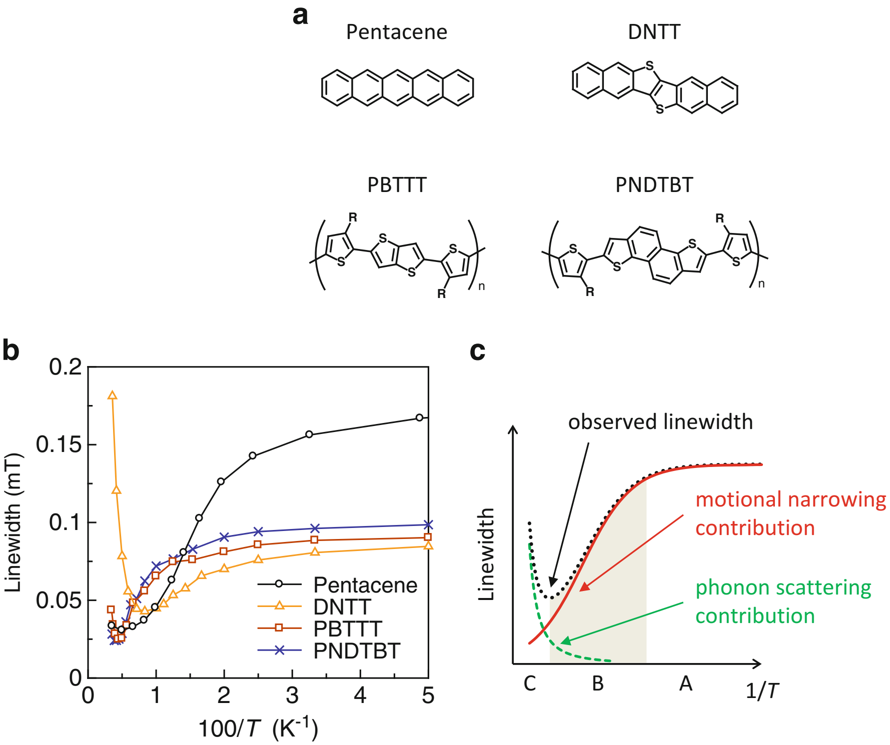

Fig. 1.14 (**a**) Molecular structures of pentacene, DNTT, and PBTTT and PNDTBT. (**b**) Temperature dependence of ESR linewidth. (**c**) Schematics of motional narrowing and phonon scattering contributions to linewidth [33]

When the ESR spectrum is narrowed by the motional narrowing effects, motion frequency of charge carriers, denoted as k_1, can be estimated by the observed ESR linewidth at respective temperature, as is given by the following relation:

$$k_1 = \gamma \left\langle \Delta B_{\text{local}}{}^2 \right\rangle / \Delta B. \tag{1.22}$$

$\left\langle \Delta B_{\text{local}}{}^2 \right\rangle$ can be estimated by the original inhomogeneous linewidth at the low-temperature range, where the carrier motion is frozen. The estimated k_1, presented in Fig. 1.15a, is in the range of 10^7–10^9 s^{-1}, indicating that the residence time of charge carriers at respective trap sites is estimated at about 1–100 ns. The k_1 increases by the increase of temperature, but the temperature-dependent nature is relatively gradual and the activation energy is estimated at 2–21 meV. Here we must note that the estimated average residence time of charge carriers is extremely long, if the hopping theory is tentatively assumed; k_{Marcus} should be in the range of 10^{13}–10^{14} s^{-1} under the assumption of hopping length as the intermolecular distance.

Fig. 1.15 (**a**) Intradomain charge-transfer rate k_1 evaluated by Eq. (1.22). (**b**) Schematics of the trap-and-release model

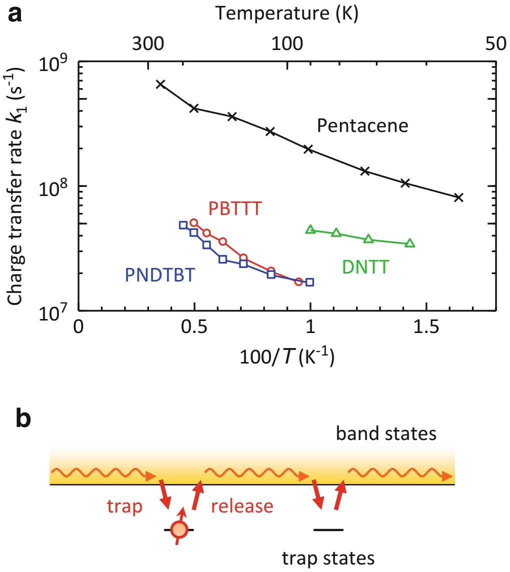

Then we deliberate what the obtained motion frequency represents for, as is related to the charge-carrier motion. According to the multiple trap-and-release (MTR) model [34, 35], the average time at traps is much longer than that for traveling from trap to trap. In this case, the average traveling length *d* between the traps is simply represented by the diffusive motion of charge carriers as [36]:

$$d = \sqrt{4D\tau_C} = \sqrt{\frac{4k_B T\mu'\tau_C}{e}}, \tag{1.23}$$

where D is the diffusion constant, k_B is the Boltzmann constant, μ' is the effective charge-carrier mobility inside the microcrystals, and e is the elementary charge. The second derivation utilizes Einstein's relation, as presented in Eq. (1.15), which implies a statistical nature for the total stochastic carrier motion, including the trap-and-release processes. From Eq. (1.23), d is calculated to be about 10–50 nm at room temperature. In Fig. 1.15b, we show the schematic of the charge-carrier motion, as achieved by the FESR experiments. The charge carriers should move from trap to trap by thermally activated trap-and-release process. The activation energy for motion frequency, which is comparable to or smaller than the thermal energy at room temperature, should correspond to the averaged depth of these traps. The motional nature between the traps should be band-like carrier transport, while the feature is not clear from the FESR experiments.

1.2.4 Density of Trap States Inside Microcrystal Domains

As we discussed in the former subsection, FESR linewidth becomes almost constant (or temperature independent) in the low-temperature range, typically below a few tens of kelvin. In this temperature range, the charge carriers lose thermal energy and become immobile, as they should be trapped by shallow or deep traps. It means that the FESR spectrum at the lowest temperature should include rich information about the trapped or weakly localized carrier states. Therefore, the analysis of the spectrum should allow the detailed investigation of these trap states that take crucial roles in the charge-carrier transport at elevated temperature [37, 38].

The low-temperature FESR spectrum is inhomogeneous, because the local magnetic field at respective sites is different with each other. As discussed above, the origin of the local magnetic field is ascribed to the hyperfine interaction with nuclear spin moments. As an example, we show the ESR spectrum of cationized pentacene molecule in solution in Fig. 1.16a [39]. The spectrum exhibits complicated hyperfine splitting. As the respective pentacene molecules are isolated with each other in solution, an unpaired electronic spin within the cationic pentacene molecule interacts with 14 proton nuclear spins. As the ESR line should split per

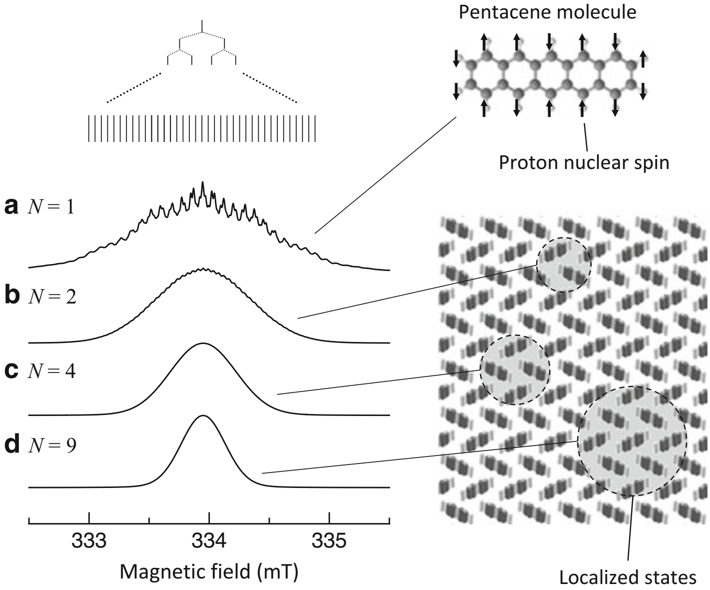

Fig. 1.16 Local magnetic field due to the combination of proton nuclear spin orientations and its effect on ESR spectrum. (**a**) Measured ESR spectrum of cationized pentacene molecule in solution and calculated ESR spectra for the electronic states with spatial extension over (**b**) $N = 2$, (**c**) $N = 4$, and (**d**) $N = 9$ molecules. The *right* shows the schematic for the shallow localized states

each proton nuclear spins ($I = 1/2$), the total number of splits amounts to $2^{14} = 16{,}384$ (the number of independent combinations is 372 from the molecular symmetry), where both ends are composed of either all up or all down spins. The ESR spectrum is composed of these resonance lines that have finite linewidth and are overlapped with each other. Although the actual spectrum is waved as presented in Fig. 1.16a, the envelope of the resonance lines is close to the normal (or Gaussian) distribution function.

On the other hand, the electronic spins in solids should be extended over several molecules. Namely, the electronic wave function in solids is not restricted to a single molecule. When we assume that the wave function is extended over N molecules, the electronic spin interacts with nuclear spins included in all the N molecules, so that the split number exhibits exponential dependence on N. Eventually, the linewidth becomes narrowed by a factor of $\sqrt{1/N}$, as compared to the case of cationic single molecule, according to the central limit theorem. Based on the presumption, Marumoto and Kuroda pointed out that the wave function is extended over about 10 molecules in pentacene OTFTs, because the observed spectral linewidth is almost 1/3 of the linewidth of radical molecules in solution. But they did not take account of the fact that the obtained spectrum is not Gaussian and also of the fact that the linewidth is temperature dependent at least at room temperature.

In order to reveal the spatial extension of trapped charge states, spectral analyses could be conducted where the spectrum is decomposed into several Gaussian curves with different linewidths. Considering that there are several kinds of weakly localized states, the actual spectrum, denoted as $S(B)$, should be composed of the sum of several Gaussian curves, denoted as $G(B, \mathrm{N})$ with different widths for N, as is given by:

$$S(B) = \int_{1}^{+\infty} \frac{\partial G(B,\, N)}{\partial B} D(N)dN, \tag{1.24}$$

$$G(B,N) = \sqrt{\frac{N}{2\pi\sigma_0^2}}\ \exp\left[-\frac{(B-B_0)^2}{2\left(\sigma_0^2/N\right)}\right]. \tag{1.25}$$

Equation (1.25) is the definition of the Gaussian curve. By solving the integral equation numerically, we can obtain the density of localized states, $D(N)$, from the ESR spectrum. In Fig. 1.17, we show the $D(N)$ as obtained by the analyses of FESR spectrum of pentacene OTFTs. As seen, the $D(N)$ is composed of two discrete peaks (denoted as A and B) and a broad structure (denoted as C) whose spatial extension is over 6–20 molecules. Such shallow localized states should originate from a weak attractive potential that may be ascribed to the possible slight deviation of molecular location from the equilibrium position or a chemical change in molecules. These localized states should take crucial roles in the device operation of pentacene OTFTs at room temperature.

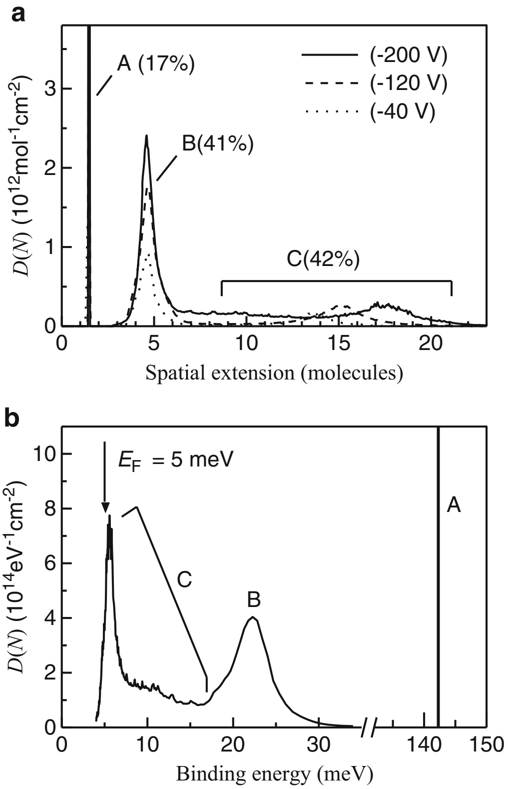

Fig. 1.17 Distribution of trap density of states, $D(N)$, in pentacene TFTs is plotted against (**a**) the spatial extent N and (**b**) the binding energy of the trap states, as obtained by stochastic optimization analysis of FESR spectrum at 20 K and at gate voltage of −200 V [37]

1.2.5 Carrier Transport Across Domain Boundaries

As discussed in the former subsections, channel semiconductor layers of the OTFTs with showing relatively high mobility are composed of uniaxially oriented layered microcrystals whose layers are parallel to the substrate plane. When the magnetic field is applied perpendicular to the substrate, the same ESR signal should be obtained for all the layered microcrystals where the magnetic field is parallel to the normal of the layer (which is denoted as *c*-axis). In striking contrast, when the magnetic field is applied parallel to the substrate, static magnetic field is applied with different angles on each microcrystal domains within the layers (crystal axes within the layer are denoted as *a*- and *b*-axes). Because of the anisotropy of *g* values, resonance magnetic field should be distributed in the latter measurements. Here we demonstrate that these measurements allow us to observe motional narrowing between microcrystals and to estimate grain boundary potential.

Figure 1.18 shows the temperature dependence of the FESR spectra obtained by the measurement with applying the magnetic field parallel to the film (or substrate) plane. Single monotonous peak is observed at room temperature, while the

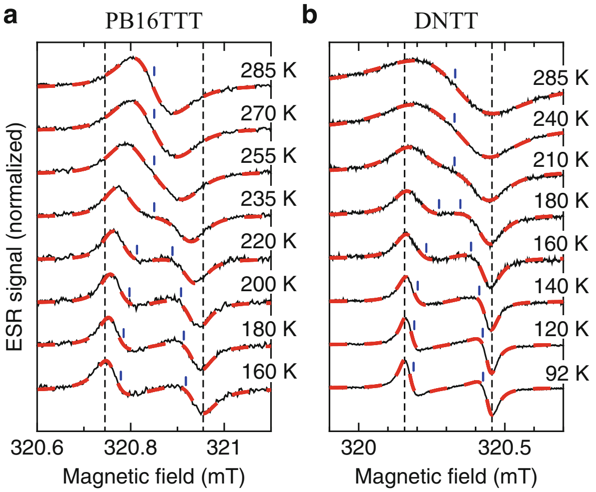

Fig. 1.18 Temperature-dependent ESR spectra for (**a**) PBTTT and (**b**) DNTT, both at the magnetic field perpendicular to the film plane. Fitting curves are indicated by red dotted lines (Reprinted with the permission from ref. [33]. Copyright 2012 American Chemical Society)

spectrum split into the two peaks by the decrease of the temperature. The respective peaks observed at low temperature should correspond to the resonance signals and at magnetic field applied parallel to the *a*- and *b*-axes, respectively. We note that such a clear peak splitting is observed in DNTT and PBTTT OTFTs, but not in pentacene OTFTs. This difference is associated with the relatively large *g* anisotropy in DNTT and PBTTT, due to the large spin–orbit interactions of sulfur.

The peak of the spectrum obtained at room temperature is located almost at the center between the two peaks that are split at low temperature. It is clear that the spectrum at room temperature cannot be reproduced by the simple sum of the split peaks at low temperature. The temperature dependence of the spectrum can be understood in terms of the motional narrowing effect where the anisotropy of *g* values is averaged by the motion of charge carriers across the domain boundaries.

In order to analyze the motional narrowing effect due to the averaging of the two different local magnetic fields, it is necessary to make fitting analyses by the theoretical curves. Figure 1.18 also presents the result of fitting, which is found to reproduce well the experiment. In addition, it is possible to estimate the motion frequency moving across the domain boundaries. Figure 1.19 presents the temperature dependence of motion frequency k_2 across the boundaries for the case of DNTT and PBTTT. The k_2 is about an order of magnitude smaller than the k_1 which is the motion frequency between the traps inside microcrystal domains as described in the former subsection. In addition, activation energy estimated by the temperature dependence of k_2 is 42 meV for DNTT and 86 meV for PBTTT. The result indicates that there are large energy barriers at the grain boundaries.

It is thus concluded that the effective mobility values in polycrystalline OTFTs are rate determined by the motion across the grain boundaries. Although the PBTTT films are known to show high degree of crystallinity as polymer semiconductor, observation of surface morphology by AFM measurements is not effective to identify the domain structures. Nonetheless, it was clearly demonstrated in this measurement that the grain boundary is the rate-determining process for the PBTTT.

Fig. 1.19 (**a**) Intra- (k_1) and interdomain (k_2) motion frequencies and (**b**) field-effect mobility for the PBTTT, DNTT, and pentacene OTFTs. The mobility calculated from interdomain motion frequencies is also shown. (**c**) Diffusion model in polycrystalline films (Reprinted with the permission from ref. [33]. Copyright 2012 American Chemical Society)

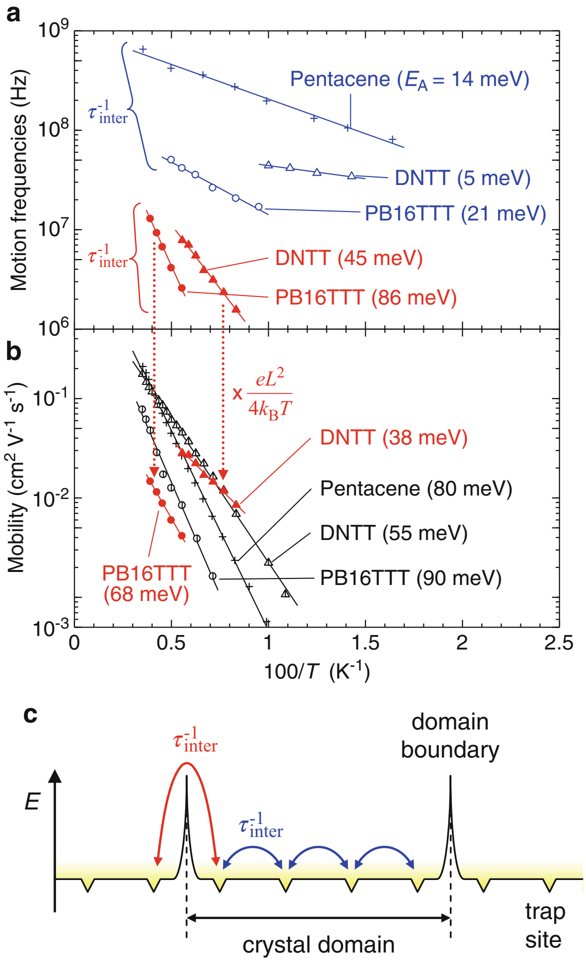

1.2.6 Short Summary and Outlook

A microscopic charge-carrier dynamics that is crucial to understand device operation of OTFTs is discussed, by the experimental results using FESR experiments that probe charge carriers accumulated at the organic semiconductor interfaces. By the analyses of motional narrowing effects in the FESR spectrum, it was shown that the charge-carrier transport can be understood in terms of the two aspects: the trap-and-release transport within the microcrystal domain and the transport across the domain boundaries with a relatively high barrier potential (a few times larger than k_BT).

1.3 Print Production of Layered-Crystalline Organic Semiconductors

1.3.1 Introduction

Studies of “organic electronics” have had a new outlook in recent years, in responding to a strict requirement from industrial circles to demonstrate a clear comparative advantage of the organic semiconductors over the other semiconducting materials. The concept of the “printed electronics” was born against such a background [40]. In the printed electronics, printing technologies that are used to produce documents or photo images on papers are used to manufacture electronic devices at ambient conditions. Particularly, it is expected that the printed electronics technology should replace the vacuum, lithography, and heat-treatment technologies that have been indispensable for the production of all the electronic devices thus far. By these replacements, massive vacuum facilities become unnecessary and/or the use of flexible plastic sheets as base plates becomes possible, allowing us to realize flexible electronic products that have lightweight, thin, and impact-resistant characteristics. Among other semiconducting materials, π-conjugated organic molecular materials should take key roles in the innovation of the electronic device productions by the use of printing technologies. This is because the organic materials are soluble in kinds of solvents and also because the convenient thin-film formation is possible for the materials by convenient solution processes such as spin coating or drop casting at ambient conditions.

A possible future role of the printed OTFTs in the printed electronics technologies can be considered as that any plastic surfaces are decorated electronically by arraying a large number of OTFTs by the printing technologies to function as active backplanes for displays or sensors to realize what is called “ubiquitous electronics” society (Fig. 1.20). Because it is now possible to utilize commercially available inkjet printers, as an example, to print documents or photo images on papers with a spatial resolution higher than 1,200 × 1,200 dpi, it appears auspiciously easy to

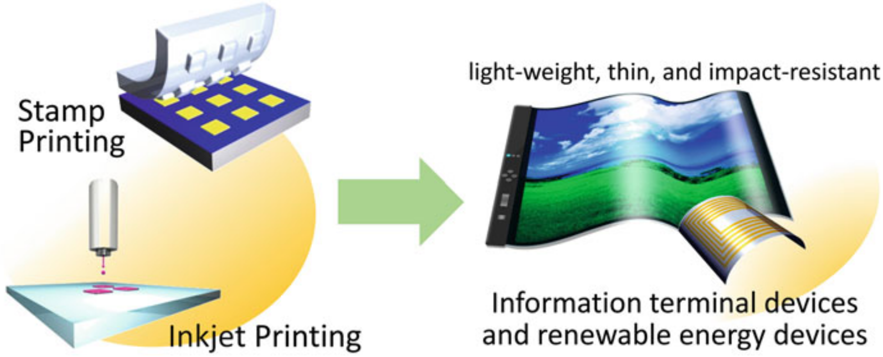

Fig. 1.20 Future image of the printed electronics

manufacture electronic devices with a similar high pattern resolution by the printing technologies. However, it is also true that there is a crucial difference between document printing and production of electronic devices. In order to power electronic devices, it is absolutely necessary to form and stack patterned layers of electronic functional materials that are uniform at atomic or molecular scales, on flat substrate surfaces.

In this section, we first discuss various problems to encounter for producing semiconductor devices by the use of conventional printing technologies. Then we outline two new printing technologies [41, 42], as particular examples, which take advantage of high degree of layered crystallinity of organic semiconductors for manufacturing high-quality semiconductor layers.

1.3.2 Printing Semiconductor Devices?

The printing technologies generally cover a wide range of methods and techniques which include the stamp printing that transfers ink by the convex part of the resin stamp or by the concave part of the metal stamp (the former is called as flexography and the latter as rotogravure), the screen printing that transfers inks through minute opening in the stencil, the inverse printing that removes unnecessary part of deposited inks by a stamp (above all are so-called stamp printings), and the inkjet printing that directly deposits microdroplet inks without stamps (which is the plateless printing). These technologies are now respectively utilized, depending on their costs and uses in a wide variety of fields. It is possible for us to define and characterize all these printing technologies as to freely allocate and deposit a tiny amount of fluidic medium including coloring matters (i.e., ink) on such as papers. The inks as used also have a wide variety, whose viscosity ranges from high to low, and are used depending on the respective printing techniques. In the conventional printing technologies, crystallinity, grain size, or grain boundaries of coloring matters are not a matter of concern after the deposited inks are dried out, as long as the coloring matter is precisely positioned. However, the most important subject for "printing semiconductor devices" is to obtain the semiconductor layers with high uniformity in atomic or molecular scale, after the microdroplet ink is positioned.

As we demonstrated in Sects. 1.1 and 1.2, high-performance OTFTs can be obtained when we use π-conjugated organic molecular materials that show high degree of layered crystallinity as the channel semiconductor layers. This feature is quite useful for producing OTFTs whose carrier transport occurs along the interface between the semiconductor layer and insulator layer. So it is necessary, for manufacturing high-performance OTFTs by a printing technology, to use solution of layered-crystalline organic semiconductors as ink, to deposit the solution ink on flat substrate surface, and to produce uniform patterned semiconductor films composed of the layered crystals whose layers are parallel to the substrate surface. In order to uniformly crystallize the materials from the solution, it should be much

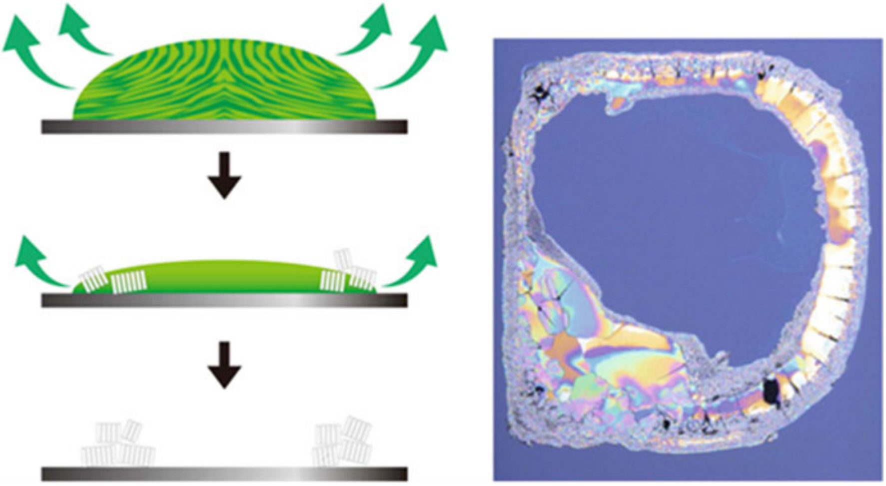

Fig. 1.21 Schematic for the formation of coffee-ring-like deposits by solvent evaporation and outward capillary flow within the deposited microdroplet. The *right image* shows an example

more advantageous to utilize low-viscous solution fluid of semiconducting materials possibly with no additives. On the other hand, it is known to be quite difficult to form uniform thin solid layers from a tiny volume of low-viscous droplets – volume of printed microdroplets produced by such as inkjet printing technique is in the range of 1–100 pL – by precipitation within the droplet through solvent evaporation. In particular, according to the fluid science, solvent evaporation occurs efficiently at around the (solid–liquid–air) contact line of the sessile droplets, so that the resultant outward capillary flow carries solutes toward the contact line of microdroplets and form ringlike deposits at around the contact line [43, 44]. (This is the so-called “coffee-ring effect”; see Fig. 1.21.) In the conventional printing, papers are used as printed medium where the surfaces are highly uneven in mesoscopic level including opening or mesoscopic pore that efficiently absorbs solvents, so that the colored matters are dispersed and adhered to the fabrics in papers by solvent absorption, where these nonuniformity problems are not apparently exposed. However, in order to manufacture uniform semiconductor layers for “printing semiconductor devices,” it should be necessary to control the convection flow and solvent evaporation within the microdroplets.

In order to find out a clue to resolve this issue, it would be meaningful to look back on the birth course of the concept of printed electronics. The concept has an origin in the spin coating of solution-processible π-conjugated polymer semiconductors to manufacture organic light-emitting diodes, organic solar cells, and OTFTs [45–47]. It was later discovered that the spin coating is also applicable to fabricate high-quality thin films of soluble small-molecule semiconductors that shows layered crystallinity and thus to manufacture high-performance OTFTs [48, 49]. Due to these progresses, the spin coating is now widely accepted as a standard technique for manufacturing thin films in the studies of developing soluble organic semiconductor materials [50, 51]. Spin coating is the process to produce thin solution layer on top of the substrate surfaces by centrifugal force as a result of spinning of substrates and to subsequently produce thin solid films by uniform solvent evaporation from the entire liquid–air interfaces [52]. However, the usability of the spin coating is limited as an industrial production process of semiconductor layers, both due to the enormous loss of raw materials during the process and to the difficulty in scaling up the device area which is strongly demanded in the application of flexible electronic devices. Nonetheless, the film formation mechanism may be quite reasonable to realize uniform thin films for the materials showing high degree of layered crystallinity.

In the subsequent subsections, we illustrate two new printing technologies that are designated to produce uniform thin films with layered-crystalline organic semiconductors. The first one is the "double-shot" inkjet printing technique that allows us to form single-crystalline films of some small-molecule semiconductors [41]. The second one is the "push-coating" technique that can alternate the (high material loss) spin coating [42]. We give basic concepts and concrete procedures for these new printing processes. We discuss that in these processes, the thin semiconductor solution layer is formed and is followed by gradual and uniform solvent extraction from the solution layer, as is similar to the spin coating.

1.3.3 Double-Shot Inkjet Printing Technique

The double-shot inkjet printing (IJP) is a novel concept to use two inkjet printheads and to deposit two kinds of microdroplets at the same positions on the substrate surfaces. It was recently reported that when antisolvent crystallization, i.e., a binary liquid mixture of a material solution and an antisolvent, is incorporated into an IJP-based microdroplet process, it becomes possible to manufacture highly uniform thin films as precipitates, where the coffee-ring effect can be eliminated. The scheme of double-shot inkjet printing technique is presented in Fig. 1.22. In the process, an antisolvent microdroplet is first deposited by the inkjet head on substrates, and then the semiconductor solution microdroplet is over-deposited at the same position by the other inkjet head, to form mixed sessile droplets on the substrate surfaces. In the mixed droplets, the semiconductor layer is first formed and then is dried by evaporating solvent after several minutes. Finally, the uniform crystalline semiconductor layer with uniform thickness of about 200 nm is formed over the area, if the suitable semiconductor material is utilized.

It was expected that the use of antisolvent crystallization could separate the time of occurrence of the solute crystallization and the solvent evaporation [53]. However, as it will be shown later, the semiconductor thin films grew at the whole area over the liquid–air interfaces of the mixed droplets. This feature is in striking contrast to conventional macroscopic antisolvent crystallization that produces a large mass of microcrystals due to rapid turbulent mixing inside the liquids. It is

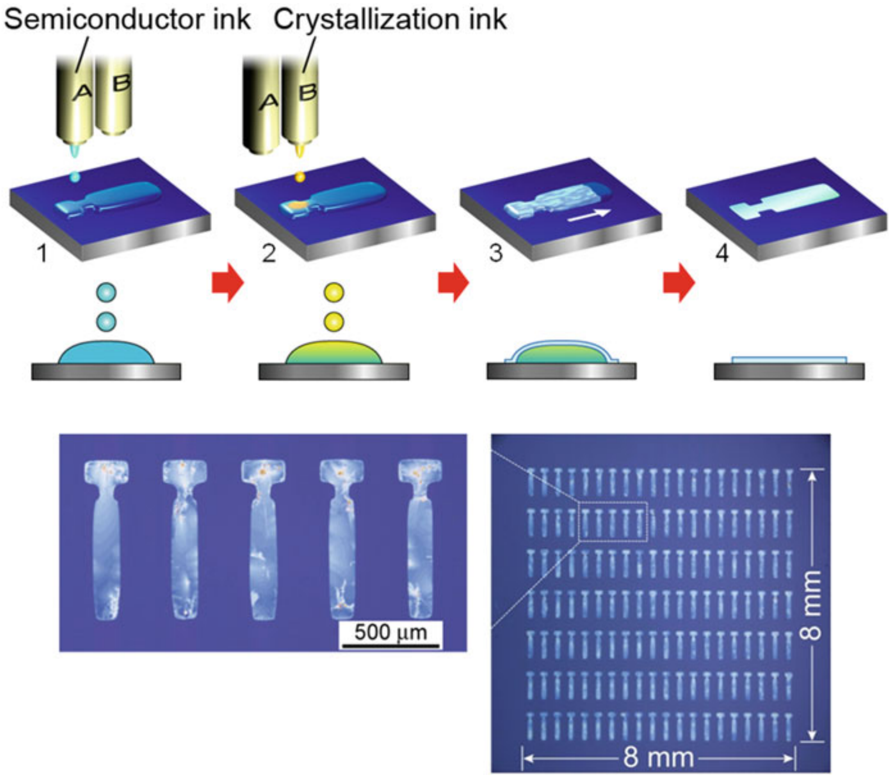

Fig. 1.22 Schematic for producing semiconductor single-crystal thin films by the double-shot inkjet printing technique (*upper*). Micrographs for single-crystal thin-film arrays produced by double-shot IJP technique (*lower*) [41]

thus quite likely that the chemically different binary microdroplet will exhibit unique mixing phenomena essentially different from macroscale fluids [54], as described below. Furthermore, the use of drop-on-demand process which is unique to the inkjet printing process allows us to control the crystal growth and to form single-crystalline thin films.

1.3.3.1 Mixing Process of Chemically Different Microdroplets

It has been frequently pointed out that microfluids present distinct dynamical characteristics that are different from those of macroscale fluids. For example, it is difficult to mix two kinds of microfluids rapidly inside microchannels [55, 56]. This feature has been discussed in terms of the low Reynolds number of the fluid flow in microchannels, which causes laminar flow to dominate over turbulent flow. Another unique characteristic of microfluids is that the surface (or interfacial) tension becomes predominant because it is primarily attributed to the high surface-area-to-volume

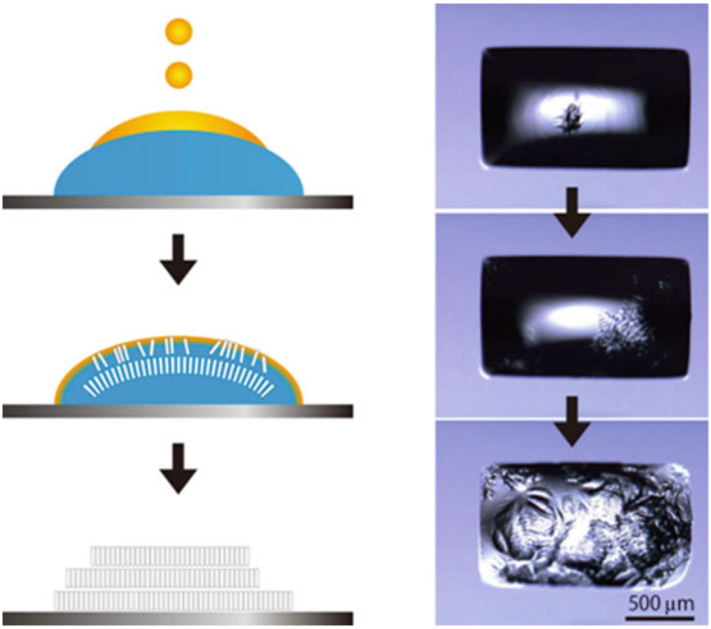

Fig. 1.23 Schematic for the microdroplet mixing process in the double-shot IJP process (*left*) and time-lapse micrographs of the droplets after the deposition of semiconductor solution microdroplet on top of the antisolvent sessile droplet. It is observed that the over-deposited microdroplet rapidly covers the entire surface of the sessile droplet, and the thin films are grown (Reproduced from ref. [54] by permission of John Wiley & Sons Ltd)

ratio of microfluids. Specifically, microdroplets that have free liquid–gas interfaces may exhibit more diversified dynamics in terms of the surface transformation than those confined within microchannels. It is thus expected that the mixing dynamics of the microdroplets should be considerably affected by the difference in surface tension between the mixed liquids. However, the dynamic nature of mixing binary microdroplets on solid surfaces has not been extensively studied so far.

We found that the mixing process between microdroplets is predominated by the difference of surface tension between liquids, the feature of which is much different from the mixing of macroscale fluids that is accompanied by turbulent flow. Particularly, the over-deposited microdroplets whose surface tension is lower than the sessile droplet rapidly cover the entire surface of the sessile droplet, as presented in Fig. 1.23. This is a type of Marangoni effect whose surface flow along the droplet surface is driven by the surface tension gradient. Therefore, it is possible to form thin semiconductor solution layer on top of the antisolvent droplet surface by the use of suitable combination of solvents. Then the solvent molecules are slowly diffused and mixed in the droplet, which contribute to the layered self-organization of the semiconductor molecules within the thin solution layer and thus to form the uniform crystalline films.

1.3.3.2 Single-Crystalline-Domain Formation

The “drop-on-demand (DOD)” feature, which means to allocate and deposit required volume of functional ink at a predefined position, is unique to the inkjet printing technology. If the nucleus is randomly generated at the surface of mixed microdroplets, the films are obtained as polycrystalline films. In contrast, it is found that the DOD function is also useful to form suitable concentration gradient within the droplet, which allows to control the nucleus generation and thus to grow single-domain crystal. Particularly, the single-domain formation should be advantageous to improve the device characteristics, because the domain boundaries between the grains are eliminated. We found that the single-domain formation is possible over the films by a tactic design of the droplet shape of the deposited sessile droplet by the surface modification of the substrate.

For the single-domain formation, we first controlled the droplet shape by hydrophilic/hydrophobic surface modification of substrates. The surface modification on silicon dioxide surface is conducted by the combination of the hydrophobization (formation of $SiO\text{-}Si(CH_2)_5CH_3$) with hexamethyldisilazane (HMDS) and the partial silanol (SiOH) formation by UV/ozone treatment. It was found that the droplet-shape formation of rectangular hydrophilic area with the necked region, as depicted in Fig. 1.22, is effective to produce concentration gradient and to control the growth direction of the films: When we deposit semiconductor ink at the head region beyond the neck part, a part with semiconductor ink with high concentration is formed which accelerates the formation of nucleus.

1.3.3.3 Thin-Film Characteristics

Here we present examples for the double-shot IJP process. We used 2,7-dioctyl[1]-benzothieno[3,2-b][1]benzothiophene (denoted as diC_8BTBT) as the solute organic semiconductors that has high degree of layered crystallinity [57–59]. We used 1-mM solution of diC_8BTBT in 1,2-dichlorobenzene (DCB) as the over-deposited microdroplet and *N*,*N*-dimethylformamide (DMF) as the antisolvent sessile droplet. Note that the process temperature for producing the single-crystal thin films and the subsequent devices is below 30 °C.

The obtained thin film is 30−100 nm in thickness, depending on the printing condition such as ink concentration, and is quite high uniform to exhibit molecularly flat surfaces. The synchrotron x-ray study was performed for the films, and it was found that all the diffractions were observed as clear spots (Fig. 1.24). The result clearly indicates the high crystallinity of the films. The refined unit cell based on the analyses of the observed Bragg diffractions is also consistent with that of diC_8BTBT. Additionally, the films were also investigated by a crossed-nicols microscope that is suitable for the observation of anisotropic crystals. It was found that the color of almost the entire film changes from bright to dark, simultaneously, on rotating the film about an axis perpendicular to the substrate (Fig. 1.25).

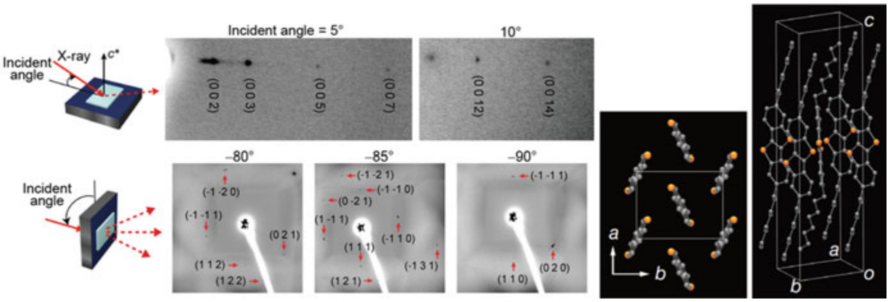

Fig. 1.24 Right: x-ray oscillation photographs of the organic semiconductor single-crystal thin films. Out-of-plane (*upper*) and in-plane diffractions (*lower*). *Left*: crystal structure of diC8BTBT [41]

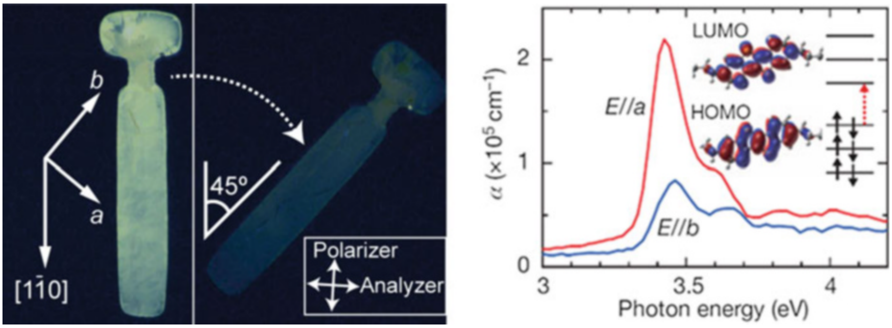

Fig. 1.25 Crossed-nicols polarized micrographs (*left*) and polarized optical absorption spectra with polarization parallel to the *a*- and *b*-axes (*right*) in the inkjet-printed single-crystal film of diC8BTBT [41]

The results imply the single-domain nature of the whole semiconductor thin films. Furthermore, stripe-like features with intervals of several micrometers to several tens of micrometers were observed in the ordinary optical microscope images of the films (Fig. 1.26). In the atomic-force microscope image, the similar stripe-like features are observed, and are found to correspond to the step-and-terrace structure with step height of 2.3−2.8 nm. The stripes are associated with the molecular step in diC$_8$BTBT and can be ascribed to the step-and-terrace structure that is characteristic of the semiconductor single-crystal thin films.

Field-effect transistors were fabricated with the organic semiconductor single-crystal thin films by forming source and drain electrodes (Au) and the gate dielectric layer (organic polymer film). The mobility of the device in the saturation regime reaches 16.4 cm^2/Vs on average. The on/off current ratio is $10^5 - 10^7$, and the subthreshold slope was about 2 V per decade with a threshold voltage of about 10 V. As presented above, the double-shot inkjet printing technique is quite useful for manufacturing organic semiconductor thin films with highly uniformity and with considerably improved performance in the TFTs, having been the main challenge in the printed electronics technology.

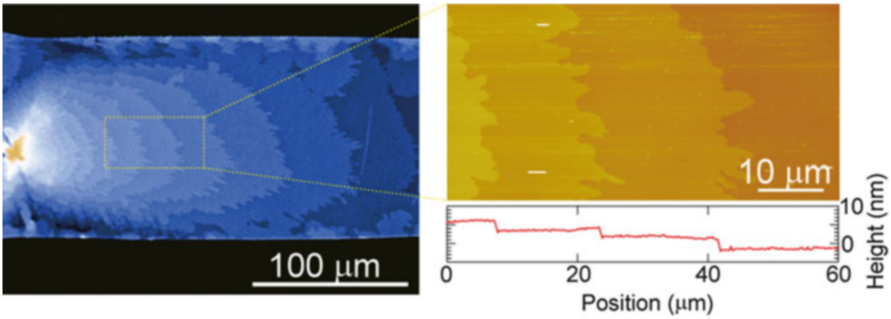

Fig. 1.26 Optical micrograph (*left*) and atomic-force microscopy image (*right*) showing the step-and-terrace structure on the organic semiconductor single-crystal thin film of diC8BTBT [41]

1.3.4 Push-Coating Technique

As discussed in Sec. 3-2, the spin-coating technique is widely utilized for the production of plain thin films of organic semiconductors. There are many problems, however, in the spin-coating technique, with regard to the large material loss and limited controllability for the thin film growth. For example, it is known that crystallinity of organic semiconductors can be improved by the use of highly hydrophobic substrates or the use of high-boiling point solvent, whereby the device characteristics can be improved [60–62]. However, it is quite difficult by spin coating to form uniform thin films with use of such a substrate or solvent, as most of the material will be lost.

We have developed a "push-coating technique," as an alternative, which uses viscoelastic silicone stamp using polydimethylsiloxane (PDMS) to spread polymer solution on the substrate and subsequently to absorb solvent slowly from the thin solution layer. Figure 1.27 shows the schematic of the process. First, we deposit a tiny amount of polymer semiconductor solution on the substrate and then press a viscoelastic stamp on to spread the solution, by which the uniform thin solution layer is formed between the stamp and the substrate. Subsequently, thin solid film is formed by extracting solvent with the stamp. Finally, the stamp is peeled off from the film. The uniform thin-film formation process is quite similar with the spin-coating technique, in terms of the thin solution layer formation and subsequent extraction of solvent. The feature is quite fitted to the organic semiconductors that have high degree of the layered crystallinity.

In the lower part of Fig. 1.27, we present an example of the obtained plain organic semiconductor films by the push-coating technique; the typical polymer semiconductor, poly-3-hexylthiophene (P3HT), is used to form films on highly hydrophobic silicon substrate whose surface (water contact angle is 110°) is treated with a silane-coupling agent. Although the high-boiling point solvent (1,2,4-trichlorobenzene with boiling point at 214 °C) is used, uniform thin films can be manufactured with eliminating the material loss. It takes about a few minutes to

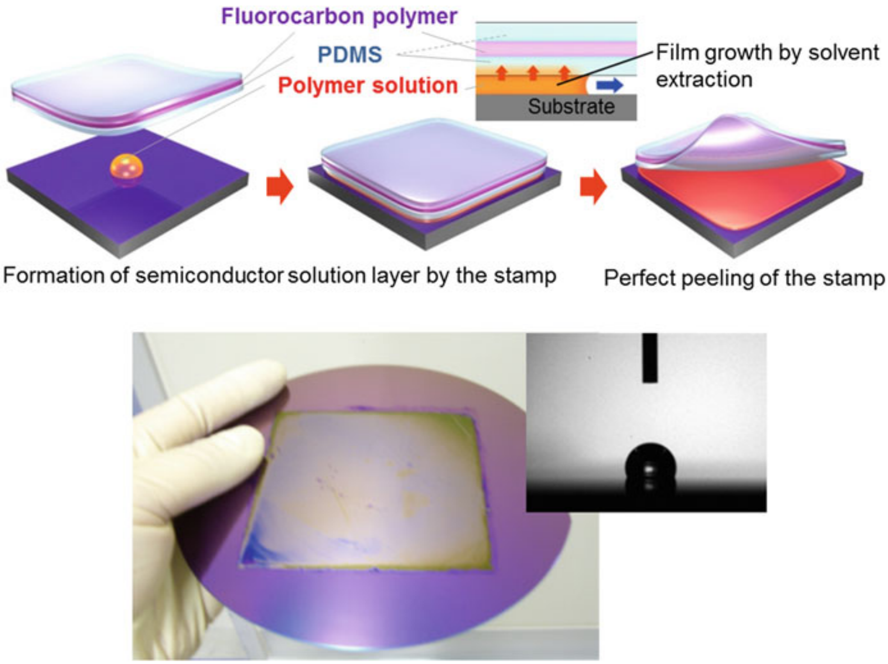

Fig. 1.27 Schematic of the film production process by the push-coating technique (*upper*). P3HT film produced by the push-coating technique on highly hydrophobic surface (*lower left*) and water contact angle on the substrate surface (*lower right*) [42]

absorb solvent from the solution layer. As the absorbing velocity of the solvent is slower than the spreading velocity of the solution, it was easy to form larger-area films.

It was advantageous to use the stamp with trilayer structure which is composed of PDMS both-sided surface layer and solvent-resistant fluorinated silicone layer. There are two advantages in the use of the stamp with the trilayer structure. The first one is the shape stability of the stamp. If the single-layer PDMS is used, the stamp will be easily deformed by the solvent absorption, so that it is not easy to form uniform thin solution layer. In contrast, the stamp with trilayer structure is not deformed against the solvent absorption. In addition, the repeated use of the stamp is also possible after the solvent extraction due to such shape stability. The second advantage is that the stamp can be easily detached from the film. As the solvent retains within the PDMS stamp for a long period of time, the semiwet nature is retained at the stamp surface during the film formation. As a result, adhering force between the film and stamp is always weaker than that between the film and substrate. Therefore, it is possible to detach the stamp with all the films left on the substrate.

Various types of patterning method are applicable in the push-coating technique, as it can form thin films on any substrate surfaces. In Fig. 1.28, we show an example

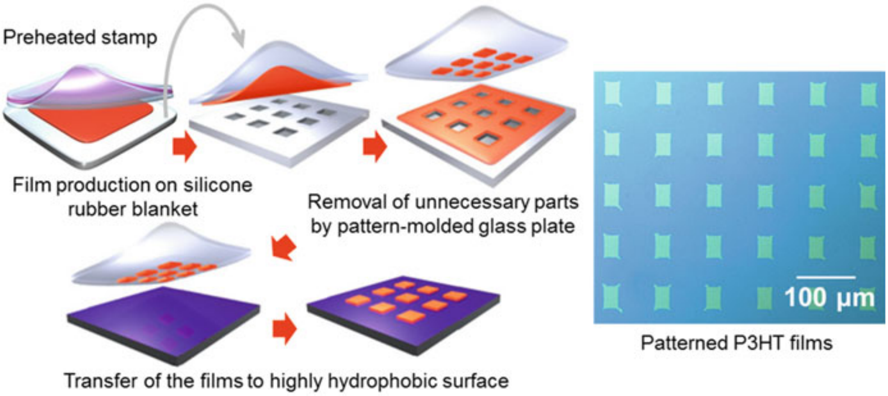

Fig. 1.28 Negative image patterning process for a push-coated film [42]

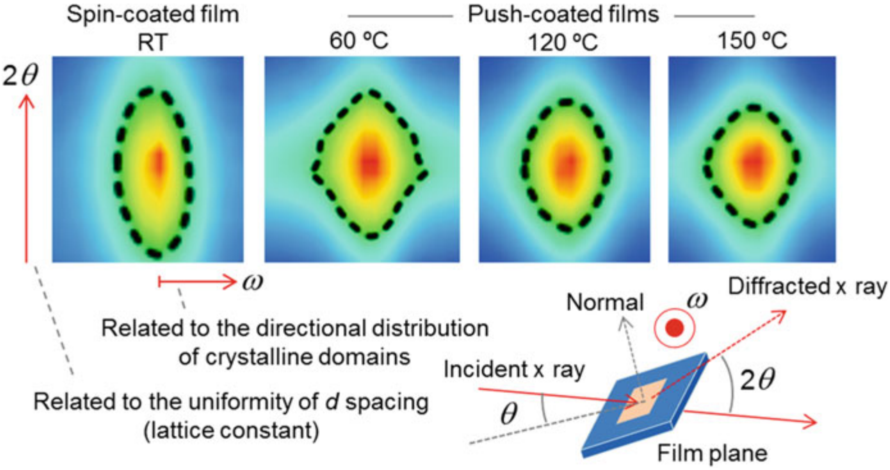

Fig. 1.29 Peak profiles of the x-ray diffractions for the films processed at different conditions [42]

for the thin-film patterning with use of the inverse printing method. First we fabricated polymer semiconductor films on a silicone blanket. When we heat the stamp at 35 °C, by which the solvent-absorbing capability of the stamp is higher than that of the blanket, all the films are left on the blanket, after the stamp is peeled off. Next we remove the unnecessary part of the film by attaching the molded glass plate. The films left on the blanket can be then transferred even to the substrate with any highly hydrophobic surface, and as a result, high-resolution pattern film is obtained.

Additionally, it is possible to use high-boiling point solvent in the push-coating technique, so that the temperature and duration for the film growth can be widely controlled. In Fig. 1.29, we show the intensity profile of (100) diffraction peak as measured, where the 1,2,4-trichlorobenzene is used to grow the P3HT films at various temperatures. By the increase of temperature for the film growth, it is seen that the diffraction profile is narrowed. From the analyses of the peak profile, interlayer distance is distributed (1.34−1.39 nm) in the spin-coated films, while the interlayer distance of the films fabricated at 150 °C is uniform at 1.34 nm. It means that the high-temperature process is quite effective to improve the structural order between the polymer chains. With use of the push-coated films, we fabricated bottom gate/bottom contact OTFTs. We used silicon dioxide as gate dielectric layer and gold film as the source/drain electrode (with channel length at 5−100 μm and width at 5 μm). As a result, the OTFTs based on the push-coated films exhibit mobility (0.5 cm^2/Vs) about one order higher than the OTFTs based on the spin-coated films.

1.3.5 Short Summary and Outlook

The flatness and uniformity of the semiconductor layers at atomic or molecular level are the key factors to obtain excellent device performance in the semiconductor devices. In order to realize such a semiconductor layer by printing technology, we have introduced double-shot inkjet printing technique and push-coating technique, both of which are designed to promote self-organization of semiconductor molecules to form layered crystals. Especially, the formation of thin semiconductor solution layer and the subsequent uniform evaporation solvent from the solution layer are the key factors for the uniform thin-film formation. In order to realize the printed electronics technology, it would be further necessary to establish the basic understanding of the microdroplet-based device process, to design of molecules with higher degree of molecular ordering, and to sophisticate the printing process. By these studies, we consider that the semiconductor device performance should be more improved. Furthermore, in order to realize the printed electronics, it would be also necessary to develop print production technology for metal wires and insulator layers in addition to the semiconductor layers. For this, the development of printing technology that takes advantage of the material characteristics should be utmost important. In this meaning, it becomes more and more important to utilize the outcome of molecular nanotechnology that has been studied, for a couple of these decades, to promote the self-organization of molecules, nanometal inks that disperse metal nanoparticles, or surface chemical modification with use of surfactant molecules to manipulate microdroplets.

Acknowledgement The author is grateful to Dr. Hiroyuki Matsui, Dr. Hiromi Minemawari, Dr. Yuki Noda, and Dr. Satoru Inoue, for their help in the preparation of the manuscript.

References

1. M. Pope, C.E. Swenberg, *Electronic Processes in Organic Crystals and Polymers*, 2nd edn. (Oxford University Press, New York, 1999)
2. G.H. Wagniere, *Introduction to Elementary Molecular Orbital Theory and to Semiempirical Methods*. Lecture Notes in Chemistry (Springer, Berlin/Heidelberg, 1976)

3. T. Bally, W.T. Borden, in *Reviews in Computational Chemistry*, ed. by K.B. Lipkowitz, D.B. Boyd, vol. 13 (Wiley, New York, 1999)
4. P. Prins, K. Senthilkumar, F.C. Grozema, P. Jonkheijm, A.P.H.J. Schennin, E.W. Meijer, L.D. A. Siebbeles, J. Phys. Chem. B **109**, 18267–18274 (2005)
5. *ADF calculation were performed by using the PW91/TZP package*. ADF2013.01, Scientific Computing & Modeling (SCM), Theoretical Chemisty, Vrije Universiteit: Amsterdam, The Netherlands. http://www.scm.com
6. C. Kittel, *Introduction to Solid State Physics* (Wiley, New York, 2014)
7. W. Clegg (ed.), *Crystal Structure Analysis: Principles and Practice* (Oxford University Press, New York, 2009)
8. M. Yoneya, M. Kawasaki, M. Ando, J. Mater. Chem. **20**, 10397–10402 (2010)
9. F. Seitz, N.G. Einspruch, *Electronic Genie: The Tangled History of Silicon* (UI Press, Illinois, 1998)
10. S.M. Sze, *Semiconductor Devices: Physics and Technology* (Wiley, New York, 1985)
11. S.F. Nelson, Y.-Y. Lin, D.J. Gundlach, T.N. Jackson, Appl. Phys. Lett. **72**, 1854 (1998)
12. V. Podzorov, E. Menard, A. Borissov, V. Kiryukhin, J.A. Rogers, M.E. Gershenson, Phys. Rev. Lett. **93**, 086602 (2004)
13. M.E. Gershenson, V. Podzorov, A.F. Morpurgo, Rev. Mod. Phys. **78**, 973 (2006)
14. R.A. Marcus, Rev. Mod. Phys. **65**, 599 (1993)
15. J. Brédas, D. Beljonne, V. Coropceanu, J. Cornil, Chem. Rev. **104**, 4971 (2004)
16. J. Jortner, J. Chem. Phys. **64**, 4860 (1976)
17. J. Takeya, J. Kato, K. Hara, M. Yamagishi, R. Hirahara, K. Yamada, Y. Nakazawa, S. Ikehata, K. Tsukagoshi, Y. Aoyagi, T. Takenobu, Y. Iwasa, Phys. Rev. Lett. **98**, 196804 (2007)
18. J.S. Miller, J.S. Miller (eds.), *Extended Linear Chain Compounds*, vol. 2 and 3 (Plenum Press, New York, 1983)
19. T. Ishiguro, K. Yamaji, G. Saito, *Organic Superconductors*. Springer Series in Solid-State Sciences, vol. 88 (Springer, Berlin, 1998)
20. A. Troisi, G. Orlandi, Phys. Rev. Lett. **96**, 086601 (2006)
21. J.-D. Picon, M.N. Bussac, L. Zuppiroli, Phys. Rev. B **75**, 235106 (2007)
22. S. Fratini, S. Ciuchi, Phys. Rev. Lett. **103**, 266601 (2009)
23. V. Coropceanu, M. Malagoli, D.A. da Silva Filho, N.E. Gruhn, T.G. Bill, J.L. Brédas, Phys. Rev. Lett. **89**, 275503 (2002)
24. N. Ueno, S. Kera, Prog. Sur. Sci. **83**, 490 (2008)
25. I.N. Hulea, S. Fratini, H. Xie, C.L. Mulder, N.N. Iossad, G. Rastelli, S. Ciuchi, A.F. Morpurgo, Nat. Mater. **5**, 982 (2006)
26. W.L. Kal, B. Batlogg, Phys. Rev. B **81**, 035327 (2010)
27. C.P. Slichter, *Principles of Magnetic Resonance*. Springer Series in Solid-State Sciences, vol. 1 (Springer, Berlin, 1996)
28. K. Marumoto et al., J. Phys. Soc. Jpn. **73**, 1673 (2004)
29. K. Marumoto et al., Phys. Rev. Lett. **97**, 256603 (2006)
30. H. Matsui, T. Hasegawa, Y. Tokura, M. Hiraoka, T. Yamada, Phys. Rev. Lett. **100**, 126601 (2008)
31. R. Kubo, K. Tomita, J. Phys. Soc. Jpn. **9**, 888 (1954)
32. P.W. Anderson, J. Phys. Soc. Jpn. **9**, 316 (1954)
33. H. Matsui, D. Kumaki, E. Takahashi, K. Takimiya, S. Tokito, T. Hasegawa, Phys. Rev. B **85**, 035308 (2012)
34. G. Horowitz, P. Delannoy, J. Appl. Phys. **70**, 469 (1991)
35. G. Horowitz, R. Hajloui, P. Delannoy, J. Phys. III **5**, 355 (1995)
36. M.F. Calhoun, C. Hsieh, V. Podzorov, Phys. Rev. Lett. **98**, 096402 (2007)
37. H. Matsui, A.S. Mishchenko, T. Hasegawa, Phys. Rev. Lett. **104**, 056602 (2010)
38. A.S. Mishchenko, H. Matsui, T. Hasegawa, Phys. Rev. B **85**, 085211 (2012)
39. J.R. Bolton, J. Chem. Phys. **46**, 408 (1967)

40. T. Kawase, T. Shimoda, C. Newsome, H. Sirringhaus, R.H. Friend, Thin Solid Films **279**, 438 (2003)
41. H. Minemawari, T. Yamada, H. Matsui, J. Tsutsumi, S. Haas, R. Chiba, R. Kumai, T. Hasegawa, Nature **475**, 364 (2011)
42. M. Ikawa, T. Yamada, H. Matsui, H. Minemawari, J. Tsutsumi, Y. Horii, M. Chikamatsu, R. Azumi, R. Kumai, T. Hasegawa, Nat. Commun. **3**, 1176 (2012)
43. J.C. Berg, *An Introduction to Interfaces & Colloids – The Bridge to Nanoscience* (World Scientific, Singapore, 2010)
44. R.D. Deegan, O. Bakajin, T.F. Dupont, G. Huber, S.R. Nagel, T.A. Witten, Nature **389**, 827 (1997)
45. J.H. Burroughes, D.D.C. Bradley, A.R. Brown, R.N. Marks, K. Mackay, R.H. Friend, P.L. Burns, A.B. Holmes, Nature **347**, 539 (1990)
46. H. Sirringhaus, P.J. Brown, R.H. Friend, M.M. Nielsen, K. Bechgaard, B.M.W. Langeveld-Voss, A.J.H. Spiering, R.A.J. Janssen, E.W. Meijer, P. Herwig, D.M. de Leeuw, Nature **401**, 685 (1999)
47. H. Sirringhaus, T. Kawase, R.H. Friend, T. Shimoda, M. Inbasekaran, W. Wu, E.P. Woo, Science **290**, 2123 (2000)
48. J.E. Anthony, J.S. Brooks, D.L. Eaton, S.R. Parkin, J. Am. Chem. Soc. **123**, 9482 (2001)
49. H. Ebata, T. Izawa, E. Miyazaki, K. Takimiya, M. Ikeda, H. Kuwabara, T. Yui, J. Am. Chem. Soc. **129**, 15732 (2007)
50. H. Yan, Z. Chen, Y. Zheng, C. Newman, J.R. Quinn, F. Doetz, M. Kastler, A. Facchetti, Nature **475**, 679 (2009)
51. X. Zhang, S.D. Hudson, D.M. DeLongchamp, D.J. Gundlach, M. Heeney, I. McCulloch, Adv. Funct. Mater. **20**, 4098 (2010)
52. D.W. Schubert, T. Dunkel, Mat. Res. Innovat. **7**, 314 (2003)
53. M. Hiraoka, T. Hasegawa, T. Yamada, Y. Takahashi, S. Horiuchi, Y. Tokura, Adv. Mater. **19**, 3248 (2007)
54. Y. Noda, H. Minemawari, H. Matsui, T. Yamada, S. Arai, T. Kajiya, M. Doi, T. Hasegawa Adv. Funct. Mater. **25**, 4022 (2015)
55. A.D. Stroock et al., Science **295**, 647 (2002)
56. J.M. Ottino, S. Wiggins, Phil. Trans. R Soc. Lond. Math. Phys. Sci. **362**, 923 (2004)
57. T. Izawa, E. Miyazaki, K. Takimiya, Adv. Mater. **20**, 3388 (2008)
58. T. Uemura, Y. Hirose, M. Uno, K. Takimiya, J. Takeya, Appl. Phys. Expr **2**, 111501 (2009)
59. T. Minari, C. Liu, M. Kano, K. Tsukagoshi, Adv. Mater. **24**, 299 (2012)
60. B. Meredig, A. Salleo, R. Gee, ACS Nano **3**, 2881 (2009)
61. T. Umeda, D. Kumaki, S. Tokito, J. Appl. Phys. **105**, 024516 (2009)
62. W.L. Kalb, T. Mathis, S. Haas, A.F. Stassen, B. Batlogg, Appl. Phys. Lett. **90**, 092104 (2007)

Chapter 2
Organic Light-Emitting Diodes (OLEDs): Materials, Photophysics, and Device Physics

Chihaya Adachi, Saeyoun Lee, Tetsuya Nakagawa, Katsuyuki Shizu, Kenichi Goushi, Takuma Yasuda, and William J. Potscavage Jr.

Abstract Currently, organic light-emitting diodes (OLEDs) have reached the stage of commercialization, and there has been an intense drive to use them in various applications from small- and medium-sized mobile devices to illumination equipment and large television screens. In particular, room-temperature phosphorescent materials have become core OLED components as alternatives to conventionally used fluorescent materials because devices made with phosphorescent materials exhibit excellent light-emitting performance with internal electroluminescence efficiencies (η_{int}) of nearly 100 %. However, phosphorescent materials have several intrinsic problems, such as being limited to metal–organic compounds containing rare metals, for example, Ir, Pt, Au, and Os, and difficulty in realizing stable blue light emission. As a result, researchers have attempted to develop new materials for use as emissive dopants in OLEDs that overcome these limitations. In this chapter, first we briefly review the progress of OLED materials and device architectures mainly based on fluorescent (first-generation) and phosphorescent (second-generation) emitters. Then, we discuss third-generation OLEDs that use a new light-emitting mechanism called thermally activated delayed fluorescence (TADF). Recently, highly efficient TADF, which had been difficult to realize with conventional molecular design, has been achieved by very sophisticated molecular structures, allowing access to the unlimited freedom of molecular design using carbon-based materials. This has led to the production of ultimate OLEDs that are made of common organic compounds without precious metals and can convert electricity to light at η_{int} of nearly 100 %.

C. Adachi (✉) • S. Lee • K. Goushi • W.J. Potscavage Jr.
Center for Organic Photonics and Electronics Research (OPERA), Kyushu University,
744 Motooka, Nishi, Fukuoka 819-0395, Japan

JST, ERATO, Adachi Molecular Exciton Engineering Project, c/o Center for Organic
Photonics and Electronics Research (OPERA), Kyushu University, 744 Motooka, Nishi,
Fukuoka 819-0395, Japan
e-mail: adachi@cstf.kyushu-u.ac.jp; chihaya_adachi@me.com

T. Nakagawa • K. Shizu • T. Yasuda
Center for Organic Photonics and Electronics Research (OPERA), Kyushu University,
744 Motooka, Nishi, Fukuoka 819-0395, Japan

S. Ogawa (ed.), *Organic Electronics Materials and Devices*,
DOI 10.1007/978-4-431-55654-1_2

Keywords OLED • TADF • Electroluminescence

2.1 Introduction

Materials can be classified into three groups in terms of electrical conductivity: insulators, semiconductors, and metals. In general, organic molecules composed of carbon skeletons act as insulators, as exemplified by plastics. However, very different conductivity can be obtained by forming an ultrathin film (approximately 0.1 μm thick) of such insulating organic molecules. When an organic thin film is sandwiched between two electrodes and a voltage of approximately 10 V is applied, electrons and holes are injected from the cathode and anode, respectively, into the film by overcoming the energy barriers at the corresponding interfaces. These injected carriers hop toward the opposite electrode, following the electric potential gradient. When an electron and hole recombine at a molecule, an excited state, namely, a molecular exciton, is induced. Photons are emitted when the excited state relaxes to the ground state. This entire process is called organic electroluminescence (EL). Because their emission mechanism is similar to that of inorganic light-emitting diodes (LEDs), devices that emit organic EL are widely known as organic LEDs (OLEDs). The ultrathin-film architecture of OLEDs means that a high electric field of over 10^6 V/cm can be applied to the organic thin film. Under such extreme conditions, carriers are injected from the electrodes into the organic thin film and can easily hop between molecules. Thus, unprecedented high current injection and transport can be realized in this case, even though the organic thin film behaves as a complete insulator under low electrical fields of $<10^3$ V/cm.

In 1950, Japanese scientists Inokuchi and Akamatsu [1], who demonstrated the doping of donors and acceptors into organic solids based on a similar idea in inorganic semiconductors, first discovered electrical conduction in organic materials and established the category of organic semiconductors (Fig. 2.1). In 1965, clear EL was confirmed from a single crystal of anthracene by Helfrich and Schneider [2]. They also carried out pioneering research on liquid crystals, developing twisted nematic liquid crystals. At that time, scientists discussed whether OLEDs or liquid crystals were more suitable for display devices, as can be seen in the literature of the time. Eventually, liquid crystals were chosen as the main research focus for targeting practical display devices, and the target of research on OLEDs shifted from single crystals to ultrathin films in an attempt to realize low-voltage operation. Because the initial OLEDs used single crystals with a thickness of a few millimeters, they required a few thousand volts to emit light and thus were thought to be far from commercialization. After almost 50 years of development focusing on novel organic molecules and device architectures, OLEDs have now reached the stage of commercialization, albeit 20 years behind the commercialization of liquid crystals. In particular, the research and development of OLEDs has rapidly accelerated since 1990, and their practical application

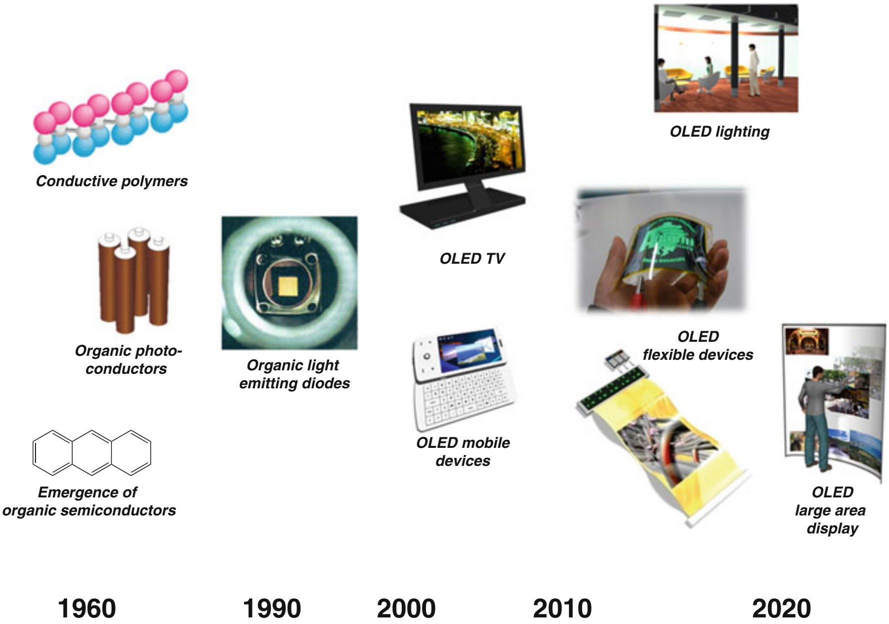

Fig. 2.1 History of research and development of organic semiconductors. The concept of organic semiconductors was established in the 1950s and 1960s. The research fields of conductive polymers and OPCs were established in the 1970s and 1980s. The full-scale research and development of organic electronic devices actively using a current density in the order of mA/cm^2 started from the 1980s. Since then, extensive research and development of OLEDs, OSCs, organic transistors, and organic memories has been carried out, from basic research to practical application. Organic semiconductors are expected to be applied to bioelectronics in the future

has leaned toward small display devices, such as mobile phones and MP3 players, and flat-panel TV screens since 2000. In this span, it has been undoubtedly confirmed that electric charges can transport between adjacent molecules through suitable π-electron orbitals under a high electric field; consequently, thin films of organic molecules can be used as semiconductor thin films. Such unique organic semiconductor behavior has been established through the development of OLEDs and has led to the emergence of novel semiconductors.

Organic photoconductor (OPC) units in the xerographic process were the first commercialized electronic devices using organic semiconductors and are the heart of copiers and laser printers used daily in homes and offices. When the charged layer formed on the surface of an OPC is irradiated with light, current flows through the organic semiconductor layer to form a latent image. OPCs have now become a main component of the printing industry as a result of the dramatic spread of laser printers and copiers. In fact, the organic molecules currently used in OLEDs are an extension of the materials developed for OPCs. Also we note that the progress of conducting polymers has considerably influenced the research and development of OLEDs from the perspectives of both materials and device design. Since the early

1990s, various molecular skeletons for carrier transport of both holes and electrons have been designed and synthesized based on the molecular design for OPCs. Also in the 1990s, a wide variety of fluorescent molecules for use as emitters and their optimum device architectures were developed, while phosphorescent emitters and their device architectures have been in development since around 2000. In particular, we stress that electron transport materials are a major point in the development of OLED materials, because until around 2000, almost all organic semiconductors used for OPCs were hole-transport materials, and few electron transport materials had been identified. Thus, the molecular design for organic materials that conduct electrons was established through research on OLEDs [3]. On the basis of research achievements regarding OLEDs, a wide range of research and development of next-generation organic devices, such as organic solar cells (OSCs), organic transistors, organic memories, and organic semiconductor lasers, is now ongoing, and these technologies will be connected to future bioelectronics.

We note that in the history of research on the aforementioned organic optoelectronics, OLEDs were the first devices based on organic thin films capable of being operated at current densities as low mA/cm^2 levels and are considered to be the core organic optoelectronic devices realized by using organic molecules as active semiconductors. Since 2000, organic electronics has become not only an independent academic field but also an established industry and is beginning to gain market value. The new organic semiconductor materials, device physics, and device engineering developed in relation to OLEDs have been applied to produce novel next-generation devices. Thus, a new industrial field of electronics has evolved.

2.2 Basics of Organic Light-Emitting Diodes (OLEDs)

In this section, the recent progress in OLED device architectures, organic fluorescent and phosphorescent materials, roll-off characteristics of external quantum efficiency (η_{ext}) of OLEDs, white OLEDs, and solution processing is introduced.

2.2.1 Progress of Device Structures

In OLEDs, excitons can be formed by the recombination of holes and electrons. The excitons can lose their energy through a radiative decay process in an emitting layer (EML). In an EL process, recombined holes and electrons generate excitons with four different spin combinations of one singlet (antiparallel spins) and three triplets (parallel spins). Therefore, statistically, 25 % of the formed excitons are singlets and 75 % are triplets, the relaxation of which results in the different radiative decay processes of fluorescence and phosphorescence, respectively. The fundamental structure of OLEDs that allows carrier flow is shown in Fig. 2.2. Holes are injected

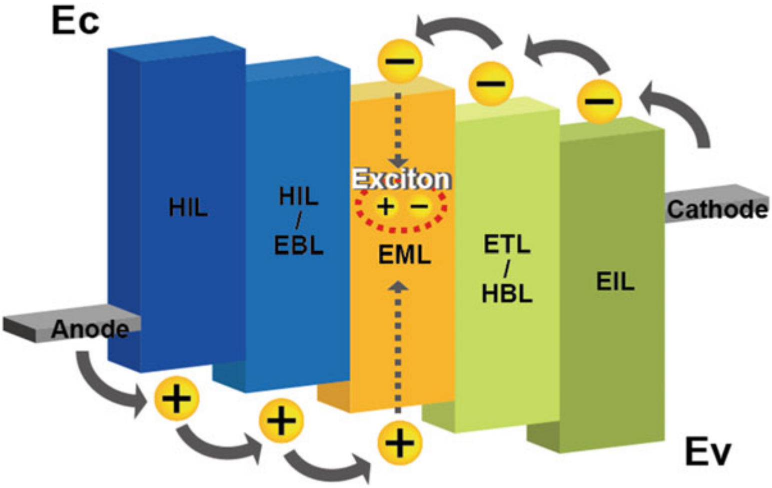

Fig. 2.2 Operating mechanism of OLEDs (*HIL* hole-injection layer, *HTL* hole-transport layer, *EBL* electron-blocking layer, *EML* emitting layer, *ETL* electron-transport layer, *HBL* hole-blocking layer, *EIL* electron-injection layer)

into the hole conduction level (E_v) and electrons are injected into the electron conduction level (E_c) from the anode and cathode, respectively. We call this phenomenon carrier injection. Holes and electrons are successively transported through a hole-transport layer (HTL) and an electron-transport layer (ETL), respectively. In addition, on the anode side, a hole-injection layer (HIL), which has a small energy gap with respect to both the work function of the anode layer and E_v of the HTL and thus facilitates the injection of holes, is often included. In a similar manner, on the cathode side, an electron-injection layer (EIL) with an intermediate E_c between that of the ETL and the work function of the cathode layer has been introduced for effective electron injection and transport. This multilayer structure can improve the carrier injection and transport efficiencies of OLEDs, resulting in the enhancement of the recombination of holes and electrons in an EML at lower driving voltage. Furthermore, electron- and hole-blocking layers (EBL and HBL, respectively) are also widely included in OLEDs to improve the charge balance of holes and electrons and confinement of excitons by preventing the leakage of charge carriers and excitons from the EML to adjacent layers. Thus, present high-performance OLEDs are composed of multiple layers.

The very first report on EL can be traced to Bernanose’s observation of EL from organic dye-containing polymer thin films when applying a high alternating current (AC) voltage in 1950. In 1965, blue EL was observed from an anthracene single crystal by applying a rather high voltage of over 1000 V [4]. It should be noted that the recombination of holes and electrons was found to result in the direct generation of both singlet and triplet excitons [5]. In the 1980s, a wide variety of thin-film device architectures were examined, and OLEDs based on a thin film of anthracene fabricated by vacuum deposition were shown to emit light at a low voltage of 12 V

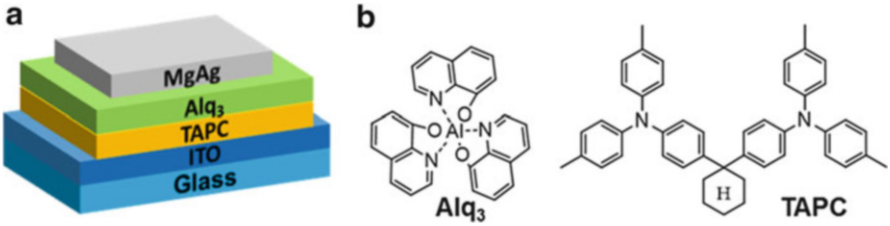

Fig. 2.3 (**a**) Device structure of a double-layered OLED reported by Tang et al. (**b**) Molecular structures of tris(8-quinolinolato)aluminum(III) (Alq_3) as an emitter and 4,4′-cyclohexylidenebis [*N*,*N*-bis(4-methylphenyl)benzenamine] (TAPC) as a hole-transport layer

[6]. Advanced studies on multilayer OLEDs were reported by Tang et al. in 1987 [7]. An OLED using tris(8-quinolinolato)aluminum(III) (Alq_3) and aromatic amines as an ETL (EML) and HTL, respectively, and Mg:Ag as a cathode, exhibited a high luminance of 1000 cd A^{-1} at 10 V and η_{ext} of nearly 1 % (Fig. 2.3). In successive work, by doping the EML with dicyanomethylene and coumarin, the emission color was finely controlled and η_{ext} was more than doubled [8]. At the same time, the concept of an ETL that confined charge carriers and molecular excitons was confirmed by using novel electron transport materials [3, 9].

In addition, not only small molecules but also polymers are being used in thin-film OLEDs. In an early study using poly(vinylcarbazole) (PVCz) as a host material, light emission by EL was confirmed [10]. In the 1990s, Burroughes reported polymer OLEDs containing poly(*p*-phenylene vinylene) (PPV) as an EML [11]. After that, luminescent polymer materials including polyphenylenes and polythiophenes have been actively developed.

In 1997, the first commercial application of OLEDs in a car radio system was realized. At present, OLEDs are widely used in mobile phones, tablet computers, lighting, and televisions. Since the first reports of OLEDs, a wide variety of organic semiconducting and luminescent materials, probably over one hundred thousand, have been designed and synthesized.

2.2.2 *Luminescence Mechanisms of Organic Molecules and Solid Films*

The luminescence phenomenon of organic materials when they are excited by a light source can be explained by the following photophysical interpretation. The absorption of a photon in an organic material causes an electron to be excited from its ground state (S_0) to a singlet excited state (S_1). After photoexcitation, the excited electron loses its energy through photoluminescence (PL), intermolecular energy transfer, intramolecular energy transfer, isomerization, or dissociation (Fig. 2.4) [12].

Organic luminescent materials can be characterized by their absolute PL quantum efficiency (Φ_{PL}), which is defined as the ratio of photons emitted to photons absorbed

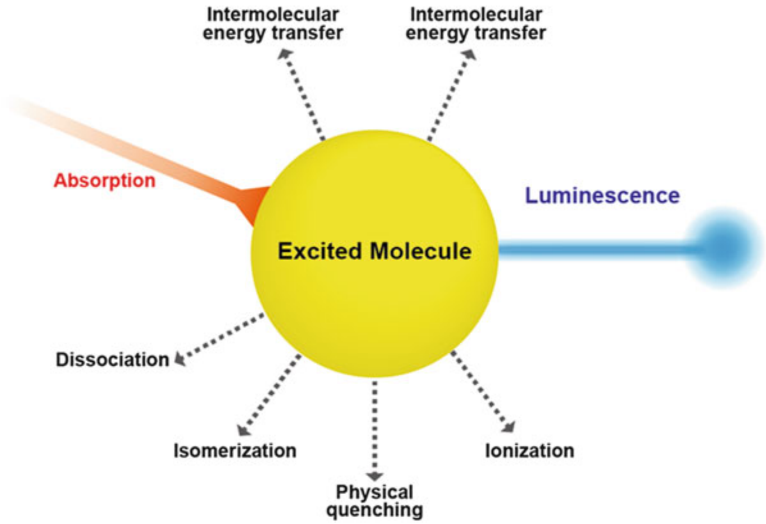

Fig. 2.4 Relaxation routes of optically excited organic molecules

Table 2.1 Transition times of absorption, internal conversion, intersystem crossing, fluorescence, phosphorescence, and thermally activated delayed fluorescence (TADF)

	Transition time
Absorption	10^{-15} s
Internal conversion	10^{-15} s – 10^{-10} s
Fluorescence	10^{-9} s – 10^{-5} s
Intersystem crossing	10^{-8} s – 10^{-5} s
Phosphorescence	10^{-6} s – 10^{2} s
TADF	10^{-6} s – 10^{-2} s

by the molecules, transient lifetime (τ), and emission spectrum. The occurrence of nonradiative decay decreases both Φ_{PL} and τ. The luminescence from organic materials can be more specifically described as fluorescence or phosphorescence. These two emission processes can be distinguished by τ. While τ for fluorescence ranges from 10^{-9} to 10^{-8} s, τ for phosphorescence is much longer and ranges from 10^{-6} to 10^{2} s (Table 2.1). In the case of fluorescence, excited electrons relax directly from S_1 to S_0 to emit light (Eq. 2.1). In contrast, phosphorescence occurs from a triplet excited state (T_1), which is formed by intersystem crossing (ISC) from S_1 (Eq. 2.2). Because phosphorescence is a spin-forbidden process, its τ is usually longer than that of fluorescence.

$$\text{(Fluorescence)} \qquad S_0 + h\nu_{ex} \rightarrow S_1 \rightarrow S_0 + h\nu_{em} \tag{2.1}$$

$$\text{(Phosphorescence)} \qquad S_0 + h\nu_{ex} \rightarrow S_1 \rightarrow T_1 \rightarrow S_0 + h\nu_{em} \tag{2.2}$$

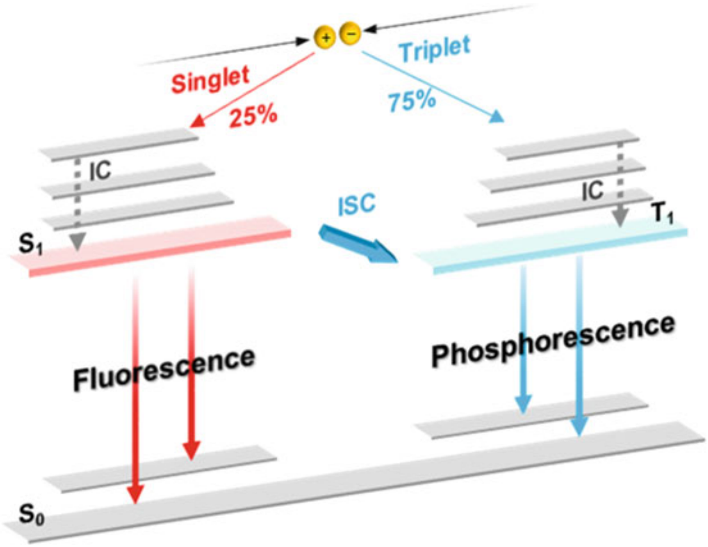

Fig. 2.5 Jablonski diagram of electronic transitions for fluorescence (S_1–S_0) and phosphorescence (T_1–S_0) after recombination of holes and electrons

When luminescence is produced by electrical excitation, i.e., EL, rather than by exposure to light, it can again originate from both fluorescence and phosphorescence (Fig. 2.5). Fluorescent OLEDs emit through the radiative relaxation of singlet excitons, while the emission of phosphorescent OLEDs originates from triplet excitons. Because of the 1:3 branching ratio of singlet and triplet excitons under electrical excitation mentioned earlier [12], the production efficiency of singlet excitons is limited to just 25 %. In contrast, phosphorescent OLEDs can utilize both singlet and triplet excitons for phosphorescent emission by taking advantage of the ISC of nearly 100 % in metal complexes, which means that nearly 100 % of electrogenerated excitons can be harvested for EL. Here, η_{ext} of OLEDs is given by the following equation:

$$\eta_{\mathrm{ext}} = \eta_{\mathrm{int}} \times \eta_{\mathrm{out}} = \gamma \times \eta_{\mathrm{ST}} \times \Phi_{\mathrm{PL}} \times \eta_{\mathrm{out}}, \tag{2.3}$$

where γ is the charge balance factor, η_{ST} is exciton production efficiency, η_{int} is internal quantum efficiency, and η_{out} is light out-coupling efficiency (Fig. 2.6). To maximize η_{ext}, all of these factors should be nearly 100 %. A high γ can be attained by the construction of appropriate multilayer structures [8, 13]. High Φ_{PL} can be achieved by using emissive materials that suppress nonradiative recombination, and these materials are often doped into a host layer with a wide energy gap to minimize the concentration quenching of excitons that usually occurs at high concentrations. In the case of fluorescence-based OLEDs, the maximum η_{ext} is limited to 5 % assuming an η_{out} of 20 %, because of optical reflection and loss in organic layers [14]. Meanwhile, phosphorescent OLEDs can utilize both singlet and triplet excitons for emission, allowing η_{ST} and η_{ext} to reach 100 % and 20 %, respectively [15].

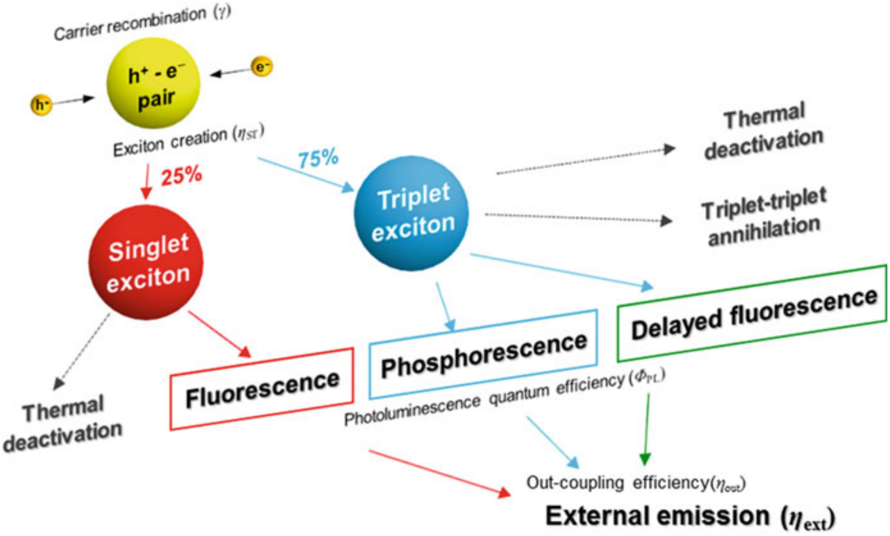

Fig. 2.6 Schematic representation of OLED processes: charge carrier recombination, production of molecular excitons; internal emissions of fluorescence, phosphorescence, and delayed fluorescence; and external emission

However, we note that the rather long τ of phosphorescence leads to strong nonradiative exciton annihilation, resulting in roll-off of η_{ext} at high current density [16].

In OLEDs, it has been well established that the use of guest–host (doping) systems substantially enhances η_{ext}. Because most neat films of emitter molecules show rather strong concentration quenching, emissive materials are usually doped in a host matrix at very low concentration; i.e., typically 1–2 %. In a guest–host system, there are two kinds of energy transfer mechanisms from host (exciton donor) to guest (exciton acceptor): Förster and Dexter energy transfer processes (Fig. 2.7) [17, 18]. In OLEDs, both Förster and Dexter processes contribute to energy transfer between the host and guest molecules because both singlet and triplet excitons are formed in host and guest molecules under electrical excitation.

Förster energy transfer is a long-range (up to ~10 nm) dipole–dipole coupling interaction between host and guest molecules [19]. Förster energy transfer is only allowed between singlet states of a host and guest because only transitions between states with the same spin multiplicity are allowed, whereas those between singlet and triplet states with different spin multiplicity are forbidden. The rate constant of Förster energy transfer for a guest–host system is given by the following equation:

$$k_{\text{FET}} = k_{\text{H}}\left(\frac{R_0}{R_{\text{HG}}}\right)^6, \tag{2.4}$$

where k_{H} is the rate of radiative decay of the host, R_{HG} is the separation between the host and guest molecules, and R_0 is the Förster transfer radius. R_0 can be calculated as follows:

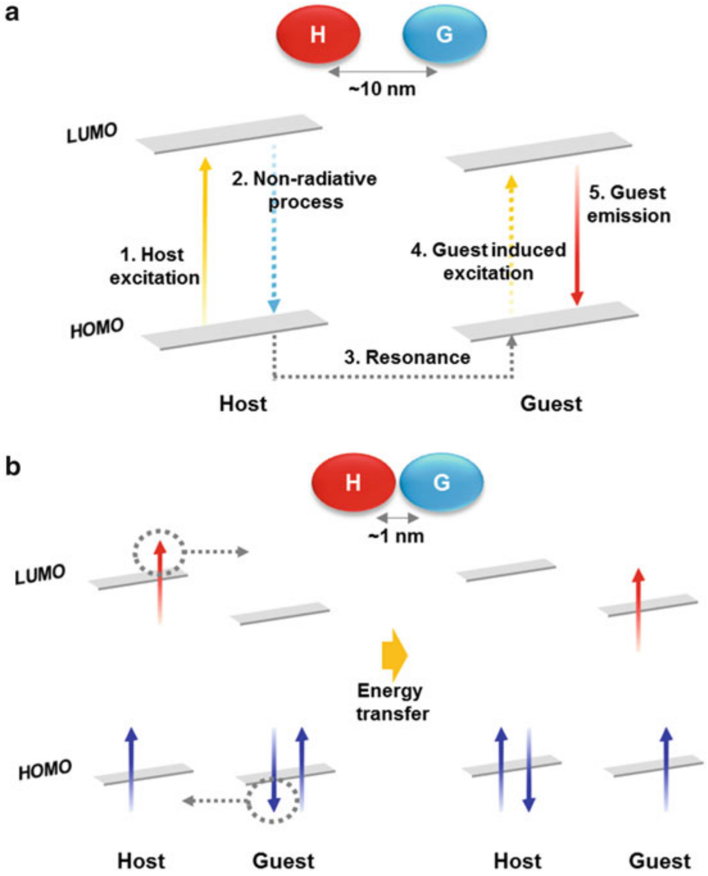

Fig. 2.7 Schematic diagrams showing (**a**) Förster and (**b**) Dexter energy transfer

$$R_0^6 = \frac{9000\kappa^2 \ln 10 \varphi_{\mathrm{H}}}{128\pi^5 n^4 N_{\mathrm{A}}} \int_0^\infty F_{\mathrm{H}}(\lambda)\varepsilon_{\mathrm{G}}(\lambda)\mathrm{d}\lambda, \tag{2.5}$$

where κ is an orientation factor, φ_{H} is Φ_{PL} of the host, n is the refractive intensity of the medium, N_{A} is the Avogadro constant, F_{H} (λ) is normalized host PL intensity, $\varepsilon_{\mathrm{G}}(\lambda)$ is the molar absorption coefficient of the guest, and λ is wavelength. From these equations, the rate constant of Förster energy transfer can be determined using the fluorescence spectrum of the host and absorption spectrum of the guest. To increase the Förster rate constant, a large overlap of host emission and guest absorption spectra, large $\varepsilon_{\mathrm{G}}(\lambda)$, and small distance between host and guest molecules are required.

Dexter energy transfer is a short-range (up to ~1 nm) intermolecular electron exchange process from host to guest. Dexter energy transfer is allowed between host and guest singlet states and host and guest triplet states. The rate constant of Dexter energy transfer is given by the following equation:

$$k_{\mathrm{DEX}} = \left(\frac{2\pi}{h}\right)\kappa^2 \exp\left(\frac{-2R_{\mathrm{HG}}}{L}\right) \int_0^\infty F_{\mathrm{H}}(\lambda)\varepsilon_{\mathrm{G}}(\lambda)\mathrm{d}\lambda, \tag{2.6}$$

where R_{HG} is the distance between host and guest molecules and L is the sum of the van der Waals radii of the two molecules. The rate constant of Dexter energy transfer strongly depends on the distance between the host and guest molecules and is also affected by the overlap between F_{H} (λ) and $\varepsilon_{\mathrm{G}}(\lambda)$. Therefore, not only the PL decay processes in a single molecule but also the energy transfer processes in emitter layers should be taken into account to maximize OLED performance.

2.2.3 Efficiency Roll-Off in OLEDs

Roll-off of η_{ext}, which is a decrease in efficiency with an increase of current density, has been widely observed in OLEDs. To realize high-performance OLEDs in displays and lighting sources, high brightness with low roll-off must be achieved. Roll-off characteristics can be described using the critical current density ($J_{50\%}$), at which η_{ext} decreases to 50 % of its maximum value [16].

Figure 2.8 illustrates exciton annihilation processes that lead to roll-off. For instance, polaron–exciton and exciton–exciton annihilation, field-induced quenching, charge carrier imbalance, Joule heating, and degradation can all affect η_{ext} [20]. The most relevant roll-off process in phosphorescent OLEDs is triplet–triplet annihilation (TTA) because of the long τ of phosphorescence emission and the high density of triplet excitons [21]. Shortening the distance between dopant molecules in a guest–host system can further decrease TTA [22]. The process of TTA can be characterized by the following equations:

$$4({}^3M^* + {}^3M^*) \rightarrow {}^1M^* + 3({}^3M^*) + 4M, \tag{2.7}$$

$$\frac{d[{}^3M^*]}{\mathrm{d}t} = -\frac{[{}^3M^*]}{\tau} - \frac{k_{\mathrm{q}}}{2}[{}^3M^*]^2 + \frac{J}{qd} \tag{2.8}$$

$$\frac{\eta_{50\%}}{\eta_0} = \frac{J_{50\%}}{4J}\left[\sqrt{1 + 8\frac{J}{J_{50\%}}} - 1\right] \tag{2.9}$$

where ${}^3M^*$, ${}^1M^*$, and M refer to molecules in triplet excited, singlet excited, and ground states, respectively, $[{}^3M^*]$ is triplet exciton density, d is the width of the recombination zone, k_{q} is the rate constant of TTA, q is the fundamental electric charge, J is current density, and η_0 is maximum η_{ext}.

Among the processes that contribute to roll-off in OLEDs, singlet–singlet annihilation (SSA) has been observed in anthracene crystals and affects the density and lifetime of singlet excitons [23]. Singlet–triplet annihilation (STA) usually

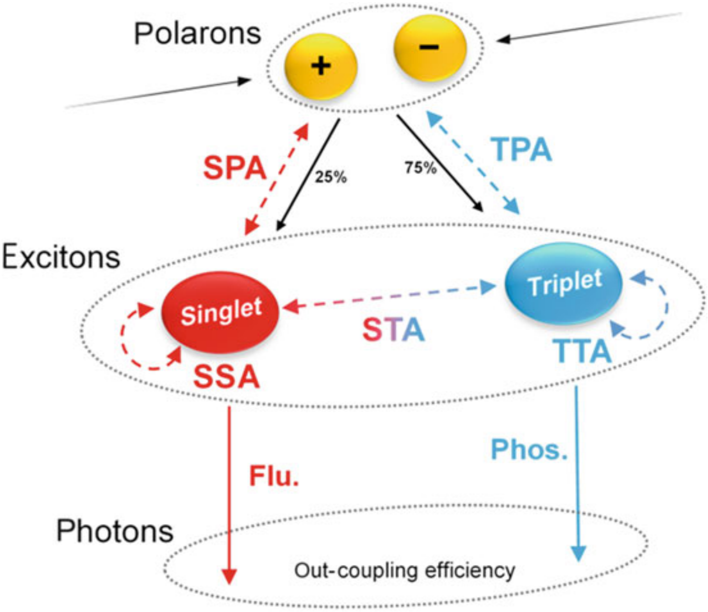

Fig. 2.8 Schematic illustration of processes leading to roll-off in OLEDs (*SPA* singlet–polaron annihilation, *TPA* triplet–polaron annihilation, *SSA* singlet–singlet annihilation, *TTA* triplet–triplet annihilation, *STA* singlet–triplet annihilation)

occurs at high concentrations of guest doping and high current densities exceeding 100 mA cm^{-2} [24]. Polarons can also interact with both singlet and triplet excitons, leading to exciton–polaron annihilation. Triplet–polaron annihilation (TPA) occurs in both fluorescent and phosphorescent OLEDs because of the long lifetime of triplet excited states. Holes generally lead to stronger TPA than electrons. Singlet–polaron annihilation (SPA) is of great concern in organic lasers, where very high current densities are used [25].

To suppress roll-off and achieve high brightness in OLEDs, it is crucial to decrease the local exciton density. This may be achieved by decreasing the lifetime of luminescent excitons [26], reducing molecular aggregation [27], and broadening the recombination zone [28]. Moreover, minimizing the spectral overlap between emission and polaron absorption can decrease polaron annihilation [25].

2.2.4 White OLEDs

White OLEDs (WOLEDs) are receiving great attention and being developed as the next generation of solid-state light sources. However, the low brightness, suboptimal

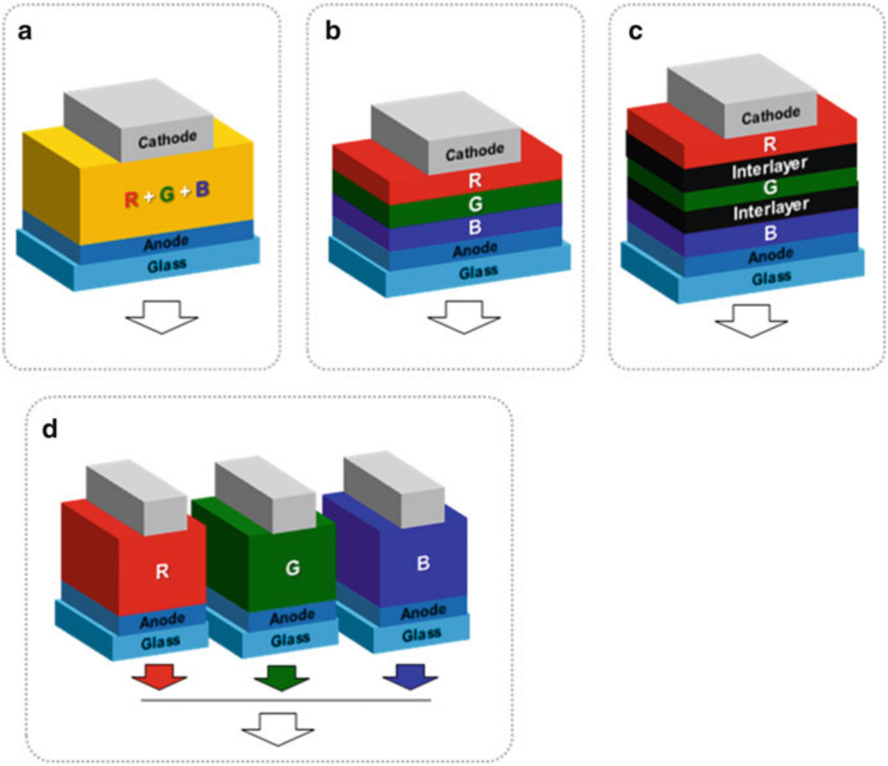

Fig. 2.9 Schematic illustration of the structure of white OLEDs (WOLEDs). (**a**) Single layer, (**b**) multi-RGB layer, (**c**) multi-RGB layer with interlayer, and (**d**) RGB side by side

device stability, and expensive manufacturing cost of WOLEDs currently limit their use. To overcome these disadvantages, many researchers have been attempting to develop effective emitter molecules and optimized device structures.

White emission is obtained when the emission spectrum covers the wide visible region from 400 to 800 nm. Typically, emissive molecules exhibit narrow emission with a width of 50–100 nm that can be recognized as colors such as red (R), green (G), and blue (B). To realize white emission, different colors of emission should be mixed to produce a broad emission spectrum, for example, by combining red, green, and blue emission or blue and orange emission. The combination of emission can be controlled by various device structures to give highly efficient white emission (Fig. 2.9) [29, 30].

The simplest method to obtain white emission is by blending emitters with different emission colors in a single layer. The first single-layer WOLEDs were fabricated by blending PVCz with orange, green, and blue dyes using solution processing [31]. Subsequently, WOLEDs were produced by vacuum deposition of a blend of three kinds of phosphorescent emitters [32]. WOLEDs with a multilayer device structure have also been fabricated [33, 34]. In this device structure, excitons can be generated in an EML by direct recombination of holes and electrons or by energy transfer from a neighboring EML. Such multilayer structures exhibit the best efficiency, spectral coverage, and device lifetime compared to those of other WOLED architectures. While the emission spectrum of multilayer devices often depends on the applied driving voltage, this problem can be solved by controlling the recombination zone and width of the EMLs [35].

The EMLs can be further isolated to reduce their interaction and suppress brightness-dependent color shifts even at very high operating voltages [36]. In striped WOLEDs, which is the extreme case of isolated EMLs, white emission can be generated from monochrome pixels each consisting of an OLED. Striped WOLEDs generate white emission using independent red-, green-, and blue-emitting devices. However, the manufacturing process of these types of devices is rather complicated, which makes them expensive.

2.2.5 Solution-Processed OLEDs

The main methods used to fabricate multilayer OLEDs are thermal evaporation under high vacuum [7] and solution processing [11]. Thermal evaporation is the most widely employed method to fabricate efficient, stable OLEDs, even though it has the disadvantages of complexity and high production cost [37]. Solution-processing methods such as spin coating [38], ink-jet printing [39], and spray processing [40] have attracted considerable attention for the fabrication of flexible and large-area OLEDs because of their simplicity and low cost.

Many phosphorescent polymers and small molecules have been studied as emitters for highly efficient solution-processed OLEDs. After the first reports of solution-processed OLEDs using the polymer PPV [11], conjugated polymers possessing high solubility and good morphology were developed as hosts for phosphorescent emitters with the aim of producing highly efficient polymer-based OLEDs [41–43]. However, the long conjugation length of polymers leads to a low T_1 energy level and decreased device efficiency [44, 45]. To solve these problems, phosphorescent emitters have been dispersed in nonconjugated polymers, resulting in improved efficiency [46, 47].

Small molecules are mainly used in vacuum thermal evaporation and have the advantages of high Φ_{PL} and easy purification. For application of small molecules in solution-processed OLEDs, the problems of low solubility, poor morphology, and tendency to crystallize should be solved. Newly designed small molecules bearing alkyl or alkoxy and flexible groups have been developed for use in solution processes [48, 49]. Rigid molecules such as spirofluorene have been introduced in core unit to increase the glass transition temperature (T_g), which suppresses crystallization [50]. Using small molecules based on Ir(III) and Pt(II) complexes, numerous highly efficient solution-processed OLEDs have been reported [51, 52].

2.2.6 Problems Facing OLEDs

OLEDs have many excellent basic characteristics, such as self-luminescence, surface luminescence, high flexibility, high resolution, and high EL efficiency. Through research and development over the past 25 years, some device characteristics superior to those of liquid crystals have been obtained. However, OLEDs still have several problems that need to be solved to improve their performance: their high cost arising from the use of noble metals such as Ir and Pt as emitting materials, difficulty in achieving stable blue light emission, and low device stability and high-cost production because of the use of ultrathin organic films with a thickness of approximately 100 nm. Thus, the potentially excellent device characteristics of organic semiconductors have not yet been fully realized. In addition, improving the efficiency of light extraction from thin films by introducing photonic crystals and light scattering techniques has been widely discussed; however, no decisive solutions have been reached [53]. The greatest challenge facing medium- and small-sized OLED displays is sufficiently high definition. To achieve this, RGB coloring with an order of accuracy of 10 μm is required, and an innovative process must be developed to allow low-cost mass production. Currently, the following five developments are necessary to obtain next-generation OLEDs: (1) realization of highly efficient luminescence without using phosphorescent materials, (2) utilization of the intrinsic optical and electronic anisotropies of molecules, (3) development of an RGB coloring process to achieve high definition, (4) development of thick-film devices with organic layers thicker than 10 μm, and (5) development of a low-cost fabrication process.

2.3 Thermally Activated Delayed Fluorescence (TADF) for OLEDs

2.3.1 Principles of TADF in OLEDs

At present, OLEDs are expected to be practically applied as flat-panel displays and illumination sources because they have unique characteristics, such as high EL efficiency and flexibility, and can be processed at low temperatures. To date, various fluorescent and phosphorescent materials have been developed to improve the EL efficiency of OLEDs [21, 54, 55]. As a result, highly durable and practically applicable OLEDs using fluorescent materials have been realized. However, the internal quantum efficiency (η_{int}), which is defined as the ratio of the number of photons produced by EL inside the device (i.e., before out-coupling) to the injected current (i.e., the number of injected carriers), of fluorescent OLEDs is typically at most only 25 % because of the limit imposed by the statistics of the electron spin states formed under electrical excitation [56, 57]. In contrast, OLEDs containing phosphorescent materials that display luminescence from the triplet state can achieve $\eta_{\mathrm{int}} = 100$ % [15]. However, the design of molecules used in such OLEDs

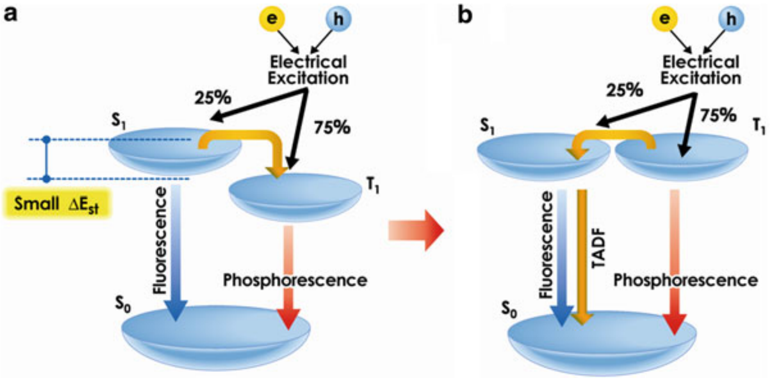

Fig. 2.10 Energy alignment of singlet and triplet energy levels to achieve efficient TADF

is greatly limited because the heavy atom effect (spin–orbital interaction) must be induced, for example, by using rare metals, to realize a highly efficient radiative transition from a triplet excited state to the ground state.

Researchers have reported several methods to achieve η_{int} higher than the theoretical limit of 25 % for OLEDs without using Ir complexes. Specifically, a method to prepare phosphorescent materials that are free of rare metals [58, 59] and another to generate singlet excited states by TTA [60] have been reported. For OLEDs using phosphorescent materials, TTA leads to the deactivation of triplet excitons and thus decreases the EL quantum efficiency; however, for OLEDs using fluorescent materials, the concentration of singlet excitons can be increased by TTA. Delayed fluorescence attributed to TTA was already confirmed from the EL observed from an anthracene single crystal in the 1960s, indicating that triplet excitons actively move around and interact in an organic solid thin film. Therefore, scientists have examined the possibility of generating singlet excitons from TTA to improve EL efficiency [60]. In actuality, η_{ext} has been reported to exceed its theoretical limit (5 %) in some OLEDs using fluorescent materials, demonstrating the potential of TTA to improve device performance as confirmed by transient EL characteristics. However, the efficiency of generating singlet excitons by TTA is at most only 37.5 %, so a novel luminescence mechanism is required to exceed this limit.

Recently, our research group has proposed a method of achieving an η_{int} of 100 % through up-conversion from the triplet excited state, which is generated with a probability of 75 % by electrical excitation, to the singlet excited state (Fig. 2.10) [61]. This method can be used to cause the triplet excited state to contribute to luminescence without needing rare metals. The method involves the up-conversion of triplet excitons to singlet excitons using thermal energy and has long been known as E-type delayed fluorescence in the field of photochemistry, but here we call it thermally activated delayed fluorescence (TADF). Well-known materials that exhibit TADF are eosin [62], fullerene [63], and porphyrin [64] derivatives.

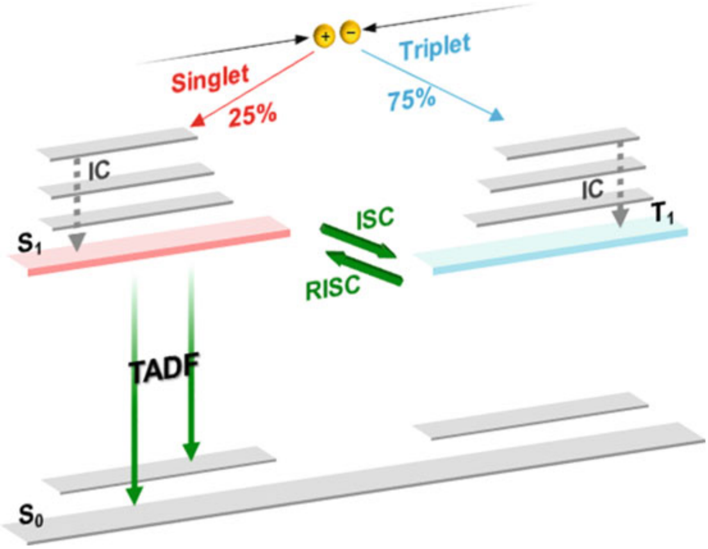

Fig. 2.11 Jablonski diagram of electronic transitions after recombination of holes and electrons for TADF. A small energy gap between T_1 and S_1 substantially promotes up-conversion (RISC)

Although the TADF process was considered to show a low power conversion efficiency because it is generally an endothermic reaction, recent studies have revealed that highly efficient delayed fluorescence can be achieved by optimizing molecular design.

TADF characteristics depend on the probability of reverse intersystem crossing (RISC) from triplet to singlet excited states (Fig. 2.11). The EL efficiency increases as the energy difference between the singlet and triplet excited states (ΔE_{ST}) decreases. For example, condensed polycyclic aromatic compounds, such as anthracene, exhibit very intense fluorescence but are not expected to show efficient TADF because their ΔE_{ST} exceeds 1 eV. In contrast, ketone-based materials, such as benzophenone derivatives, have a relatively small ΔE_{ST} of 0.1–0.2 eV but do not exhibit intense luminescence at room temperature and only exhibit phosphorescence at low temperatures [65].

Here, the dominant factor affecting TADF, ΔE_{ST}, is examined from the viewpoint of quantum chemistry. To obtain TADF with a high conversion efficiency, a luminescent material needs to possess a small ΔE_{ST} between S_1 and T_1 levels, which can be realized by having a small orbital overlap between its highest occupied molecular orbital (HOMO) and lowest unoccupied molecular orbital (LUMO) [66]. The ΔE_{ST} of luminescent molecules can be described by the following equations:

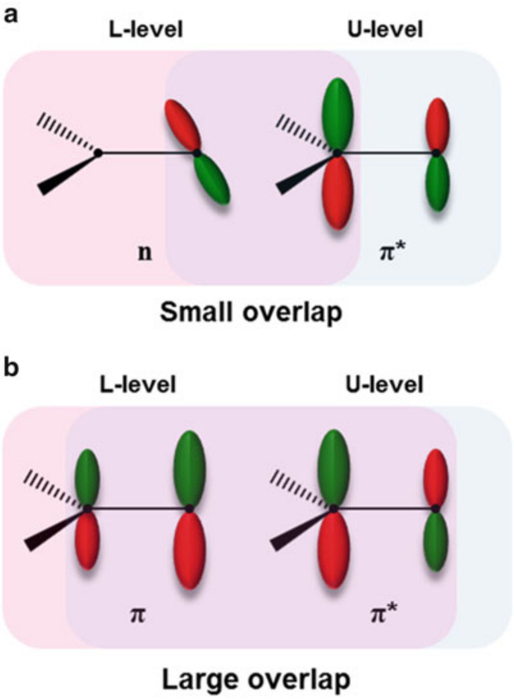

Fig. 2.12 (**a**) *n*–*π** orbital overlap and (**b**) *π*–*π** orbital overlap in benzophenone

$$E_S = (E_U - E_L) + K_{LU}, \tag{2.10}$$

$$E_T = (E_U - E_L) - K_{LU}, \tag{2.11}$$

$$\Delta E_{ST} = E_S - E_T = 2K_{LU}, \tag{2.12}$$

where E_{U} is a ground level (the highest occupied molecular level, U-level), E_{L} is an excited level (the lowest unoccupied molecular level, L-level), and K_{LU} is an exchange energy. Furthermore, K_{LU} is given by the following equation [67]:

$$K_{\mathrm{LU}} = \iint \varphi_{\mathrm{U}}(1)\varphi_{\mathrm{L}}(2)\frac{1}{r_{12}}\varphi_{\mathrm{U}}(2)\varphi_{\mathrm{L}}(1)\mathrm{d}\tau_1\tau_2 \tag{2.13}$$

where φ_{L} and φ_{U} are the wave functions of the U- and L-level orbitals, respectively, and r_{12} is the distance between electron (1) and (2). As shown in Eq. 2.13, K_{LU} is determined by φ_{L} and φ_{U} and should generally decrease as their overlap decreases.

Evidence of this relationship can be found in several known materials. A small ΔE_{ST} can be obtained as a consequence of the orthogonal overlap between *n* and *π** orbitals (Fig. 2.12a). In contrast, *π*–*π** transitions normally possess large ΔE_{ST} because of the parallel overlap between *π* and *π** orbitals (Fig. 2.12b) [68].Thus, small orbital overlap between the HOMO and LUMO should be necessary for small

ΔE_{ST}. However, a high luminescence efficiency could not be attained in conventional materials with small ΔE_{ST} because n–π* characteristics usually cause a small radiative decay rate (k_r). Therefore, the development of new luminescent materials possessing both small ΔE_{ST} and large k_r is required to realize highly efficient TADF.

Here, a relatively large k_r is required to obtain high EL efficiency. In the case of the aforementioned aromatic compounds, however, a large overlap between the wave functions of the ground and excited states is required. Therefore, it is necessary to design molecules that exhibit highly efficient EL while maintaining a small ΔE_{ST}. Because a large k_r and small ΔE_{ST} are conflicting, judicious molecular design is required to realize them simultaneously. We carefully designed and synthesized a novel molecule that has a small ΔE_{ST} and can exhibit highly efficient EL. Specifically, we designed and synthesized novel compounds that contained both electron-donating and electron-accepting substituents and successfully created a luminescent molecule exhibiting an EL efficiency of nearly 100 % while maintaining a very small ΔE_{ST} (<0.2 eV). This molecule allows up-conversion from the triplet excited state generated upon electrical excitation to the singlet excited state, enabling highly efficient EL equivalent to that of phosphorescent devices from the singlet excited state. In particular, an ultimate level of external efficiency close to 20 % was achieved in the green range (wavelength of 530 nm) for an OLED with carbazolyl dicyanobenzene (CDCB) as an emitting layer [69]. In addition, we found that an intrinsically small ΔE_{ST} can be achieved in exciplexes, which are intermolecular complexes, and successfully obtained an η_{ext} higher than 10 % by selecting the optimal materials [70].

In the following sections, we will introduce a method of up-conversion based on intramolecular charge transfer (ICT) that achieves a high η_{int} that exceeds its theoretical limit of 25 % for traditional fluorescent OLEDs, new organic light-emitting materials suitable for this approach, and the organic EL characteristics of devices employing these new materials. We will also introduce the concept of an exciplex system, which is the excited state formed between donor and acceptor molecules, as an alternative method to improve η_{int} through up-conversion.

2.3.2 TADF Characteristics of Triazine Derivatives

To develop high-efficiency TADF materials, it is necessary to design molecules with excellent EL characteristics while maintaining a small ΔE_{ST}. Namely, the key is to design molecules that can simultaneously achieve both large k_r and small ΔE_{ST}. Here, the design of molecules that achieve small ΔE_{ST} is examined. In general, the HOMO is distributed in the electron-donating units, whereas the LUMO is distributed in the electron-accepting units. Therefore, a small ΔE_{ST} can be obtained by introducing electron-donating and electron-accepting groups onto molecules to decrease the spatial overlap between the HOMO and LUMO. On the

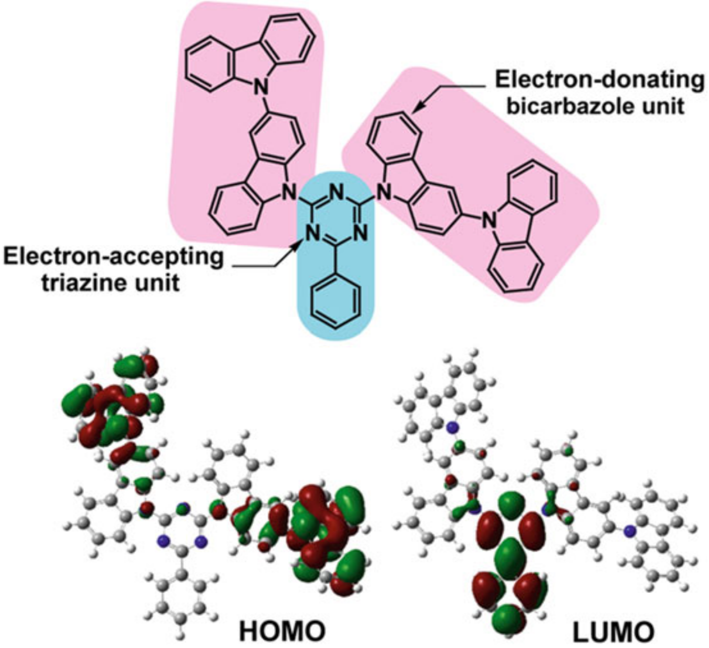

Fig. 2.13 Molecular structure and orbitals of a TADF material with a triazine skeleton (CC2TA)

basis of this direction of molecular design, we designed and synthesized a novel molecule, 2,4-bis{3-(9*H*-carbazol-9-yl)-9*H*-carbazol-9-yl}-6-phenyl-1,3,5-triazine (CC2TA), in which the acceptor phenyltriazine unit is used as the central skeleton and donor bicarbazole units are appended to both ends of the skeleton (Fig. 2.13) [71]. Molecular orbital calculations revealed that the HOMO and LUMO are locally distributed mainly in the bicarbazole and phenyltriazine units, respectively. As a result, the molecule successfully showed a very small ΔE_{ST} of 0.06 eV. In CC2TA, the introduction of bicarbazole with a Wurster structure (>N-aryl-N<) as a donor resulted in a small ΔE_{ST}. When a simple carbazole was included as a donor, the HOMO and LUMO overlapped to some extent, resulting in an increased ΔE_{ST} of 0.35 eV.

To evaluate the TADF characteristics of CC2TA, the PL characteristics of a co-evaporated thin film obtained by dispersing 6 wt% CC2TA in a bis[2-(diphenylphosphino)phenyl]ether oxide (DPEPO) host were measured, as shown in Fig. 2.14. The triplet energy (E_{T}) of the DPEPO host is 3.1 eV, so triplets in CC2TA ($E_{\mathrm{T}} = 2.85$ eV) can contribute to efficient luminescence without being transferred to the host. Figure 2.14a shows time-resolved PL spectra (streak images) of the CC2TA:DPEPO co-evaporated thin film. At room temperature, both prompt (lifetime, $\tau = 27$ ns) and delayed ($\tau = 22$ μs) PL components were observed in the same wavelength range. Figure 2.14b shows the temperature dependence of the transient PL waveform. The intensity of the delayed PL component markedly increases with increasing temperature. This result suggests that RISC from triplet to singlet excited

Fig. 2.14 (**a**) Time-resolved PL spectra of 6 wt% CC2TA:DPEPO co-evaporated thin film and (**b**) temperature dependence of transient PL waveform

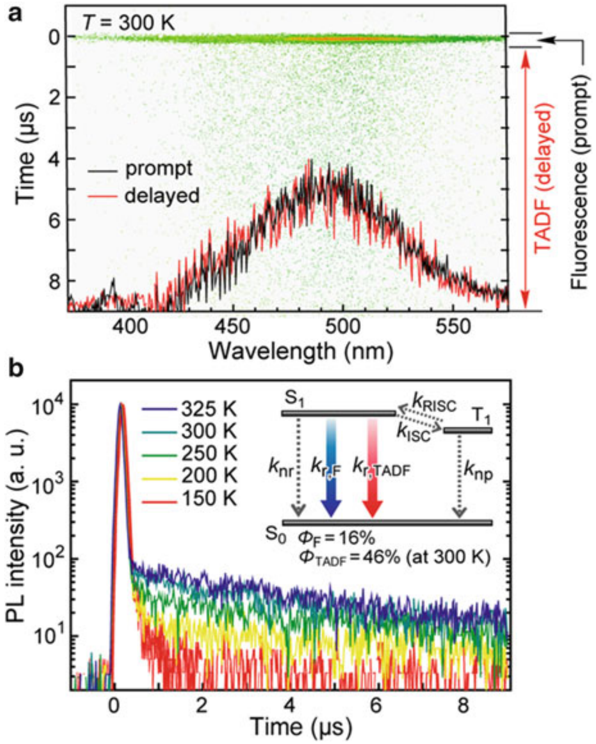

states actively occurs around room temperature because of sufficient thermal energy, resulting in efficient TADF. In contrast, the triplet excitons cannot overcome the energy barrier to the singlet excited state at a low temperature (150 K). Therefore, RISC seldom occurs and intense delayed fluorescence is not observed.

$$\eta_{\mathrm{int(TADF)}} = \eta_{\mathrm{r,S}} \times \Phi_F \times \eta_{\mathrm{r,S}} \times \Phi_{\mathrm{TADF}} + \eta_{\mathrm{r,T}} \times \Phi_{\mathrm{TADF}} / \Phi_{\mathrm{ISC}} \tag{2.14}$$

The characteristics of an OLED containing the CC2TA:DPEPO co-evaporated thin film as an emitting layer were then examined (Fig. 2.15). The maximum external quantum efficiency η_{ext} reached 11 %. Here, the efficiency of EL involving TADF can be expressed by Eq. 2.14 above. In Eq. 2.14, $\eta_{\mathrm{r,S}}$ and $\eta_{\mathrm{r,T}}$ are the probabilities of generation of singlet and triplet excitons, respectively ($\eta_{\mathrm{r,S}} = 25$ %, $\eta_{\mathrm{r,T}} = 75$ %), Φ_{F} is the fluorescence quantum yield ($\Phi_{\mathrm{F}} = 16$ %), Φ_{TADF} is the TADF quantum yield ($\Phi_{\mathrm{TADF}} = 46$ %), and Φ_{ISC} is the probability of intersystem crossing ($\Phi_{\mathrm{ISC}} = 84$ %). From Eq. 2.14, $\eta_{\mathrm{int(TADF)}}$ is calculated to be 56 %. Assuming that the efficiency of light extraction is 20 %, the theoretical η_{ext} is 11 %, which is in good agreement with the value obtained for our experimental device.

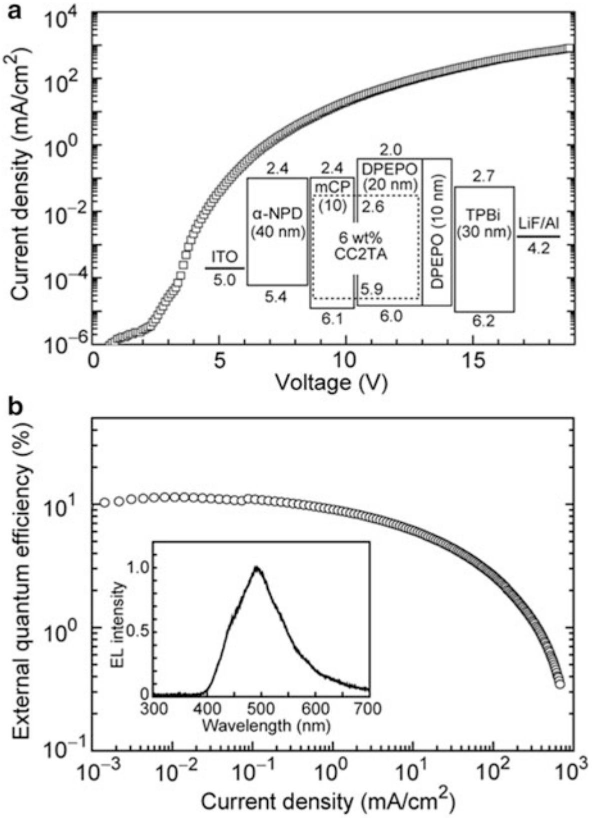

Fig. 2.15 (**a**) Device structure and relationship between current density and voltage and (**b**) dependence of external quantum efficiency (η_{ext}) on current density for a TADF-OLED containing CC2TA as an emitting layer

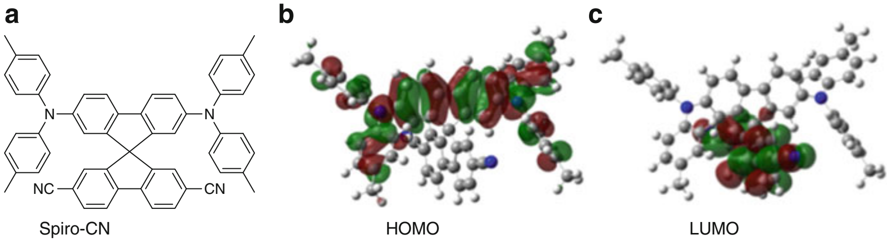

Spiro-CN

HOMO

LUMO

Fig. 2.16 (**a**) Molecular structure, (**b**) HOMO, and (**c**) LUMO of Spiro-CN

2.3.3 TADF Characteristics of Spiro Derivatives

Spiro compounds are expected to exhibit TADF because donor and acceptor units can be introduced into their orthogonal π-conjugated system and the HOMO and LUMO can be spatially separated [66]. Figure 2.16 shows the molecular structure of a spirobifluorene derivative (Spiro-CN) that exhibits TADF. This molecule has

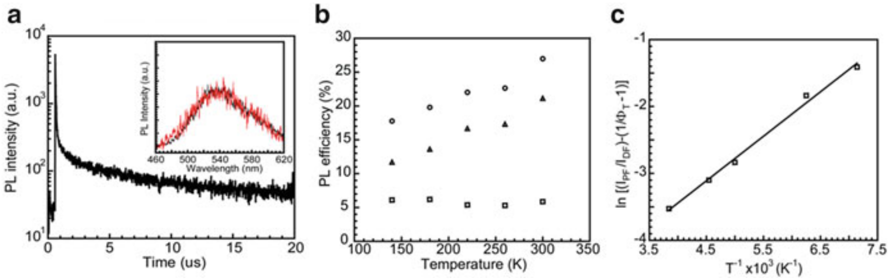

Fig. 2.17 (**a**) Transient PL spectrum of a 6 wt% Spiro-CN:*m*-CP co-evaporated thin film. The *inset* shows time-resolved PL spectra (*red line*, PL spectrum attributed to prompt fluorescence component; *black line*, PL spectrum attributed to delayed fluorescence component). (**b**) Temperature dependence of PL quantum yield (○, total; △, delayed fluorescence component; □, prompt fluorescence component). (**c**) Berberan–Santos plots of the temperature dependence of PL intensity

two donor triarylamine groups and two acceptor cyano groups. The molecules between these groups are distorted by the spirobifluorene skeleton to form a twisted steric structure. The results of molecular orbital calculations in Fig. 2.16 reveal that the HOMO and LUMO are locally distributed in the triarylamine-based fluorene and cyano-based fluorene, respectively.

Figure 2.17a shows the PL spectrum of a Spiro-CN:1,3-bis(9-carbazolyl)benzene (*m*-CP) co-evaporated thin film, in which 6 wt% Spiro-CN guest is dispersed in *m*-CP host. The transient waveform consists of a prompt PL component with τ of ~24 ns and a delayed PL component with τ of ~14 μs. Figure 2.17b illustrates the temperature dependence of the PL characteristics of the 6 wt% Spiro-CN:*m*-CP co-evaporated thin film. The prompt fluorescence component shows no temperature dependence, whereas the PL intensity of the delayed fluorescence component clearly increases with temperature. This indicates that RISC from triplet to singlet excited states actively occurs in Spiro-CN with increasing temperature. ΔE_{ST} of Spiro-CN was then evaluated using the Berberan–Santos equation on the basis of the abovementioned temperature dependence of PL characteristics. Here, Φ_{prompt} is the quantum yield of prompt fluorescence, Φ_{delayed} is the quantum yield of delayed fluorescence, Φ_{T} is the efficiency of generating triplet excitons, k_{p} is the radiative rate constant from the triplet excited state, k_{nr} is the nonradiative rate constant from the triplet excited state, k_{RISC} is the rate constant for RISC, and R is the gas constant. Then, the Berberan–Santos equation is given by

$$\ln\left[\frac{\Phi_{\mathrm{prompt}}}{\Phi_{\mathrm{delayed}}}-\left(\frac{1}{\Phi_{\mathrm{T}}}-1\right)\right]=\ln\left(\frac{k_{\mathrm{p}}+k_{\mathrm{nr}}}{k_{\mathrm{RISC}}}\right)+\frac{\Delta E_{\mathrm{ST}}}{RT}. \tag{2.15}$$

Figure 2.17c shows the Berberan–Santos plots of the PL characteristics of the 6 wt% Spiro-CN:*m*-CP co-evaporated thin film. ΔE_{ST} of Spiro-CN is estimated to be 0.057 eV from the slope of the straight line in this figure. This calculation

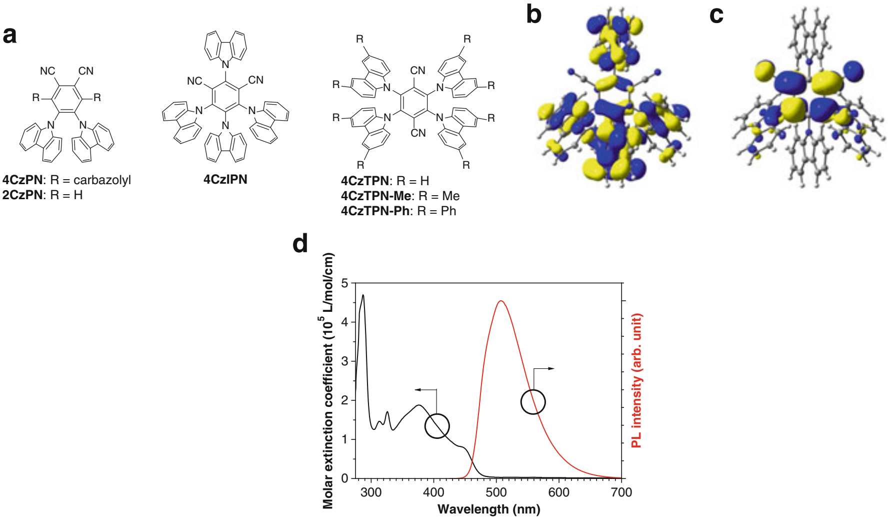

Fig. 2.18 (**a**) Molecular structure of CDCB derivatives and (**b**) HOMO, (**c**) LUMO, and (**d**) absorption and PL spectra of 4CzIPN

demonstrates that ΔE_{ST} of Spiro-CN is much smaller than that of conventional delayed fluorescent materials, such as C_{70} (0.26 eV) and tin(IV)fluoride–porphyrin (0.24 eV).

Next, the PL characteristics of an OLED employing the 6 wt% Spiro-CN:*m*-CP co-evaporated thin film as an emitting layer were measured. A maximum η_{ext} of 4.4 % was obtained for an OLED with a structure of indium tin oxide (ITO)/α-*N*, *N*'-di(1-naphthyl)-*N*,*N*'-diphenylbenzidine (NPD)/6 wt% Spiro-CN:*m*-CP/ 4,7-diphenyl-1,10-phenanthroline (Bphen)/MgAg/Ag. This value greatly exceeds the theoretical value of η_{ext} when a conventional fluorescent material with a fluorescence quantum yield of 27 % is used as an emitting layer (i.e., $\eta_{ext} = 1.4$ %), meaning that the efficiency of exciton generation in this OLED is increased by TADF.

2.3.4 TADF Characteristics of CDCB Derivatives

Although a small ΔE_{ST} can be achieved by spatially separating the HOMO and LUMO as mentioned above, this spatial separation generally decreases the transition dipole moment μ and thus decreases the EL quantum yield. To realize highly efficient TADF, a small ΔE_{ST} and large μ must be simultaneously achieved while maintaining the appropriate level of overlap between the HOMO and LUMO.

Figure 2.18a, b, c shows the molecular structure, HOMO, and LUMO, respectively, of a CDCB derivative designed following the abovementioned theory [69]. The HOMO and LUMO are locally distributed in the donor carbazolyl groups

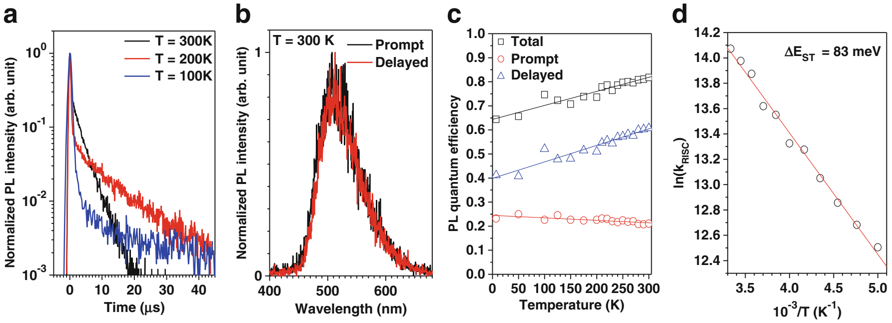

Fig. 2.19 (**a**) PL transient decay, (**b**) time-resolved PL spectra, (**c**) temperature dependence of PL quantum yield, and (**d**) Arrhenius plots of the rate constant for RISC for a 6 wt% 4CzIPN:CBP co-evaporated film

and acceptor dicyanobenzene units, respectively. It is apparent that the HOMO and LUMO moderately overlap on the central benzene ring. This indicates that the CDCB derivative achieves both small ΔE_{ST} and large μ. Quantum chemical calculations also reveal that the change in molecular structure among the S_0, S_1, and T_1 states is small in 4CzIPN. As a result, 4CzIPN is expected to achieve a high EL quantum yield because the nonradiative deactivation process is suppressed.

Figure 2.18d shows the absorption and PL spectra of 4CzIPN in toluene solution. 4CzIPN has a wide PL band with a peak at approximately 507 nm attributed to ICT. The Stokes shift of 4CzIPN is smaller than that in conventional ICT-based luminescence. This means that the change in the molecular structure of 4CzIPN is small upon electronic excitation from the S_0 to S_1 states.

Next, the TADF characteristics of a 6 wt% 4CzIPN:4,4-N,N-dicarbazole-biphenyl (CBP) co-evaporated film will be discussed. Figure 2.19a shows the PL transient decay characteristics of this film at 100, 200, and 300 K. The PL transient decay characteristics exhibited two components, a nanosecond-order short-lifetime component and a microsecond-order long-lifetime component, at all temperatures. Figure 2.19b depicts time-resolved PL spectra of the short- and long-lifetime components at 300 K. Luminescence attributed to the long-lifetime component is delayed fluorescence because the PL spectrum of this component is in agreement with the fluorescence spectrum of the short-lifetime component. Figure 2.19c shows the temperature dependence of the PL quantum yield of the prompt and delayed fluorescence components. The quantum yield of prompt fluorescence increases slightly with decreasing temperature. This is because the nonradiative deactivation process is suppressed. In contrast, the quantum yield of delayed fluorescence decreases markedly as temperature is lowered. This is caused by the suppression of RISC from the T_1 to S_1 states with decreasing temperature.

The ΔE_{ST} of 4CzIPN can be estimated from the temperature dependence of its PL quantum yield observed above. Here, k_{RISC} is expressed using the rate constant for prompt fluorescence (k_p), the rate constant for delayed fluorescence (k_d), the

Fig. 2.20 External quantum efficiency (η_{ext})-current density (J) characteristics of OLEDs using CDCB derivatives as an emitting layer. The inset shows EL spectra

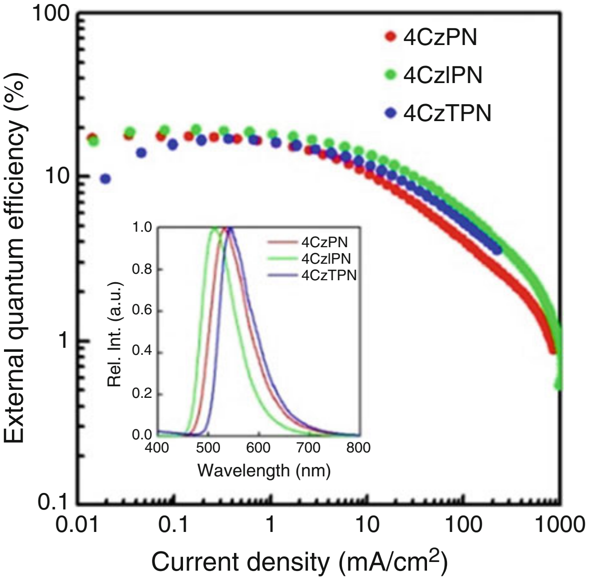

quantum yield of prompt fluorescence (Φ_p), the quantum yield of delayed fluorescence (Φ_d), and k_{ISC} from the S_1 to T_1 states as follows:

$$k_{\text{RISC}} = \frac{k_p k_d}{k_{\text{ISC}}} \frac{\Phi_d}{\Phi_p}. \tag{2.16}$$

Because k_p and k_d can be determined from the transient PL curve and Φ_p and Φ_d can be measured, k_{RISC} can be evaluated using Eq. 2.16. The relationship between k_{RISC} and ΔE_{ST} can be expressed as

$$k_{\text{RISC}} = A \exp\left(-\frac{\Delta E_{\text{ST}}}{k_B T}\right) \tag{2.17}$$

where A is a constant, k_B is the Boltzmann constant, and T is temperature. Therefore, ΔE_{ST} can be calculated from the temperature dependence of k_{RISC}. Figure 2.19d shows the Arrhenius plot of k_{RISC} for 4CzIPN between 200 and 300 K. ΔE_{ST} is calculated to be 83 meV from the slope of the straight line in this figure. This analysis demonstrates that the energy difference between the S_1 and T_1 states is small for 4CzIPN.

Figure 2.20 illustrates the characteristics of OLEDs with the structure of ITO/α-NPD (35 nm)/6 wt%-CDCB:CBP (15 nm)/1,3,5-tris(N-phenylbenzimidizol-2-yl) benzene (TPBi; 65 nm)/LiF (0. 8 nm)/Al (80 nm) containing different CDCB derivatives as an EML. η_{ext} of the CDCB derivatives were all very high (17.8 %, 19.3 %, and 17.1 %). This means that 4CzIPN has an η_{int} of nearly 100 %.

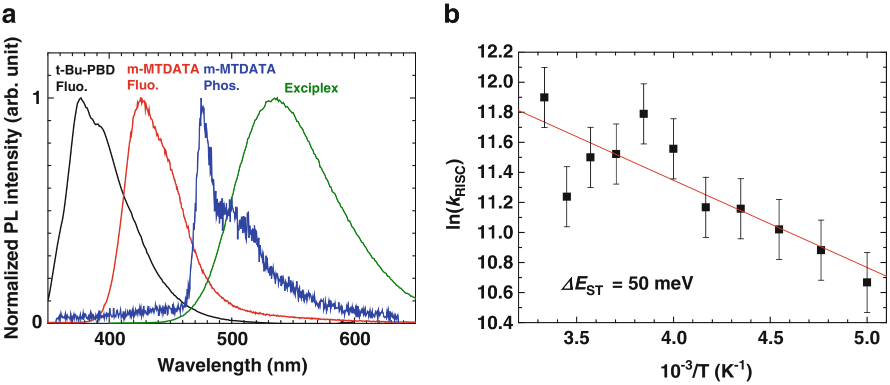

Fig. 2.21 (**a**) PL spectrum of a 50 mol% *m*-MTDATA:*t*-Bu-PBD co-evaporated film and fluorescence and phosphorescence spectra of *m*-MTDATA and *t*-Bu-PBD single-component thin films. (**b**) Temperature dependence of k_{RISC}

2.3.5 TADF Characteristics of Exciplexes

In the radiative transition of organic compounds, electrons generally transit from the LUMO to the HOMO within a single molecule. In the excited state formed within a single molecule, therefore, the HOMO and LUMO are confined in the molecule, so the electron exchange integral is large, which results in an increased ΔE_{ST}. In an attempt to identify an additional pathway to maximize η_{int} of OLEDs, we focused on the exciplex state, which is the excited state formed between electron-donating and electron-accepting molecules. In the radiative process of exciplexes, charges transit from the LUMO of the electron-accepting molecule to the HOMO of the electron-donating molecule. Therefore, the electron exchange integral of the exciplex is small because the HOMO and LUMO are spatially separated, resulting in a very small ΔE_{ST}. This increases the probability of up-conversion from triplet to singlet excited states.

Here, the up-conversion from triplet to singlet excited states is explained using the exciplex formed between electron-donating 4,4′,4″-tris[3-methylphenyl(phenyl)amino]triphenylamine (*m*-MTDATA) and electron-accepting 2-(biphenyl-4-yl)-5-(4-*tert*-butylphenyl)-1,3,4-oxadiazole (*t*-Bu-PBD) [72]. Figure 2.21a shows the PL spectrum of a 50 mol% *m*-MTDATA:*t*-Bu-PBD co-evaporated film as well as the fluorescence and phosphorescence spectra of thin films of *m*-MTDATA and *t*-Bu-PBD alone. The maximum PL intensity for the co-evaporated film appears at a wavelength of 540 nm, which is longer than that of the fluorescence maxima of the *m*-MTDATA and *t*-Bu-PBD thin films. This is because an exciplex is formed between the molecules of *m*-MTDATA and *t*-Bu-PBD in the co-evaporated film.

To achieve a high probability of up-conversion, attention should be paid to the confinement of the triplet excited state of the exciplex formed from the triplet excited states of the electron-donating and electron-accepting materials because energy can be transferred from the triplet excited state of the exciplex to those of electron-accepting and electron-donating materials to cause nonradiative deactivation of each triplet excited state, which markedly decreases the probability of up-conversion. The maximum phosphorescence intensity for the *m*-MTDATA thin film appears at 475 nm, which means that the triplet excited state of the exciplex is sufficiently confined. The phosphorescence peak of the *t*-Bu-PBD thin film appears at approximately 510 nm [73], again indicating that the triplet excited state of the exciplex is sufficiently confined by that of *t*-Bu-PBD, so a high up-conversion probability can be expected. Delayed fluorescence resulting from the fluorescence component of the exciplex and up-conversion from the triplet to singlet excited states was then confirmed by measuring the transient PL characteristics of a 50 mol% *m*-MTDATA:*t*-Bu-PBD co-evaporated film at room temperature.

ΔE_{ST} of the exciplex formed between *t*-Bu-PBD and *m*-MTDATA was estimated by measuring the temperature dependence of k_{RISC}, which is given as Eq. 2.17. k_{RISC} can be estimated from the rate constants and PL quantum yields of the prompt and delayed fluorescence components using Eq. 2.16 [72]. k_p, k_d, Φ_p, and Φ_d can be experimentally determined from the PL decay curve and the temperature dependence of PL intensity. The Arrhenius plot of k_{RISC} calculated using Eq. 2.16 is presented in Fig. 2.21b. Here, k_{ISC} is assumed to be independent of temperature. ΔE_{ST} calculated for the exciplex was 50 meV, demonstrating that its singlet and triplet excited states are very close in energy.

Although ΔE_{ST} of the exciplex formed between *m*-MTDATA and *t*-Bu-PBD was small, the EL efficiency of OLEDs with the *m*-MTDATA:*t*-Bu-PBD co-evaporated film as an emitting layer was still low (~2 %). We then examined delayed fluorescence from the exciplexes formed between various donor and acceptor materials. Intense delayed fluorescence was observed from the exciplex formed between *m*-MTDATA as the donor material and 2,8-bis(diphenylphosphoryl)dibenzo[*b*,*d*]thiophene (PPT) as the acceptor material [70]. Figure 2.22a

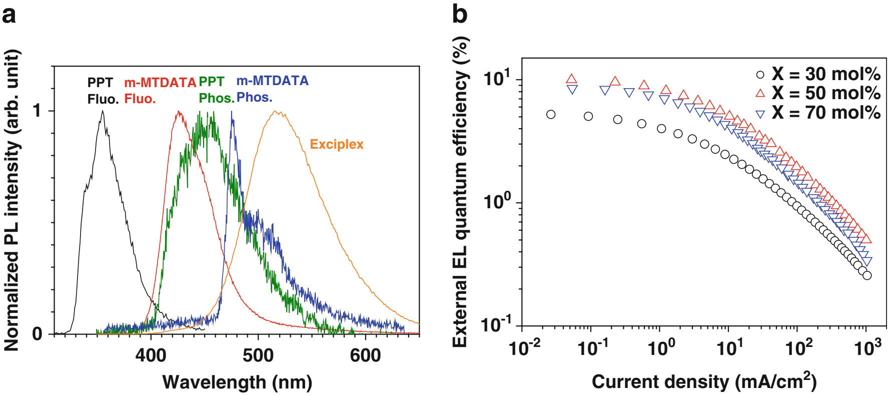

Fig. 2.22 (**a**) PL spectrum of a 50 mol% *m*-MTDATA:PPT co-evaporated film and fluorescence and phosphorescence spectra of *m*-MTDATA and PPT single-component thin films. (**b**) Dependence of external quantum efficiency (η_{ext}) on current density (J) for an OLED with the structure ITO/*m*-MTDATA (35 nm)/*X* mol% *m*-MTDATA:PPT (30 nm)/PPT (35 nm)/LiF/Al

shows the PL spectrum of a 50 mol% *m*-MTDATA:PPT co-evaporated film as well as the fluorescence and phosphorescence spectra of thin films of *m*-MTDATA and PPT alone. The maximum PL intensity of the co-evaporated film appeared at a wavelength of 520 nm, which is longer than the fluorescence maxima of the *m*-MTDATA and PPT single-component thin films, meaning that exciplexes were formed in the co-evaporated film. The PL quantum yield of the exciplex formed between *m*-MTDATA and PPT was 28.5 %, which is higher than that of the exciplex formed between *m*-MTDATA and *t*-Bu-PBD (19.6 %). In addition, the PL quantum yield of the delayed fluorescence component was 25.4 %, considerably higher than that for the exciplex formed between *m*-MTDATA and *t*-Bu-PBD (8.2 %). To evaluate the effect of the increased PL quantum efficiency of delayed fluorescence in the *m*-MTDATA:PPT system, the characteristics of OLEDs with the structure ITO/*m*-MTDATA (35 nm)/*X* mol% *m*-MTDATA:PPT (30 nm)/PPT (35 nm)/LiF/Al were examined, as shown in Fig. 2.22b. η_{ext} of the OLED is 10.0 %, which exceeds the theoretical limit of 5 % for devices using fluorescent materials. Thus, delayed fluorescence from the exciplex state, which is an intermolecular charge-transfer excited state, can be enhanced by selecting appropriate donor and acceptor materials.

2.4 Outlook

TADF technologies can greatly improve the performance of future OLEDs to enable their practical application. Also, from the viewpoints of photochemistry and material chemistry, TADF technologies have given rise to a new category of luminescent materials, contributing to the academic progress in this field. The appeal of organic compounds lies in the diversity of molecular structures, and TADF materials are novel materials that are designed making full use of that diversity. Namely, new luminescent materials other than the previously known fluorescent and phosphorescent materials have become available. The TADF phenomenon was named hyperfluorescence. If the luminescent materials used in OLEDs greatly shift to third-generation TADF materials in the future, the problem of the high cost of phosphorescent materials can be solved and the risk of resource depletion can be avoided by using this rare-metal-free strategy. Moreover, TADF materials are expected to facilitate production of luminescent materials that exhibit highly efficient blue emission and highly efficient cost-effective organic EL illumination, which will contribute substantially to the vitalization of the OLED market in the future. Molecular materials can be designed in an infinite number of patterns. We hope that the advance of organic optoelectronics will be driven by the development of new molecular materials.

Part of this discussion was reproduced from Jpn. J. Appl. Phys., 53, 6, 060101, 2014.

References

1. H. Akamatsu, H. Inokuchi, J. Chem. Phys. **18**, 810 (1950)
2. M. Pope, C.E. Swenberg, *Electronic Processes in Organic Crystals and Polymers* (Oxford University Press, New York, 1999)
3. C. Adachi, T. Tsutsui, S. Saito, Appl. Phys. Lett. **55**, 1489 (1989)
4. W. Helfrich, W.G. Schneider, Phys. Rev. Lett. **14**, 229 (1965)
5. W. Helfrich, W.G. Schneider, J. Chem. Phys. **44**, 2902 (1966)
6. P.S. Vincentt, W.A. Barlow, R.A. Hann, G.G. Roberts, Thin Solid Films **94**, 171 (1982)
7. C.W. Tang, S.A. Vanslyke, Appl. Phys. Lett. **51**, 913 (1987)
8. C.W. Tang, S.A. Vanslyke, C.H. Chen, J. Appl. Phys. **65**, 3610 (1989)
9. C. Adachi, T. Tsutsui, S. Saito, Appl. Phys. Lett. **57**, 531 (1990)
10. R.H. Partridge, Polymer **24**, 748 (1983)
11. J.H. Burroughes, D.D. Bradley, A.R. Brown, R.N. Marks, K. Mackay, R.H. Friend, P.L. Burns, A.B. Holmes, Nature **347**, 539 (1990)
12. C.E. Wayne, R.P. Wayne, *Photochemistry*, Oxford Chemistry Primers, Oxford University Press, Tokyo (1996)
13. E. Aminaka, T. Tsutsui, S. Saito, J. Appl. Phys. **79**, 8808 (1996)
14. J.S. Kim, P.K.H. Ho, N.C. Greenham, R.H. Friend, J. Appl. Phys. **88**, 1073 (2000)
15. C. Adachi, M.A. Baldo, M.E. Thompson, S.R. Forrest, J. Appl. Phys. **90**, 5048 (2001)
16. C. Adachi, M.A. Baldo, S.R. Forrest, Phys. Rev. B **62**, 10967 (2000)
17. T. Förster, Discuss Faraday Soc. **27**, 7 (1959)
18. D.L. Dexter, J. Chem. Phys. **21**, 836 (1953)
19. B.P. Lyons, A.P. Monkman, Phys. Rev. B **71**, 235201 (2005)
20. C. Murawski, K. Leo, M.C. Gather, Adv. Mater. **25**, 6801 (2013)
21. M.A. Baldo, D.F. O'Brien, Y. You, A. Shoustikov, S. Sibley, M.E. Thompson, S.R. Forrest, Nature **395**, 151 (1998)
22. J. Kalinowski, J. Mezyk, F. Meinardi, R. Tubino, M. Cocchi, D. Virgili, J. Appl. Phys. **98**, 063532 (2005)
23. S.D. Babenko, V.A. Benderskii, V.I. Gol'Danskii, A.G. Lavrushko, V.P. Tychinskii, Chem. Phys. Lett. **8**, 598 (1971)
24. D. Kasemann, R. Brückner, H. Fröb, K. Leo, Phys. Rev. B **84**, 115208 (2011)
25. M.A. Baldo, R.J. Holmes, S.R. Forrest, Phys. Rev. B **66**, 035321 (2002)
26. D. Song, S. Zhao, H. Aziz, Adv. Funct. Mat. 21, 2311 (2011)
27. E. B. Namdas, A. Ruseckas, I. D. W. Samuel, S.-C. Lo, P. L. Burn, J. Phys. Chem. B **108**, 1570 (2004)
28. S. Reineke, K. Walzer, K. Leo, Phys. Rev. B **75**, 125328 (2007)
29. M.C. Gather, A. Kohnen, K. Meerholz, Adv. Mater. **23**, 233 (2011)
30. S. Reineke, M. Thomschke, B. Lussem, K. Leo, Rev. Mod. Phys. **85**, 1245 (2013)
31. J. Kido, K. Hongawa, K. Okuyama, K. Nagai, Appl. Phys. Lett. **64**, 815 (1994)
32. H.A. Al Attar, A.P. Monkman, M. Tavasli, S. Bettington, M.R. Bryce, Appl. Phys. Lett. **86**, 121101 (2005)
33. G. Schwartz, K. Fehse, M. Pfeiffer, K. Walzer, K. Leo, Appl. Phys. Lett. **89**, 083509 (2006)
34. Y. Tomita, C. May, M. Toerker, J. Amelung, M. Eritt, F. Loeffler, C. Luber, K. Leo, K. Walzer, K. Fehse, Q. Huang, Appl. Phys. Lett. **91**, 063510 (2007)
35. Y.R. Sun, N.C. Giebink, H. Kanno, B.W. Ma, M.E. Thompson, S.R. Forrest, Nature **440**, 908 (2006)
36. T.W. Lee, T. Noh, B.K. Choi, M.S. Kim, D.W. Shin, J. Kido, Appl. Phys. Lett. **92**, 043301 (2008)
37. H. Kim, Y. Byun, R.R. Das, B.K. Choi, P.S. Ahn, Appl. Phys. Lett. **91**, 093512 (2007)
38. J.P.J. Markham, S.-C. Lo, S.W. Magennis, P.L. Burn, I.D.W. Samuel, Appl. Phys. Lett. **80**, 2645 (2002)

39. F. Villani, P. Vacca, G. Nenna, O. Valentino, G. Burrasca, T. Fasolino, C. Minarini, D.D. Sala, J. Phys. Chem C **113**, 13398 (2009)
40. J. Ju, Y. Yamagata, T. Higuchi, Adv. Mater. **21**, 4343 (2009)
41. H. Yersin, *Highly Efficient OLEDs with Phosphorescent Materials* (Wiley-VCH, Hoboken, 2008)
42. W. Zhu, W. Mo, M. Yaun, W. Yang, Y. Cao, Appl. Phys. Lett. **80**, 2045 (2002)
43. C. Jiang, W. Yang, J. Pengm, S. Xiao, Y. Cao, Adv. Mater. **16**, 537 (2004)
44. M. Sudhakar, P.I. Djurovich, T.E. Hogen-Esch, M.E. Thompson, J. Am. Chem. Soc. **125**, 7796 (2003)
45. A. van Dijken, J.J.A.M. Bastiaansen, N.M.M. Kiggen, B.M.W. Langeveld, C. Rothe, A. Monkman, I. Bach, P. Stossel, K. Brunner, J. Am. Chem. Soc. **126**, 7718 (2004)
46. K. M. Vaeth, C. W. Tang, J. Appl. Phys. **92**, 3447 (2002)
47. B.C. Krummacher, M.K. Mathai, V.E. Choong, S.A. Choulis, F. So, A. Winnacker, Org. Electron. **7**, 313 (2006)
48. J.A. Cheng, C.H. Chen, C.H. Liao, Chem. Mater. **16**, 2862 (2004)
49. J. Qiao, L.D. Wang, J.F. Xie, G.T. Lei, G.S. Wu, Y. Qui, Chem. Commun. **5**, 4560 (2005)
50. Y. Shirota, J. Mater. Chem. **15**, 75 (2005)
51. N. Rehmann, D. Hertel, K. Meerholz, H. Beckers, S. Heun, Appl. Phys. Lett. **91**, 103507 (2007)
52. G.J. Zhou, W.Y. Wong, B. Yao, Z. Xie, L. Wang, J. Mater. Chem. **18**, 1799 (2008)
53. Y.R. Do, Y.C. Kim, Y.W. Song, C.O. Cho, H. Jeon, Y.J. Lee, S.H. Kim, Y.H. Lee, Adv. Mater. **15**, 1214 (2003)
54. N. Tessler, G.J. Denton, R.H. Friend, Nature **382**, 695 (1996)
55. S. Lamansky, P. Djurovich, D. Murphy, F. Abdel-Razzaq, H.-E. Lee, C. Adachi, P.E. Burrows, S.R. Forrest, M.E. Thompson, J. Am. Chem. Soc. **123**, 4304 (2001)
56. T. Tsutsui, S. Saito, *Organic Multilayer-Dye Electroluminescent Diodes: Is There Any Difference with Polymer LED?* (Kluwer, Dordrecht, 1993)
57. L.J. Rothberg, A.J. Lovinger, J. Mater. Res. **11**, 3174 (1996)
58. J.C. Deaton, S.C. Switalski, D.Y. Kondakov, R.H. Young, T.D. Pawlik, S.B. Harkins, A.J.M. Miller, S.F. Mickenberg, J.C. Peters, J. Am. Chem. Soc. **132**, 9499 (2010)
59. O. Bolton, L. Kangwon, H.-J. Kim, K.Y. Lin, J. Kim, Nat. Chem. **3**, 205 (2011)
60. D.Y. Kondakov, T.D. Pawlik, T.K. Hatwar, J.P. Spindler, J. Appl. Phys. **106**, 124510 (2009)
61. A. Endo, M. Ogasawara, A. Takahashi, D. Yokoyama, Y. Kato, C. Adachi, Adv. Mater. **21**, 4802 (2009)
62. C.A. Parker, *Photoluminescence of Solutions* (Elsevier, Amsterdam, 1968)
63. M.N. Berberan-Santos, J.M.M. Garcia, J. Am. Chem. Soc. **118**, 9391 (1996)
64. M. Furukawa, S. Igarashi, presented at the 81st Spring Mtg. of the Chem. Soc. Jpn. (2), F7-30 (2002)
65. B. Valeur (ed.), *Molecular Fluorescence: Principles and Applications*, 1st edn. (Wiley-VCH, Wheinheim, 2002)
66. T. Nakagawa, S.-Y. Ku, K.-T. Wong, C. Adachi, Chem. Commun. **48**, 9580 (2012)
67. G. Mehes, H. Nomura, Q. Zhang, T. Nakagawa, C. Adachi, Angew. Chem. Int. Ed. **51**, 11311 (2012)
68. A. Endo, K. Sato, K. Yoshimura, T. Kai, A. Kawada, H. Miyazaki, C. Adachi, Appl. Phys. Lett. **98**, 083302 (2011)
69. H. Uoyama, K. Goushi, K. Shizu, H. Nomura, C. Adachi, Nature **492**, 234 (2012)
70. K. Goushi, C. Adachi, Appl. Phys. Lett. **101**, 023306 (2012)
71. S.Y. Lee, T. Yasuda, H. Nomura, C. Adachi, Appl. Phys. Lett. **101**, 093306 (2012)
72. K. Goushi, K. Yoshida, K. Sato, C. Adachi, Nat. Photon. **6**, 253 (2012)
73. M. Suzuki, S. Tokito, F. Sato, T. Igarashi, K. Kondo, T. Koyama, T.Yamaguchi, Appl. Phys. Lett. **86**, 103507 (2005)

Chapter 3
Organic Solar Cells

Shuzi Hayase

Abstract Printable solar cells including dye-sensitized solar cells, perovskite solar cells, and organic thin-film solar cells are summarized. Structures, working principles, and recent progresses on these printable solar cells are reported. Printable solar cells are able to be prepared by coatings at ambient temperature and ambient atmosphere. Therefore, reduction of the preparation cost is expected. Solar cells are composed of n-type semiconductive layer (electron collection layer), light harvesting layer, and p-type semiconductive layer (hole collection layer). In dye-sensitized solar cells, these three roles are allocated to each layer, such as porous titania, dyes, and electrolyte (or hole transport layer). Perovskite layers worked as light harvesting layer as well as carrier transport layer for perovskite solar cells. Directions to enhancing efficiencies are discussed from the viewpoint of individual working principle.

Keywords Printable solar cells • Dye sensitized • Perovskite • OPV • Organic thin film • Efficiency • Principle

3.1 Introduction

Solar light energy reaching on Earth is 1 kW/m^2 (100 mW/cm^2) with spectra covering from 400 nm to infrared area, which is called 1 sun. The standard spectra of the light are called air mass 1.5 (AM 1.5). Therefore, the standardized light is called AM1.5 with 1 sun energy density. 100 mW is gained by 1 m x 1 m solar modules with 10 % efficiency. Solar cells are generally composed of n-type semiconductor and p-type semiconductor, one of which absorbs light as light harvesting layers. The charge separation occurs at the interface (p/n junction) between them. Electrons and holes are collected by n-type layer and p-type layer, respectively.

Solar cells are classified by the light absorber material and divided roughly into silicon solar cells, compound solar cells, and organic solar cells as shown in Fig. 3.1

S. Hayase (✉)
Kyushu Institute of Technology, Kitakyushu, Fukuoka, Japan
e-mail: hayase@life.kyutech.ac.jp

S. Ogawa (ed.), *Organic Electronics Materials and Devices*,
DOI 10.1007/978-4-431-55654-1_3

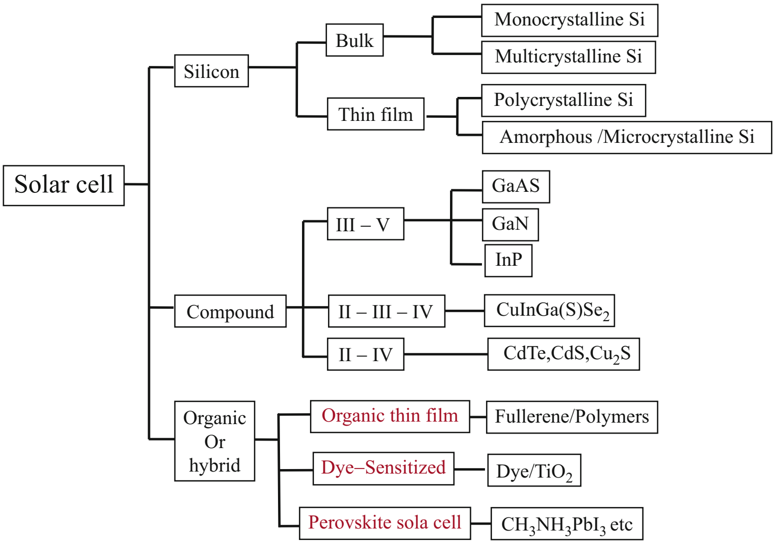

Fig. 3.1 Solar cell groups

Crystalline Si, multi-crystalline Si, polycrystalline Si, and amorphous silicon are the group of silicon solar cells. The representatives of compound-type solar cells are CuInGa(S)Se and CdTe which have been put into practical uses. Dye-sensitized solar cells and organic solar cells contain dyes on titania or blend of n-type fullerene and p-type polymers as the light harvesting materials. These materials are soluble in organic solvents, and organic solar cells can be prepared by coating processes. Therefore, they are also called printable solar cells. Recently, hybrid solar cells consisting of organic and inorganic compounds have been reported. The representatives of the hybrid solar cells are perovskite solar cells which have attracted attention due to the high solar cell efficiency over 20 %. Figure 3.2 summarizes certified efficiencies for various solar cells [1]. The efficiency of single-crystalline Si solar cells is 25.6 % (144 cm^2) which is higher than other Si (20.8 %) and compound-type solar cells (CIGS (20.5 %) and CdTe (21 %)). The efficiency of amorphous Si solar cell is 10.1 % with 1 cm^2 cell size. At first, the target efficiency for organic solar cells was that of amorphous Si solar cells (10 %). Efficiency of dye-sensitized solar cells and thin-film organic solar cells is now 11.9 % and 11.0 % with 1 cm^2 cell size, respectively, which surpassed the efficiency of amorphous Si solar cells. In this chapter, structures and working principles for printable solar cells including dye-sensitized solar cells, thin-film organic solar cells, and perovskite solar cells are reviewed.

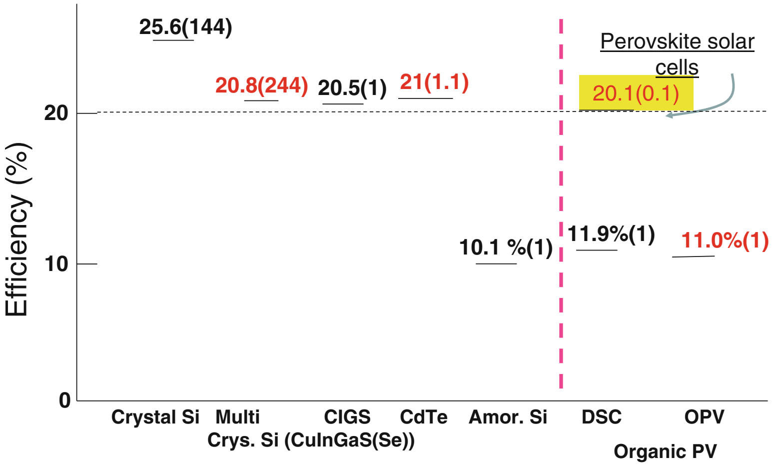

Fig. 3.2 Certified efficiency for representative solar cells at AM1.5 1 kW/m^2

3.2 Dye-Sensitized Solar Cell (DSSC) [2, 3]

DSSC are composed of transparent conductive oxide layered glass (F-doped SnO_2: FTO), porous titania layer with dye molecules, and electrolyte consisting of I^-/I_3^- redox species and counter electrode (FTO glasses with Pt or Pt/Ti metal plate) as shown in Fig. 3.3. The porous titania layer is the aggregate of nano titania particles with 20–30 μm diameter. Paste containing titania nanoparticles is printed on the FTO glasses, and the substrate is baked at 400–450 °C for 30 min to evaporate organic materials and make necking among titania nanoparticles. The samples are dipped in dye solutions from 30 min to 20 h, depending on the dye structure. The dye has carboxylic moieties which make bonding with Ti-OH on titania nanoparticles to form Ti-O-CO dye structure. These dyes are adsorbed by mono-layer structure on the porous titania. Ru compounds are commonly employed because they have broad absorption originating from metal to ligand charge transfer (MLCT), which covers wide range of visible spectrum region. Dye aggregations sometimes cause serious decrease on photovoltaic performances, which should be avoided to design molecularly. A counter electrode was coupled with the working electrode by employing thermoplastic films such as ionomer films. Pt was sputtered on Ti metal sheet or FTO glasses to prepare the counter electrode. Electrolyte is injected into the space between the working electrode and the counter electrode. All can be prepared by printing process. The process mentioned above is summarized in Fig. 3.4. Electrolyte consists of LiI (I^- species) and I_2 (I_3^-) species. In addition, t-butylpyridine is added in order to increase the open-circuit voltage (Voc), which neutralizes carboxylic acid of dyes, or adsorbed on the titania surface to go up the conduction band level of the titania. Other additives, such as imidazolium cation and guanidinium cation, are added to increase stability.

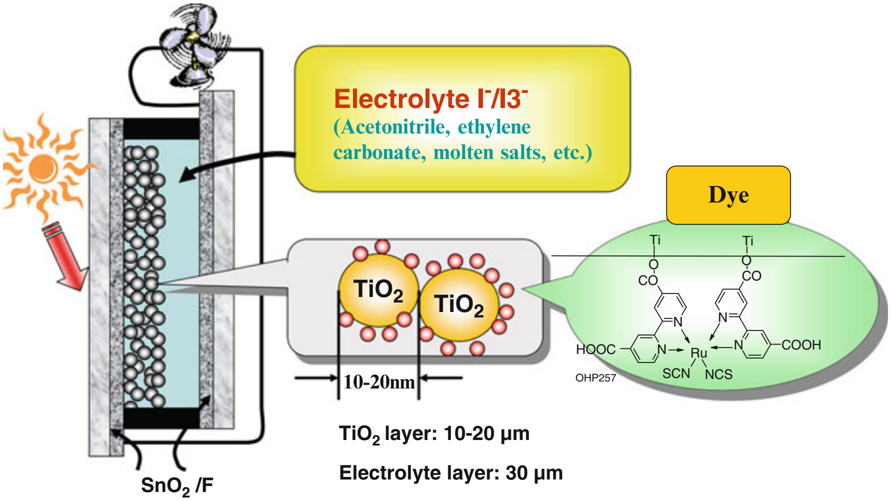

Fig. 3.3 Structure of dye-sensitized solar cells

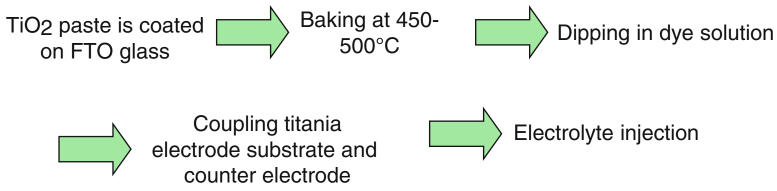

Fig. 3.4 Cell preparation process for dye-sensitized solar cells

Figure 3.5 shows the working principle for the DSSC. On dye excitation, electrons in the highest occupied molecular orbital (HOMO) go up to the lowest unoccupied molecular orbital (LUMO). The electrons in LUMO are injected into a porous titania layer (n-type wide-gap semiconductor) and are diffused in the porous titania. On the counter electrode with Pt catalyst layer, I_3^- species are reduced to form I^- which diffuses in the electrolyte and gives the electron to oxidize dye. Charge recombination occurs through routes 9, 10, 11, and 12. The electron injection (route 2) occurs on the order from 10^{-11} to 10^{-13} s, which is faster than that of the charge recombination of the order from 10^{-2} to 10^{-4} s. Therefore, charge collection by porous titania exceeds the charge losses by the recombination. Charge collection (route 3) (10^{-3} s) seems to compete with charge recombination (route 11) (10^{-4} s). However, electron from redox species (route 8) is faster (10^{-6} s) than that of route 11 and charge collection (route 3) exceeds.

The extremely long electron diffusion length in titania is associated with the high efficiency of the dye-sensitized solar cells. Electron lifetime (τ) in porous titania is the order of 10–100 msec, and the electron diffusion coefficient (D) is on the order of 10^{-5} cm^2/s. The electron diffusion length (L) expressed by $(D\tau)^{1/2}$ reaches 50–

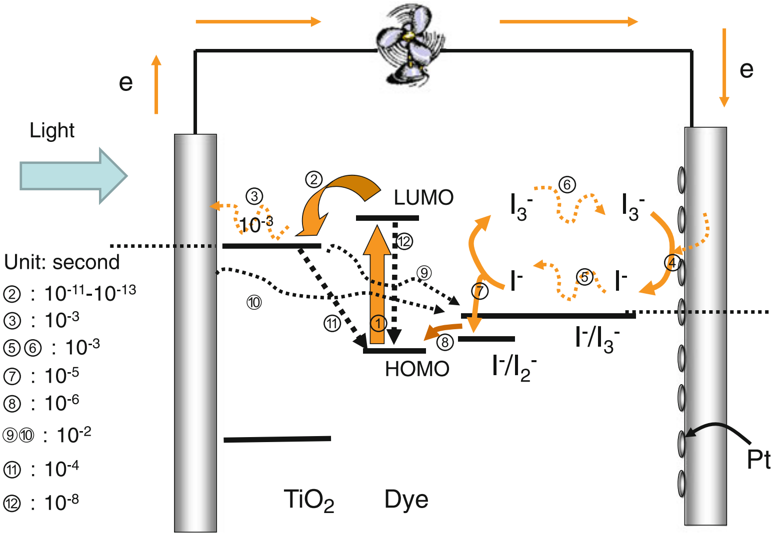

Fig. 3.5 Working principle for DSSC

100 μm when porous layer is filled with electrolytes. D and τ can be measured by impedance spectroscopy (intensity-modulated photovoltage spectroscopy, IMVS) [4–9] or open-circuit voltage decay method [10]. The long electron diffusion is explained by ambipolar diffusion mechanism, where Li cation is adsorbed on the titania surface and screens the electric field from the outside of the titania nanoparticles. Therefore, coupling of nano-size titania and electrolytes plays an important role for the high efficiency. I^-/I_3^- diffusion process in electrolyte is one of the other diffusion processes. I^- carries electrons from the counter electrode. After I^- gives the electron to the oxidized dye, the resultant I_3^- (containing I_2) diffuses from working electrode to counter electrode. Bigger I_3^- ions diffuse 1.3 times slower than that of small I^- ions. Therefore, diffusion of I_3^- is the rate-determining steps in an electrolyte. The diffusion rate is from 10^{-5} cm^2/s to 10^{-7} cm^2/s, depending on the viscosity of electrolytes. The diffusion coefficient increases with a decrease in viscosity of solvent and follows Stokes-Einstein relation as shown in Eq. 3.1:

$$D = RT/6\pi N_a r_a \zeta_a \eta \tag{3.1}$$

D, diffusion coefficient
T, temperature
r_a, ion radius
ζ_a, microviscosity factor
η, viscosity

The diffusion coefficient is determined by a limiting current method in electrolyte from Eq. 3.2:

$$D = (I_{\text{lim}} \times d)/(2n \times F \times C_{\text{o}}) \tag{3.2}$$

D, diffusion coefficient (cm^2/sec)
d, distance between two electrodes (cm)
I_{lim}, limiting current (mA/cm^2)
F, faraday constant (C/mol)
C_{o}, iodide concentration

Short-circuit current Jsc is affected by diffusion resistances, such as diffusion of electrons in titania, diffusion of I^- and I_3^- in electrolytes, and interfacial series resistance of Pt/electrolyte, electrolyte/dye, porous titania/FTO interfaces, and so on. In order to enhance the efficiency, it is necessary to increase these diffusion coefficients and decrease the charge transfer resistances on each interface.

Maximum Voc corresponds to the difference of TiO_2 conduction band energy level and I^-/I_3^- redox potential (around 0.9 V). One of the approaches to increase Voc is to deepen the potential level of redox shuttle. Figure 3.6 shows the representative redox shuttle potentials which are compared with I^-/I_3^- redox shuttle. Among them, Co redox shuttles gave the best results. The Voc increased from 0.75 V for I^-/I_3^- redox shuttle to 0.95 V for $Co(dpy)_3$. 12.3 % efficiency has been reported for DSSC stained with cocktail dyes consisting of porphyrin dye and

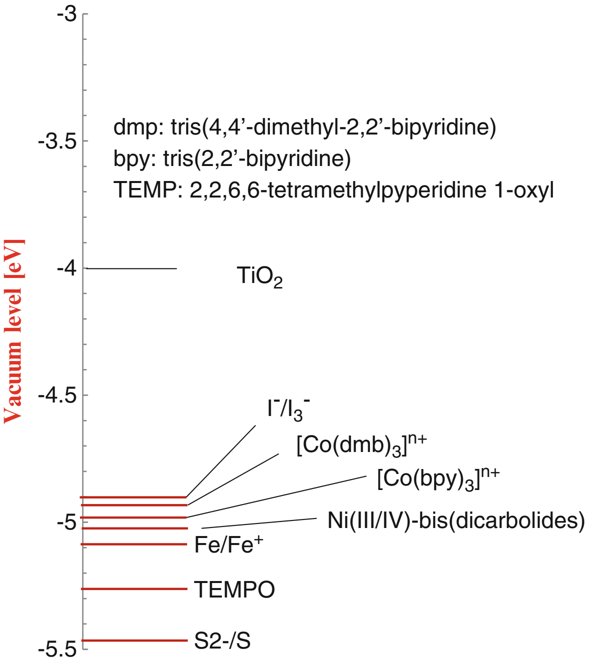

Fig. 3.6 Representative iodine-free redox shuttles for DSSC

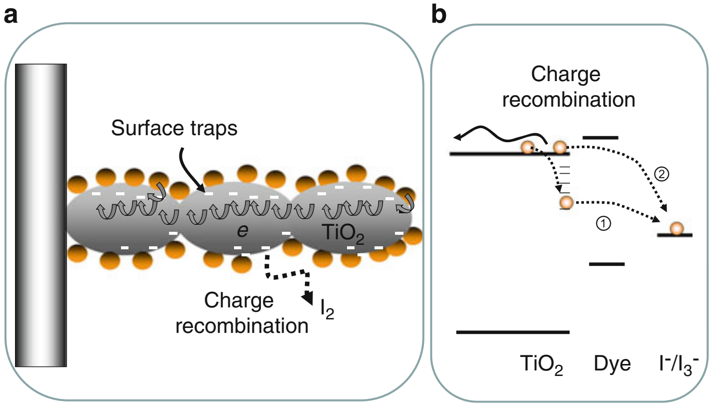

Fig. 3.7 Voc losses caused by charge recombination for DSSC. (**a**) Electron diffusion in titania, (**b**) charge recombination on energy diagram

organic Ru-free dye [11]. Recently, 13 % with Voc of 0.91 V, Jsc of 18.1 mA cm^{-2}, fill factor of 0.78, and a power conversion efficiency of 13 % have been reported [12]. The anxiety for the Co redox is slow diffusion in electrolytes. The diffusion coefficient for the Co redox shuttle is about a half of that of iodine/iodide redox shuttle. The high efficiency has been reported only in acetonitrile with low viscosity.

Voc decreases when back electron transfer or charge recombination (routes 9 and 10 in Fig. 3.5) occurs. Electrons in titania diffuse in the titania by hopping shallow traps which are on the surface as well as inside the titania nanoparticles as shown in Fig. 3.7. Among them, shallow surface traps on the titania surface are centers for the charge recombination. Surface passivation of titania with dyes is effective and decreases the surface trap densities and decreases the opportunities for charge recombination [13–16]. Another approach to decrease the opportunities for the charge recombination is to separate physically the titania surface from I_3^- (holes) [5–9] as shown in route 2 in Fig. 3.7b. We employed five model compounds with different alkyl chain lengths [6] as shown in Fig. 3.8. The adsorption density of dyes on titania increased with an increase in the length of these chains, followed by increase in the Voc. Longer alkyl chains enable closely packed adsorption of dye molecules, which passivate well the surface traps of the nanoporous titania [6, 8]. The passivation of traps by these dye molecules is measured by thermally stimulated current method [17], where electrons trapped at low temperature come out as the temperature goes up. The current and the temperature at which electrons come out are associated with trap density and trap depth. Therefore, the trap distribution can be expected. It was found that the trap density of titania nanoparticles decreased from 10^{17}/cm^3 to 10^{16}–10^{15}/cm^3 after the surface passivation by these dyes, which suppressed the charge recombination route 1 in Fig. 3.7. In addition, long alkyl chains retard the charge recombination route 2 in Fig. 3.7 as well. As the results, electron lifetime and Voc increased with an increase in the chain length of the dye as shown in Fig. 3.9.

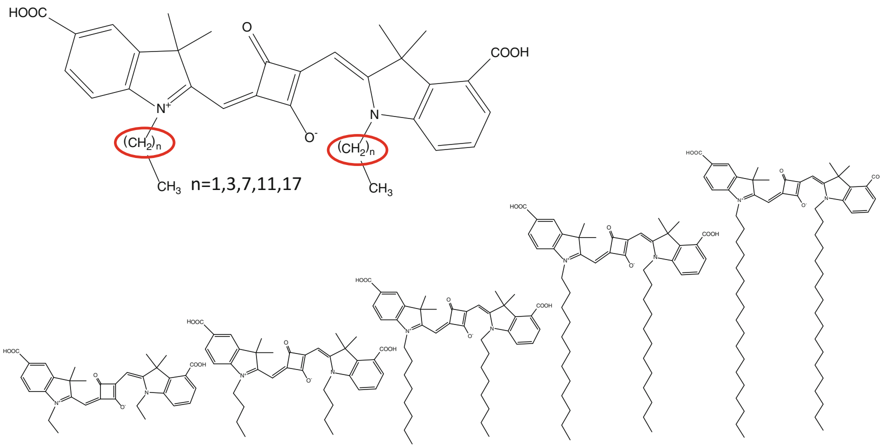

Dye-2
(alkyl chain=2)

Dye-4
(alkyl chain=4)

Dye-8
(alkyl chain=8)

Dye-12
(alkyl chain=12)

Dye-18
(alkyl chain=18)

Fig. 3.8 Model dyes for surface passivation

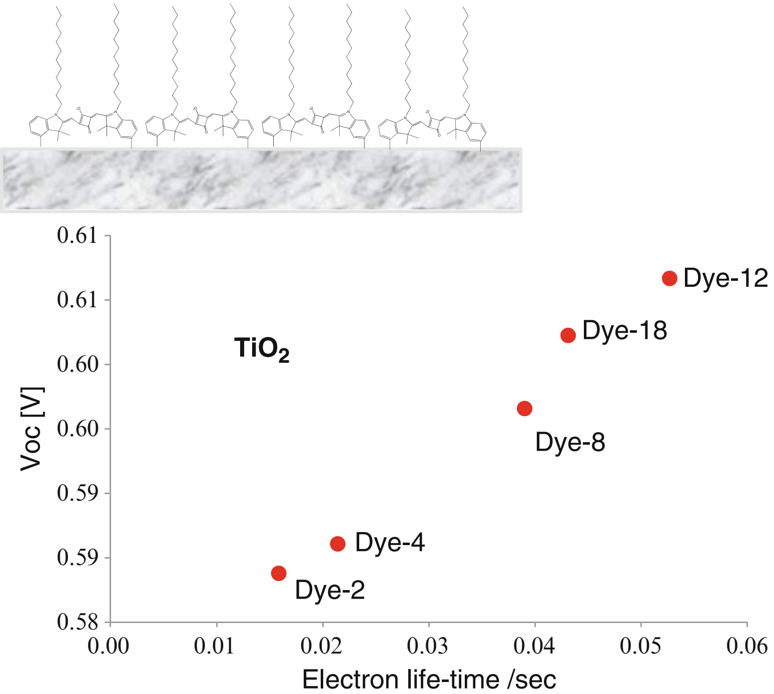

Fig. 3.9 The relationship between Voc and electron lifetime

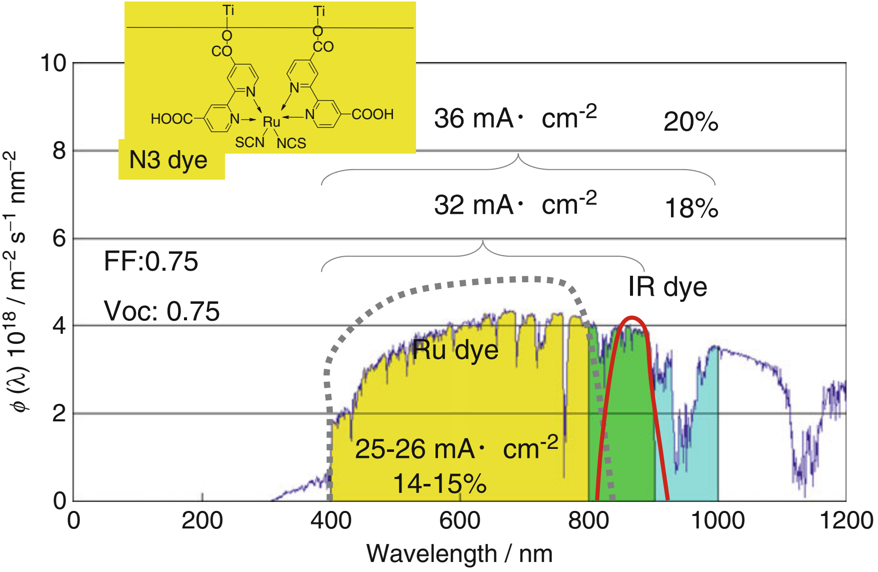

Fig. 3.10 Solar light spectrum (AM1.5,100 mW/cm^2)

Light harvesting in the area of infrared regions which have not been harvested by Ru dyes is another approach for increasing Jsc. Figure 3.10 shows the relationship between solar light spectrum and coverage of spectrum area by representative Ru dye (N3). The representative dye covers the wavelength from 400 nm to 800 nm. Supposing that the internal quantum efficiency is 100 %, 25–26 mA/cm^2 is expected. The coverage of wavelength becomes longer to 900 nm and 1000 nm; 32 and 36 mA/cm^2 are expected. Actually Os dyes cover the wavelength region up to 1100 nm. However, the incident photoconversion efficiency (IPEC) in visible region decreased to about 0.6 which was lower than 0.8 of N3 dye. Consequently total Jsc did not change even if IR light was harvested. In addition, serious Voc losses were observed [18].

Jsc is coupled with Voc and does not discuss separately. Figure 3.11 shows working principle and voltage losses predicted for dye-sensitized solar cell. Dye is excited by the light having x nm absorption spectrum edge (associated with X/1240 eV(ΔG4)). However, the expected maximum efficiency is ΔG3 (ΔG4-Δ G1-ΔG2), where ΔG1 and ΔG2 stand for voltage loss for electron injection and hole injection, respectively. Therefore, at least, ΔG1 and ΔG2 becomes voltage losses. In addition, voltage loss associated with charge recombination (route 1 and 4 in Fig. 3.11) occurs. Figure 3.12 shows the relationship between absorption spectrum edge and expected solar cell efficiency when voltage losses are varied. For DSSC with 0.6 eV loss, expected maximum efficiency is 14.8 % by using light absorber with 900 nm edge (under the condition of average incident photon to current conversion efficiency (IPCE) = 0.8, FF 0/7). With this 0.6 eV loss, trying to harvest light of wavelength longer than 900 nm does not succeed because obtained Voc becomes low and the expected efficiency decreases as the absorption spectrum

Fig. 3.11 Working principle for dye-sensitized solar cells and voltage loss

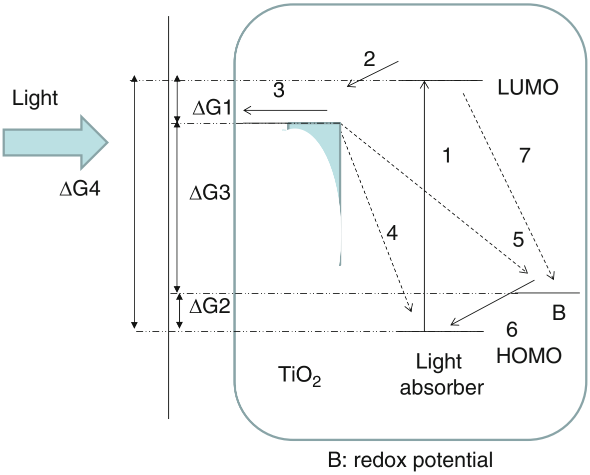

Fig. 3.12 The relationship between expected solar cell efficiency and absorption spectrum edge

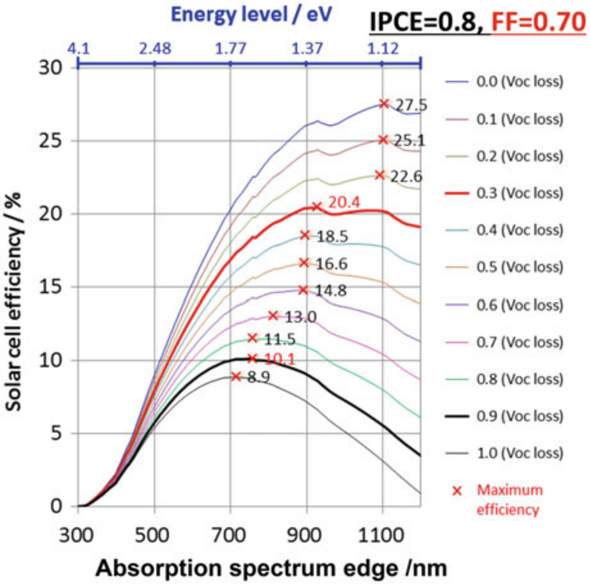

edge of light absorber becomes shifted to longer wavelength as shown in Fig. 3.12. Therefore, it is recommended to synthesize dyes with 900 nm spectrum edges in order to enhance the efficiency for DSSC with iodide redox shuttles [19]˙

The following items have to be at least satisfied with for high-efficiency light absorbers:

1. LOMO of the light absorber is shallower than that of titania conduction band by 0.2 V.
2. HUMO of the light absorber is deeper than that of redox potential by 0.4 V.

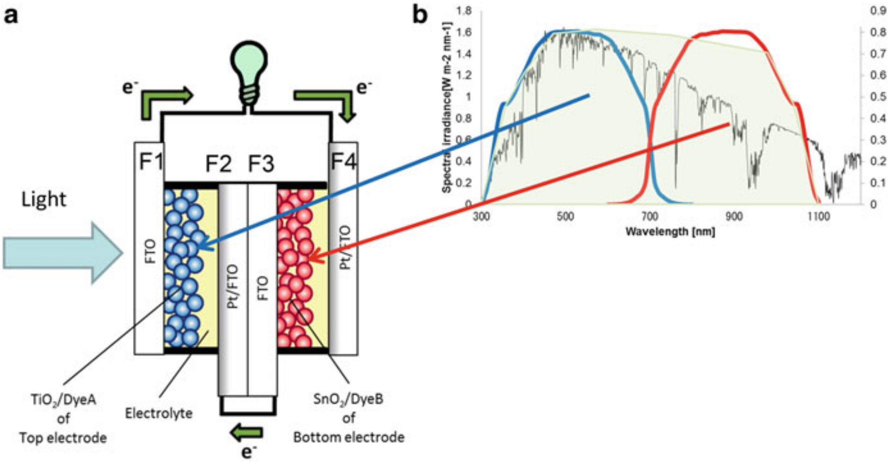

Fig. 3.13 Structure of mechanically stacked DSSC tandem cells. (**a**) Tandem cell structure, (**b**) spectral coverage for top and bottom cells

3. Molecular orbital for LUMO of the light absorber is distributed on COOH anchor groups.
4. Excitation lifetime of dye itself is longer than the order of *n*sec.
5. Dye aggregation has to be avoided because the aggregation usually shortens the excitation lifetime. For suppressing the dye aggregation, it is effective to add aggregation inhibitors with light absorbers.

Based on the efficiency curves, higher efficiency is expected for DSSC with Co redox shuttle, because the voltage loss for electron shift from the Co redox to the HOMO of the oxidized dye ($\Delta G2$) is expected to be 0.2 V which is less than 0.4 V of iodine redox shuttle. Electrons shift from I^- to HOMO of the dye by two-step process as shown in Fig. 3.5; however, electron shift from Co^{2+} to HOMO of the dye occurs in one step. Therefore, voltage loss ($\Delta G1 + \Delta G2$) in Fig. 3.11 is expected to be 0.4 V which is smaller than 0.6 V of iodine shuttle redox. The expected solar cell efficiency for Co shuttle is 18.5 %, employing light absorbers with 900 nm spectrum edge as shown in Fig. 3.12. Recently, it has been reported that direct transition from dye HOMO to conduction bond of titania and Ru dyes with spin-orbital coupling decreases $\Delta G1$ [20, 21].

Tandem cell is the next step to achieve high-efficiency cells. Tandem cells are composed of at least two cells which are connected in series. The top cell harvests light with shorter wavelength, and the bottom cell covers the area with longer wavelength. The voltage of the tandem cell is the sum of voltages for both top and bottom cells. Therefore, high voltages are obtained. Harvesting light in IR region in single cells does not directly lead to high-efficiency solar cells as shown Fig. 3.12. Tandem cell makes it possible. Figure 3.13a shows the mechanically stacked tandem cell structure for DSSC. The top cell harvests light with shorter wavelength, and the bottom cell absorbs light with longer wavelength. In order to suppress the

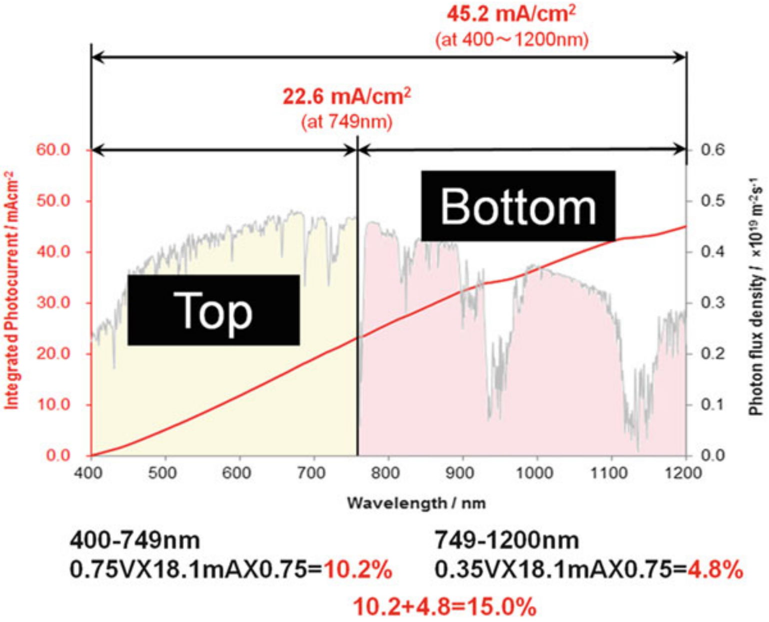

Fig. 3.14 Estimation of efficiency for tandem cell and current matching

current losses for both of top and bottom cells, current in the top cell has to match with that in the bottom cell. Figure 3.14 shows the example for efficiency estimation for tandem cells. Top cell harvests light from 400 nm to 749 nm and obtains the photovoltaic performance of Voc 0.75 V, Jsc 18.1 mA (out of 22.6 mA/cm^2), and fill factor (FF) 0.75. Bottom cell harvests the light from 749 nm to 1200 nm to obtain the photovoltaic performance of Voc 0.35 V, Jsc 18.1 mA (out of 22.6 mA/cm^2), and fill factor (FF) 0.75. Totally, photovoltaic performance of Voc is 1.1 V, Jsc 18.1 mA/cm^2 (out of 22.6 mA/cm^2), fill factor (FF) 0.75, and efficiency 15.0 %. To harvest the IR light, semiconductors with narrower band gaps such as SnO_2 coupled with IR dyes have to be developed for future works.

Light harvesting loss in the bottom cells causes serious problems for the mechanically stacked tandem cells, because the light has to pass a FTO glass (F1 in Fig. 3.13) of working electrode in the top cell, a FTO glass (F2 in Fig. 3.13) of counter electrode in the top cells, and a FTO glass (F3 in Fig. 3.13) of working electrode in the bottom electrode. In addition, FTO glasses absorb near-IR and IR light longer than 800 nm which causes serious light harvesting losses in the area of IR. We have reported tandem cells with transparent conductive oxide (TCO less) bottom cell [22] structure as shown in Fig. 3.15b. The bottom cell has back-contact electrode structure, and TCO (FTO) glass is not needed. Figure 3.15a also shows I-V curves for the model cell for proving the tandem performances by using two model dyes having visible-light absorption. The absolute efficiency is not high, but observed Voc for the tandem cell was the sum of the top and the bottom

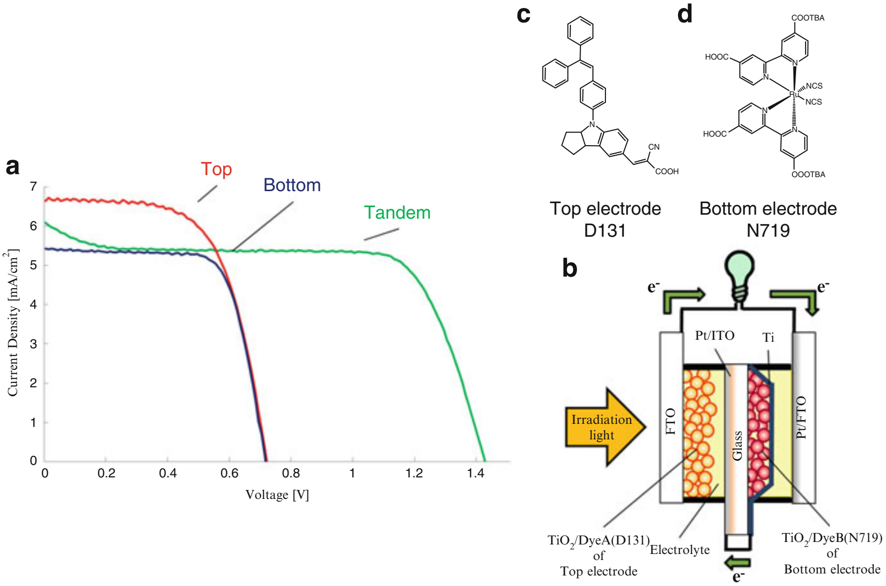

Fig. 3.15 Model tandem cells with TCO-less structure. (**a**) I-V curves for tandem, top, and bottom cells, (**b**) tandem cell with top cell and TCO-less bottom cell. (**c**) D131 dye structure, (**d**) N719

cells, proving that the TCO-less tandem cell actually works. IR dye/SnO_2 electrode working as light harvesting layer in the bottom cell is needed to complete the TCO-less tandem cells.

3.3 All-Solid-State Dye-Sensitized Solar Cells and Perovskite Solar Cells

All-solid-state dye-sensitized solar cells are prepared by replacing electrolyte layers to solid hole transport layers (HTL), such as 2,2’,7,7’-tetrakis(N,N-di-p-methoxyphenylamine)-9,9′-spirobifluorene (spiro-OMeTAD), CuI, CuSCN, polythiophene, polypyrrole, and $CsSnI_3$ [2, 23, 24]. All-solid-state DSSCs differ from the liquid-type DSSCs from the following points. The fundamental structure and the working principle are shown in Figs. 3.16 and 3.17. The working principle is almost the same as that of liquid-type DSSCs. Maximum Voc is the difference between the conduction band of titania and HOMO of HTL. Charge recombination of routes 6, 8, and 9 is faster than that of liquid-type DSSCs. Thickness of porous titania layer is around 1–2 μm, which is extremely thinner than 15–20 μm of the liquid-type DSSCs, because the hole diffusion length of p-type organic semiconductor is not as large as that of redox shuttles in electrolytes. In order for the thin porous layer to harvest the light effectively, organic dyes with high extinction

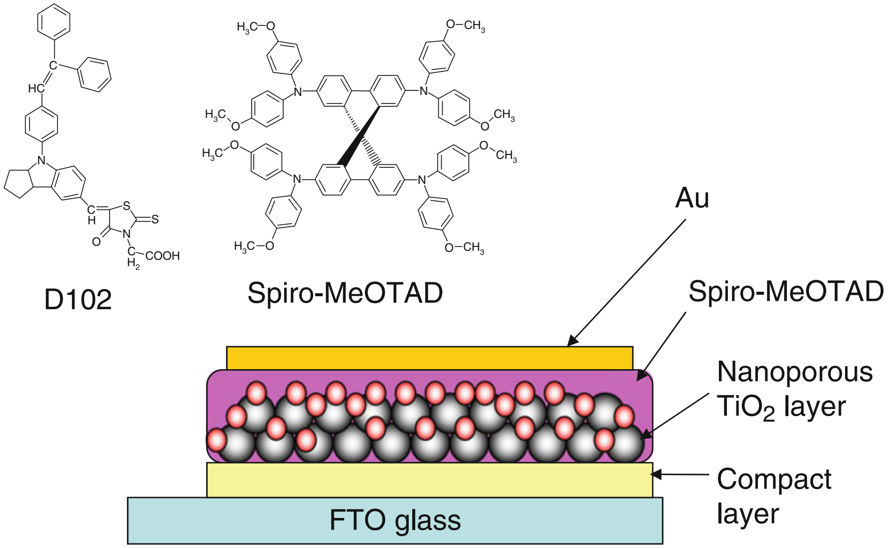

Fig. 3.16 Structure of all-solid-state DSSC

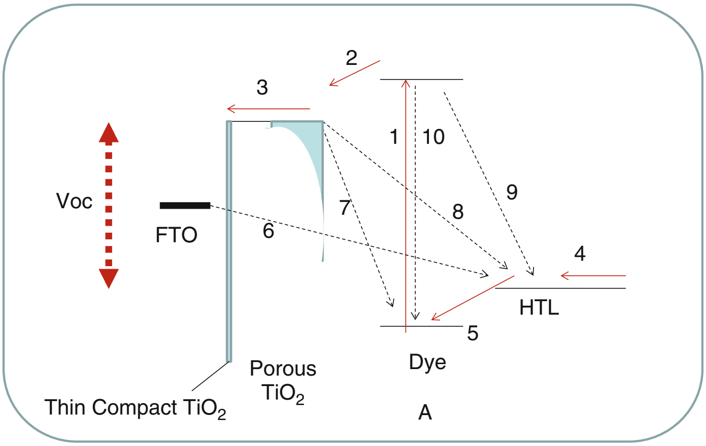

Fig. 3.17 Working principle for all-solid-state DSSC

coefficient were employed. Amorphous spiro-OMeTAD was selected in order to make a good contact between dyes and spiro-OMeTAD. t-Butylpyridine was added in the spiro-OMeTAD to suppress the charge recombination of oxidized dyes with holes in spiro-OMeTAD (routes 6, 8, and 9). In addition, thin compact titania layer (50 nm) was inserted between FTO layer and porous titania layer because contact between FTO and HTL causes serious charge recombinations. Li ion ($Li(CF_3SO_2)_2$) N and $N(PhBr)_3SbCl_6$ were added in spiro-OMeTAD. The former is probably

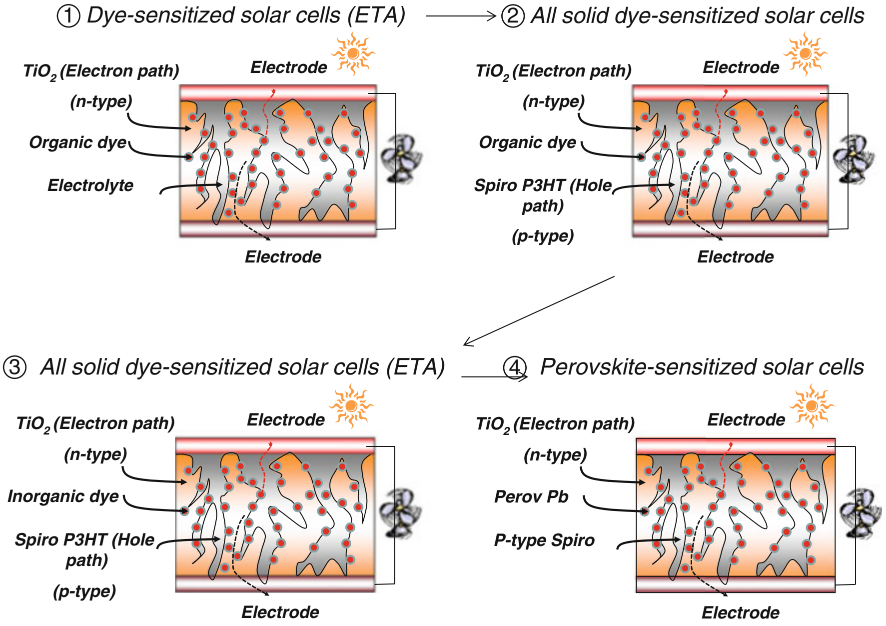

Fig. 3.18 History from all-solid-type DSSC to perovskite solar cells

added for promoting ambipolar diffusion of electrons in TiO_2, and the latter is for increasing carrier density in spiro-OMeTAD (doping) to decrease series resistances. The efficiency of 5.1 % has been reported in the first paper.

Perovskite solar cells is an extension of this conventional all-solid-state DSSC as shown in Fig. 3.18(4). Started from conventional DSSC with liquid electrolytes (1), the research moved toward the development of all-solid-state DSSC (2), where liquid electrolyte was replaced with hole transport materials as described before. Then the organic dyes were replaced with inorganic light absorbers, such as CdSe, CdTe, CdS, Sb_2S_3, and so on as shown in 3 of Fig. 3.18 [25]. The light absorber is called extremely thin absorber (ETA). After that, the inorganic dye was replaced with perovskite materials to give perovskite solar cells (4).

The first reported perovskite solar cell structures were composed of FTO glass/compact titania layer, porous titania layer or alumina layer/Pb perovskite layer/HTL, and electrode, as shown in Fig. 3.19. Figure 3.20a shows cross-sectional view for PVK solar cell with porous titania layer. Compact layer with 20 nm thickness was observed on the FTO layer with light scattering structures as shown in Fig. 3.20b, c. Preparation of compact layer without pin holes is important for high-efficiency solar cells. Figure 3.21b, c is elemental distribution of TEM picture of Fig. 3.21a. Pb and I are distributed homogeneously in porous titania layers shown in Fig. 3.21c [26]. Pb perovskites (Pb PVK) are a kind of ionic crystal and composed of Pb^{2+}, I^-, and $CH_3NH_4^+$ (MA). They are separated to PbI_2 and MA^+I^- in solution, and the color of solution is light yellow consisting of PbI_2

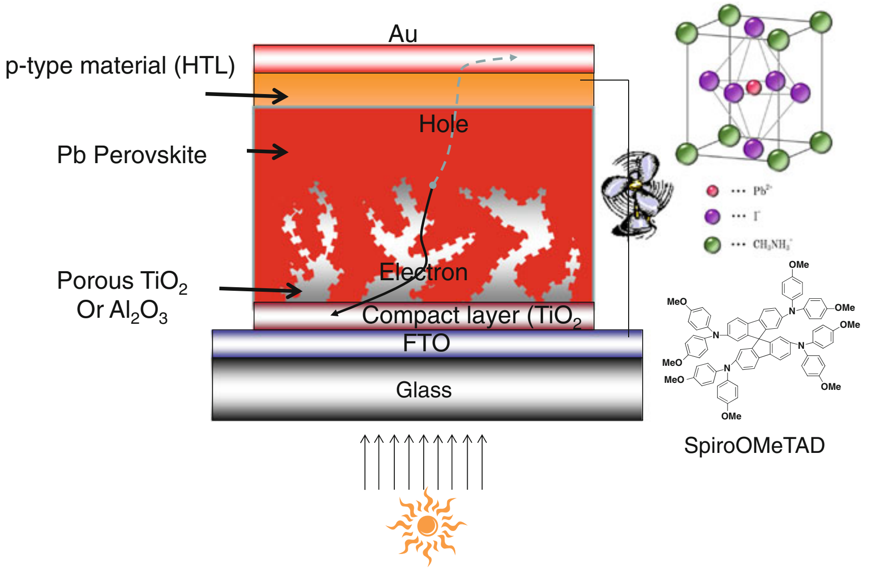

Fig. 3.19 Perovskite solar cell structure

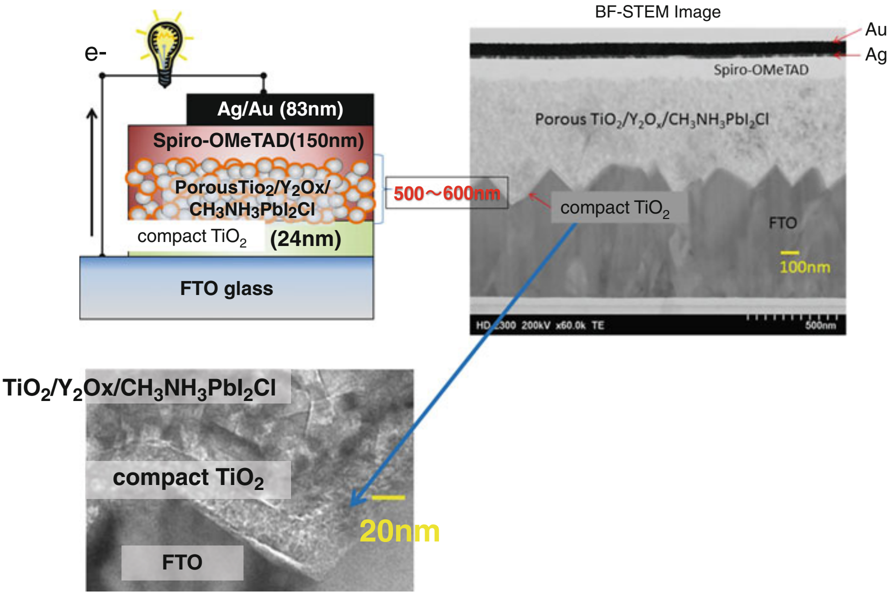

Fig. 3.20 Cross-sectional view for PVK solar cell with porous titania layer

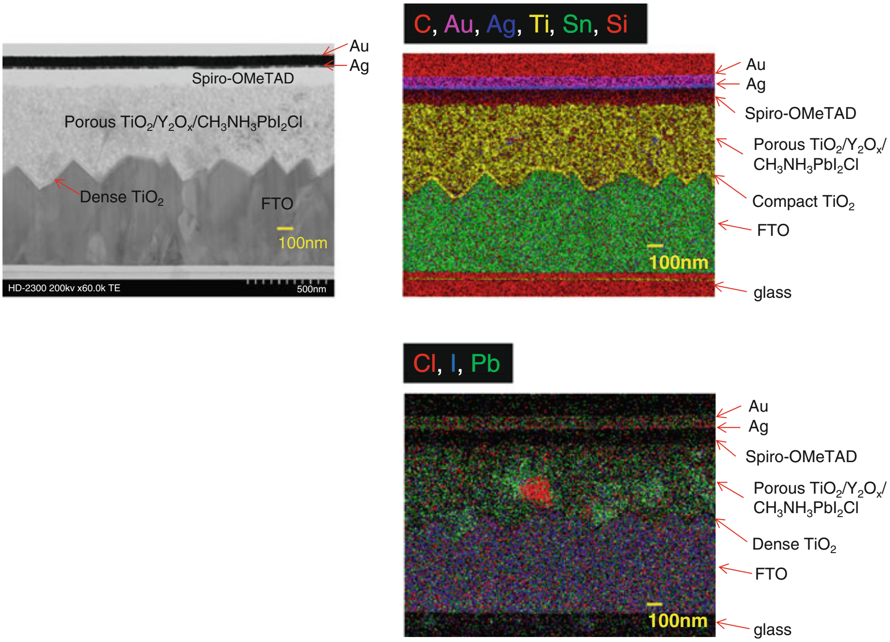

Fig. 3.21 Elemental distribution map

and MAI (methyl ammonium iodide). After solvent is removed, Pb PVK crystals (black) are spontaneously formed. The energy diagram and working principle for perovskite solar cells are shown in Fig. 3.22. The porous layer is called a scaffold layer and worked for making better crystal of perovskite layers. Perovskite is excited by the light exposure and then exciton forms. The exciton binding energy of the perovskite is very small (30–50 meV) [27, 28] which is almost comparative to 25 meV of room temperature energy and immediately separated into carriers of electrons and holes. For comparison, the exciton binding energy of organic materials, ZnO, and Si are around 300, 60, and15 meV. The exciton binding energy of Pb PVK is on the order of that of Si solar cells. In perovskite solar cells with porous alumina, electrons are collected through Pb PVK itself [29]. The oxidized Pb PVK was reduced by electrons from HOMO of HTL. The maximum Voc is the difference between Pb PVK-LUMO and HTL-HOMO. For perovskite solar cells with porous titania [30–32], electrons are collected with both titania and Pb PVK layers. Charge recombination occurs through routes 4, 5, 7, and 8 of A and B in Fig. 3.22.

Recently, bilayer perovskite solar cells without scaffold layers have been reported [33]. The perovskite solar cell structures are now classified roughly into four types as shown in Fig. 3.23. A and B were already explained. C and D are perovskite solar cells with bilayer structure which does not consist of porous scaffold layers. C has PVK layer on compact titania layer and HTL, where PVK works as n-type semiconductor. D has PVK layer on compact p-type semiconductors such as PEDOT-PSS and electron transport layer (ETL) such as C60 [33]. In

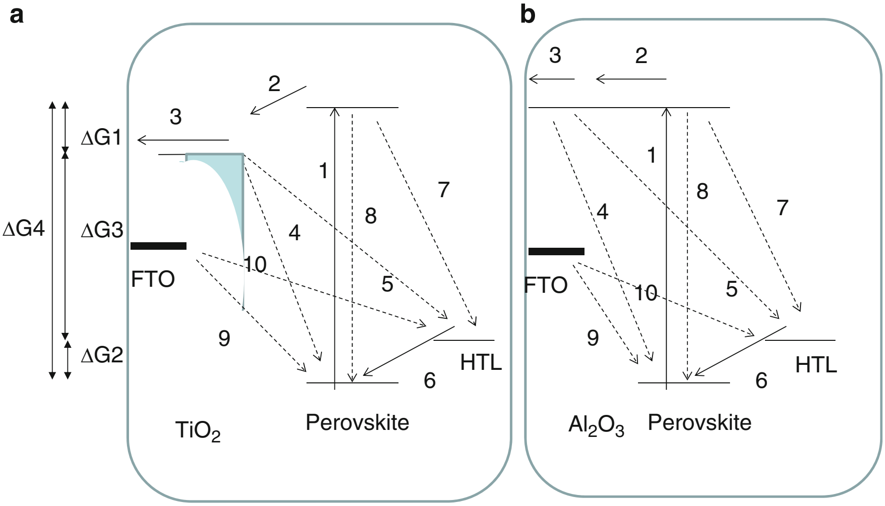

Fig. 3.22 Energy diagrams and working principle for perovskite solar cells. (**a**) Electron collection: TiO_2 layer, (**b**) electron collection: perovskite

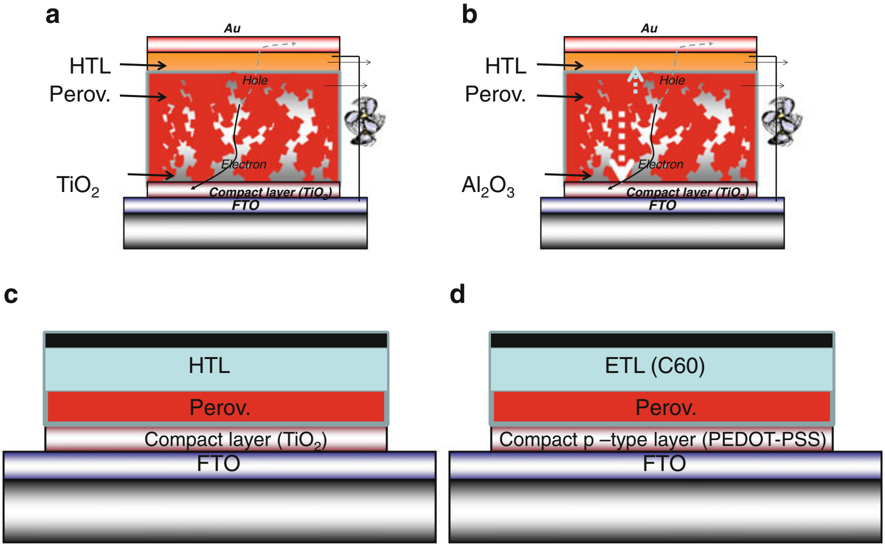

Fig. 3.23 Energy diagrams and working principle for perovskite solar cells

this device, the PVK works as p-type semiconductor. Efficiencies over 10 % have been reported for both of the structures. Pb PVK has bipolar properties. The effective mass for the electron (me*) and the hole (mh*) is calculated to be me*/m0 = 0.23 and mh*/m0 = 0.29 [34]. For reference, Si has me*/m0 = 0.26 and mh*/m0 = 0.39. The effective mass of Pb PVK is almost the same as that of Si.

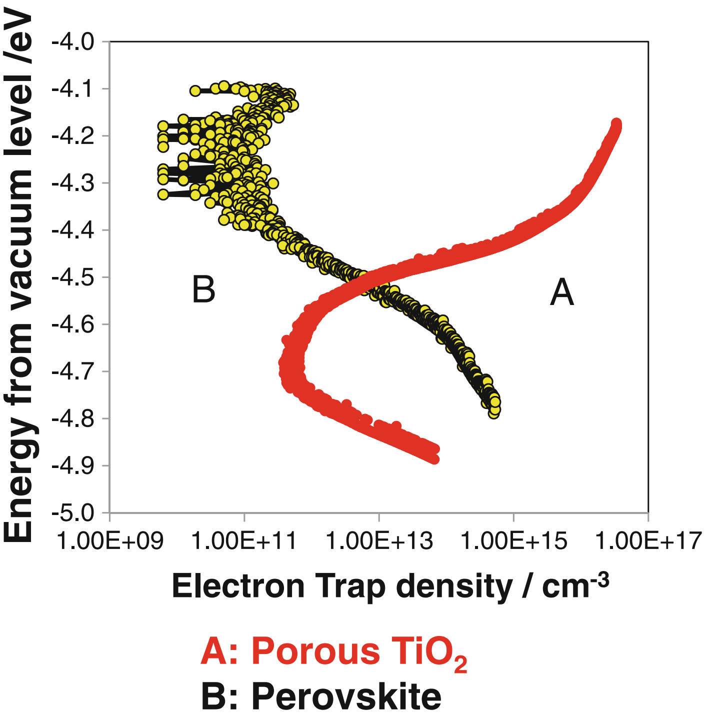

Fig. 3.24 Trap distribution after passivation of TiO_2 surface

The high efficiency is brought about by the following items:

1. Long carrier lifetime in Pb perovskite layer (μsec)
2. Low shallow-trap density
3. Low crystal defect
4. Light-induced ferroelectric effect
5. Low voltage loss

The long carrier lifetime of Pb PVK is associated with items 2,3, 4, and 5. We have reported that the shallow-trap density at around −4.3 eV from vacuum level was $10^{11}/cm^3$ which was extremely lower than $10^{17}/cm^3$ of the porous titania layer as shown in Fig. 3.24 [26]. Crystal defect of Pb PVK was estimated from Urbach tail of absorption coefficient [35]. Crystal defect makes sub-bands between the conduction band and valence band, which makes the slope of the spectrum edge less steep, and Urbach energy goes higher. Urbach energy of a-Si, GaAs, c-Si, CIGS, and PbPVK is reported to be 40–45 meV, 7.5 meV, 11 meV, 24 meV, and 15 meV, respectively. The crystal defect density of Pb PVK corresponds to that of GaAs and c-Si [35]. Voltage losses decrease linearly with decrease in the Urbach energy. The voltage loss for Pb PVK solar cells is about 0.3–0.4 V. For reference, the voltage loss of CIGS, c-Si, and GaAs has been reported to be 0.5–0.6 V, 0.35 V, and 0.3 V, respectively. Therefore, Pb PVK solar cells have a higher potential than CIGS. In addition, it has been reported that Pb PVK has photoferroics [36]. The photoinduced dipole domain separates hole from electrons.

It has been reported that some PVK solar cells show serious hysteresis, which is more remarkable for B, C, and D structures in Fig. 3.23 where electrons are collected by PVK itself [37, 38]. The voltage is swept from Voc to Jsc; higher FF and Voc are observed. The voltage sweeping should be from Jsc to Voc, and sweeping rate with delay time for taking in data should be described in this paper.

The charge recombination through routes 4 and 5 in Fig. 3.22a, b occurs seriously. These charge recombination routes are suppressed by surface passivation of porous titania by thin-film Al_2O_3 and Y_2O_3 [26]. Passivation can be also made by amino acid HI salts such as $HOCO\text{-}CH_2\text{-}CH_2\text{-}CH_2\text{-}NH_3I$ [39]. In addition, crystal growth on the passivation is controlled [39]. It was confirmed that the trap density of titania was decreased by the surface passivation, which was measured by thermally stimulated current method [26].

The perovskite layer can be prepared by one step in Scheme 3.1:

$$\begin{array}{l}\text{One step process}\\ 3MeNH_3{}^+I^- + PbCl_2 \rightarrow \underbrace{MeNH_3{}^+PbI_3{}^-}_{\text{Perovskite materials}} + \overset{\text{by products}}{2MeNH_3{}^+Cl}\end{array} \qquad \text{(Scheme 3.1)}$$

Another way to prepare the perovskite is called two-step process, where PbI_2 is spin-coated first and then methylammonium iodide (MAI) is introduced to the PbI_2 layer to form perovskite layers. MAI was introduced into PbI_2 layer by dipping the PbI_2/porous titania/FTO glass substrate in the solution of MAI or by spin-coating MAI solution on the PbI_2/porous titania/FTO glass substrate. The later gives the better results so far.

Pb PVK covers only visible region up to 800 nm. Assuming that voltage loss is 0.3–0.4 V, maximum efficiency is obtained by harvesting light up to 1100 nm (see Fig. 3.12). $MASnI_3$, $MAPbSnI_2$, and $MASnI_xBr_{(1\text{-}x)}$ have been reported for IR-sensitive perovskite solar cells [19, 40–42]. Figure 3.25 shows the comparison of IPCE curves for Pb PVK and Sn/Pb cocktail PVK solar cells [19]. The IPCE curve for the latter covered the wavelength region up to 1,040 nm. Internal quantum efficiency (IQE) kept high value up to 1000 nm as shown in Fig. 3.26. The efficiency of these IR-sensitive solar cells is still low, from 4 to 6 %. In order to increase the efficiency more and decrease in crystal defect, surface state control and confinement of light in the cell are needed. Sn PVK solar cells are air sensitive, and those colors disappear within one hour in the air. The Sn/Pb cocktail PVK has improved stability in the air by introducing Pb in the Sn PVK layer [19]. Light absorption spectrum edge can be tunable for changing Sn/Pb ratio from 800 nm to 1200 nm as shown in Fig. 3.27. Spectral tuning can be made for changing x ratio of $MASnI_xBr_{(1\text{-}x)}$ [40].

Organic ammonium ion-free PVK as well as Pb-free PVK have attracted interest recently [43–45]. Solar cells consisting of $CsSnI_3$ as the light harvesting layer

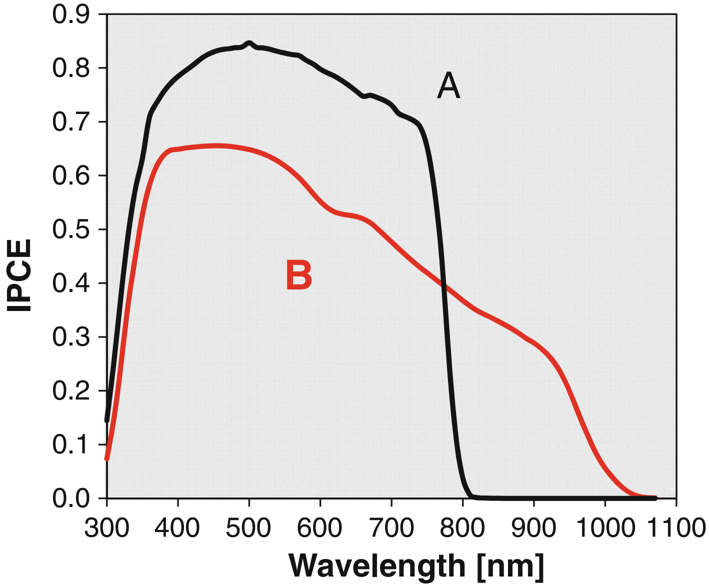

Fig. 3.25 IPCE curves for Pb PVK and Sn/Pb cocktail PVK solar cells. (**a**) Pb PVK/spiro-OMeTAD. (**b**) Sn/Pb perov/P3HT

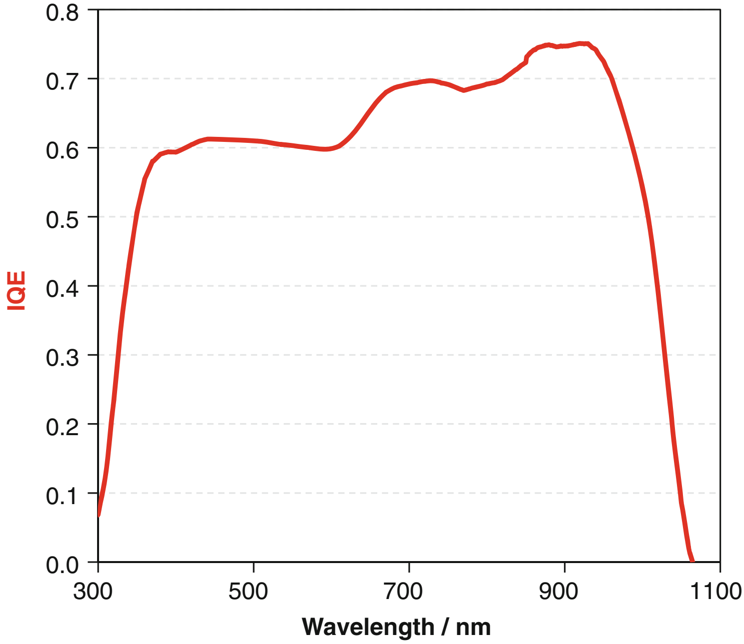

Fig. 3.26 Internal quantum efficiency for Sn/Pb PVK/P3HT solar cell

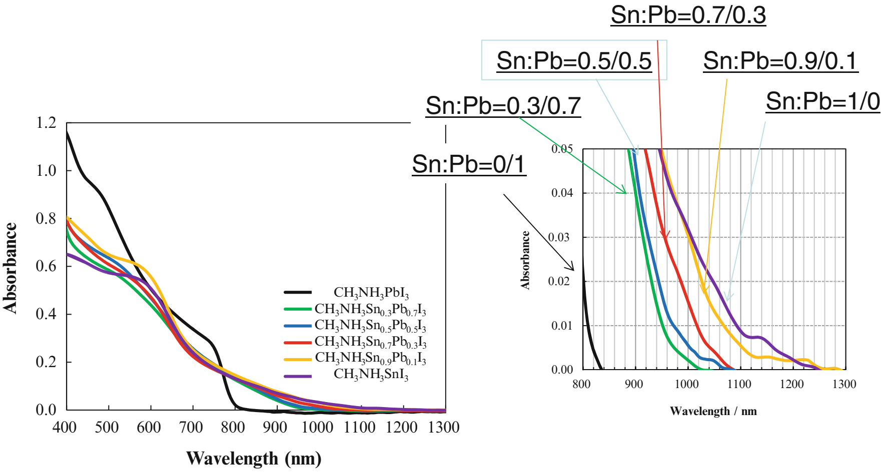

Fig. 3.27 Light absorption spectra for Sn/Pb cocktail PVK with various Sn/Pb ratios

(efficiency 4 %) have been reported. $CsSnI_3$ and Cs_2SnI_6 [40] have hole-transporting properties and employed for HTL for all-solid-state dye-sensitized solar cells.

3.4 Thin-Film Organic Solar Cells (OPV)

OPV is classified into OPV with flat p/n junction (see the experiment in Introduction) and OPV with bulk hetero p/n junction [46]. Since the two have the same working principle, OPV with bulk heterojunction is explained in this section. OPV consists of ITO glass/electron-blocking layer/bulk heterojunction layer of p- and n-type semiconductor/hole-blocking layer/counter electrode. Figure 3.28 shows one of representative OPV structures consisting of P3HT as a hole transport layer and PCBM as an electron transport layer whose structures are described in Fig. 3.28. P3HT as a light absorber has limited coverage of absorption spectrum up to around 600 nm. In order to increase the efficiency more, polymers with extended τ conjugation have been extensively developed. Figure 3.29 shows the working principle for OPV, where P3HT and PCBM are employed as the example of the explanation. P3HT works as light absorber as well as HTL. P3HT is excited and forms excitons in the P3HT layer. Because of low dielectric constant in P3HT, the exciton does not dissociate as it is. The exciton diffuses to the P3HT/PCBM interface (route 2 in Fig. 3.29) and is dissociated to electron and hole. The electron is injected in PCBM layer (3) and diffuses in the PCBM layer. Hole diffuses in the P3HT layer and reaches the electrode A. hole-blocking layer blocks for the hole to recombine to the electrons in electrode B, and electron-blocking layer suppresses for electron to recombine to the holes in electrode A. In addition, electron-blocking

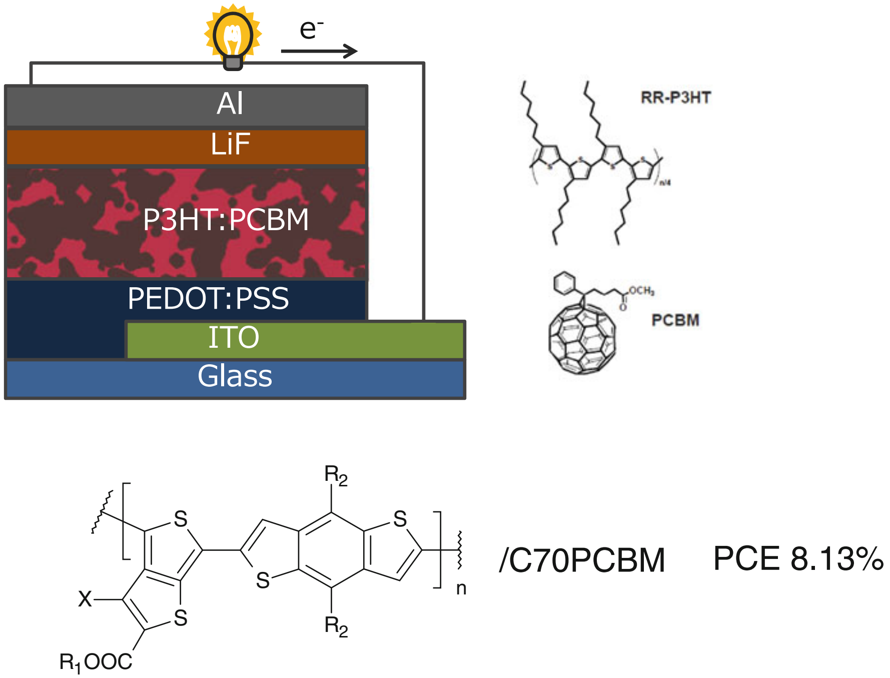

Fig. 3.28 Structure of thin-film organic solar cells

layer also works as exciton-blocking layer. Exciton diffusion is only on the order of 10 nm in organic semiconductors. Therefore, in order for the exciton to reach the P3HT/PCBM interface, bulk heterojunction structure is needed, where P3HT and PCBM have interpenetrated and bi-continuous structures. Charge recombination occurs through routes 6 and 7 in Fig. 3.29. Maximum Voc is the gap between LUMO of PCBM and HOMO of P3HT. In bulk heterojunction solar cells, both of P3HT and PCBM have an opportunity to contact with both electrodes. Fabrication of electron- and hole-blocking layer without pin holes is necessary for suppressing Voc and enhancing efficiencies. Figure 3.30 summarizes the representative electron and hole-blocking materials reported so far.

One of the advantages for OPV is the simple fabrication process. Organic material with p-type character such as P3HT and that with n-type character such as PCBM are blended in a solvent and make once a homogeneous solution. After the solution is spin-coated on the substrate and the solvent is evaporated, p-type materials are segregated from n-type materials to form bi-continuous structures with the order of 10–50 nm width, which is appropriate distance for exciton to dissociate into charge carriers [47]. In order to enhance the efficiency, tandem solar cells also have been reported [48].

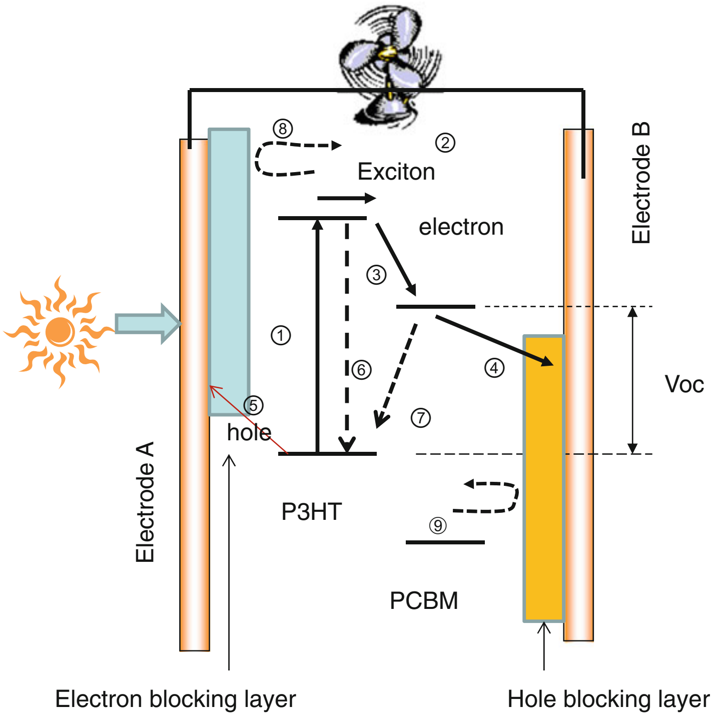

Fig. 3.29 Working principle for OPV

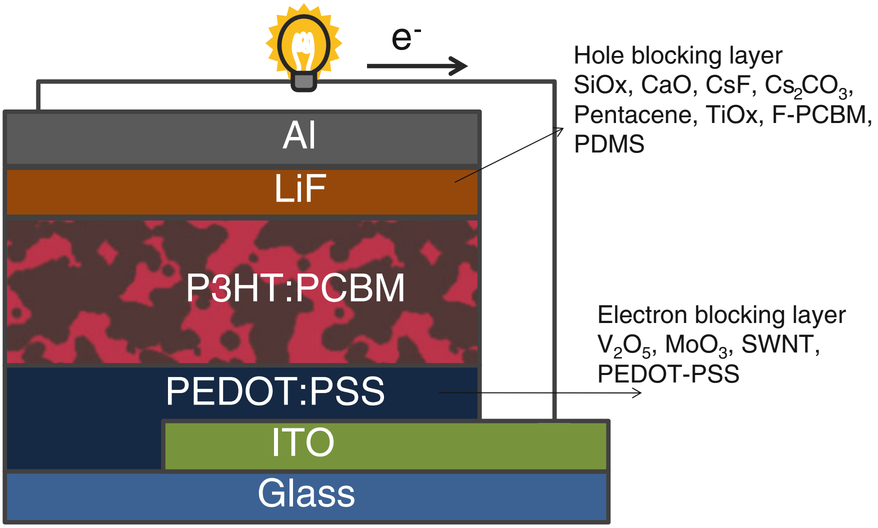

Fig. 3.30 Various charge- and exciton-blocking layers

3.5 Conclusion

Structures, working principle, and resent research trends for organic solar cells including DSSC, perovskite solar cells, and OPV were summarized. Since DSSC consists of layers in which each function is allocated to each layer and it is easy to explain the working function for organic solar cells, many pages were employed for the explanation of DSSC. These working principles are applicable to the other organic solar cells. I hope this chapter is useful for understanding organic solar cells.

References

1. M. Green, K. Emery, Y. Hishikawa, W. Warta, E.D. Dunlop, Prog. Photovolt: Res. Appl **23**, 1–9 (2015)
2. For review: A. Hagfeldt, G. Boschloo, L.Sun, L. Kloo, H. Pettersson, Chem. Rev. **110**, 6595–6663 (2010)
3. B. O'Regan, M. Graetzel, Nature **353**, 737 (1991)
4. Y. Ogomi, S. Sakaguchi, T. Kado, M. Kono, Y. Yamaguchi, S. Hayase, J. Electrochem. Soc. **153**, A2294 (2006)
5. K. Sayama, S. Tsugakoshi, K. Hara, Y. Ohga, A. Shinpou, Y. Abe, S. Suga, H. Arakawa, J. Phys. Chem. B **106**, 1363 (2002)
6. S.S. Pandey, T. Inoue, N. Fujikawa, Y. Yamaguchi, S. Hayase, J. Photochem. Photobiol. A **214**, 269 (2010)
7. S.S. Pandey, T. Inoue, N. Fujikawa, Y. Yamaguchi, S. Hayase, Thin Solid Films **519**, 1066 (2010)
8. T. Inoue, S.S. Pandey, N. Fujikawa, Y. Yamaguchi, S. Hayase, J. Photochem. Photobiol. A **213**, 23 (2010)
9. M. Miyashita, K. Sunahara, T. Nishikawa, Yu Uemura, N. Koumura, K. Hara, A. Mori, T. Abe, E. Suzuki, S. Mori, J. Am. Chem. Soc. **130**, 17874 (2008)
10. J. Bisquert, A. Zaban, M. Greenshtein, I. Mora-Seró, J. Am. Chem. Soc. **126**, 13550–13559 (2004)
11. A. Yella, H.-W. Lee, H. N. Tsao, C.Yi, A. K. Chandiran, Md..K. Nazeeruddin, E. W.-G. Diau, C.-Y. Yeh, S. M. Zakeeruddin, M. Grätzel, Science **334**, 629 (2011)
12. S. Mathew, A. Yella, P. Gao, R. Humphry-Baker, B.F.E. Curchod, N. Ashari-Astani, I. Tavernelli, U. Rothlisberger, K. Nazeeruddin, M. Grätzel, Nat. Chem. **6**, 242–247 (2014)
13. A. Kay, M. Graetzel, Chem. Mater. **14**, 2930 (2002)
14. Y. Diamant, S. Chappel, S.G. Chen, O. Melamed, A. Zaban, Coord. Chem. Rev. **248**, 1271 (2004)
15. E. Palomares, J.N. Clifford, S.A. Haque, T. Thierry Lutz, J.R. Durrant, J. Am. Chem. Soc. **125**, 475 (2003)
16. F. Fabregat-Santiago, J. Bisquert, L. Cevey, P. Chen, M. Wang, S.M. Zakeeruddin, M. Graetzel, J. Am. Chem. Soc. **131**, 558 (2009)
17. Y. Noma, T. Kado, D. Ogata, Y. Hara, S. Hayase, Jpn. J. Appl. Phys. **47**, 505 (2008)
18. A.C. Onicha, F.C. Castellano, J. Phys. Chem. **114**, 6831–6840 (2010)
19. Y. Ogomi, A. Morita, S. Tsukamoto, T. Saitho, N. Fujikawa, Q. Shen, T. Toyoda, K. Yoshino, S.S. Pandey, T. Ma, S. Hayase, J. Phys. Chem. Lett. **5**, 1004–1011 (2014)
20. S. Manzhos, R. Jono, K. Yamashita, J. Fujisawa, M. Nagata, H. Segawa, J. Phys. Chem. C **115**, 21487–21493 (2011)
21. A. Kinoshita, J.T. Dy, S. Uchida, T. Kubo, H. Segawa, Nat. Photonics **7**, 535–539 (2013)
22. A.K. Baranwal, T. Shiki, Y. Ogomi, S.S. Pandey, T. Ma, S. Hayase, RCS Adv. **4**, 47735–47742 (2014)

23. I. Chung, B. Lee, J. He, R.P.H. Chang, M.G. Kanatzdis, Nature **485**, 486 (2012)
24. H.J. Snaith, A. Petrozza, S. Ito, H. Miura, M. Graetzel, Adv. Func. Mater. **19**, 1810–1818 (2009)
25. G. Hodes, D. Cahen, Acc. Chem. Res. **45**, 705–713 (2012)
26. Y. Ogomi, K. Kukihara, Q. Shen, T. Toyoda, K. Yoshino, S. Pandey, H. Momose, S. Hayase, Chem. Phys. Chem. **15**, 1062–1069 (2013)
27. S. Sun, T. Salim, N. Mathews, M. Duchamp, C. Boothroyd, G.C. Xing, T.C. Sum, Y.M. Lam, Energy Environ. Sci. **7**, 399–407 (2014)
28. T.J. Savenije, C.S. Ponseca Jr., L. Kunneman, M. Abdellah, K. Zheng, Y. Tian, Q. Zhu, S.E. Canton, I.G. Scheblykin, T. Pullerits, A. Yartsev, V. Sundström, J. Phys. Chem. Lett. **5**, 2189–2194 (2014)
29. M.M. Lee, J. Teuscher, T. Miyasaka, T.N. Murakami, H.J. Snaith, Science **338**, 643–647 (2012)
30. L. Burschka, P.N. Norman, S.-J. Moon, R. Humphry-Baker, P. Gao, M. K.; Graetzel, M. Nazeeruddin, Nature, (2013) doi:10.1038/nature12340
31. H.-S. Kim, C.-R. Lee, J.-H. Im, K.-B. Lee, T. Moehl, A. Marchioro, S.-J. Moon, R. Humphry-Baker, J.-H. Yum, J. E. Moser, M. Grätzel, N.-G. Park, Sci. Reports, **2**, 591 (2012). doi:10.1038/srep00591
32. J.H. Noh, S.H. Im, J.H. Heo, T.N. Mandal, D. Seok, Nano Lett. **13**, 1764 (2013)
33. J. You, Z. Hong, Y. Yang, Q. Chen. M. Cai, T.-B. Song, C.-C. Chen, S. Lu, Y. Liu, H. Ahou, Y. Yan, ACS Nano, **8**, 1674–1680 (2014)
34. Gi.acomo Giorgi, J. Fujisawa, H. Segawa. K. Yamashita, J. Phys. Chem. Lett., **4**, 4213–4216 (2013)
35. S. De Wolf, J. Holovsky, S.-J. Moon, P. Lper, B. Niesen, M. Ledinsky, F.-J. Haug, J.-H. Yum, C. Ballif, J. Phys. Chem. Lett. **5**, 1035–1039 (2014)
36. J.M. Frost, K.T. Butler, F. Brivio, C.H. Hendon, M. van Schilfgaarde, A. Walsh, Nano Lett. **14**, 2584–2590 (2014)
37. H.J. Snaith, A. Abate, J.M. Ball, G.E. Eperon, T. Leijtens, N.K. Niel, S.D. Stranks, J.T.-W. Wang, K. Wojciechowski, W. Zhang, J. Phys. Chem. Lett. **5**, 1511–1515 (2014)
38. T. Hoke, C.D. Bailie, W.H. Nguyen, A.R. Bowring, T. Heumuller, M.G. Christoforo, M.D. McGehee, Energy Environ. Sci., doi:10.1039/C4EE02465F
39. Y. Ogomi, A. Morita, S. Tsukamoto, T. Saitho, Q. Shen, T. Toyoda, K. Yoshino, S.S. Pandey, T. Ma, S. Hayase, J. Phys. Chem. C **118**, 16651–16659 (2014)
40. F. Hao, C.C. Stoumpos, D.H. Cao, R.P.H. Chang, M.G. Kanatzidis, Nat. Photon. **8**, 489–494 (2014)
41. N.K. Noel, S.D. Stranks, A. Abate, C. Wehrenfennig, S. Guarnera, A. Haghighirad, A. Sadhanala, G.E. Eperon, M.B. Johnston, A. Petrozza, L.M. Herz, H.J. Snaith, Energy Environ. Sci. **7**, 3061–3068 (2014)
42. F. Hao, C.C. Stoumpos, R.P.H. Chang, M.G. Kanatzidis, J. Am. Chem. Soc **136**, 8094–8099 (2014)
43. M.H. Kumar, S. Dharani, W.L. Leong, P.P. Boix, R.R. Prabhakar, T. Baikie, C. Shi, H. Ding, R. Ramesh, M. Asta, M. Graetzel, S.G. Mhaisalkar, N. Mathews, Adv. Mater. **5**, 7122–7127 (2014)
44. H. Choi, J. Jeong, H.-B. Kim, S. Kim, B. Walker, G.-H. Kim, J.Y. Kim, Nano Energy **7**, 80–85 (2014)
45. B. Lee, C.C. Stoumpos, Nanjia Zhou, F. Hao, C. Malliakas, C.-Y. Yeh, T. J. Marks, M.G. Kanatzidis, R.P. H. Chang, J. Am. Chem. Soc., **136**, 15379–15385 (2014)
46. For review. A. Pivrikas, N. S. Sariciftci, G. Juška, R. Österback, Prog. Photovol. Res. Appl. 15, 677–696 (2007)
47. K. Feron, W.J. Belcher, C.J. Fell, P.C. Dastoor, Int. J. Mol. Sci. **13**, 17019–17047 (2012)
48. J. Youa, L. Doua, Z. Hongc, G. Li, Y. Yang, Prog. Polym. Sci. **38**, 1909–1928 (2013)

Chapter 4
Flexible Paper Electronics

Hirotaka Koga and Masaya Nogi

Abstract In this chapter, we describe a new type of paper substrate based on cellulose nanofibers for flexible electronic applications. Cellulose nanofiber paper, referred to as nanopaper in this study, has high optical transparency like that of polyethylene terephthalate (PET) films and a low coefficient of thermal expansion comparable to that of glass. These excellent properties mean that cellulose nanopaper is expected to offer a promising alternative to glass and plastics and can be used as a transparent flexible substrate for a wide array of electronic devices. We also discuss transparent flexible electrodes based on cellulose nanopaper. The uniform coating of conductive materials such as silver nanowires and carbon nanotubes is accomplished by the simple filtration of their aqueous dispersions through cellulose nanopaper. The paper is used as a filter and a transparent flexible substrate. As-prepared conductive networks on nanopaper give superior transparent conductive performance and flexibility compared with those on PET films prepared by conventional coating processes. These findings open new doors for future flexible paper electronics.

Keywords Cellulose nanofiber paper • Paper electronics • Flexible electronics

4.1 Introduction

Flexible electronics have recently become the focus of major research because they offer new possibilities for next-generation lightweight and portable electronic devices. Glasses have traditionally been used as substrates for many electronic devices because they have high optical transparency and a low coefficient of thermal expansion (CTE). However, glasses are heavy and brittle and, therefore, they are difficult to use in flexible electronics. Plastics have been widely investigated; however, most plastics have a high CTE of about 50 ppm/K. The high CTE values of plastics frequently cause critical issues during the fabrication of flexible electronic devices. In other words, functional materials deposited on plastic substrates are damage prone because of the temperatures involved in the assembly and

---

H. Koga (✉) • M. Nogi (✉)
The Institute of Scientific and Industrial Research, Osaka University, Suita, Japan
e-mail: hkoga@eco.sanken.osaka-u.ac.jp; nogi@eco.sanken.osaka-u.ac.jp

S. Ogawa (ed.), *Organic Electronics Materials and Devices*,
DOI 10.1007/978-4-431-55654-1_4

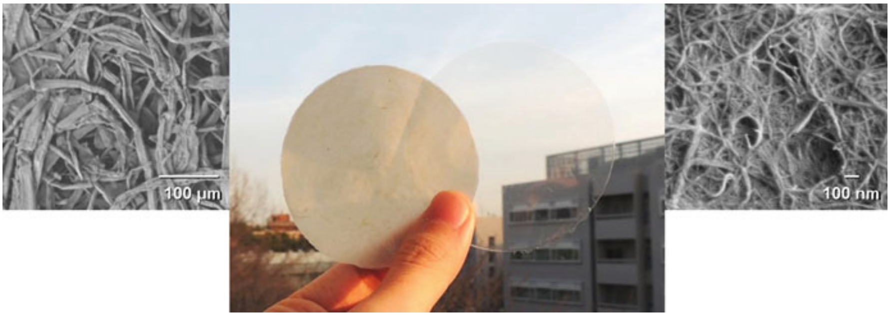

Fig. 4.1 Optical and SEM images of conventional cellulose paper made from pulp fibers with a width of tens of µm (*left*) and optically transparent nanofiber paper made from cellulose nanofibers with a width of ca. 15 nm (*right*)

mounting processes. This is because of the mismatch between the CTEs of the different materials. Therefore, research and development of transparent and flexible substrates with a low CTE has been carried out recently.

This chapter describes optically transparent and foldable paper substrates that have been prepared from wood-derived cellulose nanofibers. Cellulose nanofiber paper, denoted nanopaper in this study, offers a low CTE of less than 8.5 ppm/K. Traditional paper is made using cellulose pulp fibers of several micrometers in width and nanopaper is made using cellulose fibers of 15 nm in width. The raw materials and the preparation processes are similar for each case. The only difference is the fiber width and the size of the interstitial cavities within the paper (Fig. 4.1). Foldable, low CTE, and optically transparent nanopaper may be a perfect substrate for continuous roll-to-roll processing in the future production of electronic devices such as flexible displays, solar cells, e-paper, and a myriad of new flexible circuit technologies. A nanopaper process may replace the costly conventional batch processes based on glass substrates that are currently used [1–5]. We project that it will also replace conventional paper as an advanced information medium that can be produced using the traditional papermaking equipment currently used for production.

First, we introduce optically transparent nanopaper, which is made using densely packed cellulose nanofibers without any additives [6]. This optically transparent paper exhibits a high Young's modulus, a high strength, an ultralow CTE, and a high foldability.

Second, we discuss the maintenance of high optical transparency by transparent nanopapers even after high-temperature heating at 150 °C [7]. High-temperature heating to around 150 °C is inevitable in electronic device processing. If a PET film is held at 150 °C for tens of minutes, cyclic oligomers migrate to the film surface causing surface roughness that decreases the film's transparency. However, because cellulose nanofibers have high thermal stability, the transparent nanopapers maintain their smooth surfaces and high optical transparency, even after heating to

150 °C for tens of minutes. These findings indicate the suitability of cellulose nanopapers for continuous roll-to-roll processing.

Finally, we show the preparation and performance of transparent flexible electrodes based on nanopaper. Highly transparent and strongly adhesive conductive networks embedded in the surface of nanopaper can be prepared by a simple filtration coating process [8]. As-prepared transparent conductive paper has a sheet resistance of 12 Ω sq^{-1} with a specular transmittance of 88 %, which is up to 75 times lower than the sheet resistance of the conductive networks on a PET film prepared by conventional coating processes. Additionally, the transparent conductive paper can be folded with negligible changes in electrical conductivity, which breaks new ground in future paper electronics.

4.2 Optically Transparent Nanopaper

Cellulose nanofibers are the main component of plant cell walls and they are thus one of the most common and abundant polymers on the earth. Their tiny elements with diameters of 15–20 nm are composed of bundles of cellulose microfibrils smaller than 4 nm in width. These, in turn, are made of long cellulose molecules laterally stabilized by hydrogen bonds that form highly crystalline domains. Therefore, cellulose nanofibers have a CTE of 0.1 ppm/K [9], which is as low as that of quartz glass. They have an estimated strength of 2–3 GPa [10] making then five times stronger than mild steel. Additionally, the nanofibers have good heat transfer properties comparable with glass [11]. Another significant property of the nanofibers is that light scattering can be suppressed [12, 13]. If the cellulose nanofibers are densely packed and the interstices between the fibers are small enough to avoid light scattering, the cellulosic material can become transparent while maintaining the high performance of the material described before.

To extract the nanofibers from plants and wood fibers, it is necessary to disassemble the fibers' original structure. The cell walls of the fibers are composed of several thin layers where the cellulose nanofibers are oriented in various directions and embedded in matrix substances. To obtain uniform nanofibers from this complex structure, wood flour was used as a starting material. Because wood is composed of cellulose, hemicellulose, and lignin, the wood flour was ground in a water-swollen condition after lignin and hemicelluloses were removed [14]. Figure 4.2a shows the SEM image of the resulting fiber that was recovered by freeze-drying a 0.1 % water suspension. A sheet of nanofiber paper was prepared by first freeze-drying and then mechanically compressing at 160 MPa under vacuum to eliminate air and voids. However, this treatment did not result in transparency (Fig. 4.3a). The nanofibers deformed under load but recovered after unloading and the spaces that were created resulted in light scattering.

Thin cellulose nanofibers are prone to collapse by capillary action during the evaporation of water and a deformed condition is obtained by hydrogen bonds that form between the hydroxyl groups of the cellulose. This produces a high-strength

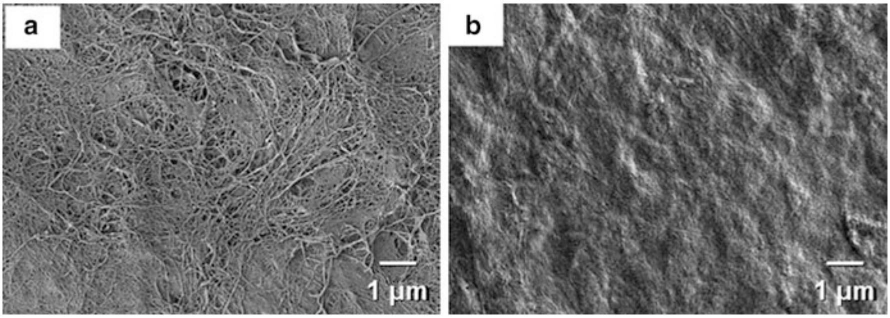

Fig. 4.2 SEM images of (**a**) freeze-dried nanofiber paper and (**b**) oven-dried nanofiber paper

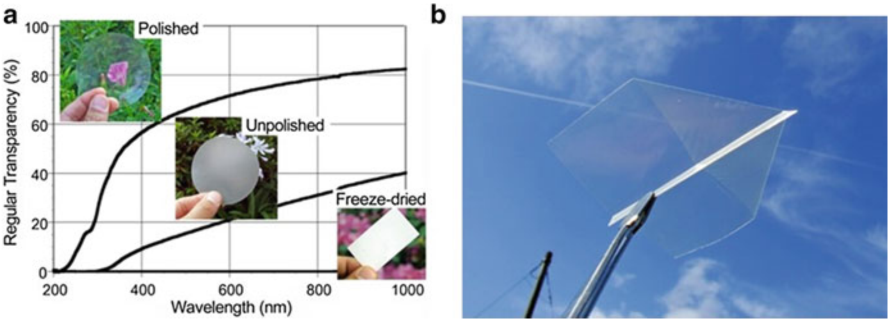

Fig. 4.3 (**a**) Light transmittance of the cellulose nanofiber sheet. (**b**) The sheet is as foldable as conventional paper

material without binders [15]. A 0.1 % water suspension of well-dispersed cellulose nanofibers was gently filtered so that nanofibers were piled uniformly in a wet sheet with a moisture content of 560 %. The wet sheet was sandwiched between a combination of wire mesh (#300 inner layer) and filter papers (outer layers), followed by hot-press drying at 55 °C for 72 h (ca. 15 kPa). The SEM image of the sheet obtained is displayed in Fig. 4.2b. The nanofibers were so densely packed that individual fibers could not be observed. The density, which was measured by a gas pycnometer, was 1.53 g/cm^3. Because the density of the cellulose crystallite is known to be 1.59 g/cm^3 [16], this result implies that the cavities in the sheet were almost removed.

The dried sheet thus obtained was semitransparent and had a plastic film-like appearance (Fig. 4.3a), suggesting that light scattering in the bulk sheet was significantly suppressed. In other words, the lack of transparency seemed to be caused by surface light scattering. When the sheet was polished using 4000 grit emery paper followed by 15000 grit emery paper, it became transparent (Fig. 4.3a). The regular light transmittance levels of the sheet before and after polishing are compared in Fig. 4.3a. Thicknesses of the sheet were 60 and 55 μm before and after polishing, respectively. The light transmittance of the cellulose nanofiber sheet upon polishing was 71.6 % including surface reflection (Fresnel's reflection) at a wavelength of 600 nm. The sheet has the plastic-like transparency and is as foldable as conventional paper (Fig. 4.3b). Thus, we have designated this new material cellulose nanofiber paper. Because the optically transparent sheet consists of high-strength and low-thermal expansion nanofibers, its Young's modulus and tensile strength reach 13 GPa and 223 MPa, respectively. Its CTE is 8.5 ppm/K, which is comparable to that of glass.

The achievement of optical transparency in the nanofiber paper by smoothing the surface suggests various approaches are possible for the production of functional transparent cellulose sheets. Smooth surfaces can be obtained by the lamination of optically transparent plastics such as polycarbonate films onto the nanofiber paper. This is done by exploiting the thermal softening temperature of thermoplastics while avoiding the thermal deterioration of cellulose. This would greatly simplify the roll-to-roll process as well. Another approach would be to deposit transparent resins onto the surface or even transparent conductive inorganic materials like indium tin oxide (ITO). Ink jet printers may allow for the drawing of precise transparent and functional patterns on the sheet by the addition of functional nanoelements to the ink. As cellulose is highly hygroscopic, transparent cellulose nanofiber sheets without chemical modification are liable to dimensional instability [17, 18]. These surface-smoothing approaches would impart high optical transparency and also act as moisture barriers to the cellulose nanofiber sheets.

4.3 High Thermal Resistance of Transparent Nanopaper

In previous reports, cellulose nanofibers with diameters of 3–15 nm were extracted from plant cell walls [14, 19]. As described above, cellulose nanofibers have a low CTE of 0.1 ppm/K, a high strength of 2–3 GPa, a high Young's modulus of 130–150 GPa, and high thermal and chemical durability [12]. Cellulose nanofibers can thus be used for many applications including high-strength lightweight materials, device substrates, porous magnetic aerogels, dietary fiber, humidity sensors, food packaging films, and nanometallic catalysts [20–24]. In particular, device substrates are promising applications because the cellulose nanofiber sheets have been capable of conductive patterning and have been used as substrates for the lighting of LED and OLED lights and for sensitive antennas [5, 25, 26].

Two types of optically transparent material based on cellulose nanofibers have been fabricated. The first material is a transparent plastic reinforced with cellulose nanofibers [12–14]. The high optical transparency of these nanofiber composites is enhanced when the refractive index values of the matrix plastics and the cellulose nanofibers are roughly matched [13]. The second material is optically transparent nanofiber paper (transparent nanopaper) consisting only of cellulose nanofibers [6, 27]. When an aqueous dispersion of cellulose nanofibers is dried, the cellulose nanofibers are densely packed by capillary action during the evaporation of water. After the drying and surface smoothing of the nanofiber films, the nanopapers become highly optically transparent because light scattering does not occur within the films or at their surfaces. Both optically transparent nanofiber materials are suitable as device substrates for applications such as solar cells and displays. In this section, the transparency of the nanopapers and their thermal stability during 150 °C heating are discussed [7].

Sitka spruce (*Picea sitchensis*) wood chips were used in this study. The wood samples were subjected to sodium chlorite and potassium hydroxide treatments [6]. A 0.5 wt% pulp water suspension of 2,000 g was mechanically nanofibrillated using a high-pressure water-jet system (Star Burst, HJP-25005E, Sugino Machine Co., Ltd., Uozu, Japan) equipped with a ball-collision chamber. The slurry was ejected from a small nozzle with a diameter of 0.15 mm under a high pressure (245 MPa). The suspensions were passed through this nozzle 100 times. After this mechanical nanofibrillation, cellulose nanofibers with width of 15 nm were obtained.

Transparent nanopapers have previously been fabricated by a three-step process [6, 27]. First, purified wet wood flour is mechanically fibrillated into cellulose nanofibers using a single-pass grinder treatment. Second, cellulose nanofiber suspensions are vacuum filtered to make wet nanofiber sheets, followed by drying using wire meshes. The resulting sheets are not optically transparent but translucent. Finally, the translucent nanofiber sheets are made transparent by surface-smoothing processes such as polishing or coating.

Herein, we show the fabrication of transparent nanopapers by the following two processes. First, purified wet wood chips were nanofibrillated by a water-jet system (pass number, 100). Second, the nanofiber suspensions were poured onto an acrylic plate and then dried at 50 °C for 24 h. After drying, the dried sheet was found to be highly optically transparent without any additional surface-smoothing processes. Because the transparent nanopaper maintained the high foldability same as conventional paper, an optically transparent origami leaf was fabricated by folding the nanopaper (Fig. 4.4). The nanopaper also had an extremely low CTE of 5–8 ppm/K, comparable with that of glass. Thus, the transparent nanopaper is a perfect material as a substrate in continuous roll-to-roll processing.

We discuss the transparency of nanopapers (thickness of 20 μm and density of 1.5 g/cm^3) and compare them with PET films in terms of their total transmittance and haze. We first introduce the transparency of nanopapers before the heating process. When light reaches a transparent medium, reflection generally occurs at the surface. The surface reflection (Fresnel reflection) depends on the difference of refractive index between air and the medium. Even ideal transparent materials without any internal light losses have a total transmittance of less than 100 % due to surface reflection. In the transparent nanopaper with a refractive index of 1.58 at a wavelength of 590 nm [27], the surface reflection at the nanopaper was 5.1 % (see Eq. 4.1). Considering multiple surface reflections (see Eq.4.2), the theoretical total transmittance of the nanopaper was estimated as 90.1 %.

Fig. 4.4 Transparent nanopaper origami leaf (*center*), a colored leaf, and a green leaf (*left* and *right*, respectively)

$$R = \frac{(n_{\mathrm{m}} - n_{\mathrm{a}})^2}{(n_{\mathrm{m}} + n_{\mathrm{a}})^2} \tag{4.1}$$

$$T\ (\%) = [1 - R]^2 \times 100 \tag{4.2}$$

where R is the surface reflection, n_{m} is the refractive index of the transparent material, n_{a} is the refractive index of air (1.00), and T (%) is the theoretical total transmittance when considering multiple surface reflections.

Before heating, the total transmittance of the nanopaper was measured in a 200–800 nm wavelength range (solid line in Fig. 4.5a) by using a UV-vis spectrometer with an integrating sphere. The total transmittance at visible wavelengths of 450–800 nm was constant at 90.1 %. This value matched the theoretical value of 90.1 %. For the transparent nanopaper, the transmittance losses in the visible wavelength range were not caused by light absorption within the nanopaper but only by surface reflection. Even transparent materials without any light absorption suffer reduced transparency, which is caused by light scattering. This light scattering is referred to as "haze" and is measured as the proportion of scattered transmittance to total transmittance. Cloudy translucent materials show more haze, while clear transparent materials have low haze. The haze was evaluated by a haze meter. The haze of the transparent nanopaper was 4.1 % (Fig. 4.5d). This low haze was due to light scattering from cellulose nanofibers with width of 15 nm and the cavities between the nanofibers. The total transmittance and haze in the PET films (T-100, Mitsubishi Plastics, Inc., Tokyo, Japan) were 89.0 % and 4.5 %, respectively (solid lines in Fig. 4.5b, d, respectively). This result suggests that transparent nanopaper with a thickness of 20 μm demonstrates high total transmittance and low haze comparable to that of 100 μm-thick PET films.

When transparent films are used as electronic device substrates, conductive patterns are deposited onto them under high-temperature conditions. In conventional device manufacturing processes, high-temperature heating to over 300 °C is needed. These high-temperature processes are obstacles to the fabrication of flexible or bendable devices on polymer substrates. Recent progress in printing with

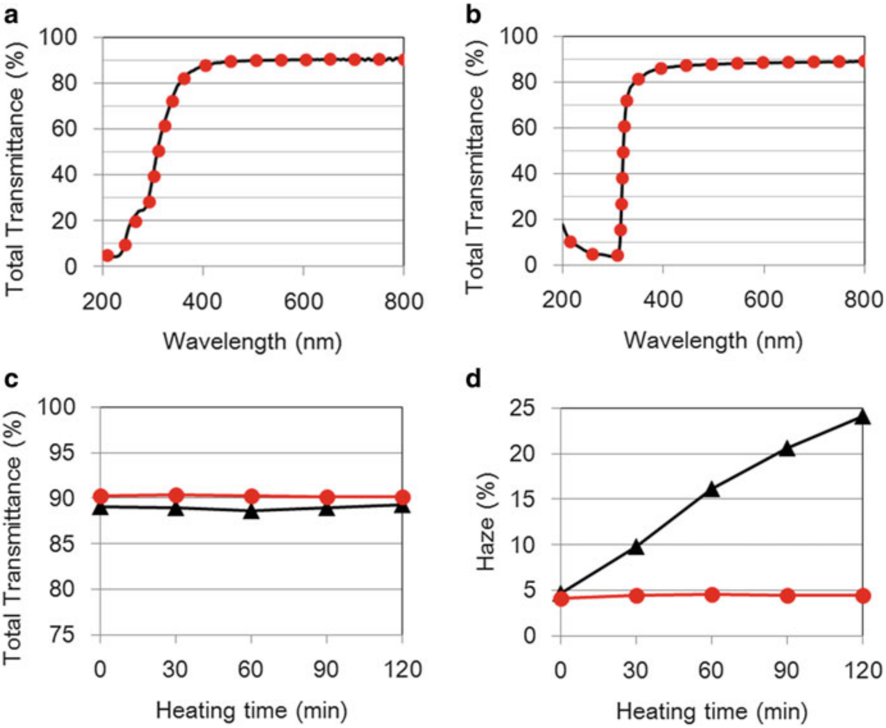

Fig. 4.5 Transparency of nanopaper and PET films. (**a**) Total light transmittance of nanopaper (*solid line*: before heating; *dotted line*: after heating at 150 °C for 120 min). (**b**) Total light transmittance of PET films (*solid line*: before heating; *dotted line*: after heating at 150 °C for 120 min). (**c**) Total light transmittance during heating at 150 °C for 120 min (*circles*: nanopaper; *triangles*: PET). (**d**) Haze values during heating at 150 °C for 120 min (*circles*: nanopaper; *triangles*: PET)

conductive nanomaterials has allowed the deposition of conductive patterns at lower temperatures of around 150 °C. Hence, the minimum requirement for transparent substrates is that their high transparency is maintained even after heating to 150 °C. We thus investigated the change in optical transparency of the nanopaper after heating at 150 °C and compared it with that of PET films.

When PET films are heated at 150 °C for 120 min, their visual appearances become cloudy; however, their total transmittance spectra are exactly the same as those before the heating process (Fig. 4.5b). Their total transmittance and haze during the heating process were evaluated as shown in Fig. 4.5c, d. After the 150 °C heating, the total transmittance was constant at 87.4–88.1 % (Fig. 4.5c), while the haze increased from 4.5 to 24.0 % (Fig. 4.5d). These results indicate that the increase in haze was derived from light scattering within or at the surface of the heated PET films. The PET films used in this study were plane and did not receive any heat stabilization treatment. When plane PET films are heated at 150 °C, cyclic oligomers migrate to the film's surface and the surface becomes rough, as reported

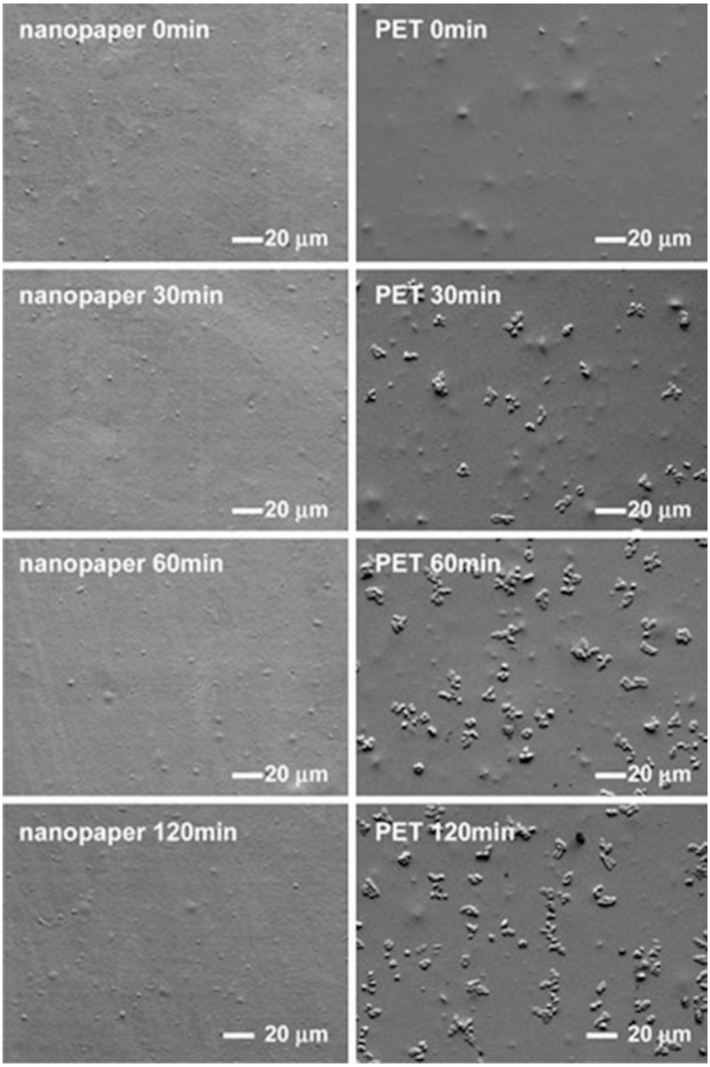

Fig. 4.6 Optical images of the surfaces of nanopaper and PET films during heating at 150 °C for up to 120 min

by MacDonald et al. [28]. When the surfaces of the PET films were observed by field emission scanning electron microscopy (FE-SEM), their surfaces were quite smooth before heating. Cyclic oligomers were found on the surfaces of the PET films after heating for 30 min (Fig. 4.6). The cyclic oligomers had a diameter of around 10 μm and a height of less than 1 μm and this was almost constant during heating, while the amount of cyclic oligomers increased with heating time. The growth of cyclic oligomers corresponds with the increasing haze of the PET films. However, migrated cyclic oligomers can be removed by washing with methylethylketone solvent. When the heated hazy PET films were washed with the solvent, their appearance and haze returned to the levels of the non-heated films. Therefore, high-temperature heating at 150 °C increased the surface roughness of the PET films, resulting in the loss of their high optical transparency. The loss of their transparency was not due to crystallization. To protect them from this loss in transparency during heating, the PET films thus should be coated with planarizers [28].

Transparent nanopaper was fabricated by the casting of nanofiber suspensions on an acrylic plate. Their surface smoothness was thus nearly the same as that of the PET films (Fig. 4.6). Cellulose has no glass transition and does not undergo thermal decomposition at temperatures under 250 °C. Because the transparent nanopaper consists only of cellulose nanofibers, the nanopaper surface remains very smooth even after heating at 150 °C for 120 min (Fig. 4.6). Hence, the haze value of the nanopaper was also constant at 4.1–4.5 % (Fig. 4.5d) and the high optical transparency of the nanopaper was almost unchanged. The total transmittance of the heated nanopaper also remained constant at around 90.1 % (Fig. 4.5c) and the total transmittance spectrum of the heated nanopaper was almost the same as that before heating (Fig. 4.5a). Due to the high thermal stability of cellulose, the transparent nanopaper maintained high optical transparency without additional stabilization treatment.

4.4 Transparent Conductive Paper

Transparent conductive films are important materials in a wide range of electronic applications such as displays and solar cells. For flexible electronics, transparent conductive films have been fabricated by the coating of conductive materials including silver nanowires (AgNW) [29–31], carbon nanotubes (CNT) [32–34], and graphene on transparent and flexible plastic films such as PET. Wet coating processes have been widely used for the deposition of these conductive materials onto plastic films because of their large-area and low-temperature production advantages. For example, these transparent conductive films have been prepared by drop coating, bar coating, and spin coating AgNW or CNT dispersions onto plastic films.

One of the current challenges in the fabrication of high-performance transparent conductive films is the enhancement of their optical transparency and their electrical conductivity. The transparent conductive performance depends on the dispersion state of the conductive materials over the substrate surface. Uniformly interconnected conductive networks without significant loss of optical transparency provide better performance [35, 36]. Although uniform coating is essential for excellent transparent conductive performance, conventional wet coating processes such as drop coating and bar coating inevitably cause self-aggregation and the uneven distribution of the suspended materials after solvent drying, as shown by the coffee-ring effect [37, 38]. An alternative coating approach that provides high spatial uniformity for the conductive networks over the substrates is urgently required. Additionally, strong adhesion between the conductive material and the substrate surface is also important to ensure mechanical robustness against friction and bending. However, AgNWs show poor adhesion to plastic films [39], while CNTs show relatively strong adhesion [33]. Therefore, various techniques including substrate surface modification, encapsulation with a thin Teflon layer, and irradiation with high-density pulsed light [40] have been investigated. Despite these efforts there is still a requirement for further progress in coating processes and substrate materials to achieve both high transparent conductivity performance and strong adhesive properties.

Herein, we show the successful fabrication of cellulose nanopaper-based transparent conductive films [8]. The uniform coating of AgNWs or CNTs onto the nanopaper was achieved by a simple filtration process. The as-prepared transparent conductive paper demonstrated both high transparent conductivity performance and strong adhesive properties.

Paper materials have been traditionally prepared by a papermaking process in which a cellulose fiber aqueous suspension is dewatered through a mesh filter to form uniformly distributed and randomly oriented fiber networks. This simple filtration technique is expected to be used as an effective coating process to prepare uniformly connected networks of fiber-like conductive nanomaterials including AgNWs and CNTs. In this study, the uniform coating of these conductive nanomaterials was accomplished by a simple filtration of their aqueous dispersions through the cellulose nanopaper. The paper was used as both a filter and a transparent flexible substrate (Fig. 4.7a). The as-prepared AgNW or CNT networks on the nanopaper were denoted AgNW@nanopaper and CNT@nanopaper, respectively, and they had high optical transparency (Fig. 4.7b). The AgNW networks on the nanopaper exhibited a sheet resistance of 12 Ω sq^{-1} with an optical transparency of 88 %. This is up to 75 times lower than that of the PET films prepared by conventional coating processes such as drop coating (sheet resistance of 900 Ω sq^{-1} with an optical transparency of 87 %), bar coating, and spin coating. These results were confirmed, even for CNT [8]. These results indicate that the "filtration coating" process offers uniformly connected conductive networks because of drainage in the perpendicular direction through the paper-specific nanopores derived from the cellulose nanofiber networks. Conventional coating processes for plastic films inevitably lead to self-aggregation and the uneven distribution of conductive materials during the drying processes, as shown by the well-known coffee-ring phenomenon. This filtration process, which was made feasible by the use of a nanopaper substrate, is an effective coating approach to achieve high transparent conductive performance.

Figure 4.8 shows side-view FE-SEM images of AgNW networks on the surfaces of nanopaper and a PET film prepared by filtration coating and drop coating, respectively. It should be noted that the AgNW networks were embedded in the nanopaper surface. The embedded AgNW networks allow strong adhesion to the nanopaper surface. The AgNW networks on the PET film were easily peeled off with adhesive tape (Fig. 4.9a) leading to a drastic increase in sheet resistance

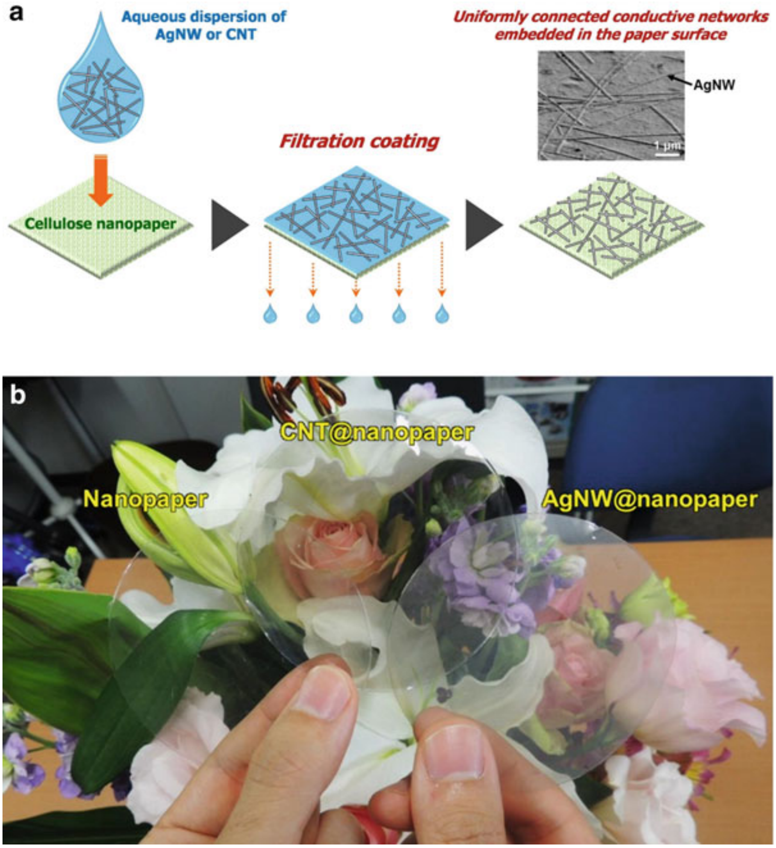

Fig. 4.7 (**a**) Schematic of the filtration coating of AgNW or CNT on cellulose nanopaper, (**b**) optical images of the as-prepared original nanopaper and transparent conductive papers

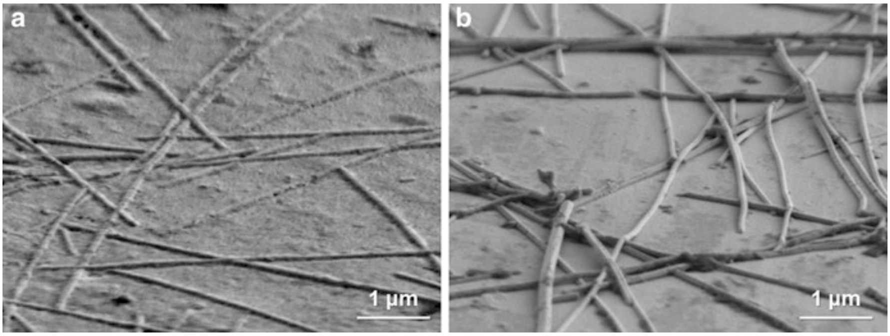

Fig. 4.8 Side-view FE-SEM images of (**a**) the AgNW@nanopaper and (**b**) the AgNW@PET film

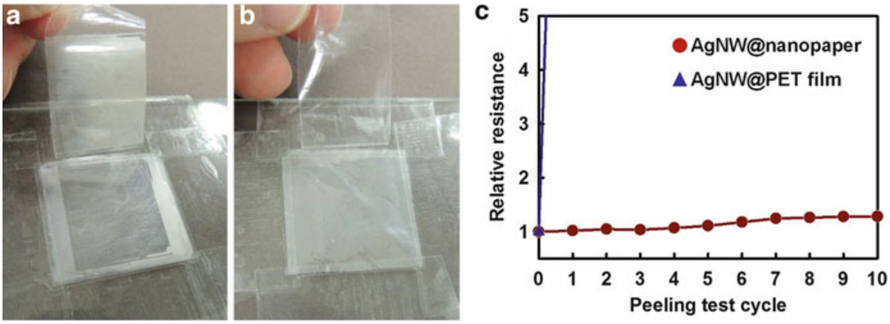

Fig. 4.9 Optical images of (**a**) the AgNW@PET film and (**b**) the AgNW@nanopaper prepared by drop coating and filtration coating, respectively, after the peeling test. (**c**) Relative resistance values of the AgNW@nanopaper and the AgNW@PET film as a function of peeling test cycles

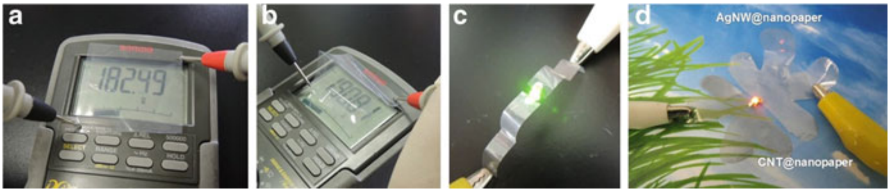

Fig. 4.10 Flexibility of the transparent conductive papers. Resistance values of the AgNW@nanopaper (**a**) before (182 Ω) and (**b**) after (191 Ω) mountain folding. (**c**) Lighting a light-emitting diode (LED) placed between mountain- and valley-folded AgNW@nanopapers. (**d**) Paper craft using transparent conductive papers

(Fig. 4.9c). In contrast, the AgNW networks made by filtration coating adhered strongly to the surface of the nanopaper (Fig. 4.9b). Low sheet resistance was maintained even after ten peeling test cycles (Fig. 4.9c). The CNT networks also adhered more strongly to the nanopaper than to the PET film [8], suggesting that a CH-π interaction between the axial plane of the cellulose and the graphene π-conjugated system [41] enhances the adhesion of CNT networks to the surface of the nanopaper. The strong adhesion of AgNW and CNT onto the nanopaper surface was also achieved using a simple filtration coating process.

As shown in Fig. 4.10a–c, these transparent conductive papers were foldable to beyond flexible. In other words, the resistance value of the AgNW@nanopaper remained almost unchanged even after mountain folding and the multiple-folded papers could light a LED. Additionally, the papers enabled versatile shape design upon cutting with scissors and provided transparent conductive paper craft (Fig. 4.10d). The high flexibility of the transparent conductive paper will open new doors for future foldable electronics.

To conclude, we have demonstrated the successful formation of highly transparent conductive networks on cellulose nanopaper by a simple filtration coating process. The cellulose nanopaper, which was made from the most ubiquitous and renewable bioresources, served as both a filter and a transparent flexible substrate for AgNWs and CNTs. This filtration coating technique can be applied to a wide range of conductive materials and extended to large-area production such as the well-established papermaking process. This work breaks new ground in the creation of next-generation paper electronics.

4.5 Conclusions

This chapter describes the successful fabrication of optically transparent and foldable cellulose nanopaper with high thermal resistance and low CTE. These excellent properties of the nanopaper offer a promising alternative to glasses and plastics. We developed flexible electronics based on nanopaper including transparent conductive films [8], organic transistors [42], nonvolatile paper memory [43], and antennas [44, 45]. These paper electronic devices demonstrated excellent flexibility as well as excellent device performance and they open new doors for next-generation flexible electronics.

References

1. J.S. Sheats, J. Mater. Res. **19**, 1974 (2004)
2. W.A. MacDonald, J. Mater. Chem. **14**, 4 (2004)
3. S.R. Forrest, Nature **428**, 911 (2004)
4. R.H. Reuss, B.R. Chalamala, A. Moussessian, M.G. Kane, A. Kumar, D.C. Zhang, J.A. Rogers, M. Hatalis, D. Temple, G. Moddel, B.J. Eliasson, M.J. Estes, J. Kunze, E.S. Handy, E.S. Harmon, D.B. Salzman, J.M. Woodall, M.A. Alam, J.Y. Murthy, S.C. Jacobsen, M. Olivier, D. Markus, P.M. Campbell, E. Snow, Proc. IEEE **93**, 1239 (2005)
5. M. Nogi, H. Yano, Adv. Mater. **20**, 1849 (2008)
6. M. Nogi, S. Iwamoto, A.N. Nakagaito, H. Yano, Adv. Mater. **21**, 1595 (2009)
7. M. Nogi, C. Kim, T. Sugahara, T. Inui, T. Takahashi, K. Suganuma, Appl. Phys. Lett. **102**, 181911 (2013)
8. H. Koga, M. Nogi, N. Komoda, T.T. Nge, T. Sugahara, K. Suganuma, NPG Asia Mater. **6**, e93 (2014)
9. T. Nishino, I. Matsuda, K. Hirao, Macromolecules **37**, 2004 (2004)
10. D.H. Page, F. El-Hosseny, J. Pulp. Pap. Sci. **9**, 99 (1983)
11. Y. Shimazaki, Y. Miyazaki, Y. Takezawa, M. Nogi, K. Abe, S. Ifuku, H. Yano, Biomacromolecules **8**, 2976 (2007)
12. H. Yano, J. Sugiyama, A.N. Nakagaito, M. Nogi, T. Matsumura, M. Hikita, K. Handa, Adv. Mater. **17**, 153 (2005)
13. M. Nogi, K. Handa, A.N. Nakagaito, H. Yano, Appl. Phys. Lett. **87**, 243110 (2005)
14. K. Abe, S. Iwamoto, H. Yano, Biomacromolecules **8**, 3276 (2007)
15. H. Yano, S. Nakahara, J. Mater. Sci. **39**, 1635 (2004)
16. J. Sugiyama, R. Vuong, H. Chanzy, Macromolecules **24**, 4168 (1991)
17. M. Nogi, K. Abe, K. Handa, F. Nakatsubo, S. Ifuku, H. Yano, Appl. Phys. Lett. **89**, 233123 (2005)
18. S. Ifuku, M. Nogi, K. Abe, K. Handa, F. Nakatsubo, H. Yano, Biomacromolecules **8**, 1973 (2007)

19. T. Saito, Y. Nishiyama, J.-L. Putaux, M. Vignon, A. Isogai, Biomacromolecules **7**, 1687 (2006)
20. R.T. Olsson, M.A.S. Azizi Samir, G. Salazar-Alvarez, L. Belova, V. Ström, L.A. Berglund, O. Ikkala, J. Nogués, U.W. Gedde, Nat. Nanotechnol. **5**, 584 (2010)
21. A. Shimotoyodome, J. Suzuki, Y. Kumamoto, T. Hase, A. Isogai, Biomacromolecules **12**, 3812 (2011)
22. J.T. Korhonen, P. Hiekkataipale, J. Malm, M. Karppinen, O. Ikkala, R.H.A. Ras, ACS Nano **5**, 1967 (2011)
23. H. Fukuzumi, T. Saito, T. Iwata, Y. Kumamoto, A. Isogai, Biomacromolecules **10**, 162 (2009)
24. H. Koga, T. Kitaoka, H. Wariishi, Chem. Commun. **46**, 5616 (2008)
25. M.-C. Hsieh, C. Kim, M. Nogi, K. Suganuma, Nanoscale **5**, 9289–9295 (2013)
26. M. Nogi, N. Komoda, K. Otsuka, K. Suganuma, Nanoscale **5**, 4395–4399 (2013)
27. M. Nogi, H. Yano, Appl. Phys. Lett. **94**, 233117 (2009)
28. W.A. MacDonald, M.K. Looney, D. MacKerron, R. Eveson, R. Adam, K. Hashimoto, K. Rakos, J. SID **15/12**, 1075 (2007)
29. J.-Y. Lee, S.T. Conner, Y. Cui, P. Peumans, Nano Lett. **8**, 689 (2008)
30. L. Hu, H.S. Kim, J.-Y. Lee, P. Peumans, Y. Cui, ACS Nano **4**, 2955 (2010)
31. T. Tokuno, M. Nogi, M. Karakawa, J. Jiu, T.T. Nge, Y. Aso, K. Suganuma, Nano Res. **4**, 1215 (2011)
32. F. Mirri, A.W.K. Ma, T.T. Hsu, N. Behabtu, S.L. Eichmann, C.C. Young, D.E. Tsentalovich, M. Pasquali, ACS Nano **6**, 9737 (2012)
33. Y. Kim, M. Chikamatsu, R. Azumi, T. Saito, N. Minami, Appl. Phys. Express **6**, 025101 (2013)
34. H. Koga, T. Saito, T. Kitaoka, M. Nogi, K. Suganuma, A. Isogai, Biomacromolecules **14**, 1160 (2013)
35. J. Groep, P. Spinelli, A. Polman, Nano Lett. **12**, 3138–3144 (2012)
36. T.Y. Kim, Y.W. Kim, H.S. Lee, H. Kim, W.S. Yang, K.S. Suh, Adv. Funct. Mater. **23**, 1250 (2013)
37. R.D. Deegan, O. Bakajin, T.F. Dupont, G. Huber, S.R. Nagel, T.A. Witten, Nature **389**, 827 (1997)
38. W. Han, Z. Lin, Angew. Chem. Int. Ed. **51**, 1534 (2012)
39. S. De, T.M. Higgins, P.E. Lyons, E.M. Doherty, P.N. Nirmalraj, W.J. Blau, J.J. Boland, J. N. Coleman ACS Nano. **3**, 1767 (2009)
40. J. Jiu, M. Nogi, T. Sugahara, T. Tokuno, T. Araki, N. Komoda, K. Suganuma, H. Uchida, K. Shinozaki, J. Mater. Chem. **22**, 23561 (2012)
41. S. Yokota, T. Ueno, T. Kitaoka, H. Wariishi, Carbohydr. Res. **342**, 259 (2007)
42. Y. Fujisaki, H. Koga, Y. Nakajima, M. Nakata, H. Tsuji, T. Yamamoto, T. Kurita, M. Nogi, N. Shimidzu, Adv. Funct. Mater. **24**, 1657 (2014)
43. K. Nagashima, H. Koga, U. Celano, F. Zhuge, M. Kanai, S. Rahong, G. Meng, Y. He, J.D. Boeck, M. Jurczak, W. Vandervorst, T. Kitaoka, M. Nogi, T. Yanagida, Sci. Rep. **4**, 5532 (2014)
44. M. Nogi, N. Komoda, K. Otsuka, K. Suganuma, Nanoscale **5**, 4395 (2013)
45. T. Inui, H. Koga, M. Nogi, N. Komoda, K. Suganuma, Adv. Mater. **27**, 1112 (2015)

Chapter 5
Highly Conductive Ink-Jet-Printed Lines

Masaya Nogi, Hirotaka Koga, and Katsuaki Suganuma

Abstract Printing techniques, such as ink-jet printing, screen printing, and flexography, are promising alternatives to conventional photolithography for the production of electronic devices. The advantages of these techniques include low manufacturing costs, environmental sustainability, manufacturing simplicity, and high material usage. Among these techniques, ink-jet printing is particularly advantageous because it is a noncontact, maskless process with drop-on-demand and scale-up feasibilities. Therefore, ink-jet printing is currently used to fully or partially fabricate advanced electronic devices. In this chapter, we introduce some ink-jet printing technologies to improve the electrical conductivity of printed lines.

Keywords Printed electronics • Ink-jet printing • Acceptance layer • Flexible substrate

5.1 Introduction

Printed electronics is a promising technology that has received much interest for the mass production of low-cost electronic devices because it increases manufacturing flexibility and decreases manufacturing costs. Of the numerous printing technologies, such as offset printing, gravure printing, screen printing, and ink-jet printing, the latter is particularly advantageous as a noncontact, maskless, drop-on-demand process with scale-up feasibility. Therefore, ink-jet printing is currently used to fully or partially fabricate advanced electronic devices, including organic light-emitting diodes [1–3], organic solar cells [4, 5], organic thin-film transistors [6–11], flat-panel displays [12], and radio-frequency identification devices [17]. In this chapter, we introduce recent studies on the production of highly electrically conductive lines with straight and sharp edges using ink-jet printers.

In the first section, the fabrication of conductive silver lines of various widths (0.04–40 mm) using dilute silver-nanoparticle (AgP) inks on polyimide films and an ink-jet printer [13] is described. The electrical properties of the lines were found

---

M. Nogi (✉) • H. Koga • K. Suganuma
The Institute of Scientific and Industrial Research, Osaka University, Suita, Japan
e-mail: nogi@eco.sanken.osaka-u.ac.jp; hkoga@eco.sanken.osaka-u.ac.jp;
suganuma@sanken.osaka-u.ac.jp

S. Ogawa (ed.), *Organic Electronics Materials and Devices*,
DOI 10.1007/978-4-431-55654-1_5

to vary with the width. In particular, wider lines (>0.4 mm) exhibited low resistivities (3.6–5.4 μΩcm), approaching that of bulk silver (1.6 μΩcm). On the other hand, narrower lines (<0.3 mm) exhibited much higher resistivities (14.6–16.5 μΩcm), presumably because of the so-called coffee-ring effect. This effect, known to strongly influence nanoparticle deposition, is caused by convection flow, during which nanoparticles segregate at the line edge. However, when the narrower lines were heated slowly from 20 to 200 °C at a heating rate of 3 °C/min in order to reduce convection flow, they redistributed uniformly, after which the lines exhibited low resistivities (3.9–4.2 μΩcm). Therefore, gradual heating appears to be an excellent method for enabling ink-jet printing technology to yield narrow, highly conductive lines.

Polyimide films are the most promising substrates for use in printed electronics because of their high thermal stability. However, the high wettability of polyimide films by conductive inks often produces thin ink-jet-printed lines with splashed and wavy boundaries, resulting in high electrical resistance of the lines. In the second section, to overcome these disadvantages, repellent pore structures composed of polyamide-imide with high thermal stability were fabricated on a polyimide film [14]. Using this film, the ink-jet-printed line thickness was increased without the penetration of the silver nanoparticles into the pore structures, thus resulting in very sharp edges without any splashing. Notably, the repellent treatment restricted the spreading of the silver nanoparticles into the pore structures, and the pore structures prevented ink splashing upon impact with the film. As a result, the electrical resistance of these lines decreased to one-fifth that of comparable lines on a pristine polyimide film. The ink-jet printing of conductive inks onto repellent pore structures should thus contribute to the future of printed electronics because this technique enables the printing of closely packed line patterns while maintaining high conductivity within a limited space.

As mentioned above, low concentrations of metallic nanoparticle inks often produce the coffee-ring effect, thereby resulting in high electrical resistance for ink-jet-printed lines. The coffee-ring effect is due to the convection flow of the ink droplets and can be overcome by reducing the flow. In the third section, we report the formation of absorption layers for ink vehicles on pristine polyimide films and the fabrication of convex-shaped lines without the coffee-ring effect, even using low concentrations of commercially available inks [15]. The coated layers increased the ink concentration and prevented the convection flow of the ink droplets. Subsequently, the electrical resistance of the ink-jet-printed lines on the polymer-coated polyimide films (8 Ω) was improved threefold over that of lines printed on pristine polyimide films (24 Ω). This improvement was similar to that obtained when ink-jet-printed lines were gradually heated (7 Ω), which is another method for reducing convection flow. Durability tests and electrical resistance measurements for the ink-jet-printed lines on the polymer-coated polyimide films were also performed. Even under harsh environments, the lines showed excellent electrical performance. Importantly, these lines should be easily integrated into practical applications.

5.2 Sintering Method for Highly Conductive, Narrow Printed Lines

To expand ink-jet printing technologies for electronic devices, the capability to produce a high-quality printed pattern of narrow width and high electrical conductivity is crucial. Narrow width is already achievable. Because a commercial ink-jet printer does not require printing masks, it can easily print narrow conductive lines (<1 mm) with proper control of the parameters, such as the linewidth (via the ink-jet nozzle), printing waveform, droplet volume, drop spacing, and the number of overprints [9, 16–20]. However, high electrical conductivity can be difficult to achieve. The electrical conductivity of a printed line depends on the composition of the conductive metallic ink and the heating conditions of sintering. Theoretically, printed patterns should be capable of exhibiting conductivity approaching that of the corresponding bulk metal, independent of the linewidth, provided that they have been heated under sufficient sintering conditions (temperature and time). However, in reality, nanoparticle segregation near the pattern edge—the so-called coffee-ring effect—is frequently observed in ink-jet-printed tracks [20, 21]. These concave ridged patterns exhibit low conductivity, even after sufficient heating [22].

Since the first report of coffee-ring stains by Deggan, line edges with distinct ridges have been widely studied. The numerous driving forces that generate coffee-ring stains in dried droplets include the substrate and ink wettabilities, ink viscosity, solvent type, particle size, droplet volume, and droplet-drying conditions [23–32]. However, the relationship between the printed linewidth, conductivity, and the coffee-ring effect has not been clarified. Recently, we reported the properties of silver lines of various widths that were ink-jet-printed on a polyimide substrate; the examined properties included the electrical resistivity, cross-sectional morphology, and silver-nanoparticle distribution within the lines [13].

Silver nanoparticles (diameters 30–50 nm) were dispersed in a mixed ethylene glycol/alcohol solvent system and then printed on the polyimide films. Printing was performed via two different methods: ink-jet printing and bar coating. Ink-jet printing produced linewidths in the range of 0.04–3 mm, whereas bar coating produced a linewidth of 40 mm. After printing, the films were heated at 200 °C for 90 min, and then their electrical resistivities were measured.

For the lines printed with the ink-jet printer, the electrical resistivity varied with the linewidth (Fig. 5.1a). Narrower lines exhibited higher resistivities, whereas wider lines exhibited lower resistivities, with the widest line (40 mm) exhibiting a low resistivity of 5.0 μΩcm. The resistivity of the narrowest line (0.3 mm) was approximately fourfold higher than that of the widest line. In theory, electrical resistance (Ω) should vary with the linewidth and thickness. However, the electrical resistivity (μΩcm) is independent of both of these factors because it is derived from the resistance and the cross-sectional area. Therefore, the substantially higher resistivity of the narrowest lines suggested that the electrical contact between the silver nanoparticles in these lines was lower.

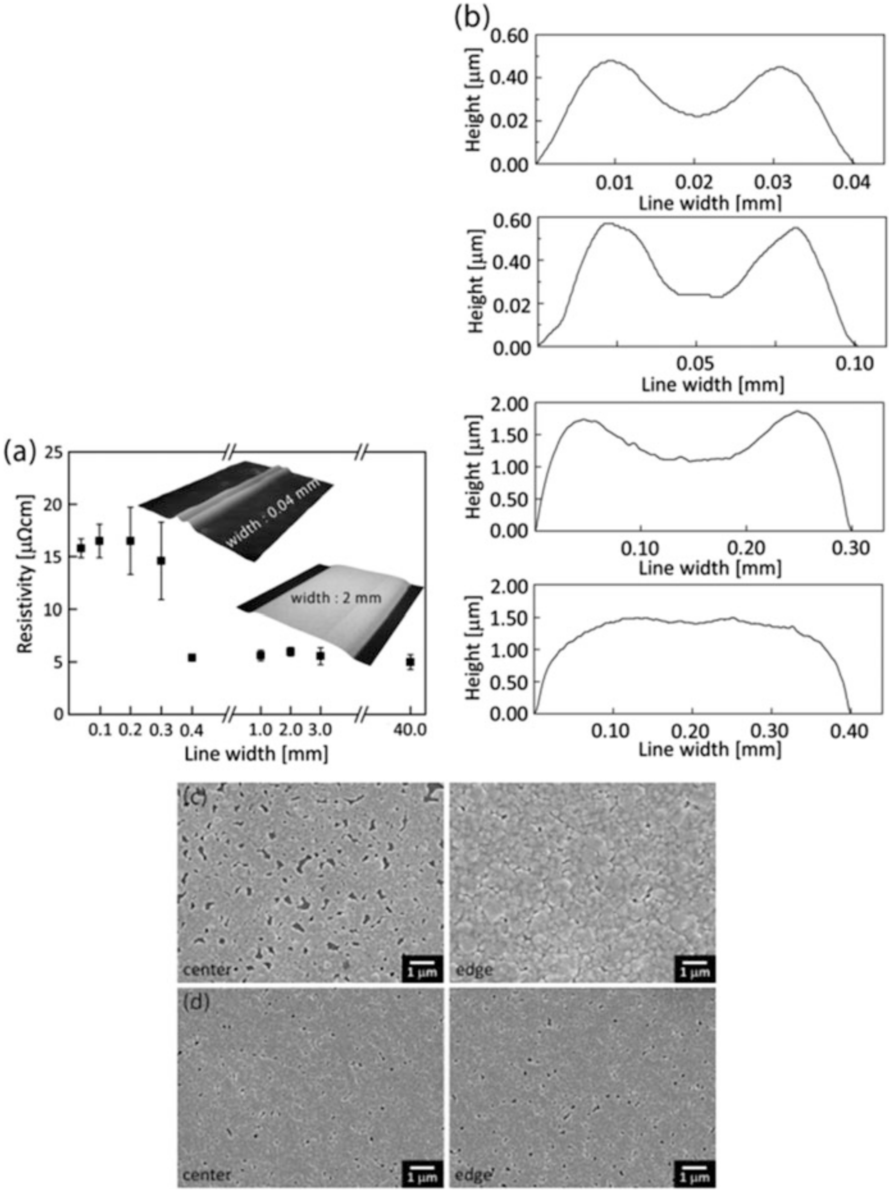

Fig. 5.1 Ink-jet-printed lines fabricated using a low-viscosity silver-nanoparticle ink after constant heating at 200 °C. (**a**) Electrical resistivity (linewidth range 0.04–40 mm), (**b**) cross-sectional morphology (linewidth range 0.04–0.4 mm), (**c**) FE-SEM images of a concave narrow line (width 0.04 mm), and (**d**) FE-SEM images of a convex line (width 0.4 mm) ([13] © IOP Publishing. Reproduced by permission of IOP Publishing. All rights reserved. http://iopscience.iop.org/0960-1317/22/3/035016)

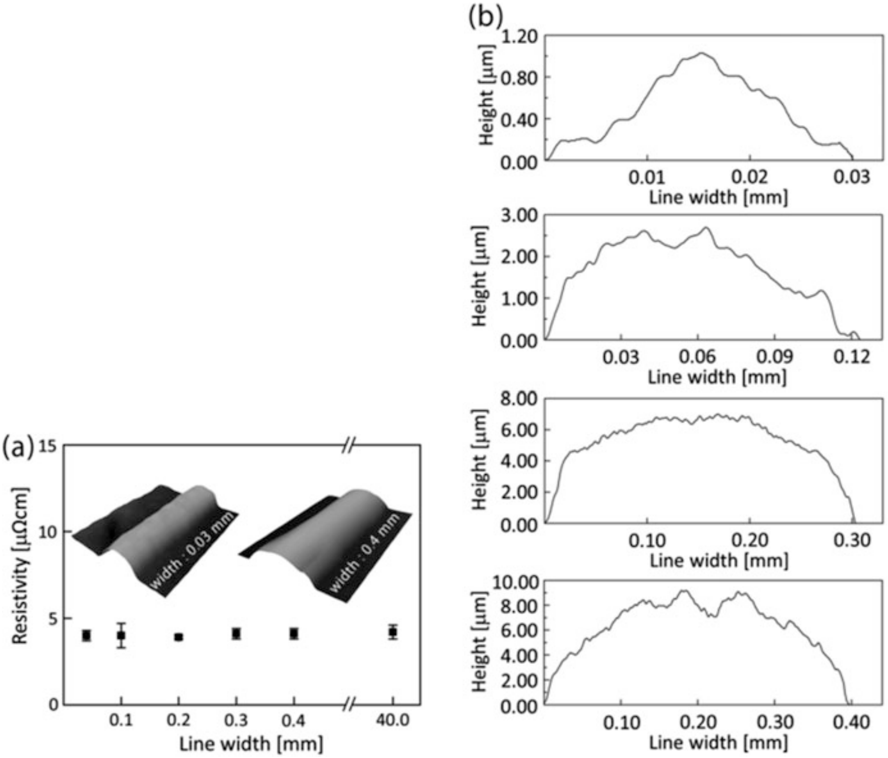

Fig. 5.2 Mask-printed lines fabricated using a high-viscosity silver-nanoparticle ink after heating at 230 °C. (**a**) Electrical resistivity (linewidth range 0.03–0.4 mm) and (**b**) cross-sectional morphology (linewidth range 0.03–0.4 mm) ([13] © IOP Publishing. Reproduced by permission of IOP Publishing. All rights reserved. http://iopscience.iop.org/0960-1317/22/3/035016)

To better understand the influence of the linewidth on the electrical resistivity, cross-sectional profiles of lines of various widths were observed. Surprisingly, the profiles showed clear differences. The profiles of the narrow ink-jet-printed lines (<0.3 mm) were concave, while those of the wide ink-jet-printed lines (>0.4 mm) were convex (Fig. 5.1b). These profile differences correspond exactly with the observed differences in the electrical resistivity. In contrast, the profiles of all of the mask-printed lines, regardless of the width in the entire studied range (0.03–40 mm), were convex and exhibit a constant resistivity of 3.9–4.2 μΩcm (Fig. 5.2a, b). For dilute inks, during drying, the solvent is known to inhomogeneously evaporate and the solute is known to self-aggregate [23–32], resulting in the well-known coffee-ring effect. Moreover, smaller droplets exhibit accelerated solvent evaporation rates, resulting in preferential evaporation of the solvent near the edges [25]. Ink-jet-printable inks possess low silver-nanoparticle loading levels, and thus, ink-jet-printed lines can become concave after sintering. In particular, narrow ink-jet-printed lines are particularly prone to inhomogeneous evaporation.

Field-emission scanning electron microscopy (FE-SEM) images of the centers and edges of the printed lines revealed why the concave lines with distinct ridges exhibited such high resistivity. The silver-nanoparticle distribution in the concave lines was clearly different from that in the convex lines (Fig. 5.1c, d, respectively). In the convex lines (0.4 mm), the nanoparticles were homogeneously aggregated, and intervening voids were nearly nonexistent at both the center and the edge (Fig. 5.1d). In the concave lines (0.04 mm), the edge morphology was similar to that for the convex lines, but the center morphology showed numerous large voids (Fig. 5.1c). The large cavities at the centers of the concave lines were produced as the result of convection flow, which transported the nanoparticles from the centers to the edges during ink solvent evaporation. This transport decreased the electrical contact between the nanoparticles remaining at the centers, causing an increase in the resistivity, even under the same heating conditions.

When the ink parameters such as concentration, solvent type, nanoparticle size, and viscosity are controlled carefully before printing, narrow lines without ridges can be obtained [26–30, 32]. However, devising precise parameters for each desired linewidth is laborious and unproductive. As described above, inhomogeneous evaporation during heating is the most significant cause of the coffee-ring effect. Therefore, we proposed a simple approach involving control of the heating conditions rather than the ink, substrate, or printing conditions for the fabrication of fine printed lines with low electrical resistivity.

Printed lines with a width of 0.3 mm are convex before heating. According to previous reports, such narrow lines maintain their convex shape after low-temperature heating (<50 °C) [33, 34]. However, such low-temperature heating generally did not decrease the electrical resistivity to the level of that of bulk silver. The silver-nanoparticle inks used in this study required heating to a high temperature (>200 °C) in order to achieve low electrical resistivity (<10 μΩcm). Therefore, the maximum heating temperature was fixed at 200 °C, and the rate at which the temperature was increased to 200 °C was adjusted in order to achieve maximal conductivity.

As mentioned above, after heating at 200 °C for 90 min, narrow ink-jet-printed lines (<0.3 mm) exhibited high resistivity (15 μΩcm) and concave cross-sectional profiles (Fig. 5.1b). For such lines, a two-step heating process was adopted; first, the lines were heated gradually from 20 to 200 °C over 60 min at a heating rate of 3 °C/min and then maintained at 200 °C for an additional 30 min. The total heating time was 90 min, as was the case for the constant heating conditions applied to obtain line profiles shown in Fig. 5.1. The gradual heating clearly changed the profiles of the narrow lines (<0.3 mm) from concave to convex (Fig. 5.3b). The nanoparticles were very densely packed, and the large voids that decreased the electrical contact were no longer evident at either the center or the edge, even in the narrowest line (0.04 mm) (Fig. 5.3c). Gradual heating therefore restricted the convection flow in the lines during evaporation, causing the lines to become convex with homogeneously distributed nanoparticles. As a result, even the narrowest ink-jet-printed lines (0.04–0.3 mm) exhibited low resistivities (3.9–4.2 μΩcm) (Fig. 5.3a).

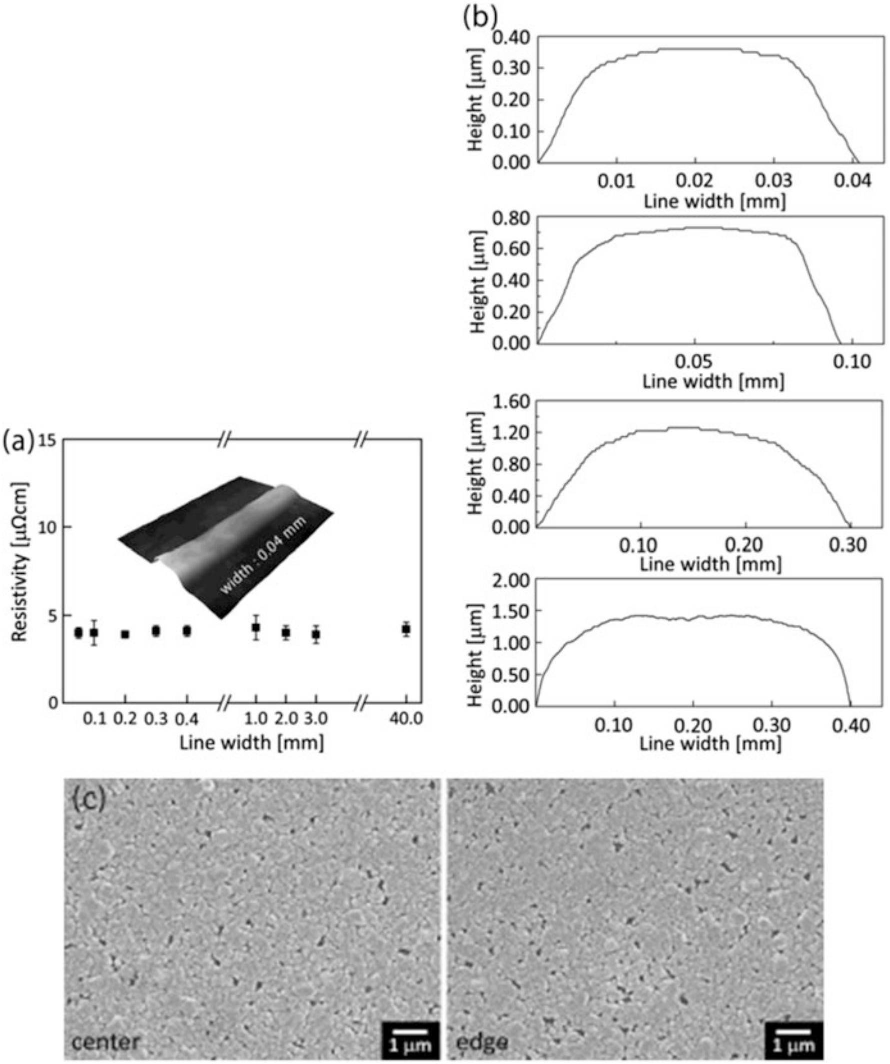

Fig. 5.3 Ink-jet-printed lines fabricated using a low-viscosity silver-nanoparticle ink after gradual heating in two phases: from 20 to 200 °C over 60 min followed by constant heating at 200 °C for an additional 30 min. (**a**) Electrical resistivity (linewidth range 0.04–40 mm), (**b**) cross-sectional morphology (linewidth range 0.04–0.4 mm), and (**c**) FE-SEM images of a concave line (width 0.04 mm) ([13] © IOP Publishing. Reproduced by permission of IOP Publishing. All rights reserved. http://iopscience.iop.org/0960-1317/22/3/035016)

In summary, numerous researchers have investigated the ink-jet printing fabrication of narrow high-conductivity lines by optimizing parameters such as the ink components, the nature of the substrate surface, and the printing conditions [9, 16–18, 22, 33, 35]. We have found that these approaches are unnecessary and insufficient. Instead, moderate heating can yield narrow lines with high conductivity. These findings should open the door to more facile fabrication of high-performance printed electronics, such as organic light-emitting diodes, organic solar cells, organic thin-film transistors, flat-panel displays, and radio-frequency identification devices.

5.3 Repellent Pore-Structured Acceptance Layers

Silver has a resistivity of 1.59 μΩcm and is a material with one of the lowest electrical resistances. Thus, silver-nanoparticle-based conductive inks have been developed that can be used to create highly conductive patterns with resistivities approximately equal to that of bulk silver [36–38]. In most of these inks, the silver nanoparticles are capped by dispersants in order to extend their storage life. To remove these nonconductive dispersants, the printed line patterns are heated to extremely high temperatures (>200 °C) [39]. As a consequence, thermally sensitive plastic films, such as polyethylene terephthalate, polypropylene, and polycarbonate, cannot be used as substrates for printed electronic devices. On the other hand, polyimide films are the most suitable candidate substrates because of their high thermal stability.

When a silver-nanoparticle ink is ink-jet-printed onto a polyimide film, however, the characteristics of the substrate and the ink often hinder the ability to obtain highly conductive line patterns with fine intervals. The low viscosity of silver-nanoparticle inks results in inhomogeneous evaporation, thus inducing the "coffee-ring effect" within the printed lines. Consequently, the inhomogeneous distribution of silver nanoparticles increases the resistance of the lines [13, 22]. In addition, the low concentration of silver nanoparticles in the ink decreases the printed line thickness after drying [40]. The high wettability of polyimide films also decreases the printed line thickness because silver-nanoparticle ink droplets spread laterally on polyimide films [16, 41, 42]. Such thin lines induce high resistance because of their small cross sections, even for printed lines with low resistivity. Therefore, ink-jet printing technologies using silver-nanoparticle inks on polyimide films must print thick lines with low electrical resistance.

In this study, the aim was to fabricate well-defined, low electrical resistance lines comprised of silver-nanoparticle inks on polyimide films via ink-jet printing. To maintain the high thermal stability of the polyimide films, fine pore structures were fabricated on their surfaces using a polyamide-imide. Decreasing the pore diameter prevented the lateral spreading of the silver-nanoparticle ink on the substrate surface. Moreover, fluorine treatment of the pore structures increased the thickness of the printed lines. Using these repellent, pore-structured polyimide films decreased the electrical resistance to one-fifth that of the lines on the pristine polyimide film for the same silver-nanoparticle ink-heating conditions and line dimensions (widths and lengths).

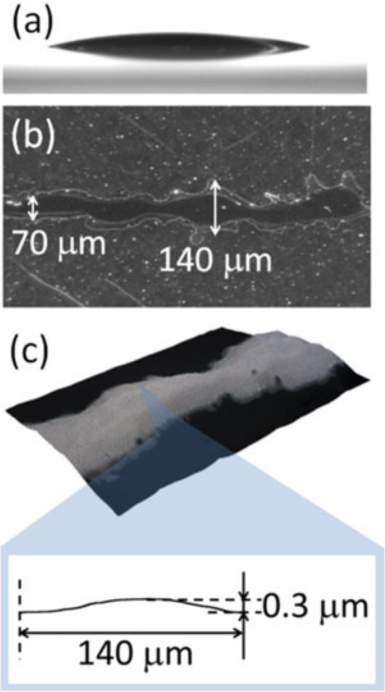

Fig. 5.4 Pristine polyimide film: (**a**) Contact angle of the ink droplets containing 4-µl silver nanoparticle and (**b**) top view and (**c**) 3D view of the ink-jet-printed line morphology (Reprinted with permission from Ref. [14]. Copyright 2012 American Chemical Society. http://pubs.acs.org/doi/abs/10.1021/am300160s)

Polyimide films have been widely used as substrates for printed electronics because of their high-dimensional stability against high sintering temperatures above 200 °C. However, when conductive inks are ink-jet-printed on these films, their high surface energy of 40 mN/m often results in widespread thin lines [16]. In this study, a silver-nanoparticle ink with tetradecane as the solvent was used. At impact, the 4-µl droplets of the silver-nanoparticle ink spread laterally on the polyimide film. The contact angle of the ink was only 11° (Fig. 5.4a). Thus, ink-jet printing on the polyimide film yielded splashed lines with wavy boundaries (Fig. 5.4b). The lateral spreading of the ink droplets also resulted in thinner lines of less than 0.3 µm with widths varying from 70 to 140 µm and a length of 40 mm (Fig. 5.4c). Given the high thermal stability of the polyimide films, the printed lines were subjected to heat sintering at 220 °C for 60 min. Consequently, the ink-jet-printed lines exhibited a low electrical resistance of 5 Ω. However, this value was 2.6 times higher than that of bulk silver, considering the line volume and resistivity of silver (1.59 µΩcm). Because these printed lines were subjected to sufficient sintering conditions, prolonged heating or heating at higher temperatures did not decrease their resistance. However, it is known that an increase in the line thickness decreases the resistance for the same ink, line width, and sintering conditions. While an increase in the ink viscosity is effective for increasing the line thickness, high-viscosity inks are difficult to inject through an ink-jet printer. Thus, surface modification of the substrate is a practical method for increasing the line thickness.

Therefore, in order to increase the line thickness, pore structures were fabricated on the polyimide film. Pore structures have been used in screen printing to obtain thicker lines with sharp edges [43, 44]. In this study, the pore structures were composed of a polyamide-imide in order to maintain the high thermal durability of the printed substrates. Similar to polyimides, polyamide-imides have high thermal stability and glass transition temperatures near 300 °C. The contact angle of the silver-nanoparticle ink droplets on the polyamide-imide was 9.5°. Thus, their wettability was similar to that on polyimide films. According to Wenzel's equation, such a spreadable surface becomes more spreadable with pore structures [45]. Thus, when the 4-μl ink droplets were impacted on pore-structured films with average pore sizes of 0.5, 3, and 5 μm, the droplets were absorbed into the pore structures, and it was not possible to measure the contact angles (contact angle 0°).

As described above, the ink-jet-printed silver-nanoparticle lines on a polyimide film resulted in splashed and wavy boundaries (Fig. 5.4b, c). In contrast, when the silver-nanoparticle ink droplets were ink-jet-printed on the polyamide-imide pore-structured film, the ink wetted the surface and then was absorbed into the capillary network. Therefore, the printed lines on the pore structures exhibited reduced splashing, and the edges were sharply defined (Fig. 5.5a). Notably, on the film with the largest pore structures (5 μm), the printed lines spread laterally, and their width of 300 μm was twice that of lines printed on the pristine polyimide film. Shrinking the pore size, however, reduced the spreading of the printed lines. Decreasing the pore size to 3 μm resulted in a narrower line width of 150 μm, which was equivalent to the width of the lines on the pristine polyimide film. The smallest pore size of 0.5 μm produced a 50-μm-wide line because it was difficult for the silver-nanoparticle ink droplets to spread laterally into the fine pore structures across the large surface area (Fig. 5.5a). Therefore, such fine pore structures prevented the splashing and spreading of the silver-nanoparticle ink, resulting in narrow lines with sharp edges. However, the silver-nanoparticle ink was completely absorbed into the substrates, resulting in a flat surface (Fig. 5.5b). This result is in agreement with the contact angle results. FE-SEM examination of the printed lines revealed many cavities due to ink penetration into the pore structures (Fig. 5.5c). As a result, the electrical resistance of the lines was 25 Ω, even after sufficient sintering at 220 °C for 60 min. This electrical resistance was five times larger than that of the lines on the pristine polyimide films.

Therefore, while the fine pore structures produced narrow lines with sharp edges, they resulted in a reduction of the electrical conductivity because of the absorption of the silver-nanoparticle ink droplets. To avoid this penetration of the silver-nanoparticle ink droplets into the pore structures, the polyimide films with 0.5-μm pore structures were chemically modified using a fluorine treatment. Then, no difference in the surface morphologies of the pore structures with and without the fluorine treatment was observed. Most importantly, the pore structures were not filled with the fluorine treatment substances. As shown in Fig. 5.6a, the contact angles on fluorine-treated polyimide films with and without pores were 95° and 98°, respectively; both fluorine-treated substrates exhibited nearly the same degree of

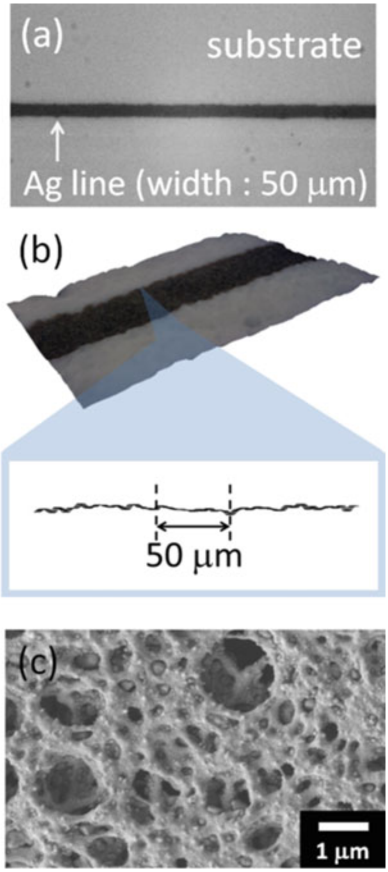

Fig. 5.5 Ink-jet-printed lines on a polyamide-imide pore-structured film with 0.5-μm pores: (**a**) top view, (**b**) 3D view, and (**c**) FE-SEM images of the silver nanoparticles after sintering (Reprinted with permission from Ref. [14]. Copyright 2012 American Chemical Society. http://pubs.acs.org/doi/abs/10.1021/am300160s)

repulsion of the 4-μl ink droplets. Surprisingly, however, significantly different line patterns were obtained on these substrates using ink-jet printing.

The silver-nanoparticle ink droplets were ink-jet-printed on fluorine-treated films with pore structures. Then, the pore structures did not absorb the ink droplets, and the silver nanoparticles remained on the surfaces of the fluorine-treated pore structures because of their repellent properties (Fig. 5.6d). In the example shown in Fig. 5.6, the printed line thickness increased to 1.0 μm (Fig. 5.6c), resulting in a narrower width of 30 μm and sharp edges (Fig. 5.6b). Thus, the fluorine-treated pore structures yielded well-defined lines that were more than three times thicker than those on the pristine polyimide films. Moreover, the printed lines on the fluorine-treated pore structure films exhibited a resistance of 8 Ω because the silver nanoparticles remained on the pore structures. This resistance is nearly equal to that for the lines printed on the pristine polyimide film. In contrast, when the silver-nanoparticle ink droplets were printed on the fluorine-treated polyimide films without pores, the droplets were effectively repelled and remained on the surface,

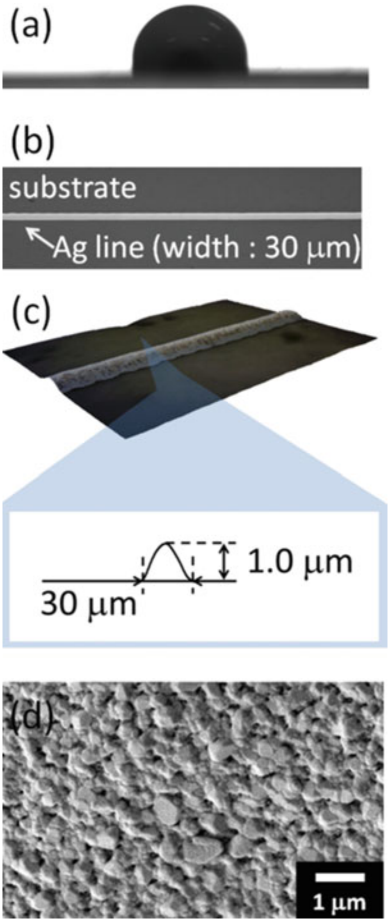

Fig. 5.6 Fluorine-treated polyamide-imide pore-structured film with 0.5-µm pores: (**a**) Contact angle of ink droplets containing 4-µl silver nanoparticles, (**b**) top view and (**c**) 3D view of the ink-jet-printed line morphology, and (**d**) FE-SEM image of the silver nanoparticles after sintering (Reprinted with permission from Ref. [14]. Copyright 2012 American Chemical Society. http://pubs.acs.org/doi/abs/10.1021/am300160s)

eventually forming dotted lines with a diameter of 40 µm and a thickness of 1.6 µm, which had no conductivity.

At the same line width and length, increasing the line thickness decreases the electrical resistance of the printed lines. Therefore, the silver-nanoparticle ink droplets were ink-jet-printed on the repellent pore-structured polyimide films in order to obtain lines with the same dimensions as those on the pristine polyimide films, i.e., a width of 140 µm and a length of 40 mm. Rectangular lines with a thickness of 1.0 µm were obtained because of the repellent pore structures. This thickness was three times larger than that on the pristine polyimide films (0.3 µm). Thus, the electrical resistance of the thicker lines was decreased to only 1 Ω, while that of the thinner lines on the pristine polyimide film was 5 Ω. Moreover, the lines showed sharp edges without any splashing, indicating that fine interval lines with close gaps could be printed on the repellent pore-structured polyimide films. Therefore, it should be possible to use ink-jet printing on repellent pore-structured films to fabricate closely packed line patterns with high conductivity within a limited space. In the future, printed electronics, such as tiny sensor tags, high-power conversion solar cells, high-speed computers, and flexible displays will be made possible with this technique.

5.4 Absorption Acceptance Layers

Producing highly conductive lines with narrow and sharp edges are major challenges in printed electronics. Of the various printing technologies, screen printing can produce such lines because highly concentrated, metallic nanoparticle inks are printed via a roller or squeegee onto the printing surface using a pre-patterned mask that has narrow, sharp edges [46–48]. Organic electronic devices, which are some of the most anticipated future devices, also require the deposition of other thin layers on various substrates for use as organic semiconductors and insulators. Screen printing, with its firm-contact printing technique, would damage these deposited components. Therefore, to decrease such damage, the fabrication of conductive lines or electrodes using a maskless, noncontact method, such as ink-jet printing, is preferred [3, 16, 22, 49, 50].

However, with ink-jet printing, it is difficult to produce highly conductive lines with narrow, sharp edges using the current technology. When conductive lines are formed via ink-jet printing, the conductive inks, which contain metallic nanoparticles, are ejected through a nozzle with a very small diameter of approximately 50 μm. Therefore, low-concentration and low-viscosity inks are required for ink-jet printing [38, 40, 51–54]. When such a low-viscosity ink is ejected from the nozzles, the printed lines often spread, splash, and take on a wave form. Increasing the ink viscosity is effective; however, high-viscosity inks are difficult to inject through an ink-jet printer because they clog the nozzles. Thus, the surface-energy adjustment of the polymer substrates is an inevitable approach to obtain sharp, straight lines using ink-jet printing [16, 41, 42, 55–58].

Even though sharp, straight lines can be printed on optimized substrates, the coffee-ring effect that results when using low-viscosity metallic nanoparticle inks remains an issue [23, 29]. Metallic nanoparticles are segregated at the line edge due to solvent convection flow during drying of ink vehicles. As a result, an inhomogeneous distribution of the silver nanoparticles (AgNPs) leads to an increase in the resistivity of the printed lines and consequently a decrease in their conductivity when the line width is decreased [13, 22]. Therefore, although ink-jet printing has the advantages of noncontact, maskless printing, creating highly conductive lines with narrow, sharp edges is difficult because of the use of low-concentration inks.

To address this problem, absorption layers for ink vehicles were formed on polyimide films. As a result, highly conductive lines with narrow, sharp edges were ink-jet-printed using a low-viscosity, commercially available silver-nanoparticle ink with a low concentration. When the ink was ink-jet-printed on a polyimide substrate modified with an absorption layer, the concentration of the silver

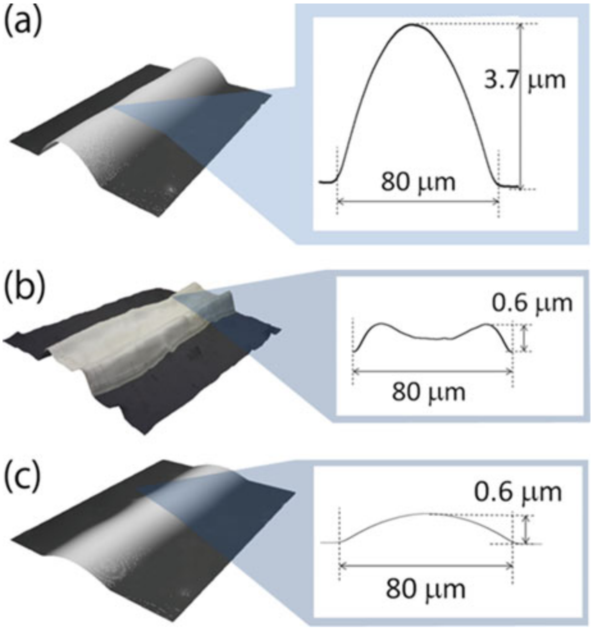

Fig. 5.7 (**a**) As-printed line on a pristine polyimide film before heating. (**b**) Concave-shaped line with a high resistance of 24 Ω obtained after constant heating at 200 °C for 30 min. (**c**) Convex-shaped line with a low resistance of 7 Ω obtained after gradual heating from 20 to 200 °C at a rate of 3 °C min^{-1} and then holding for 30 min at 200 °C ([15] Reproduced by permission of The Royal Society of Chemistry. http://pubs.rsc.org/en/content/articlelanding/2012/RA/C2RA21442C#!divAbstract)

nanoparticles in the printed lines increased. In addition, the absorption of the ink vehicle deposited via ink-jet printing caused the formation of narrow, convex lines with high conductivity. Furthermore, this technique enabled the sintering time to be shortened because the pre-sintering process, which is essential for solvent evaporation, does not require either flash or microwave sintering methods. These achievements can be applied to the high-speed, mass production of electronic devices using ink-jet printing.

When the low-concentration, silver-nanoparticle ink was ink-jet-printed on a pristine polyimide film, straight, sharp-edged lines with a width of 80 μm were obtained (Fig. 5.7a). Owing to the low concentration of the AgNPs, the as-printed lines were thick (3.7 μm). After heating at 200 °C for 30 min, the line cross-sectional profiles became concave while maintaining their width (Fig. 5.7b). During heating, the ink vehicles evaporated with convection flow, and the AgNPs aggregated at the line edges [23, 29]. This inhomogeneous distribution of the nanoparticles produced large voids at the centers of the lines, leading to a loss of electrical contact between the AgNPs [13]. As a result, the heated lines on the pristine polyimide film exhibited a high electrical resistance of 24 Ω, which was ten times greater than that of bulk silver with the same line dimensions.

In Sect. 5.2, we reported that a high concentration of AgNP ink achieved a low electrical resistance, even when it was heated at a constant temperature [13]. This result was obtained because such high-concentration inks do not undergo convection flow during evaporation of the ink vehicle. Thus, we proposed the gradual heating of low-concentration AgNP inks in order to increase their concentrations gradually without causing an inhomogeneous distribution of the AgNPs [13]. When a printed line was subjected to gradual temperature elevation to 200 °C over 60 min, and then subsequently heated at 200 °C for 30 min, the heated lines exhibited a convex shape (Fig. 5.7c) and a low electrical resistance of 7 Ω, which is equivalent to that of bulk silver. However, this prolonged heating is impractical because printed electronic devices must be fabricated using high-volume, high-speed methods, such as roll-to-roll processes. Therefore, we proposed the use of surface-coating treatments for the creation of ink-jet-printed lines with low electrical resistance without prolonged heating. The basic concept involves the deposition of a coating layer on the substrate that leads to an increase in the concentration of the AgNP ink before heating, leading to the formation of convex printed lines with low resistance after heating.

The pore-structured coating layer was formed on the pristine polyimide film by mixing a thermoplastic polymer with 10–20-nm-diameter silica nanoparticles. When an AgNP ink was ink-jet-printed on the pore-structured coating layer and heated at 200 °C for 30 min, the obtained lines were convex in shape (Fig. 5.8a). Notably, the width and height (60 and 0.5 μm, respectively) of these lines were much smaller than those of the lines printed on a pristine polyimide film (Figs. 5.7c and 5.8a). The diameter of the AgNPs in the ink was 30–50 nm, whereas the diameter of the pores in the coating layer was approximately 100 nm (Fig. 5.8b). Therefore, immediately after ink-jet printing and before heat sintering, most of the AgNPs flowed into the pore structures. Consequently, the inflow of AgNPs into the pore structures created a loss of the electrical connection between the adjacent

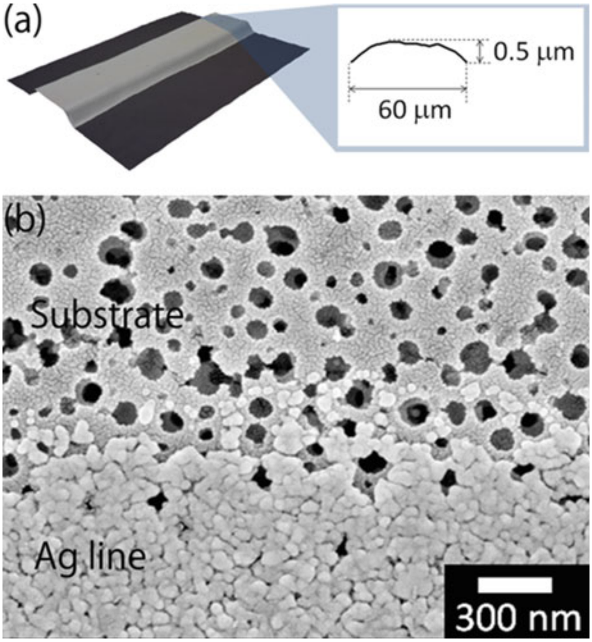

Fig. 5.8 (**a**) Convex-shaped line with a large resistance of 16 Ω after heating at 200 °C for 30 min, (**b**) FE-SEM image of the surface of a porous-structured polyimide substrate (*upper*), and ink-jet-printed line of a silver-nanoparticle ink (*lower*) (Reprinted with permission from Ref. [14]. Copyright 2012 American Chemical Society. http://pubs.acs.org/doi/abs/10.1021/am300160s)

AgNPs [14]. However, the heated lines on the pore structures exhibited a high electrical resistance of 16 Ω despite their convex shape. In general, AgNPs of less than 100 nm in diameter are used in conductive inks for ink-jet printing. The diameter of the pore structures was approximately 100 nm, even though they were fabricated with tiny silica nanoparticles with diameters ranging from 10 to 20 nm. It would be ideal if mechanical sieving of the AgNPs through the fine pores would increase the concentration of the AgNPs and, consequently, the electrical conductivity of ink-jet-printed lines.

Therefore, a coating layer was deposited on the pristine polyimide film that only absorbed the ink vehicle. The polymer-coated polyimide films (DMI-70, DIC Corp., Japan) were prepared by coating thermoplastic polymer onto the pristine polyimide films. As a result, the concentration of the AgNPs in low-concentration inks printed on these substrates was increased. Initially, it was observed that the polymer-coated polyimide films effectively absorbed ethanol, which was the main component of the nanoparticle ink used in the study. Because there were no pores in the coating layer that could be penetrated by AgNPs, it was expected that when the AgNP ink was printed on the polymer-coated polyimide film, the concentration of the AgNPs would be increased following the absorption of the ink vehicle. Consequently, it was anticipated that the highly concentrated inks would produce convex lines with low resistance and without the need for heating.

When the AgNP ink was ink-jet-printed on the polymer-coated polyimide and then heated at a constant temperature of 200 °C for 30 min, convex lines that were 70 μm wide and 1.3 μm thick were obtained (Fig. 5.9a). This width was less than that obtained for lines printed on a pristine polyimide because the highly concentrated inks produced narrower lines. In addition, their thickness of 1.3 μm was significantly greater than that of the lines printed on a pristine polyimide film (0.6 μm). An FE-SEM image of the edge of an ink-jet-printed line on the coated substrate revealed that the thickness of coated polymer layer was increased from ca. 3 μm to ca. 4 μm possibly due to swelling by absorption of ink vehicles (Fig. 5.9b). Furthermore, the cross-sectional FE-SEM image showed that the AgNPs and the coated polymer layer were not clearly merged (Fig. 5.9c). As expected, the coated polymer absorbed only the ink vehicle and not the AgNPs. After heating, all of the AgNPs remained on the surface of the coated layer and were densely packed together. As a result, the heated lines on the polymer-coated polyimide exhibited a small resistance of only 8 Ω, even after constant heating at 200 °C for 30 min. These results suggest that the coating of polyimide substrates with an appropriate polymer for the absorption of ink vehicles can enable the fabrication of printed lines with enhanced electrical conductivity, even when the ink-jet-printed lines are heated at a constant temperature. Recently, researchers have focused on photonic- and microwave-exposure techniques for roll-to-roll-compatible sintering because of the significantly short sintering times that are possible with these techniques [59]. However, these exposure processes require pre-sintering of the printed wet lines for dozens of minutes in order to prevent ink explosion during exposure [59, 60]. It is possible that the coating layer system for

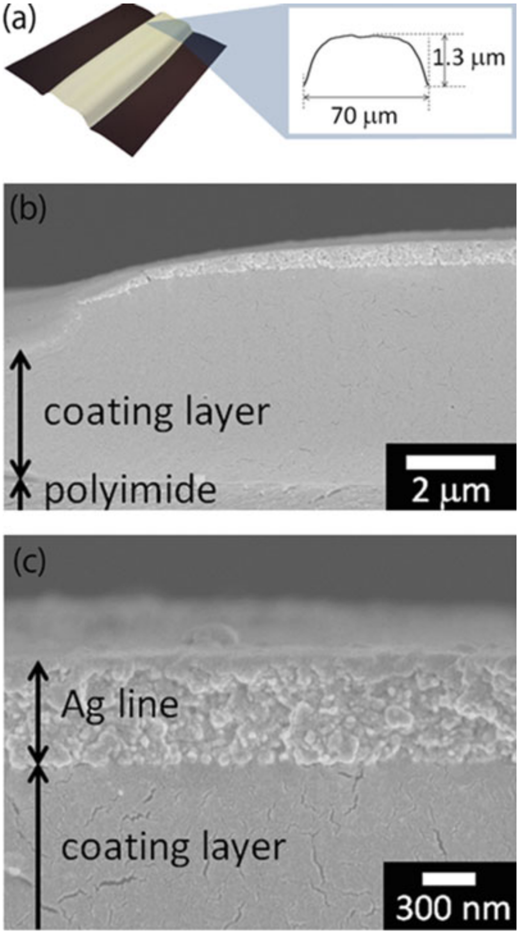

Fig. 5.9 (**a**) Convex-shaped line with a low resistance of 8 Ω after heating at 200 °C for 30 min. (**b**) Cross-sectional FE-SEM image of heated lines on a polymer-coated polyimide film. (**c**) Cross-sectional FE-SEM image of the silver-nanoparticle ink and coated polymer layer underneath the heated lines (Reprinted with permission from Ref. [14]. Copyright 2012 American Chemical Society. http://pubs.acs.org/doi/abs/10.1021/am300160s)

absorption of ink vehicles may be effective as a pre-sintering process for photonic and microwave exposure.

Finally, adhesion and thermal-reliability tests for the ink-jet-printed lines fabricated using an AgNP ink on the polymer-coated polyimide film were performed. The adhesion strength was estimated according to the international ASTM D3359-B standard. As shown in Fig. 5.9c, the heated AgNPs were clearly separated from the coating layer without any merging. However, the heated AgNPs did not peel from the coating layer after the adhesion test. This result corresponds to a 5B level of adhesion strength and indicates that the coated polymer layer adhered well not only to the polyimide substrate but also to the AgNP lines after sintering. Moreover, the ink-jet-printed lines on the polymer-coated polyimide film were subjected to three different thermal-reliability tests. After each test, the electrical resistance of the ink-jet-printed lines was measured. When the printed lines were subjected to a high-temperature storage test at 80 °C, the electrical resistance of the lines decreased to 87 % of the original value after 100 h and then was maintained at 82–88 % to 1,000 h. The drastic decrease within 100 h implies that the electrical contacts between the AgNPs were increased at 80 °C. After thermal shock (−40 °C and 80 °C) and high-temperature/humidity-exposure (85 °C and RH 85 %) tests, the electrical resistance increased slightly (by less than 20 %) at 1,000 h. These results revealed that the ink-jet-printed lines on the polymer-coated substrates could be used for common applications.

5.5 Conclusions

In this chapter, ink-jet printing technologies for improving the electrical conductivity of printed lines were introduced. High-conductivity, narrow conductive patterns are essential for electronic devices. To realize such patterns, the use of appropriate sintering conditions is important for ink-jet-printed lines. In Chapter 5.2, conductive lines of various widths (0.03–40 mm) were deposited on polyimide films using two different AgNP inks, and the electrical properties of the lines were evaluated as a function of the linewidth. When a high-viscosity silver ink (120,000–180,000 mPa · s) was mask-printed and heated at a constant temperature of 230 °C, all of the printed lines were convex in shape and essentially constant in electrical resistivity (3.9–4.2 μΩcm). When a low-viscosity silver ink (11–15 mPa · s) was ink-jet-printed and heated at a constant temperature of 200 °C, the wider (>0.4 mm), convex lines had a constant resistivity of 3.6–5.4 μΩcm, while the narrower printed lines (<0.3 mm) were concave due to the coffee-ring effect. In the narrow concave lines, the electrical contact between the AgNPs at the center of the line was diminished, and thus their resistivity was significantly higher (14.6–16.5 μΩcm). To prevent this loss of electrical contact, we gradually heated the narrow lines from 20 to 200 °C at a heating rate of 3 °C/min, causing the nanoparticles to become densely packed, the line shape to become convex, and the resistivity to decrease to 3.9–4.2 μΩcm, approaching that of bulk silver (1.6 μΩcm).

In Sects. 5.3 and 5.4, we introduced acceptance layers on the plastic substrate in order to improve the properties of ink-jet-printed lines. In Sect. 5.3, AgNP ink droplets with a tetradecane-based solvent were ink-jet-printed onto polyimide films. Because of the high wettability of polyimide films, the ink-jet-printed lines had rough shapes with lateral spreading, splashing, wavy boundaries, and low thicknesses. When pore structures were fabricated on the polyimide film using polyamide-imide, they prevented the splashing of the AgNP ink droplets at impact. Using fine pore structures of 0.5 μm yielded narrow lines with sharp edges. However, their electrical resistance was five times to that of same length lines on pristine polyimide films because the AgNPs were absorbed into the fine pore structures. However, chemical modification of the pore structures with a fluorine treatment provided repellent pore structures that restricted the spreading of the AgNPs into the pores, resulting in thicker lines while still maintaining their sharpness and decreasing their width. When the AgNP ink droplets were ink-jet-printed onto the pristine polyimide film, the printed line width was approximately 140 µm. When lines of this width were ink-jet-printed onto the repellent pore-structured polyimide film, the electrical resistance of the 140-µm-wide printed lines was decreased to one-fifth that of those on the pristine polyimide film because of the increase in thickness from 0.3 to 1.0 µm.

In Sect. 5.4, the issue of convection flow associated with low-concentration AgNP inks for ink-jet printing was considered. During the heating of ink-jet-printed lines for sintering, the ink droplets undergo convection flow, resulting in an inhomogeneous distribution of the AgNPs within the lines and, consequently, high electrical resistance. Two different absorption layers were coated on polyimide films in order to fabricate ink-jet-printed lines without the coffee-ring effect. First, a pore-structured polyimide film was prepared in which AgNPs with diameters of 30–50 nm were mechanically sieved through fine pores. Although the fine pores were fabricated with silica nanoparticles having a diameter of 10–20 nm, the pore size was much larger than the AgNPs. Therefore, the AgNPs flowed into the pore structures, resulting in a significant increase in the electrical resistance of the printed lines compared to that of lines on the pristine polyimide film. Therefore, when pore structures are fabricated on plastic films in order to obtain low-resistance printed lines, a chemical repellent treatment should be applied. In the second approach, a polymer was deposited on the polyimide film in order to absorb the ink vehicle (ethanol). The absorption of the ink vehicle increased the ink concentration and prevented the convection flow of the AgNPs during the heating of the ink-jet-printed lines. As a result, most of the AgNPs remained on the surface, and convex-shaped lines with low electrical resistance were obtained. Moreover, the ink-jet-printed lines on the coating layer adhered well to the polyimide film and exhibited high thermal reliability as determined using the cross-hatch adhesion and temperature storage, thermal shock, and high-temperature and high-humidity-exposure tests, respectively.

References

1. C. Zhong, C. Duan, F. Huang, H. Wu, Y. Cao, Chem. Mater. **23**, 326–340 (2011)
2. P. Calvert, Chem. Mater. **13**, 3299–3305 (2001)
3. B.J. de Gans, P.C. Duineveld, U.S. Schubert, Adv. Mater. **16**, 203–213 (2004)
4. A. Teichler, R. Eckardt, S. Hoeppener, C. Friebe, J. Perelaer, A. Senes, M. Morana, C.J. Brabec, U.S. Schubert, Adv. Energy Mater. **1**, 105–114 (2011)
5. M. Singh, H.M. Haverinen, P. Dhagat, G.E. Jabbour, Adv. Mater. **22**, 673–685 (2010)
6. M.B. Madec, P.J. Smith, A. Malandraki, N. Wang, J.G. Korvink, S.G.J. Yeates, Mater. Chem. **20**, 9155–9160 (2010)
7. M.L. Chabinyc, W.S. Wong, A.C. Arias, S. Ready, R.A. Lujan, J.H. Daniel, B. Krusor, R.B. Apte, A. Salleo, R.A. Street, Proc. IEEE **93**, 1491–1499 (2005)
8. S. Gamerith, A. Klug, H. Scheiber, U. Scherf, E. Moderegger, E.J.W. List, Adv. Funct. Mater. **17**, 3111–3118 (2007)
9. Y. Noguchi, T. Sekitani, T. Yokota, T. Someya, Appl. Phys. Lett. **93**, 043303 (2008)

10. H. Okimoto, T. Takenobu, K. Yanagi, Y. Miyata, H. Shimotani, H. Kataura, Y. Iwasa, Adv. Mater. **22**, 3981–3986 (2010)
11. J.A. Lim, J.H. Kim, L. Qiu, W.H. Lee, H.S. Lee, D.H. Kwak, K.W. Cho, Adv. Funct. Mater. **20**, 3292–3297 (2010)
12. S.B. Fuller, E.J. Wilhelm, J.M.J. Jacobson, Microelectromech. Syst **11**, 54–60 (2002)
13. C. Kim, M. Nogi, K. Suganuma, J. Micromech. Microeng. **22**, 035016 (2012)
14. C. Kim, M. Nogi, K. Suganuma, Y. Yamato, ACS Appl. Mater. Interfaces **4**, 2168–2173 (2012)
15. C. Kim, M. Nogi, K. Suganuma, Y. Saitou, J. Shirakami, RSC Adv **2**, 8447–8451 (2012)
16. T.H.J. van Osch, J. Perelaer, A.W.M. de Laat, U.S. Schubert, Adv. Mater. **20**, 343–345 (2008)
17. M. Henning, L. Ute, M. Dario, J.S. Patrick, G.K. Jan, Phys. Status Solidi A **206**, 1626–1630 (2009)
18. D.H. Youn, S.H. Kim, Y.S. Yang, S.C. Lim, S.J. Kim, S.H. Ahn, H.S. Sim, S.M. Ryu, D.W. Shin, J.B. Yoo, Appl. Phys. A-Mater. Sci. Process. **96**, 933–938 (2009)
19. D.J. Lee, J.H. Oh, H.S. Bae, Mater. Lett. **64**, 1069–1072 (2010)
20. M. Shlomo, G. Michael, T. Dana, K. Alexander, B. Isaac, M. Oded, Langmuir **21**, 10264–10267 (2005)
21. L. Michael, G. Michael, M. Oded, B. Isaac, A. Doron, M. Shlomo, ACS Nano **3**, 3537–3542 (2009)
22. D.J. Kim, S.H. Jeong, B.K. Park, J.H. Moon, Appl. Phys. Lett. **89**, 264101 (2006)
23. D.D. Robert, B. Olgica, F.D. Todd, H. Greb, R.N. Sidney, A.W. Thomas, Nature **389**, 827–829 (1997)
24. D.D. Robert, B. Olgica, F.D. Todd, H. Greg, R.N. Sidney, A.W. Thomas, Phys. Rev. **E62**, 756–765 (2000)
25. J.F. Benjamin, Langmuir **18**, 60–67 (2002)
26. B.J. de Gans, U.S. Schubert, Langmuir **20**, 7789–7793 (2004)
27. M. Ikegawa, H. Azuma, JSME Int. J. **B47**, 490–496 (2004)
28. K. Ozawa, E. Nishitani, M. Doi, Jpn. J. Appl. Phys. **44**, 4229–4234 (2005)
29. J.H. Park, J.H. Moon, Langmuir **22**, 3506–3513 (2006)
30. C. Poulard, P. Damman, EPL **80**, 64001 (2007)
31. D. Soltman, V. Subramanian, Langmuir **24**, 2224–2231 (2008)
32. J.A. Lim, W.H. Lee, H.S. Lee, J.H. Lee, Y.D. Park, K. Cho, Adv. Funct. Mater. **18**, 229–234 (2008)
33. D.J. Lee, J.H. Oh, Surf. Interface Anal. **42**, 1261–1265 (2010)
34. Y. Li, C. Fu, J. Xu, J. Appl. Phys. **46**, 6807–6810 (2007)
35. C.E. Hendriks, P.J. Smith, J. Perelaer, A.M.J. van den Berg, U.S. Schubert, Adv. Funct. Mater. **18**, 1031–1038 (2008)
36. K.J. Lee, B.H. Jun, T.H. Kim, J.W. Joung, Nanotechnology **17**, 2424 (2006)
37. S. Magdassi, A. Bassa, Y. Vinetsky, A. Kamyshny, Chem. Mater. **15**, 2208–2217 (2003)
38. H.H. Lee, K.S. Chou, K.C. Huang, Nanotechnology **16**, 2436–2441 (2005)
39. J. Perelaer, P.J. Smith, D. Mager, D. Soltman, S.K. Volkman, V. Subramanian, J.G. Korvink, U.S.J. Schubert, Mater. Chem. **20**, 8446–8453 (2010)
40. A.L. Dearden, P.J. Smith, D.Y. Shin, N. Reis, B. Derby, P. O'Brien, Macromol. Rapid Commun. **26**, 315–318 (2005)
41. J.H. Oh, S.Y. Lim, J. Micromech. Microeng. **20**, 015030 (2010)
42. S.H. Lee, K.Y. Shin, J.Y. Hwang, K.T. Kang, H.S. Kang, J. Micromech. Microeng. **18**, 075014 (2008)
43. D. Tobjörk, R. Österbacka, Adv. Mater. **23**, 1935–1961 (2011)
44. R. Peng, C. Xia, X. Liu, D. Peng, G. Meng, Solid State Ionics **152**, 561–565 (2002)
45. R.N. Wenzel, Ind. Eng. Chem. **28**, 988–994 (1936)
46. W.Y. Chang, T.H. Fang, H.J. Lin, Y.T. Shen, Y.C.J. Lin, Display Technol. **5**, 178–183 (2009)
47. R. Faddoul, N. Reverdy-Bruas, J. Bourel, Microelectron. Reliab. **52**, 1483–1491 (2012)
48. G. Zhang, P. Deng, W. Xu, Z. Yu, Adv. Mater. Res. **380**, 121–124 (2012)

49. B.K. Park, D. Kim, S. Jeong, J. Moon, J.S. Kim, Thin Solid Films **515**, 7706–7711 (2007)
50. J. Choi, Y.J. Kim, S. Lee, S.U. Son, H.S. Ko, V.D. Nguyen, D. Byun, Appl. Phys. Lett. **93**, 193508 (2008)
51. H.C. Jung, S.H. Cho, J.W. Joung, Y.S.J. Oh, Electron. Mater. **36**, 1211–1218 (2007)
52. J. Perelaer, A.W.M. De Laat, C.E. Hendriks, U.S.J. Schubert, Mater. Chem. **18**, 3209–3215 (2008)
53. J. Perelaer, B.J. De Gans, U.S. Schubert, Adv. Mater. **18**, 2101–2104 (2006)
54. J. Perelaer, C.E. Hendriks, A.W.M. De Laat, U.S. Schubert, Nanotechnology **20**, 165303 (2009)
55. Y.S. Goo, Y.I. Lee, N. Kim, K.J. Lee, B. Yoo, S.J. Hong, J.D. Kim, Y.H. Choa, Surf. Coat. Technol. **205**, S369–372 (2010)
56. G. Tortissier, P. Ginet, B. Daunay, L. Jalabert, P. Lambert, B. Kim, H. Fujita, H. Toshiyoshi, J. Micromech. Microeng. **21**, 105021 (2011)
57. A.M.J. Van Den Berg, A.W.M. De Laat, P.J. Smith, J. Perelaer, U.S.J. Schubert, Mater. Chem. **17**, 677–683 (2007)
58. B.J. Kang, J.H. Oh, Thin Solid Films **518**, 2890–2896 (2010)
59. J. Perelaer, R. Abbel, S. Wünscher, R. Jani, T. Lammeren, U.S. Schubert, Adv. Mater. **24**, 2620–2625 (2012)
60. D.J. Lee, S.H. Park, S. Jang, H.S. Kim, J.H. Oh, Y.W. Song, J. Micromech. Microeng. **21**, 125023 (2011)

Chapter 6
Printed Organic Thin-Film Transistors

Kenjiro Fukuda and Shizuo Tokito

Abstract This chapter focuses on the printed organic thin-film transistors (TFT) and integrated circuits and introduces requirements for high-performance printed circuits, improvement of the electrical performances of printed TFT devices and circuits, and mechanical robustness of the printed circuits fabricated on ultrathin flexible substrates.

Keywords Organic thin-film transistor • Printed electronics • Flexible electronics • Integrated circuits • Ink-jet

6.1 Introduction

Printed electronics has garnered significant attention from research and industry because the pairing of conductive, insulating, and semiconducting materials with printing technologies enables one to make large-area electronic devices and systems [1, 2]. Organic semiconductors are particularly suitable for printed electronics because they can be processed in solution [3–5]. Furthermore, organic materials possess intrinsic mechanical flexibility based on relatively weak van der Waals bonding between organic molecules, and they make durable flexible organic devices feasible [6–8]. Several novel applications using organic thin-film transistor (TFT) devices or circuits have been developed for purposes such as flexible displays [9], RFID tags [10], and sensors [11, 12]. These devices have generally been fabricated using vacuum evaporation and photolithography; these mature processes are high resolution, repeatable, and uniform. Yet there are only a few reports on fully printed organic circuits or devices [4, 13, 14], and wide disparities exist between such printing technologies and conventional photolithography processes in resolution, electrical performance, and device yield. There is also a wide variability in these device parameters in comparison with devices made using photolithographic processes.

K. Fukuda (✉) • S. Tokito
Research Center for Organic Electronics (ROEL), Yamagata University, 4-3-16, Jonan, Yonezawa, Yamagata 992-8510, Japan
e-mail: fukuda@yz.yamagata-u.ac.jp; tokito@yz.yamagata-u.ac.jp

S. Ogawa (ed.), *Organic Electronics Materials and Devices*,
DOI 10.1007/978-4-431-55654-1_6

In this chapter, we review recent progress of fully printed organic TFTs and integrated circuits. The requirements for high-performance printed circuits are summarized in Sect. 6.2. A unique technique which controls cross-sectional profiles of printed materials is introduced in Sect. 6.3. How to improve the transistor performances is reviewed in Sect. 6.4, and the integrated circuits techniques are reviewed in Sect. 6.6. Section 6.6 introduces fully printed organic TFTs and circuits fabricated on ultrathin, which enables high mechanical robustness.

6.2 Requirements for Printed Integrated Circuits

6.2.1 Flat and Thin Electrodes

The most fundamental electronic element in integrated circuits is transistor. Thin-film transistors (TFTs) are the most common for the printed electronic circuits. A TFT consists of three kinds of electrodes (viz., gate, source, and drain), insulator, and semiconductor. As shown in Fig. 6.1, a TFT has stacked layers; therefore each layer requires thin thickness and uniform profiles. Especially, the thickness of bottom electrodes and insulators affects both the operation voltage and yield of TFT devices.

When printed ink dries on the surface of a substrate, the solute is generally transported from the center to the edge, and the resulting solute film forms a nonuniform ringlike profile. Deegan et al. studied this phenomenon, known as the "coffee ring effect," for colloidal suspension systems [15]. The nonuniform profile in the cross section for printed electrodes originating from this effect is the major issue to be solved for the devices with stacked layers such as capacitors and TFTs. The thicker edges of bottom electrodes interfere with the flatness and uniformity of overlying dielectric layers. As a result, fully solution-processed TFTs have difficulty operating at high voltages due to the potential for electrical shorts between the lower and upper electrodes [16, 17]. In order to achieve low operation voltage less than 10 V, the thickness of gate insulators should be less than 500 nm because the relative permittivity of printable gate-insulating materials is usually ranging from

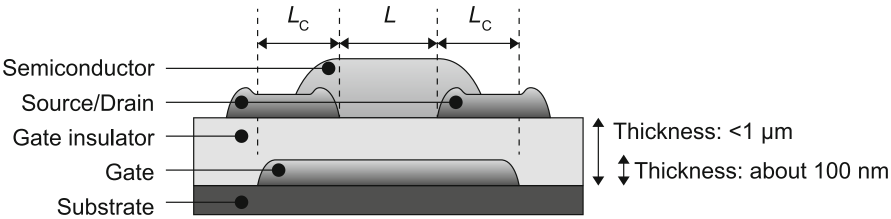

Fig. 6.1 Schematic illustration of an organic thin-film transistor. L means channel length and L_C means contact length

1 to 5. For this demand, thin (less than 100 nm) and uniform electrodes are required for electronic devices which have stacked layers.

6.2.2 Fast Operation

A cut-off frequency in saturation mode can be described by Eq. (6.1) [18]:

$$f_{\mathrm{T}} \sim \frac{\mu_{\mathrm{eff}}(V_{\mathrm{GS}} - V_{\mathrm{TH}})^2}{2\pi L(L + 2L_{\mathrm{C}})} \tag{6.1}$$

with the effective charge-carrier mobility μ_{eff}, the gate–source voltage V_{GS}, the threshold voltage V_{TH}, the channel length L, and the contact length L_{C}. Equation (6.1) clearly shows that the downscaling of channel length is the most important for improving the operation speed of the circuits.

We should also make consideration of the effect of contact resistance (R_{C}) as shown in Fig. 6.2. The total resistance (R_{total}) between a source electrode to a drain electrode through semiconducting layer is divided into channel resistance (R_{ch}) and R_{C}:

$$R_{\mathrm{total}} = R_{\mathrm{ch}} + R_{\mathrm{C}} \tag{6.2}$$

The existence of R_{C} causes the decrease of μ_{eff} from intrinsic mobility. μ_{eff} is calculated using Eq. (6.3):

$$\mu_{\mathrm{eff}} \approx \mu_0 \left[1 - \left(\frac{\mu_0 C_{\mathrm{i}} R_{\mathrm{C}} W |V_{\mathrm{GS}} - V_{\mathrm{TH}}|}{L + \mu_0 C_{\mathrm{i}} R_{\mathrm{C}} W |V_{\mathrm{GS}} - V_{\mathrm{TH}}|} \right)^2 \right] \tag{6.3}$$

with the intrinsic mobility μ_0, the gate-dielectric capacitance per unit area C_{i}, the channel width W, and threshold voltage V_{TH}. Limitations by contact resistance are becoming increasingly crucial when the channel length is reduced to about less than 10 µm [19], and finding ways to reduce these limitations has become a key issue for high-speed operation of printed organic TFTs and circuits as indicated by Eq. (6.1).

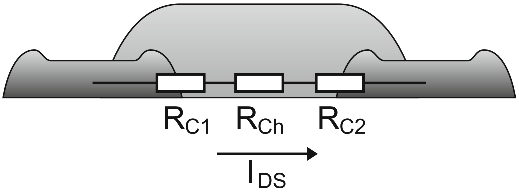

Fig. 6.2 Total resistance of the TFT. The total resistance (R_{total}) is divided into channel resistance (R_{ch}) and R_{C}. The R_{C} is divided into the resistance between source and semiconducting layer (R_{C1}) and drain and semiconducting layer (R_{C2})

6.3 Profile Control of Ink-Jet-Printed Silver Electrodes

To achieve thin (less than 1 μm) electrodes, low viscosity inks are favorable. Ink-jet print requires low viscosity (about 10 mN/m); therefore the ink-jet-printed electrodes are suitable for the use of TFTs. However, the low viscosity inks tend to cause the coffee ring effect. Okuzono et al. have proposed a simple model that predicts a final shape of a dried thin film [20]. According to the model, solvent evaporation rate (J_s) and diffusion coefficient (D) affect the final shape of the film. The smaller value J_s or the larger value D more readily induces a convex shape. This is because diffusion tends to homogenize the concentration field contrary to the outward flow. In order to control the final shape of printed silver electrodes, we focused on how to suppress the J_s of the silver nanoparticle ink. We used silver nanoparticles dispersed in a water-based solvent (DIC Corp., Japan, JAGLT). Both environmental temperature and humidity decide the J_s of water; therefore we controlled the drying conditions and assessed the dependencies of the ambient humidity and drying time on the profiles [21]. The silver nanoparticle ink was patterned with an ink-jet printer (Fujifilm Dimatix, DMP-2800) onto the cross-linked poly-4-vinylphenol (PVP) layers using a print head with 10-pl nozzles. After the printing, the substrates were stored in an environmental test chamber following the printing process (espec, SH-221) in order to evaporate the solvents from printed ink. Temperature in the chamber was held at 30 °C, and relative humidity was changed from 30 %RH to 90 %RH, while the storage time was fixed to 30 min. After the drying process, the substrates were heated at 140 °C for 1 h to sinter the silver nanoparticles.

Figures 6.3b shows line profiles (cross-sectional view) of printed silver electrodes dried at various humidity levels. The electrode profiles varied widely with the ambient humidity in the chamber. The cross-sectional profile for a line with ambient humidity of 30 %RH was concave. These nonuniformities in silver electrode thickness are a result of the "coffee ring" effect. The ratio of thickness between the edge and center of the profile (t_e/t_c) is 3.0. This concave shape was suppressed by increasing the ambient humidity from 30 %RH to 80 %RH ($t_e/t_c = 2.1$), such that a nearly trapezoidal shape was observed at an ambient humidity level of 85 %RH ($t_e/t_c = 1.3$). Furthermore, for ambient humidity levels of 90 %RH, the silver electrodes formed a convex shape ($t_e/t_c < 1$). These results clearly show that the silver electrode profiles were very sensitive to the ambient humidity levels during the drying process.

We also investigated how the flatness of the electrodes affected the functionality and performance of electronic devices with stacked layer constructions. Thin-film capacitors were fabricated. Two types of silver layers with different drying conditions were prepared as bottom electrodes: (1) 30 °C, 30 %RH for 30 min (concave) and (2) 30 °C, 85 %RH for 30 min (almost flat). After forming these electrodes, a solution of cross-linked PVP was spin coated and baked to form 210-nm-thick

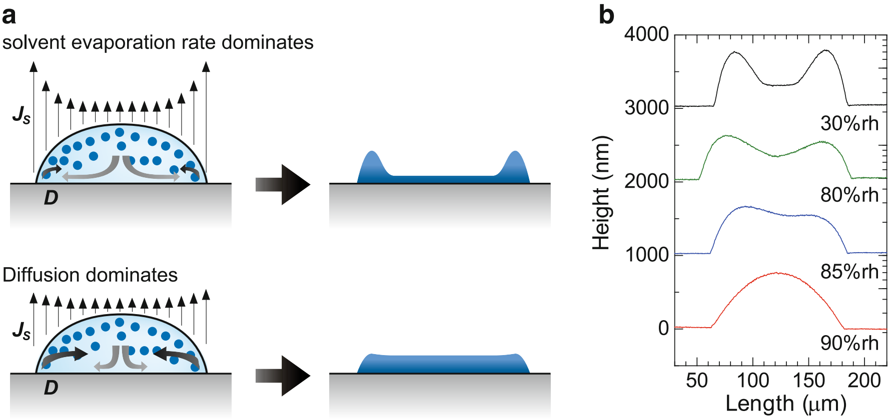

Fig. 6.3 Profile control of printed electrodes. (**a**) The correlation between the evaporation speed of the solvent and the final shape of the printed electrodes. When solvent evaporation rate (J_S) dominates, the final shape of the solute tends to be concave. On the other hand, when diffusion (*D*) dominates, convex shape can be obtained. (**b**) Controlling the shape of ink-jet-printed silver electrodes by changing the ambient humidity. Profiles of the electrodes with different drying humidity between 30 and 90 % RH. The profiles were obtained from laser microscopic images. The temperature of the chamber and drying time were 30 °C and 30 min (Adapted from Ref. [21]. Copyright 2013, American Chemical Society)

dielectric layers. Silver nanoparticle ink was then applied using ink-jet printing to form the upper source/drain electrodes. Figure 6.4a, b show histograms for the electrical breakdown voltage results of the fabricated capacitors with two different lower silver electrodes prepared at drying conditions of 30 °C, 30 %RH for 30 min (a) and 30 °C, 85 %RH for 30 min (b). The capacitors with concave-shaped electrodes did not have sufficient insulating properties; 37 % of the capacitors exhibited the breakdown voltages of less than 5 V, as shown in Fig. 6.4a, which indicates that the upper and lower electrodes had shorted. The peaks of the lower electrodes pose nonuniformity of the dielectric layers and/or the increase of the electric field at the edge of the lower electrodes, which causes the shorted capacitors. On the other hand, no capacitor electrodes shorted when the shaped electrodes were used for the lower electrodes. Additionally, the average breakdown voltage improved from 33 to 52 V by using trapezoidal-shaped electrodes. A breakdown voltage of 52 V corresponds to 2.54 MV/cm in electric field strength, which was comparable to that for cross-linked PVP used as dielectric layers and evaporated metal used as lower gate electrodes [22].

The methods for controlling the shape of printed electrodes can increase freedom in printing conditions and could help in the practical realization of printed electronics.

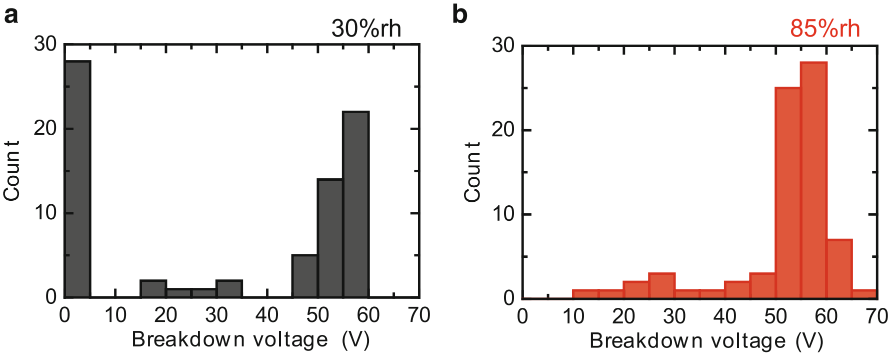

Fig. 6.4 Breakdown voltage histograms for the fabricated capacitors with different drying conditions, at 30 °C, 30 % RH for 30 min (**a**) and at 30 °C, 85 % RH for 30 min (**b**). The total number of counts was 75 for each condition (Adapted from Ref. [21]. Copyright 2013, American Chemical Society)

6.4 Improvement of Field-Effect Mobility for Printed Organic TFTs

As shown in Eq. (6.1), not the intrinsic mobility but the effective mobility of semiconducting layer decides the operation speed of the integrated circuits. This requires that both R_{ch} and R_{C} should be decreased for the printed organic TFTs. As several previous reports show, the R_{C} is decreased when the energy barrier between the work function of source/drain electrodes and highest occupied molecular orbital (HOMO) level of p-type organic semiconducting layer is suppressed by the carrier injection layer. For printed electrodes, self-assembled monolayer (SAM) can change the work function of the electrodes, which causes the reduction of energy barrier between source/drain electrodes and semiconducting layer. Figure 6.5a shows how the work function of printed silver electrodes is changed by the SAM layer. The SAM layer changed the work function of the printed silver electrodes from 4.7 eV to 5.3 eV. We also revealed how the SAM treatment affected the transistor characteristics [23]. A mesitylene-based formulation of a soluble small-molecule material with a deep ionization potential of 5.4 eV was used as organic semiconducting layer (Merck, lisicon® S1200) [24]. Figure 6.5b shows the transfer characteristics of the fabricated TFTs, having the same W/L ratio of 50, with and without applying a SAM treatment to the source–drain electrodes. The SAM modification process improved the transistor electrical characteristics dramatically, whereby on-current increased from 1.6 to 27 μA, and the estimated mobility in saturation regime increased from 0.02 to 0.9 $\mathrm{cm^2\ V^{-1}\ s^{-1}}$. We also observed the crystallinity of semiconducting layer between source/drain electrodes with a polarization microscope, as shown in Fig. 6.5c. Both devices had nearly same crystalline domains, even though there were large differences in mobility between the devices with the SAM treatment and those without it. These results indicate that the SAM

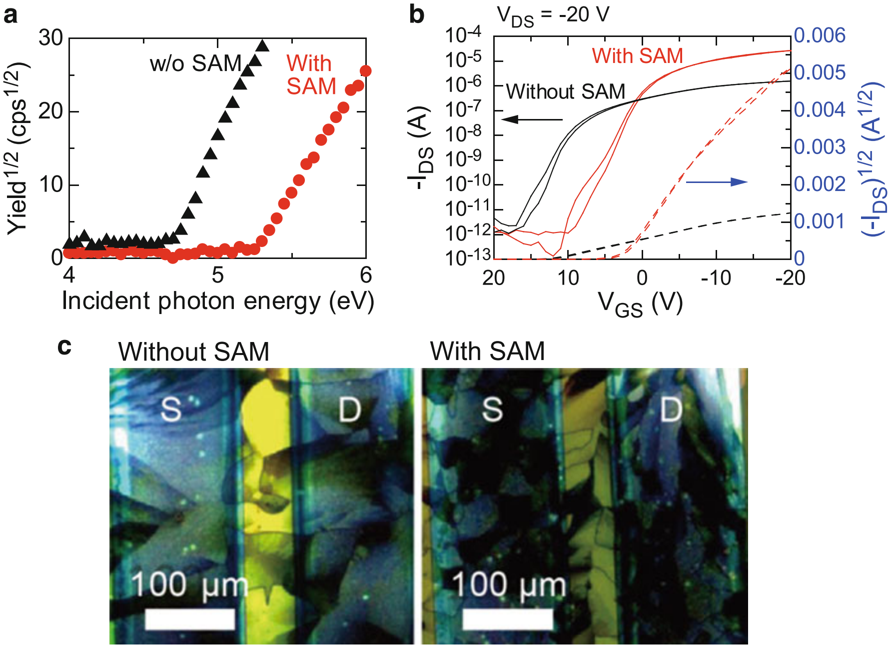

Fig. 6.5 Effect of source–drain electrode modification by SAM treatment on transistor characteristics. (**a**) Square root of the yield as a function of incident photon energy from photoemission spectroscopy. The *black dots* represent the untreated electrodes, and the red dots represent the treated electrodes. (**b**) Transfer characteristics of fabricated TFTs. The *black lines* represent the transfer curve for the device without the SAM treatment, and the red lines those with the SAM treatment. The SAM modification process improved the transistor electrical characteristics dramatically, whereby on-current increased from 1.6 mA to 27 mA and the estimated mobility in saturation regime increased from 0.02 to 0.9 cm^2 V^{-1} s^{-1}. (**c**) Polarization microscope images of channel region of fabricated TFTs with untreated and with treated electrodes. A mesitylene-based formulation of a soluble small-molecule organic semiconducting layer (Merck, lisicon® S1200) with a deep ionization potential of 5.4 eV was used as organic semiconducting layer (Adapted from Ref. [23]. Copyright 2014, Nature Publishing Group)

modification layer reduces only the R_C of the printed TFTs, which cause dramatic improvement of the transistor characteristics.

We estimated the R_C of the fabricated TFT devices using a transfer-line method. Figure 6.6a plots the channel width-normalized total on-resistance (R_{Total}) as a function of channel length. R_C was obtained by extrapolating the linear fit to a channel length of zero and plotted as a function of gate–source voltage (V_{GS}) (Fig. 6.6b). R_C decreases with increasing gate–source voltage, likely due to an increase in carrier density in the channel and near the contacts. R_C decreased to a value as low as 1.83 kΩcm, a remarkably low contact resistance value for fully solution-processed organic TFT devices, which is attributed to there being a low energy barrier between the printed organic semiconducting layer and source/drain electrodes.

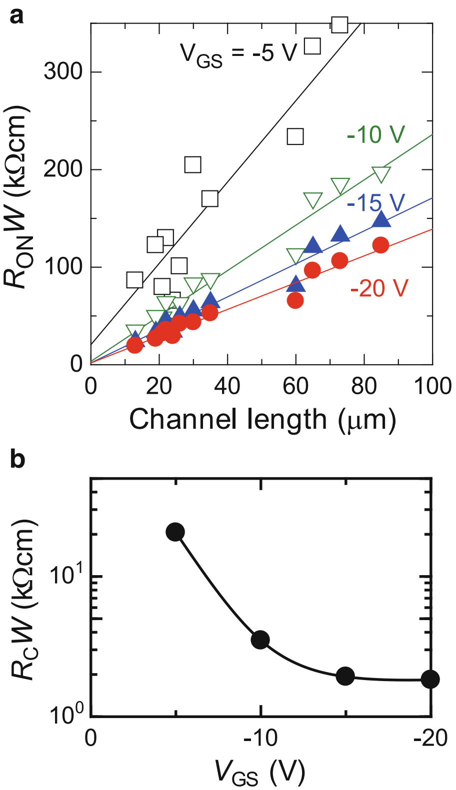

Fig. 6.6 Estimation of contact resistance. The contact resistance of the TFT devices with treated source–drain electrodes was estimated by using the transfer-line method. (**a**) Channel width-normalized total on-resistance (R_{Total}) as a function of channel length measured at VGS = −5 V (*open square*), −10 V (*open reverse triangle*), −15 V (*solid triangle*), and −20 V (*solid circle*). (**b**) Width-normalized contact resistance as a function of gate–source voltage (V_{GS}) (Adapted from Ref. [23]. Copyright 2014, Nature Publishing Group)

6.5 Application for Fully Printed Organic Integrated Circuits

Conventional organic CMOS circuits consist of both p- and n-type organic transistors. Although soluble n-type semiconductor materials have been developed in recent years [25], their performance in OTFT devices remains lower than those of p-type semiconductor materials. As a result, operation speed of the conventional CMOS circuits is determined by response of n-type organic transistors. In order to solve the problem, pseudo-CMOS logic design was suggested by Huang et al. [26]. - Pseudo-CMOS inverters comprise four p-channel organic TFTs as shown in Fig. 6.7. Excellent input–output characteristics with high gain and fast speed were reported using pseudo-CMOS logic design [27, 28]. We fabricated fully printed pseudo-CMOS integrated circuits and demonstrated good static and dynamic characteristics.

Figure 6.8 shows input–output characteristics of a fabricated fully printed diode load inverter (Fig. 6.8a) and pseudo-CMOS inverter (Fig. 6.8b) [23, 29]. The diode-load inverter exhibited low gain and small static-noise margin. On the other hand, the pseudo-CMOS inverter exhibited much better characteristics. The inverter was

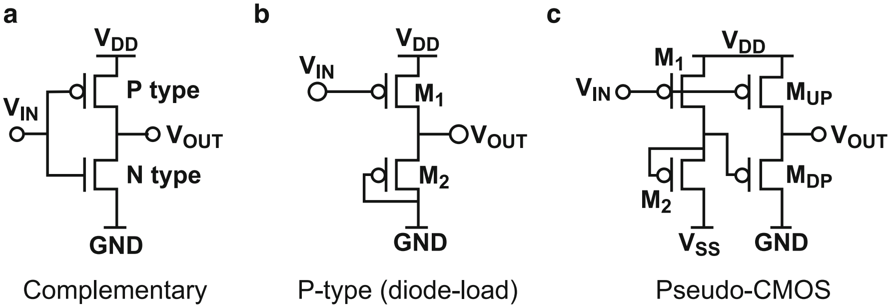

Fig. 6.7 Circuit diagrams of inverter. (**a**) Complementary, (**b**) p-type (diode-load), (**c**) pseudo-CMOS

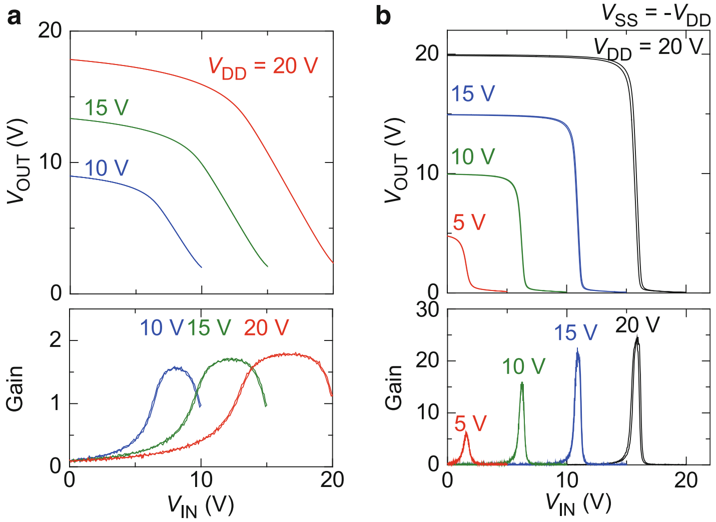

Fig. 6.8 (**a**) Static characteristics of fully printed diode-load inverter. Output voltage and signal gain as functions of driving voltage, (**b**) static characteristics of fully printed pseudo-CMOS inverter. Output voltage and signal gain as functions of driving voltage (V_{DD}) with $VSS = -VDD$. The pseudo-CMOS inverter functioned well with relatively high signal gain, even at small operating voltages of 5 V (Adapted from Ref. [23]. Copyright 2014, Nature Publishing Group)

operated successfully at small operation voltage (5 V). Table 6.1 summarizes signal gains of fully printed inverter circuits at each operating voltage *VDD*. The gain was 24 at an operation voltage of 20 V, which was 14 times larger than that of diode-load inverter. These static results clearly show that the fully printed pseudo-CMOS circuits can be comparable with conventional CMOS integrated circuits.

In order to demonstrate the applicability of our fully printed pseudo-CMOS circuits to a logic circuit, we fabricated RS flip-flop (FF) [30]. The fabricated RS-FF comprises two pseudo-NAND circuits (Fig. 6.9a). A block diagram and a truth table

Table 6.1 Summary of signal gain for the fully printed inverter circuits at each operating voltage *VDD*

Operation voltage (*V*)	Gain of diode-load inverter	Gain of pseudo-CMOS inverter
20	−2.9	−24
15	−1.9	−23
10	−1.1	−16
5	–	−6.1

of the RS-FF is shown in Fig. 6.9b. Figure 6.9c shows a photograph of a fabricated RS-FF. The RS-FF comprises 12 transistors. Figure 6.9d shows input–output characteristics of the NAND circuits when input-voltage V_{inA} was changed from 0 to 15 V at supply voltages of 15 V and tuning voltage $V_{\mathrm{SS}} = -V_{\mathrm{DD}}$. The NAND was operated successfully as the truth table; when the V_{inB} was fixed at 15 V, the fabricated NAND device exhibited good switching characteristics with a signal gain 23 at a trip point of $V_{\mathrm{inA}} = 7.24$ V, while the $\mathrm{V_{inA}}$ remained high voltage when the V_{inB} was fixed at 0 V. As shown in Fig. 6.9e, the RS flip-flop circuit exhibited switching characteristics in accordance with truth table at operating voltage of 10 V. The output (*Q*) of the fabricated RS flip-flop changed its state at the fall edge of the input signal (–set or –reset), and the rise of both –set and –reset signals did not affect *Q* value. We also evaluated the delay time of the RS-FF circuit. The delay time is the sum of rise and fall times, which are defined as the time difference between 10 and 90 % of the output signal for transient changes in the circuit input from a logically low to high level (rise time) and high to low level (fall time). A measured total delay time of the RS flip-flop was 6.4 ms at 10 V, which was quite fast speed among the fully printed integrated circuits.

6.6 Ultra-Flexible, Large-Area Circuits

Thin, ultra-flexible devices that can be manufactured in a process that covers a large area will be essential to realizing low-cost, wearable electronic applications including foldable displays and medical sensors. The evolution from rigid, heavy, and thick electronics to new flexible electronics has reached the point whereby electronics can be attached to curved and moving surfaces such as the skin of the human body without any concern to the wearer [31, 32]. Achieving flexible organic electronics based on organic TFT devices fabricated with fully printed processes will be essential for realizing wearable electronic applications that are low in cost and environmentally friendly. For this demand, we fabricated organic TFT devices with excellent electrical characteristics and mechanical stability that were fully printed on ultra-flexible polymer films [33].

Our devices were fabricated entirely by printing, enabling them to be easily fabricated on a large scale (Fig. 6.10a). The polychloro-p-xylylene (parylene-C) films with thickness of only 1 μm were used as base substrates. The parylene-C

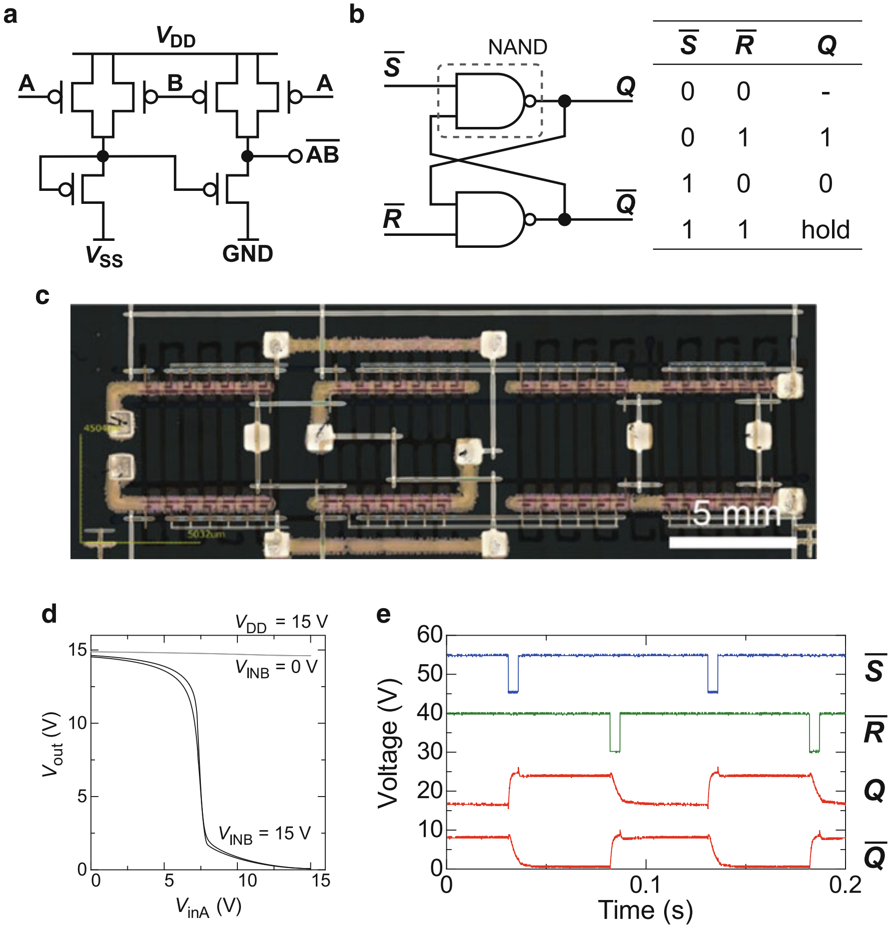

Fig. 6.9 Fully printed RS flip-flop circuit. (**a**) Circuit diagram of a pseudo-CMOS NAND circuit. (**b**) Block diagram and the truth table of the RS flip-flop circuit. (**c**) An optical image of the fabricated pseudo-CMOS NAND-based RS flip-flop circuit. (**d**) Input–output characteristics of the pseudo-NAND circuit. (**e**) The input–output characteristics of fabricated RS flip-flop circuit at a supply voltage (V_{DD}) of 10 V. (Adapted from Ref. [30]. Copyright 2014, The Japan Society of Applied Physics)

films were formed by chemical vapor deposition onto the supporting glass plates with release layer (fluoropolymer layer). The parylene-C films are attached to a release layer with weak adhesive strength (13 mN) so that the fabricated devices can be safely peeled off the supporting plates. The fabricated organic devices are extremely thin and ultra-flexible; their total thickness is less than 2 μm and total weight is only 2 g m^{-2}. Figure 6.10b illustrates their potential in health care and monitoring applications; they can be gently attached to the skin or wrapped around limbs without the wearer perceiving any discomfort. They can be bent or even

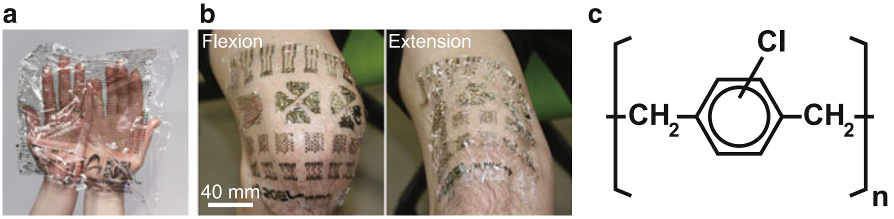

Fig. 6.10 Fully printed organic circuits fabricated on ultrathin substrate. (**a**) A photograph of organic TFT devices on 1-mm-thick parylene-C films. (**b**) Organic device films conforming to a human knee. Our devices were fabricated entirely by printing, enabling them to be easily fabricated on a large scale, which can cover whole area of a human skin as shown in (**b**). (**c**) The chemical structure of parylene-C (Adapted from Ref. [33]. Copyright 2014, Nature Publishing Group)

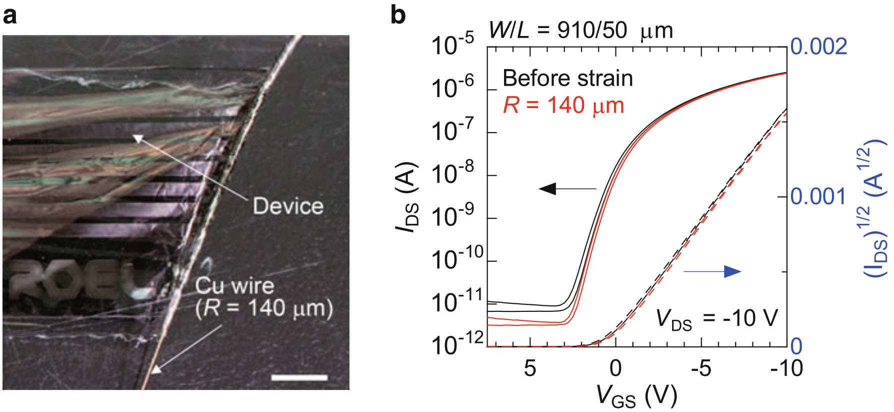

Fig. 6.11 (**a**) Photograph of a fully printed organic TFT devices on 1-mm-thick parylene-C films wrapped around a copper wire with a radius of 140 mm. Scale bar, 5 mm. (**b**) The transfer characteristics of the TFT devices were measured in the bent and unbent states, with no discernible changes in the characteristics due to bending (Adapted from Ref. [33]. Copyright 2014, Nature Publishing Group)

wrinkled so that they conform to the movements of the human body, which has uneven surfaces and a large range of motion.

The fabricated devices exhibited remarkable mechanical stability. Figure 6.11 shows a photograph of a fabricated TFT device tightly wrapped around a copper wire with bending radius of 140 μm. The transfer characteristics were measured in ambient air with and without strain due to bending, as shown in Fig. 6.11, such that there was no discernible change in the electrical characteristics during the bending. The change in the on-current was 3.9 %, and the change in the mobility was 1.6 % with bending and the on/off ratio remained more than 10^5. The ultrathin film

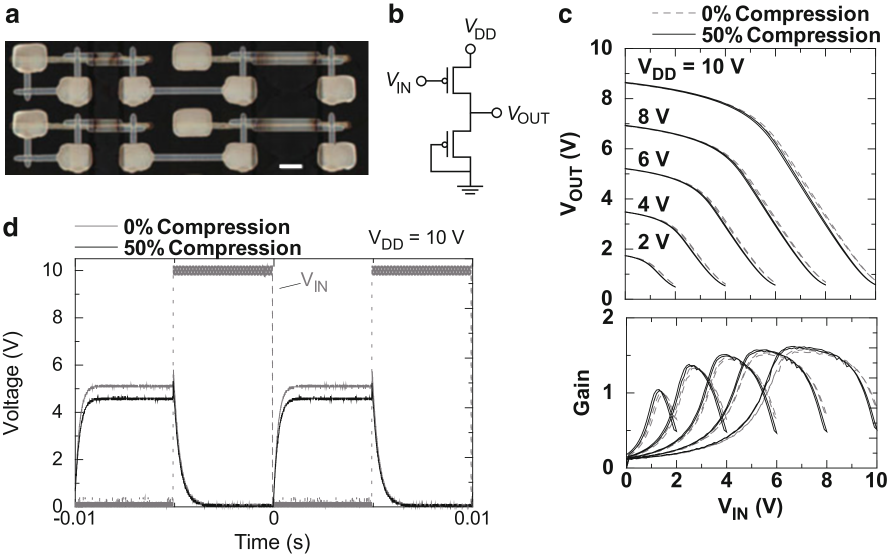

Fig. 6.12 Fast operating of printed organic circuits. (**a**) Photograph of fabricated unipolar organic diode-load inverter circuits. *Scale bar*, 1 mm. (**b**) Circuit diagram of the inverter device. (**c**) Static transfer characteristics of the inverter and small-signal gain as a function of input voltage (V_{IN}). The *black solid line* indicates the characteristics without strain, and the *red solid lines* indicate those of circuits under 50 % compressive strain. (**c**) Dynamic operation of the inverter circuit. A continuous driving voltage (V_{DD}) of 10 V and an AC input voltage with a 100-Hz rectangular waveform from 0 to 10 V (*gray*) were applied to the inverter, and the output voltage was monitored using a digital oscilloscope. The *blue line* indicates the output voltage without strain, and the *red line* indicates the output voltage under 50 % compressive strain (Adapted from Ref. [33]. Copyright 2014, Nature Publishing Group)

substrates help reduce the applied strain in the TFT devices, whereby the calculated strain was roughly 0.5 % or less, even when the devices were bent to a radius of 140 μm [34, 35]. As several research groups have already reported, such a small degree of strain does not significantly change the electrical performance of organic TFT devices [36].

We also evaluated the mechanical stability of unipolar diode-load inverters fabricated on thin parylene-C films. Figure 6.12a shows a photograph of the inverter circuit, and Fig. 6.12b shows a circuit diagram for the inverter. The ratio between the drive and load transistors is 2.6:1. Both transistors had channel lengths of 20 μm. Figure 6.12c plots static transfer characteristics measured in ambient air of a diode-load inverter under no compressive strain and under 50 % compressive strain. The output voltage (V_{OUT}) and small-signal gain were plotted as a function of input voltage (V_{IN}). There was no significant change in the electrical characteristics during bending, and the inverter functioned properly even at a driving voltage (V_{DD}) of 2 V. The trip point when the inverter was not under compression was 5.92 V at $V_{DD} = 10$ V and 0.95 V at $V_{DD} = 2$ V. The small-signal gain of the inverter without compression was 1.57 at $V_{DD} = 10$ V and 0.97 at $V_{DD} = 2$ V. The trip point of the inverter under 50 % compressive strain was 5.84 V at $V_{DD} = 10$ V and 0.92 V at $V_{DD} = 2$ V. The small-signal gain of the inverter under 50 % compression was 1.61 at $V_{DD} = 10$ V and 1.00 at $V_{DD} = 2$ V. The changes in the trip point and gain in the case of 50 % compressive strain were only less than 5 % of their values in the case of no compressive strain. Figure 6.12d shows the dynamic response of the inverter circuit. We applied a continuous V_{DD} of 10 V and an AC input voltage with 100-Hz rectangular waveform ranging from 0 to 10 V to the inverter and monitored the output voltage using a digital oscilloscope. The measured rise and fall time in the case of no compression was 427 and 691 μs, which corresponds to a total delay time of 1.12 ms. This delay is quite short for fully printed organic circuits [37, 38]. The operating speeds remained stable even when compressive strain was applied to the films and the circuits crumpled. The measured rise and fall time of the inverter under 50 % compressive strain was 495 and 705 μs, which corresponds to a total delay of 1.20 ms and only a 7 % change from the initial total delay. These results exemplify the outstanding mechanical stability of fast-operating printed organic circuits fabricated on thin films.

6.7 Conclusion

The chapter mainly focuses on the ink-jet-printed organic TFTs and circuits. In order to achieve fast operating speed for fully printed circuits, novel printing technologies which enable high-resolution patterning beyond the ability of ink-jet printing are required. Such new technologies will improve both integration and operating speed of the printed circuits. Developments of printable semiconducting layer are also important for the high-performance circuits. Development of printable n-type semiconducting materials enables conventional CMOS circuits. The large-area fabrication of the fully printed circuits demonstrated in this chapter will enable thin, lightweight, and low-cost electronic devices and systems which further illustrates the potential to these devices in novel electronic applications, such as large-area sensors.

References

1. J. Perelaer, P.J. Smith, D. Mager, D. Soltman, S.K. Volkman, V. Subramanian, J.G. Korvink, U.S. Schubert, J. Mater. Chem. **20**, 8446–8453 (2010)
2. B. Ahn, E.B. Duoss, M.J. Motala, X. Guo, S.I. Park, Y. Xiong, J. Yoon, R.G. Nuzzo, J.A. Rogers, J.A. Lewis, Science **323**, 1590–1593 (2009)
3. H. Yan, Z. Chen, Y. Zheng, C. Newman, J.R. Quinn, F. Dötz, M. Kastler, A. Facchetti, Nature **457**, 679–686 (2009)
4. E. Gili, M. Caironi, H. Sirringhaus, Appl. Phys. Lett. **100**, 123303 (2012)
5. H. Kang, R. Kitsomboonloha, J. Jang, V. Subramanian, Adv. Mater. **24**, 3065–3069 (2012)
6. T. Sekitani, U. Zschieschang, H. Klauk, T. Someya, Nat. Mater. **9**, 1015–1022 (2010)

7. H.T. Yi, M.M. Payne, J.E. Anthony, V. Podzorov, Nat. Commun. **3**, 1259 (2012)
8. M. Kaltenbrunner, M.S. White, E.D. Głowacki, T. Sekitani, T. Someya, N.S. Sariciftci, S. Bauer, Nat. Commun. **3**, 770 (2012)
9. M. Noda, N. Kobayashi, M. Katsuhara, A. Yumoto, S. Ushikura, R. Yasuda, N. Hirai, G. Yukawa, I. Yagi, K. Nomoto, T. Urabe, J. Soc, Inf. Display **19**, 316–322 (2011)
10. K. Myny, S. Steudel, S. Smout, P. Vicca, F. Furthner, B. van der Putten, A.K. Tripathi, G.H. Gelinck, J. Genoe, W. Dehaene, P. Heremans, Org. Electron. **11**, 1176–1179 (2010)
11. T. Someya, Y. Kato, T. Sekitani, S. Iba, Y. Noguchi, Y. Murase, H. Kawaguch, T. Sakurai, Proc. Natl. Acad. Sci. U. S. A. **102**, 12321–12325 (2005)
12. Y. Kato, T. Sekitani, Y. Noguchi, T. Yokota, M. Takamiya, T. Sakurai, T. Someya, IEEE Trans. Electron Devices **57**, 995–1002 (2010)
13. H.-Y. Tseng, B. Purushothaman, J. Anthony, V. Subramanian, Org. Electron. **12**, 1120–1125 (2011)
14. D.E. Schwartz, T.N. Ng, IEEE Electron. Device Lett. **34**, 271–273 (2013)
15. R.D. Deegan, O. Bakajin, T.F. Dupont, G. Huber, S.R. Nagel, T.A. Witten, Nature **389**, 827–829 (1997)
16. S. Chung, S.O. Kim, S.K. Kwon, C. Lee, Y. Hong, IEEE Electron Device Lett. **32**, 1134–1136 (2011)
17. M. Hambsch, K. Reuter, M. Stanel, G. Schmidt, H. Kempa, U. Fügmann, U. Hahn, A.C. Hübler, Mater. Sci. Eng. B **170**, 93–98 (2010)
18. H. Klauk, Chem. Soc. Rev. **39**, 2643–2666 (2010)
19. F. Ante, D. Kälblein, T. Zaki, U. Zschieschang, K. Takimiya, M. Ikeda, T. Sekitani, T. Someya, J.N. Burghartz, K. Kern, H. Klauk, Small **8**, 73–79 (2012)
20. T. Okuzono, M. Kobayashi, M. Doi, Phys, Rev. E **80**, 021603 (2009)
21. K. Fukuda, T. Sekine, D. Kumaki, S. Tokito, ACS Appl. Mater. Interfaces **5**, 3916–3920 (2013)
22. M.-H. Yoon, H. Yan, A. Facchetti, T.J. Marks, J. Am, Chem. Soc. **127**, 10388–10395 (2005)
23. K. Fukuda, Y. Takeda, M. Mizukami, D. Kumaki, S. Tokito, Sci. Rep. **4**, 3947 (2014)
24. G. Lloyd, T. Backlund, P. Brookes, L.W. Tan, P. Wierzchowiec, J.Y. Lee, S. Bain, M. James, J. Canisius, S. Tierney, K. Kawamata, T. Wakimoto, Proc. IDW **10**, 469 (2010)
25. S. Chen, Y. Zhao, A. Bolag, J. Nishida, Y. Liu, Y. Yamashita, ACS Appl. Mater. Interfaces **4**, 3994–4000 (2012)
26. T.C. Huang, K. Fukuda, C.M. Lo, Y.H. Yeh, T. Sekitani, T. Someya, K.T. Cheng, IEEE Trans. Electron Devices **58**, 141–150 (2011)
27. K. Fukuda, T. Sekitani, T. Yokota, K. Kuribara, T.C. Huang, T. Sakurai, U. Zschieschang, H. Klauk, M. Ikeda, H. Kuwabara, T. Yamamoto, K. Takimiya, K.T. Cheng, T. Someya, IEEE Electron Device Lett. **32**, 1448–1450 (2011)
28. T. Yokota, T. Sekitani, T. Tokuhara, N. Take, U. Zschieschang, H. Klauk, K. Takimiya, T.C. Huang, M. Takamiya, T. Sakurai, T. Someya, IEEE Trans. Electron Devices **59**, 3434–3441 (2012)
29. Y. Takeda, Y. Yoshimura, Y. Kobayashi, D. Kumaki, K. Fukuda, S. Tokito, Org. Electron. **14**, 3362–3370 (2013)
30. Y. Takeda, Y. Yoshimura, F. Adi Ezarudin Bin Adib, D. Kumaki, K. Fukuda, S. Tokito, Jpn. J. Appl. Phys. **54**, 04DK03 (2015)
31. M. Kaltenbrunner, T. Sekitani, J. Reeder, T. Yokota, K. Kuribara, T. Tokuhara, M. Drack, R. Schwödiauer, I. Graz, S. Bauer-Gogonea, S. Bauer, T. Someya, Nature **499**, 458–463 (2013)
32. D.H. Kim, N. Lu, R. Ma, Y.S. Kim, R.H. Kim, S. Wang, J. Wu, S.M. Won, H. Tao, A. Islam, K.J. Yu, T. Kim, R. Chowdhury, M. Ying, L. Xu, M. Li, H.J. Chung, H. Keum, M. McCormick, P. Liu, Y.W. Zhang, F.G. Omenetto, Y. Huang, T. Coleman, J.A. Rogers, Science **333**, 838–843 (2011)
33. K. Fukuda, Y. Takeda, Y. Yoshimura, R. Shiwaku, L.T. Tran, T. Sekine, M. Mizukami, D. Kumaki, S. Tokito, Nat Commun. **5**, 4147 (2014)
34. H. Gleskova, S. Wagner, W. Soboyejo, Z. Suo, J. Appl. Phys. **92**, 6224–6229 (2002)

35. T. Sekitani, Y. Kato, S. Iba, H. Shinaoka, T. Someya, T. Sakurai, S. Takagi, Appl. Phys. Lett. **86**, 073511 (2005)
36. P. Cosseddu, G. Tiddia, S. Milita, A. Bonfiglio, Org. Electron. **14**, 206–211 (2013)
37. M. Hambsch, K. Reuter, H. Kempa, A.C. Hübler, Org. Electron. **13**, 1989–1995 (2012)
38. K. Suzuki, K. Yutani, M. Nakashima, A. Onodera, S. Mizukami, M. Kato, T. Tano, H. Tomono, M. Yanagisawa, K. Kameyama, Proc. IDW **09**, 1581–1584 (2009)

Chapter 7
Functional Nanomaterial Devices

Jiang Pu and Taishi Takenobu

Abstract Nanomaterials, such as single-walled carbon nanotubes (SWCNTs) and transition metal dichalcogenide (TMDC) monolayers, are intrinsically flexible and stretchable because of their nanoscale thicknesses. Therefore, nanomaterials can be used as high-performance thin-film transistors and are possible candidates for next-generation flexible/stretchable electronics. Here, we focus on the recent development in fabricating nanomaterial-based transistors. The reported virtues and novelties of SWCNTs and TMDCs provide significant advantages for developing printed electronics that are flexible and stretchable.

Keywords Carbon nanotubes • Two-dimensional materials • Transition metal dichalcogenide monolayers • Thin-film transistors

7.1 Overview

Printed flexible and stretchable electronics have attracted considerable attention as next-generation functional electronics, as rigid substrates for electronic assemblies will ultimately be replaced by mechanically flexible or even stretchable alternatives. This trend is a consequence of the “ambient intelligence vision” in which electronic systems can be carried on or within the body. These systems must be lightweight, assume the shape of the object in which they are integrated, and follow all complex movements of these objects, resulting in the need for stretchability. These requirements necessitate the identification of suitable materials for printed, flexible, and/or stretchable electronics.

As shown in Fig. 7.1, induced strain under bending is a function of the thickness of a material, t, and the curvature of deformation radius, R. Therefore, if material flexibility is necessary to allow deformation to a given R, the induced strain is simply proportional to t. Hence, thinner materials are potentially better for printed flexible and stretchable electronics. Based on this idea, nanomaterials, such as

---

J. Pu • T. Takenobu (✉)
Department of Advanced Science and Engineering, Waseda University, 3-4-1 Ohkubo,
Tokyo 169-8555, Japan
e-mail: takenobu@waseda.jp

S. Ogawa (ed.), *Organic Electronics Materials and Devices*,
DOI 10.1007/978-4-431-55654-1_7

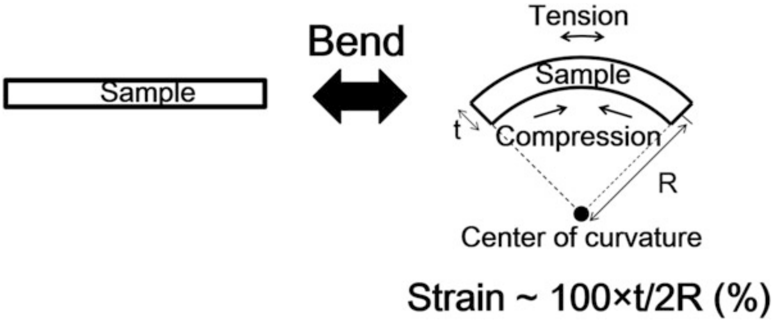

Fig. 7.1 A schematic representation of induced strain in flexible electronics

single-walled carbon nanotubes (SWCNTs) and transition metal dichalcogenide (TMDC) monolayers, are possible candidates for next-generation electronics.

7.2 Single-Walled Carbon Nanotubes (SWCNTs)

Research on SWCNTs initially focused on the use of individual or parallel arrays of nanotubes as a channel material for ultra-scaled nanoelectronic devices. However, in recent years, large-area deposition of SWCNT networks has been actively explored for high-performance thin-film transistors (TFTs). In this section, the progress of SWCNT TFTs, including material preparation, device fabrication techniques, and transistor performance control, is reviewed. State-of-the-art fabrication techniques for SWCNT TFTs are divided into two categories, chemical vapor deposition and solution-based techniques, and possible scale-up approaches for achieving the realistic production of flexible transistors are discussed.

7.2.1 Introduction

SWCNTs are graphene sheets that are rolled into seamless, hollow cylinders. Because of their nm-scale diameter (approximately 1–10 nm) and unique electronic properties, SWCNT holds big possibilities for a wide range of applications in electronic devices, and SWCNT is a promising candidate for next-generation beyond-silicon electronics. SWCNTs are categorized using their chiral vectors. The chiral vector is defined on the hexagonal crystal lattice by two integers (m and n), and it corresponds to the direction along which a monolayer graphene sheet is rolled. SWCNT's electronic properties strongly depend on their chiral vectors, and they are metallic when m–n is a multiple of 3 or $m = n$. In all other cases, they are semiconducting [1–4]. Thus, from the possible (n, m) values, two-thirds of nanotubes are semiconducting, and the other one-third are metallic.

Semiconducting nanotubes are commonly used as the active channel material of electronic devices. The advantages of semiconducting nanotubes over other conventional semiconducting materials are multifold. (1) In carbon nanotubes, the charge carriers possess long, mean free paths, on the order of a few 100 nm for the acoustic phonon-scattering mechanism. Therefore, in low electric fields, scatter-free ballistic transport of carriers can be realized in carbon nanotubes with moderate active channel lengths (e.g., sub-100 nm) [5]. (2) The carrier mobility of semiconducting SWCNTs has been experimentally investigated to be $>10{,}000\ \mathrm{cm}^2/(\mathrm{V}\cdot\mathrm{s})$ [1, 6, 7] at room temperature, which is much higher than the carrier mobility of recent silicon FETs. (3) The nm-scale diameters of semiconducting SWCNTs enable great electrostatics with excellent gate control of the transistor channel for extremely miniaturized devices. Therefore, nanotubes have stimulated enormous interest in both fundamental and practical researches in nano- and macroelectronics.

7.2.2 Individual Carbon Nanotubes and Nanotube Thin Films

Researchers have demonstrated excellent FETs [5, 8–12] and integrated logic circuits [13–17] using individual nanotubes. Despite the tremendous progress made with individual SWCNT FETs and logic circuits, major technological challenges remain, including the requirement for the deterministic assembly of SWCNTs on a handling substrate with nm-scale accuracy, minimal device-to-device performance variation, and the development of a fabrication procedure that is scalable and compatible with industry standards. The use of SWCNTs for nanoelectronic applications is, therefore, far from being realized. In contrast, nanotube network use, especially those based on semiconducting-nanotube-enriched samples, presents a highly promising path for the generation of thin-film transistors for macro-, flexible, stretchable electronics. The most important advantages obtained by the use of nanotube random networks for thin-film transistors lie in the fact that nanotube thin films are mechanically flexible and optically transparent and can be prepared using solution-based process at room temperature; none of these features can be provided by amorphous or poly-Si technologies [18–20]. Compared with organic semiconductor devices [21–25], a competing platform for flexible and stretchable thin-film transistors, nanotube random networks offer extremely higher carrier mobility (~2 orders of magnitude higher than that of organic semiconductors). Large-area TFT applications, as the results, may offer an ideal niche for SWCNT-based electronics due to their superb physical and chemical properties and their freedom from the precise assembly limitations down to the nm scale.

7.2.3 Chemical Vapor Deposition Growth of Nanotube TFTs

Numerous research efforts have been devoted to the successful realization of large-scale chemical vapor deposition (CVD) growth of high-density, horizontally aligned carbon nanotubes on single crystal quartz or sapphire substrates [26–34]. In CVD growth, a substrate with catalyst particles is placed in a furnace (generally at temperatures more than 800 °C) with a supply of carbon feedstock gas and hydrogen gas, and the nanotubes are then grown directly on the substrates. The main advantage of CVD-grown nanotubes is that they show superior electrical properties compared to nanotubes grown by other methods. Reports have suggested that some of the highest carrier mobilities for single-nanotube FETs ($>10{,}000\ \mathrm{cm}^2/(\mathrm{V}\cdot\mathrm{s})$ [1, 6, 7]) have been obtained using CVD-grown nanotubes. The high performance of CVD-produced nanotubes arises from their long length (from tens to hundreds micrometers) and their lack of bundles. These properties are advantageous for obtaining high-performance thin-film transistors, as inter-tube junctions and bundles have been indicated to significantly increase the resistance of nanotube films.

Transferring techniques have been developed to enable the demonstration of high-performance FETs and integrated circuits using aligned SWCNTs on various types of rigid and flexible substrates [35–42]. However, as roughly one-third of the as-grown nanotubes are metallic, techniques such as electrical breakdown [43] are necessary to remove leakage-causing metallic paths, a treatment that adds complexity, is not scalable, and significantly degrades device performance due to the high fields applied during the treatment. Recently, preferential growth of aligned semiconductor nanotubes was reported [32, 44, 45], which is an important step forward; however, the purity is not yet high enough to achieve TFTs with a high on/off current ratio ($I_{\mathrm{on}}/I_{\mathrm{off}}$) for digital applications. To obtain devices with a better on/off current ratio, having networks of nanotubes with a higher percentage of semiconductor SWCNTs and/or with a random orientation in which individual SWCNTs do not directly bridge the source/drain electrodes is preferred, thereby minimizing the metallic path [46–50].

CVD-grown, random SWCNT networks have also been widely investigated for thin-film transistors, and medium-scale flexible integrated circuits were demonstrated by Rogers et al. [51, 52]. For this method, metal catalysts are typically deposited over the entire substrate using either evaporation or spin-coating methods, followed by CVD growth with hydrocarbon precursors, such as methane, ethylene, ethanol, or methanol. Despite the tremendous success achieved in producing flexible SWCNT thin-film transistors and circuits with promising electrical performance, the existence of metallic SWCNTs is still a drawback because of device on/off current ratio degradation. Although stripe patterning has been proposed to improve a device's on/off current ratio by limiting percolative transport through metallic paths in the TFTs [51], the channel length must be relatively large, which limits the degree of integration for future applications. The dry filtration method has been used by Ohno and coworkers to achieve high-performance flexible

SWCNT thin-film transistors and circuits [53]. In this method, nanotubes grown by plasma-enhanced CVD are captured using a filter membrane, and the density of the SWCNTs can be easily regulated by controlling the collection time. The collected nanotube networks can be subsequently transferred to fabricate substrates, by dissolving the filter using acetone. Although the devices fabricated via this method show excellent performance, throughput and scalability issues remain.

7.2.4 Solution-Based Methods for Nanotube Thin-Film Transistors

The most common methods for assembling SWCNT networks from solution are evaporation assembly [54], spin coating [55–57], drop coating [58–63], and printing [64–68]. The IBM group has used a novel evaporation assembly method to obtain aligned SWCNT strips with high-purity semiconductor SWCNTs (Fig. 7.2) [54]. Although submicron devices with good properties have been achieved, the scalability of this assembly method may be a problem. Carbon nanotube networks can also be obtained by dropping a SWCNT solution onto a spinning substrate [55]. This method is also limited in its scalability because the deposited nanotubes often align along different orientations depending on their location on the substrate, preventing wafer-scale fabrication with high uniformity. The other two solution-based nanotube assembly methods, drop coating and printing, are considered more promising for large-scale applications of nanotube thin-film transistors. In the drop-coating method, substrates are first functionalized with amine-containing molecules, which are effective adhesives for nanotubes. By simply immersing substrates into a SWCNT solution, highly uniform nanotube networks can be obtained throughout the wafer, enabling the fabrication of SWCNT thin-film transistors with high yields and small device-to-device variations [59, 60, 62, 63]. Printing represents another low-cost approach for fabricating large-scale SWCNT thin-film transistors and circuits; in this technique, the nanotube channel, electrodes, and gate dielectric can all be printed using ink-jet [64, 65] or gravure printing [66–68] processes. This approach is useful for producing cost-effective, large-area SWCNT circuits requiring only moderate performance, as the resolution that can be achieved using printing processes is generally lower than that of conventional photolithography. Each of the methods discussed above presents unique opportunities and challenges. In this chapter, we primarily focus on nanotube thin-film transistors produced by ink-jet printing. We will first discuss ink-jet techniques for nanotube networks and fabrication schemes for high-performance thin-film transistors on mechanically rigid and flexible substrates.

Fig. 7.2 A nanotube film grown by the evaporation assembly method. (**a**) Optical micrographic image. (**b**) and (**c**) Scanning Electron Microscope (SEM) image (Reprinted with permission from M. Engel et al. [54]. Copyright © 2008 American Chemical Society)

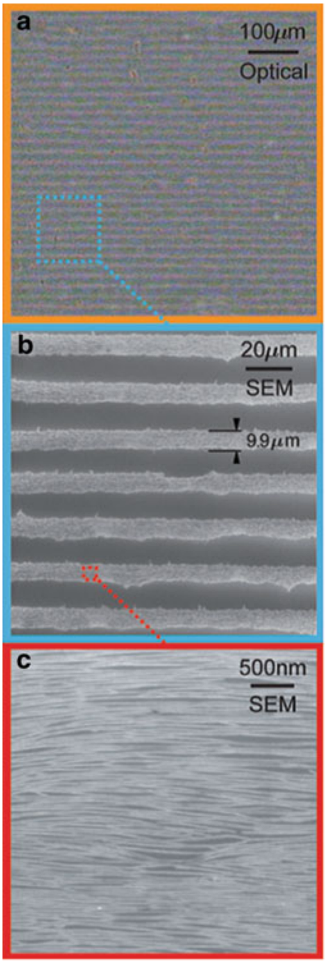

7.2.5 Ink-Jet Printing of Flexible Nanotube Thin-Film Transistors

Printable technology has the potential to drastically reduce ecological impact, energy consumption during manufacturing, and wasted materials by controlling the quantity and location of ink deposition. Ink-jet technology is exceptionally promising method because patterns can be easily generated without any material waste, leading to drastic reductions in production costs and environmental impact. Materials for printable electronics must satisfy several requirements, including high electrical properties, chemical stability, and low-temperature processability. High

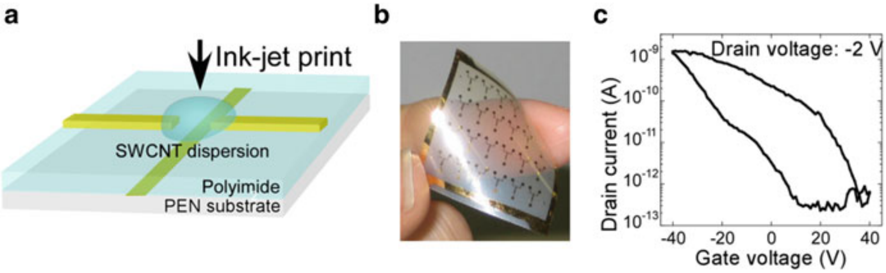

Fig. 7.3 The first reported ink-jet-printed nanotube transistors. (**a**) Schematic representation. (**b**) Optical micrographic image. (**c**) Transfer characteristics (Reproduced with permission from Takenobu et al. [75]. Copyright © 2009 The Japan Society of Applied Physics)

carrier mobilities (>1 cm^2/(V · s)) have been reported for spaghetti-like, solution-processed, random-network carbon nanotubes, which can be obtained from an ink-jet method [69–75]. Moreover, the fabrication temperature is generally <100 °C, enabling its application to flexible plastic substrates. Therefore, nanotubes are one of the most promising materials for ink-jet printable electronics.

The first ink-jet-printed flexible thin-film transistors were reported in 2009 [75]. An ink-jet printable water-based nanotube dispersion was prepared from 100 mg of HiPco nanotubes (Carbon Nanotechnologies, Inc.) and 1 g of sodium deoxycholate (Wako Pure Chemical Industries, Ltd.) with five hours of ultrasonic agitation and gentle stirring (270 rpm). Subsequently, the nanotube dispersion was centrifuged at $10{,}000 \times g$ for 5 h and then decanted, leaving behind a sediment formed by centrifugation. The solution was then printed from a piezo-driven dispenser head. For simpler solution application, the authors added 0.15 % glycerin by weight to adjust the nanotube dispersion viscosity.

Figure 7.3a shows a cross-sectional representation of the fabricated devices. Firstly, gold gate electrodes were thermally fabricated through a shadow mask on flexible polyethylene naphthalate (PEN) films (Teijin Dupont). A high-purity polyimide precursor (KEMITITE CT4112, Kyocera Chemical) was then spin coated to obtain plastic gate dielectric layers. Before the nanotube thin films were fabricated, the gold source and drain electrodes were fabricated on the polyimide dielectric layer. Finally, the nanotube dispersion was ink-jet-printed between two gold electrodes, and the substrate was then washed with deionized water. Figure 7.3b shows an optical image of the flexible nanotube thin-film transistors, and Fig. 7.3c presents the transistor transfer characteristics of a typical flexible nanotube thin-films transistor. The observed on/off current ratio was approximately 10^4, without any additional processing steps to remove the effect of metallic nanotubes. However, the typical carrier mobility was $10^{-3} \sim 10^{-4}$ cm^2/(V · s), which is three or four orders of magnitude smaller than that obtained from other solution-based fabrication methods.

7.2.6 Fabrication Schemes for High-Performance, Ink-Jet-Printed Nanotube Thin-Film Transistors

In high-density nanotube networks, especially in the form of small bundles, metallic nanotubes (normally coexisting with semiconductor nanotubes at a 1:2 volume ratio) form a percolating network that behaves like a conducting film. With moderate nanotube density, only the semiconductor nanotubes create a percolating network, and the film displays semiconductor conducting properties. In the past, carbon nanotube thin-film transistors have been ink-jet-printed without precise nanotube density control, resulting in low carrier mobility ($10^{-3} \sim 10^{-4}$ $\text{cm}^2/(\text{V} \cdot \text{s})$). To solve this problem, very dilute carbon nanotube dispersions have been adapted to control nanotube network density and electrical transport properties by optimizing the ink-jet printing process (Fig. 7.4) [76]. Figure 7.4c shows a schematic representation of the materials, device layout, and fabrication processes. The authors ink-jet-printed nanotube networks on a SiO_2 (500 nm)/Si wafer, creating source/drain metallic electrodes and semiconductor active channels. In the electrode regions, the carbon nanotube dispersion was deposited 100 times at each position. For the active semiconductor regions, the authors printed four-type networks by printing 40, 20, 10, or 2 droplets per position. Figure 7.4c shows an optical image of printed carbon nanotube transistors with a clear contrast between networks, strongly suggesting successful nanotube density control.

Figure 7.5 depicts atomic force microscopy (AFM) images of ink-jet-printed carbon nanotube films. The film density was well controlled and uniform. Networks with high density (4.20 %, Fig. 7.5a) and moderate density (0.61 %, Fig. 7.5d) acted as metallic and semiconducting nanotube films, respectively. Importantly, the authors observed clear boundaries between the metallic (0.85 % surface coverage) and semiconducting (0.61 % surface coverage) percolating networks. These results indicate that the electrical transport properties of nanotube networks can be tailored via the ink-jet process. The authors controlled the $I_{\text{on}}/I_{\text{off}}$ from 1.5 to 10^4 and the field-effect carrier mobility from 4.2 to 49 $\text{cm}^2/(\text{V} \cdot \text{s})$ (1.6–4.2 $\text{cm}^2/(\text{V} \cdot \text{s})$ with an $I_{\text{on}}/I_{\text{off}}$ of 10^4 to 10^5).

Ink-jet-printed carbon nanotube thin-film transistors can potentially be used in flexible electronics due to their high carrier mobility and low-temperature processability. However, various properties must be improved before application to realize less hysteresis, low-operation voltage, and fully printability with printable dielectric layers. To this end, the authors changed the dielectric material from solid-state SiO_2 to an ionic liquid (Fig. 7.6a) as a high-capacitance gate dielectric material compatible with thin-film transistors and solution process [76, 77]. Figure 7.6b shows a schematic representation of the device layout and fabrication process for exclusively ink-jet-printed carbon nanotube thin-film transistors. The authors fabricated high-performance nanotube thin-film transistors using the ink-jet method and then printed a nanotube gate electrode. The surface nanotube coverage of this film was 0.93 %. In the final fabrication step, the authors ink-jet-printed an ionic liquid as a gate dielectric layer. Figure 7.6d compares the transistor characteristics

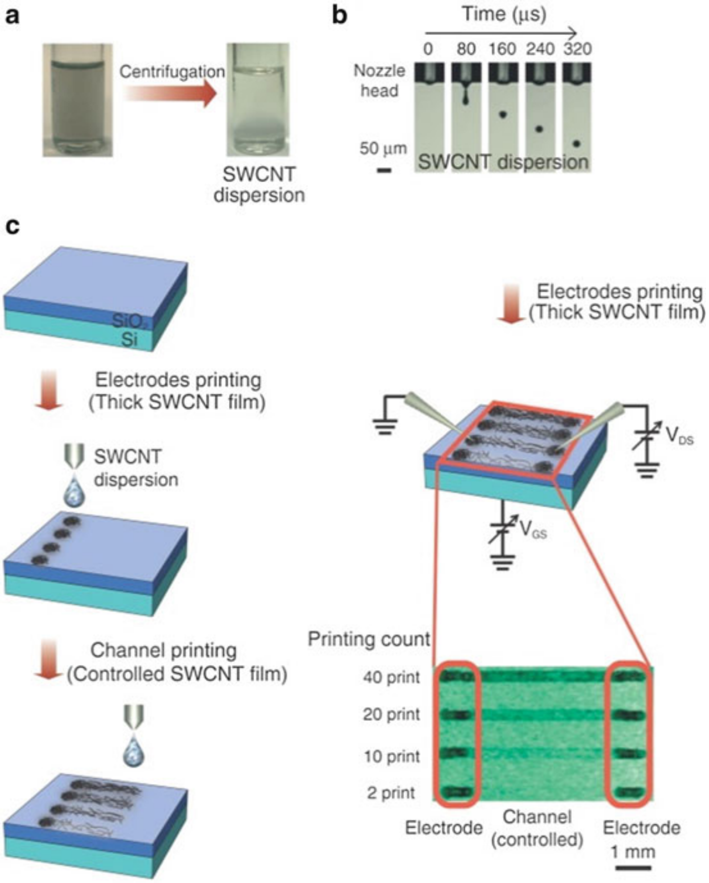

Fig. 7.4 Fabrication of ink-jet-printed nanotube transistors. (**a**) An optical micrograph image of DMF-based nanotube dispersion. (**b**) Time-dependent snapshots of a DMF-based nanotube droplet during ink-jet printing. The *top gray* stripe corresponds to the ink-jet head nozzle. The *black sphere* corresponds to the droplet of the nanotube dispersion. (**c**) A schematic representation of the fabrication processes for ink-jet-printed nanotube transistors. The *black lines* indicate nanotube bundles. An optical micrograph image of ink-jet-printed nanotube transistors on a SiO_2 base substrate is also illustrated (Reproduced with permission Okimoto et al. [76]. Copyright © 2010 WILEY-VCH Verlag GmbH & Co. KGaA, Weinheim)

of the back-gate-operated solid-state SiO_2 and ionic liquid gating. With ionic liquid gating, the transistor operating voltage was significantly decreased, and the hysteretic response against gate voltages was improved, possibly due to the efficient screening of charged impurities by the ionic liquid.

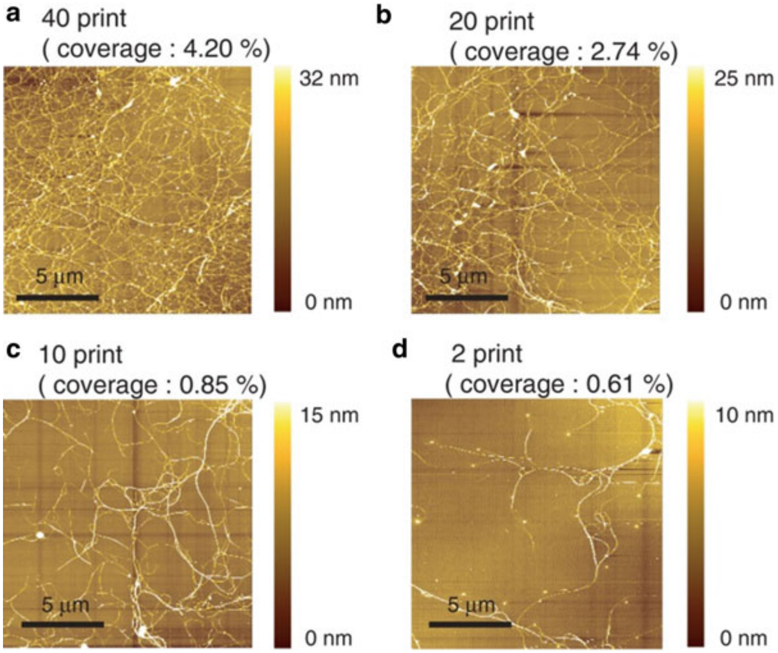

Fig. 7.5 Atomic force microscopic images and printing-time dependence of substrate surface coverage in ink-jet-printed nanotube films. Atomic force microscopic images of the four types of nanotube networks grown by deposition of (**a**) 40, (**b**) 20, (**c**) 10, or (**d**) 2 prints per position (Reproduced with permission from Okimoto et al. [76]. Copyright © 2010 WILEY-VCH Verlag GmbH & Co. KGaA, Weinheim)

7.2.7 Ink-Jet Printing of Nanotube Complementary Metal–Oxide–Semiconductor (CMOS) Inverters

Currently, doping carriers for most materials via ink-jet printing remain difficult; although organic materials can provide high-performance complementary logic circuits, p- and n-type semiconducting materials must be combined for their preparation because the doping method is poorly defined. Furthermore, doping processes for inorganic materials generally require high-temperature and/or vacuum processes, which are incompatible with simple printing method. Among these materials, it may be possible for SWCNTs to control the transistor polarity using a printing technique.

The carrier doping method for SWCNTs differs from conventional semiconducting material because incorporating foreign atoms, such as nitrogen or boron, into the substitutional or interstitial sites of carbon nanotubes is difficult. As a result, adsorbates (atoms [78, 79], molecules [79–82], and polymers [83–85] with appropriate functional groups) have been adapted to the SWCNT surface. The charge transferring between adsorbates and carbon nanotubes leads to a shift of

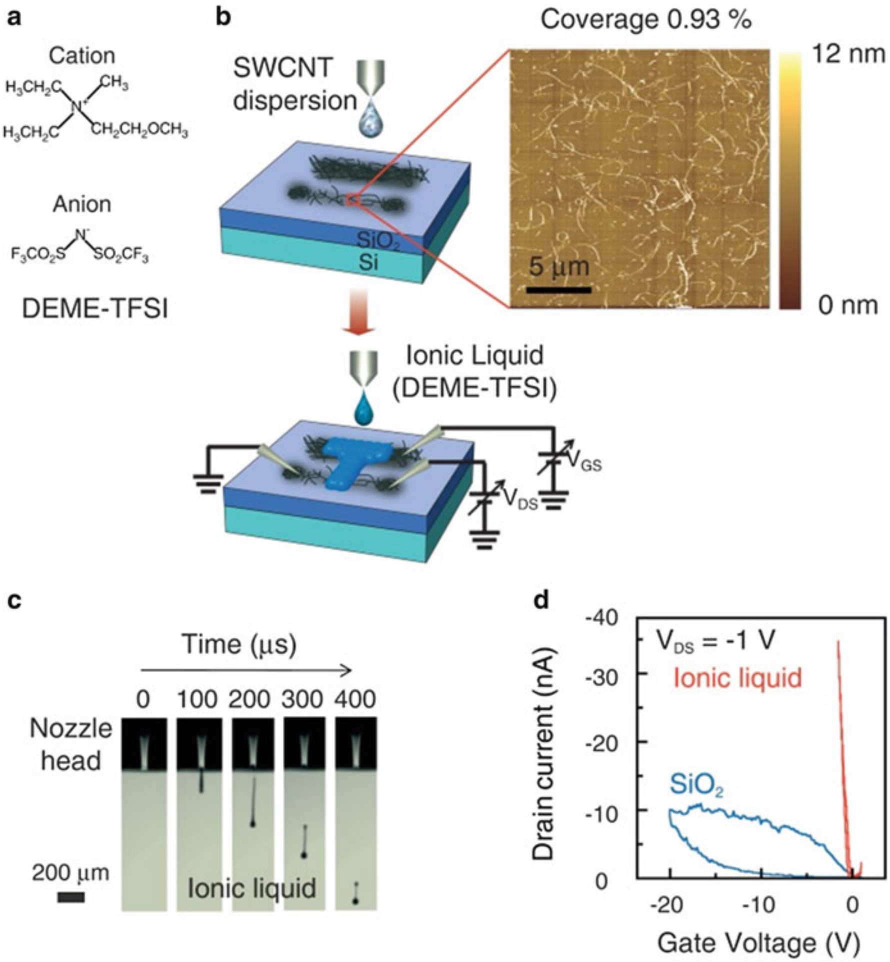

Fig. 7.6 Fabrication of exclusively ink-jet-printed nanotube transistors. (**a**) A schematic illustration of N,N-diethyl-N-methyl-N-(2-methoxyethyl) ammonium bis(trifluoromethanesulfonyl) imide (DEME-TFSI). (**b**) A schematic illustration of the fabrication processes for exclusively ink-jet-printed nanotube transistors and a corresponding atomic force microscopic image. (**c**) Time-dependent snapshots of an ionic liquid droplet during ink-jet printing. Owing to the higher viscosity of the ionic liquid, the authors heated up the head of ink-jet printer to 65 °C. (**d**) Transistor transfer characteristics of (*blue*) SiO_2 back-gated and (*red*) ionic liquid-gated nanotube transistors (Reproduced with permission from H. Okimoto et al. [76]. Copyright © 2010 WILEY-VCH Verlag GmbH & Co. KGaA, Weinheim)

nanotube Fermi level. For low-temperature, ink-jet carrier doping to SWCNTs, the authors selected polyethyleneimine (PEI, average molecular weight of ~2000; Sigma Aldrich, Japan) as their electron dopant, as PEI is a well-known soluble electron donor for SWCNTs [83–85]. Importantly, the charge transferring between PEI and SWCNTs occurs at room temperature.

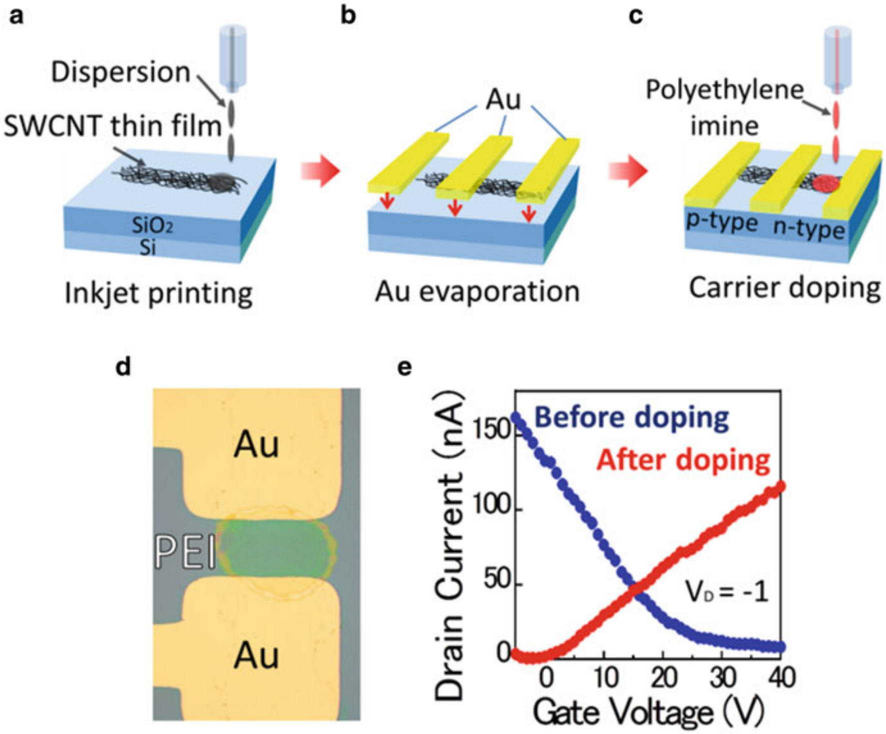

Fig. 7.7 A schematic illustration of the ink-jet-doped nanotube transistor fabrication process. (**a**) Ink-jet printing of nanotube transistors. (**b**) Gold electrode evaporation. (**c**) Ink-jet printing of polyethylene imine (PEI) for electron doping to nanotube transistors. (**d**) A photograph of a PEI-printed nanotube transistor. (**e**) Transistor transfer characteristics of nanotube transistors before and after PEI printing (Reproduced with permission from Matsuzaki et al. [86]. Copyright © 2011 The Japan Society of Applied Physics)

SWCNT TFTs and an ethanol/PEI solution were ink-jet-printed using a method described by Okimoto et al. [76, 77]. Firstly, as shown in Fig. 7.7a, Matsuzaki et al. printed 7 droplets per dot with a 10-μm dot-to-dot distance [86]. Si substrates were used as back gate electrodes, and as shown in Fig. 7.7b, gold source and drain electrodes were evaporated. Finally, the authors ink-jet-printed PEI inks onto the SWCNT films, and as shown in Fig. 7.7c, d, samples were baked at 45 °C for 5 min to remove the solvent. Figure 7.7e demonstrates the transistor transfer characteristics before and after PEI ink-jet printing on a nanotube thin-film transistor. After ink-jet carrier doping of PEI, these devices clearly displayed n-type transistor characteristics.

The authors ink-jet-printed nanotube CMOS inverters by combining n- and p-type nanotube thin-film transistors (Fig. 7.7c). PEI ink was ink-jet-dropped onto the nanotube thin-film transistor to fabricate CMOS inverters using ink-jet method. Because threshold voltages of p-type nanotube transistors are not controllable, we

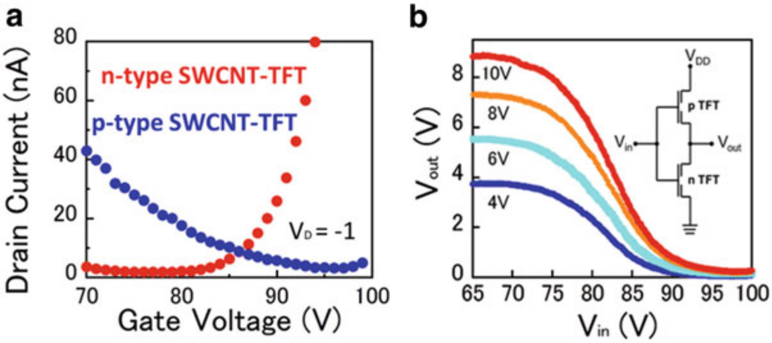

Fig. 7.8 (**a**) Transistor transfer characteristics of p- and n-type nanotube transistors. (**b**) Transistor transfer characteristics of a nanotube complementary inverter at different supply voltages (V_{DD}). The inset shows a schematic circuit of nanotube complementary inverters (Reproduced with permission from Matsuzaki et al. [86]. Copyright © 2011 The Japan Society of Applied Physics)

prepared several p-type nanotube transistors with different threshold voltages and selected one transistor for CMOS inverter fabrication. The characteristics of the fabricated nanotube CMOS inverter are shown in Fig. 7.8a, b. As shown in Fig. 7.8b, clear on and off states were observed for a supply voltage (V_{DD}) ranging from 4 to 10 V, suggesting the correct switching action of the ink-jet-printed nanotube CMOS inverter. Inverter performance can be determined by a signal gain ($\Delta V_{out}/\Delta V_{in}$). As shown in Fig. 7.8b, the transfer curves exhibit gains ~1.4 in a given voltage range. Very importantly, although the collected gain of 1.4 is smaller than that of other nanotube CMOS inverters, this work is the first fabrication of ink-jet-printed nanotube CMOS logic circuits printed at moderate temperatures.

7.2.8 Ink-Jet Printing of Aligned Nanotube Films

Individual carbon nanotubes have excellent charge carrier mobility, but a random nanotube network exhibits electrostatic screening at nanotube/nanotube junctions. Therefore, the nanotube network geometry strongly influences transistor performance, and reducing or eliminating the number of junctions can improve charge carrier transport [12–16]. Consequently, the alignment of SWCNTs is significantly important for high-performance thin-film transistors, and the efficient nanotube alignment using printing method is highly required. Recently, Takagi et al. successfully aligned carbon nanotubes by ink-jet printing method [87].

Single-walled carbon nanotube films were ink-jet-printed by the method of Okimoto et al. [76, 77]. The authors used self-assembled monolayers (SAMs) to control the substrate wettability [88, 89]. Highly doped silicon wafers with 500-nm thick oxide dielectric layers were used as base substrates. The authors immersed

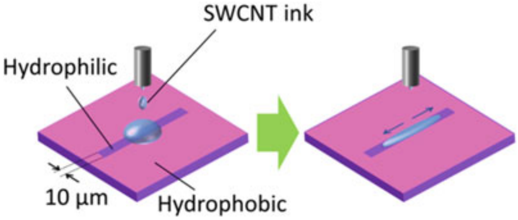

Fig. 7.9 A schematic representation of ink-jet-printed droplet movement on a SiO_2 substrate with HMDS-SAM coating, which is partially converted to hydrophilic surface by irradiation of UV through a 3-μm gap handmade photomask (Reproduced with permission from Takagi et al. [87]. Copyright © 2013 AIP Publishing LLC)

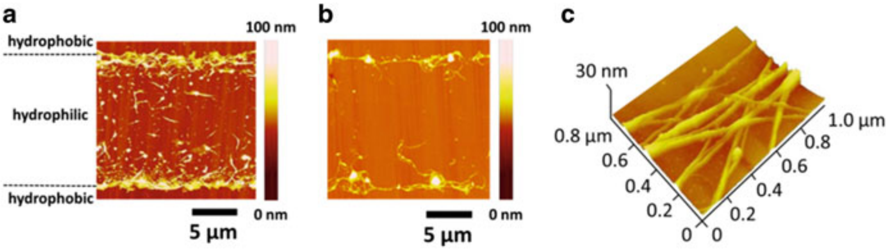

Fig. 7.10 Atomic force microscopic images of ink-jet-printed nanotube films. (**a**) s-SWCNT and (**b**) laser-SWCNT thin films ink-jet-printed onto SiO_2 substrates with HMDS-SAM coating, which are partially converted to hydrophilic surface by irradiation of UV through a 3-μm gap handmade photomask. These prepared substrates were sonicated in deionized water before ink-jet printing the nanotube dispersions. (**c**) A high-resolution atomic force microscopic image of laser-SWCNTs (Reproduced with permission from Takagi et al. [87]. Copyright © 2013 AIP Publishing LLC)

these Si base substrates in a solution of 1,1,1,3,3,3-hexamethyldisilazane (HMDS) and then rinsed them with chloroform. The HMDS SAMs lead to uniform hydrophobicity over the entire Si base substrate surface, and they can be removed by irradiation of UV light (wavelength ranging from 184.9 to 253.7 nm) to change the hydrophobic substrate surface to a hydrophilic substrate surface. To control the drying behavior of the carbon nanotube ink, the authors adopted the method described by Nobusa et al. (SAM-based patterning) [88, 89], and this method is schematically illustrated in Fig. 7.9. The authors changed specific areas of SAM-coated substrate by applying UV irradiation through a photomask with 3-μm gap, tuning both the movement of the nanotube dispersion and the drying behavior.

The nanotube film topography was characterized by AFM (MultiMode 8, Bruker), and the nanotubes of these films were mainly concentrated along the boundary of the wettability contrast; this tendency was observed more frequently for the longer laser nanotubes (Fig. 7.10b) than for the shorter semiconducting-enriched nanotubes (Fig. 7.10a). This difference arises from the differences in the interactions between SWCNTs, which are proportional to length of nanotubes. These results strongly suggest that we can obtain well-oriented nanotube films from longer nanotubes using the ink-jet printing technique.

7.2.9 Summary of Carbon Nanotube Thin Films

Although fabrication of nanotube thin-film transistors using ink-jet printing method was very difficult prior to 2009, recent rapid progress of this field has enabled a wide variety of ink-jet-printed nanotube films, such as density-tuned nanotube film transistors, fully printed electrolyte-gated TFTs, ink-jet-printed nanotube CMOS inverters, and ink-jet-printed, aligned nanotube thin films. Flexible nanotube devices open routes for realizing high-mobility and environmentally friendly nanotube-printed electronics. Future targets may be fully ink-jet-printed, stretchable nanotube devices.

7.3 Transition Metal Dichalcogenides (TMDCs) Thin Films

The outstanding materials properties of two-dimensional (2D) materials, including graphene and transition metal dichalcogenides (TMDCs) thin films, have allowed important applications in next-generation electronics. In particular, atomically thin molybdenum disulfide (MoS_2) has attracted widespread attention because MoS_2 monolayers possess large bandgap, high carrier mobility, and mechanical flexibility. In addition, recent developments in preparation methods of chemical vapor deposition (CVD)-grown, large-area, high-quality sample have enabled the use of molybdenum disulfide in novel functional devices, such as flexible and stretchable thin-film transistors. In this section, we focus on the recent progress in generating MoS_2-based flexible and stretchable thin-film transistors. The reported virtues and novelties of molybdenum disulfide provide great advantages for developing flexible and stretchable two-dimensional material-based electronics.

7.3.1 Introduction

Recently, two-dimensional materials such as graphene and TMDCs have attracted significant interest because they possess the unique electronic, optical, and mechanical properties [90–94]. One of the most promising two-dimensional materials for electronic applications is molybdenum disulfide due to its large intrinsic bandgap [94–101]. MoS_2 has an indirect bandgap (~1.2 eV) in the layered bulk structure and can be scaled down to atomically thin two-dimensional monolayer films and changed to a direct bandgap semiconductor (~1.8 eV) [99, 100]. Because of this large bandgap, thin-film transistors of MoS_2 monolayers fabricated on SiO_2 base substrates exhibit excellent I_{on}/I_{off} (~10^8) [95]. In addition to the excellent charge carrier transport, the flexible and stretchable mechanical properties are superior in nm-scale thick MoS_2 films. Within its two-dimensional forms, the strong bonding between the chalcogen (S) and transition metal (Mo) atoms results in in-plane mechanical strength which is comparable to that of steel, realizing unique device fabrications, such as flexible and/or stretchable thin-film transistors [102–104]. Although many researches have been performed on mechanically exfoliated thin-layer molybdenum disulfide, such molybdenum disulfide can only produce approximately 10-μm-size films, which hampers the practical applications of molybdenum disulfide in large-area, flexible, and stretchable devices. Accordingly, recent developments in scalable CVD growth can be transferred onto any other substrates, which leads to the flexible and stretchable electronics of molybdenum disulfide films [105]. CVD growth can yield large-area molybdenum disulfide thin films and is applicable to flexible and stretchable device fabrications on bendable polymer and elastic rubber functional substrates [106, 107].

This section focuses on the recent developments of generating molybdenum disulfide thin-film transistors for flexible and stretchable applications. Firstly, film preparation researches and the thin-film transistor fabrication of these two-dimensional films are introduced. Secondly, the fabrication of flexible molybdenum disulfide transistors and their unique advantages are highlighted. As the final topics, we discuss device and material strategies for the molybdenum disulfide-based flexible and stretchable applications, providing perspective on future research directions.

7.3.2 Material Synthesis and Transistor Fabrications

7.3.2.1 Synthesis of Molybdenum Disulfide Films

To establish reliable methods for synthesizing high-quality, atomically thin molybdenum disulfide films to investigate the fundamental electronic, optical, and mechanical properties, as well as their possible applications is a most important research topic. Recent approaches for fabricating MoS_2 thin films have been demonstrated by two methods. One of the methods is the top-down exfoliation (e.g., by mechanical or liquid exfoliation) of bulk crystalline samples, which can generate μm-scale high-quality, single-crystalline MoS_2 thin films. Another approach is the bottom-up CVD growth for producing cm-scale, large-area, uniform polycrystalline MoS_2 films. Here, we review the current understandings from reports using each method and describe their respective applications to field-effect transistor fabrication.

7.3.2.2 Mechanical Exfoliation of Molybdenum Disulfide Films

The most widely adopted fabrication method for preparing atomically thin molybdenum disulfide films is mechanical exfoliation by scotch tape, which was originally developed for obtaining graphene films and can be applied to bulk single crystals of molybdenum disulfide [92, 94–100]. In this fabrication method, the layered structure of the bulk material, which is composed of vertically stacked monolayers held together by weak van der Waals interactions, can be easily peeled from the bulk single crystal, resulting in two-dimensional films of molybdenum disulfide (Fig. 7.11a) [96]. The layer dependence of optical and vibrational properties of molybdenum disulfide two-dimensional films has currently attracted attention because significant changes from the bulk samples have been reported in the electronic structure of two-dimensional samples [99–101, 108–112]. One important optical change, layer thickness decrease, appeared in the associated Raman spectra. Analytical and experimental researches have demonstrated the shift in the main two Raman peaks of molybdenum disulfide, the in-plane vibration of $E^1{}_{2g}$ and the out-of-plane A_{1g} phonon mode, which showed a frequency decrease in $E^1{}_{2g}$ mode and a frequency increase in A_{1g} mode [108–110]. These peak shifts in $E^1{}_{2g}$ mode and A_{1g} mode originate from interactions within the layered structure and an associated increase in the dielectric screening of long-range Coulombic interlayer interactions [109]. Therefore, the Raman peak positions of molybdenum disulfide can be used to identify the thickness of MoS_2 thin films. Another significant layer-dependent effect is the variations observed in electronic band structure. The indirect bandgap of bulk MoS_2 sample transitions into a direct bandgap with two-dimensional thin films as a result of quantum confinement [99, 100]. Particularly in molybdenum disulfide monolayer (thickness of approximately 0.8 nm), an intrinsic direct bandgap (~1.8 eV) emerges at the K point and can be detected by strong photoluminescence (PL) and absorption spectra [99, 100]. Due to this large direct bandgap, atomically thin molybdenum disulfide is a promising two-dimensional material for electronic and optoelectronic devices. The strong spin–orbital interaction that originates from the transition metal (Mo) attribute of this material leads to energy splitting of the valence band [113–119]. The combination of a symmetric band structure and strong spin–orbital interaction also enables “valley polarization,” logic operations controlled with spin–valley coupling, and the possibility of “valleytronics” [117–119].

One of the most promising electronic devices of atomically thin molybdenum disulfide films is a thin-film transistor fabricated for logic electronics due to its intrinsic direct bandgap [95–98, 120–130]. As shown in Fig. 7.11b, Radisavljevic et al. firstly reported monolayer molybdenum disulfide thin-film transistors using HfO_2 as a high-κ top-gate dielectric on SiO_2-base substrates and achieved an extremely high I_{on}/I_{off} (~1×10^8) [95]. Back-gate-based, multilayer molybdenum disulfide thin-film transistors exhibited high carrier mobility >100 $cm^2/(V \cdot s)$ and sufficient I_{on}/I_{off} (~1×10^6) [120]. The great switching properties of these field-effect transistors immediately led to the fabrication of logic circuits [121, 122]. Currently, integrated circuits based on bilayer molybdenum disulfide, including inverters, NAND gates, and ring oscillators, were successfully fabricated [122]. The oscillation frequency of a demonstrated five-stage ring oscillator is up to 1.6 MHz, which is a significant step toward high-performance two-dimensional nanoscale electronics. Further advances in logic circuits require CMOS inverters composed of p-type and n-type field-effect transistors. Although molybdenum disulfide TFTs typically show only n-type transport, ambipolar molybdenum disulfide TFTs have been demonstrated by ionic liquids as gate dielectric materials [131–133]. Figure 7.11c represents a simple schematic illustration of ionic liquid-gated molybdenum disulfide TFTs. When a gate voltage (V_g) is applied, a transistor active channel is formed by a single carrier type (Fig. 7.11c, top). However, when V_g is much smaller than the applied drain voltage (Fig. 7.11c, bottom), the effective V_g at the drain electrode is inverted, resulting in the accumulation of opposite

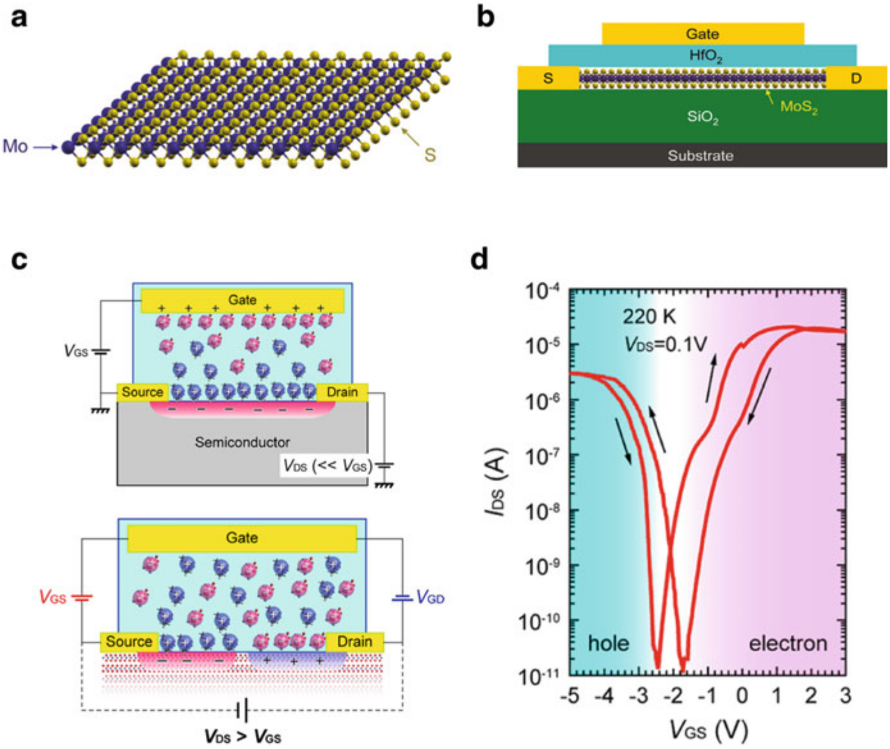

Fig. 7.11 (**a**) A three-dimensional schematic illustration of the monolayer MoS_2 crystal structure. (**b**) A schematic representation of HfO_2 top-gated monolayer MoS_2 FETs. (**c**) A schematic illustration of unipolar and ambipolar carrier accumulation in an ionic liquid-gated MoS_2 FET. *Top*: unipolar accumulation mode. The drain voltage (V_{DS}) is relatively smaller than the gate voltage (V_{GS}). *Bottom*: ambipolar accumulation mode. The drain voltage is relatively larger than the gate voltage. (**d**) Transistor transfer curve of an ambipolar MoS_2 thin-flake FET. The figures are reprinted with permission from Refs. [96] and [133] (Copyright © 2013 American Chemical Society)

carrier and inducing hole carrier transport (Fig. 7.11d). Furthermore, the extremely large capacitance of the electric double layer (~10 μF/cm^2) is able to accumulate a magnitude higher density of carriers than that of typical SiO_2 dielectric layers, resulting in a strong depletion of donor carriers and efficient electrostatic carrier doping [134, 135]. Very interestingly, electric-field-induced superconductivity in molybdenum disulfide thin films has also been demonstrated [136, 137]. Realization of ambipolar carrier transport will enable the construction of CMOS-like applications and the formation of p–n junctions for optoelectronic devices [133, 138].

Another important application of molybdenum disulfide TFTs is in optoelectronic devices as photodetectors and photovoltaic cells [139–143]. The direct bandgap of molybdenum disulfide thin films offers effective light absorption of visible light and luminescence capabilities, allowing molybdenum disulfide films to be used as an active material for phototransistors. Lee and coworkers demonstrated the thickness dependence of the photo-response in various layers of molybdenum disulfide films, suggesting that different wavelengths of light can be detected as a result of thickness-dependent bandgap [141]. For example, mono- and bilayer molybdenum disulfide films, which possess respective optical absorption peaks of 1.8 and 1.6 eV, are useful for green-light detection; trilayer molybdenum disulfide film exhibits an optical absorption peak of 1.4 eV and is suitable for red-light detection. More currently, ultrasensitive, monolayer molybdenum disulfide phototransistors with a broad spectral range were reported [143]. The maximum external photo-responsivity reached 880 AW^{-1}, and the noise under dark current was lower than that of commercial state-of-the-art Si avalanche photodiodes, suggesting ultrahigh sensitivity due to the direct bandgap and efficient carrier excitation. These results support the understanding that monolayer molybdenum disulfide film is a promising semiconductor film for use in imaging circuits, light-sensing devices, and photovoltaic cells. Furthermore, electroluminescence (EL) has also been demonstrated with monolayer molybdenum disulfide film in a TFT configuration, opening up the possibility of applications in light-emitting devices (LEDs), such as diode lasers [144].

The high surface-to-volume ratio of molybdenum disulfide two-dimensional thin films provides natural opportunities for sensor devices [145–147]. The first report of a gas sensor based on mono- and few-layered molybdenum disulfide TFTs was reported by Li et al., who developed a sensing device that can detect the NO gas adsorption [145]. Because molybdenum disulfide TFTs show n-type transport, certain changes occur in carrier transfer, doping level, and conductivity as a result of the exposure of TFTs to NO gas, which is most likely a p-donor. These sensing behaviors extend to chemical-sensing devices with a wide range of analytes, exhibiting a critical response upon exposure to nerve gas [146]. Moreover, humidity sensors have been demonstrated, showing a clear response to water vapor at room temperature and atmospheric pressure [147]. Followed by the rapid developments in electronic and optoelectronic applications, molybdenum disulfide monolayer TFTs will enable novel functionalities, such as thermopower generation and energy harvesting. A large Seebeck coefficient for molybdenum disulfide films was currently observed, and this Seebeck coefficient can be controlled by an electric field application (ranging from -4×10^2 to -1×10^5 μVK^{-1}) [148]. The obtained Seebeck coefficient is 70–25,000 times larger than that of graphene, suggesting further potential for thermoelectric applications.

7.3.2.3 Liquid Exfoliation of Molybdenum Disulfide Films

Although the mechanical exfoliation method yields highly single-crystalline films that can be used to prepare high-performance devices from which intrinsic physical phenomena can be demonstrated, growth techniques able to yield enough quantities are strongly required for future applications, such as energy storage, composites, and hybrids. In liquid exfoliation method, layered materials are dispersed in common organic solvents, such as *N*-methyl-2-pyrrolidone (NMP). These methods can produce gram-scale quantities of various flakes or few-layered samples from their dispersions, such as molybdenum disulfide, tungsten disulfide, or boron nitride (BN) [149–153]. Another effective method for the gram-scale mass production of layered samples is electrochemical lithium (Li) intercalation [154–156]. Lithium-intercalated samples can be easily exfoliated by ultrasonication, producing few- or monolayer thin films. However, lithium intercalation generally results in a significant loss of semiconductor properties due to an emerging metallic phase. In response to this drawback, Eda et al. reported the recovery of the semiconductor properties of pristine samples by adopting mild annealing to the preparation procedure [156]. The chemically exfoliated molybdenum disulfide thin films that were obtained exhibited specific direct bandgap PL, indicating a low defect density. Moreover, these solution-based procedures can be applied to the transfer of two-dimensional films to arbitrary substrates, including flexible plastic substrates (Fig. 7.12a, b) [156]. In addition to these reports, Zeng and coworkers realized high-yielding, monolayer semiconductor nanosheets of molybdenum disulfide and tungsten disulfide based on a controllable lithiation procedure [154, 155]. Particularly, the prepared monolayer molybdenum disulfide is in excess of 90 %, suggesting the effectiveness of large-scale material production [154]. The solution processability of molybdenum disulfide thin films has enabled various devices, such as photo-electrochemical applications and flexible arrays [157, 158]. For example, as represented in Fig. 7.12c, flexible gas-sensing devices prepared by molybdenum disulfide thin-film transistors have been demonstrated and have performed high sensitivity and excellent reproducibility [158]. Reduced graphene oxides (rGOs) were patterned on plastic substrates (PET) as electrodes, and suspended monolayer molybdenum disulfide thin films were used as the active material. Thin-film transistor-sensing arrays can detect the common toxic gas NO_2 and can survive 5,000 cycles of bending without any degradation of sensing performance. The use of solution-processed film formation through spin coating enables simple, low-cost, and environmentally friendly methods to the high-yielding production of molybdenum disulfide films, as well as a wide range of potential devices [159]. In contrast, in liquid exfoliation method, it is relatively difficult to control the thickness of samples, resulting in a low concentration of monolayer molybdenum

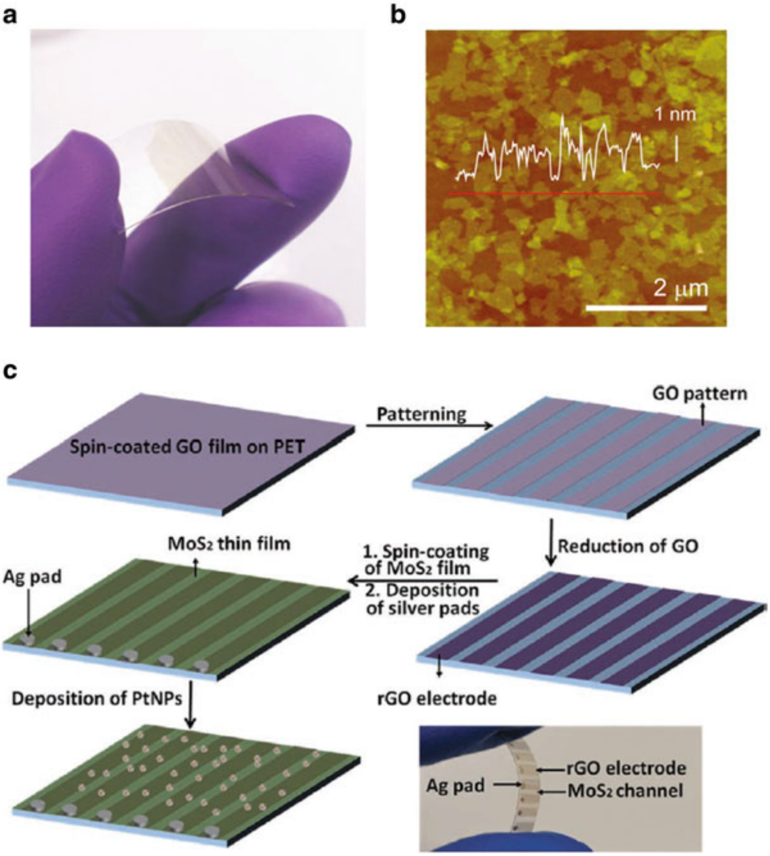

Fig. 7.12 (**a**) A photo of as-deposited MoS_2 thin films on a PET substrate. (**b**) An atomic force microscopic image of a deposited ultrathin film with an average thickness of 1.3 nm. The *white line* indicates a height profile obtained at the *red line* position. (**c**) A schematic illustration of the fabrication process of MoS_2 thin-film transistor arrays on PET substrates and an optical image of flexible thin-film transistor sensor arrays. The figures are reprinted with permission from Refs. [156] (Copyright © 2011 American Chemical Society) and [158] (Copyright © 2012 Wiley)

disulfide films. This technique easily yields few-layer or monolayer molybdenum disulfide films; however, the size of the samples tends to be very small (< a few μm); this method cannot deliver layer-controlled, highly uniform, and large-area molybdenum disulfide films. Large-area, monolayer molybdenum disulfide films are strongly required for electronic or optoelectronic devices; thus, novel synthesis methods are critically desired for sorting the thickness, obtaining scalability, and maintaining reproducibility as key steps toward the practical applications.

7.3.2.4 Chemical Vapor Deposition (CVD) of Molybdenum Disulfide Films

Following the breakthrough of the CVD method for graphene thin films, the synthesis of large-area, uniform, atomically thin molybdenum disulfide films is recently feasible [160, 161]. Some CVD approaches have been developed to grow monolayer or few-layer molybdenum disulfide films on rigid insulator substrates [162–168]. Lee and coworkers reported the growth of large-area, monolayer molybdenum disulfide film on rigid Si/SiO_2 substrates through the co-deposition of sulfur films and MoO_3 films, as represented in Fig. 7.13a [163]. Growth conditions of this method are very sensitive to the surface treatment of substrates, where aromatic molecules, such as rGO, perylene-3,4,9,10-tetracarboxylic acid tetrapotassium salt (PTAS), and perylene-3,4,9,10-tetracarboxylic dianhydride (PTCDA), promote layer growth (Fig. 7.13a). As-grown molybdenum disulfide thin films remain typical n-type semiconducting materials, and bottom gate transistors exhibit semiconductor properties with an excellent I_{on}/I_{off} ($>10^8$) and excellent charge carrier mobility (>10 $cm^2/(V \cdot s)$) [169–172]. Using the same CVD method, highly crystalline domains that can scale up to the size of 120 μm were demonstrated, and the resultant sample revealed optical and electronic properties comparable or superior to that of exfoliated single-crystalline molybdenum disulfide films [164]. Although the co-deposition of different precursors can prepare high-quality, single-domain molybdenum disulfide films, full coverage of the whole substrate surface is extremely difficult. The lateral size of the obtained molybdenum disulfide layer is typically less than a millimeter, which is not suitable for future wafer-scale applications intended for large-area or flexible devices.

An alternative scalable growth strategy is represented in Fig. 7.13b and was demonstrated by Liu and coworkers for the deposition of trilayer molybdenum disulfide films [173]. Highly crystalline and large-area molybdenum disulfide films were prepared through a two-step, high-temperature annealing procedure of a thermally decomposed ammonium thiomolybdate layer that was dip coated on substrates (sapphire or SiO_2/Si). The addition of sulfur during the second annealing procedure improved the crystallinity of molybdenum disulfide films such that various spectroscopic and microscopic properties could be investigated [173]. In addition, we fabricated thin-film transistors with CVD-grown polycrystalline molybdenum disulfide flakes and ion gels, i.e., gelated ionic liquids [174], as gate dielectric materials [106]. Due to the extremely huge specific capacitance of ion gels (~10 $\mu F/cm^2$) [175–177], the transistor exhibits a low operational voltage (<1 V), good electron carrier mobility (>12 $cm^2/(V \cdot s)$), and good I_{on}/I_{off} (10^5) on rigid SiO_2/Si substrates, as shown in Fig. 7.13c, d [106]. Moreover, the temperature dependence of transport properties is shown in Fig. 7.13e. At the on state of the transistor, the drain current is inversely proportional to the temperature, indicating band-like transport in polycrystalline molybdenum disulfide films. The strong interaction of molybdenum disulfide domains may assist in charge carrier transport across domain boundaries, meaning the capability of stable carrier

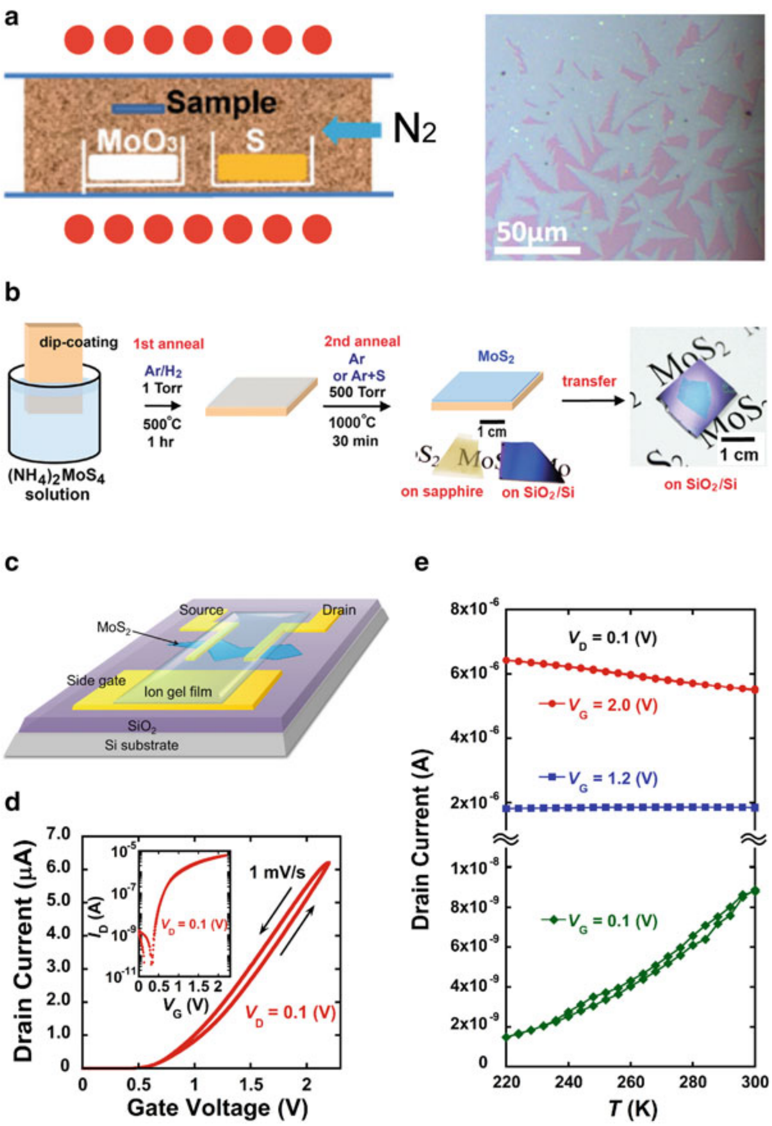

Fig. 7.13 (**a**) *Left*: a schematic illustration of the experimental setup used for co-deposition of MoO_3 and sulfa powders through a vapor phase reaction. The *red circles* indicate the chamber for heating reaction. *Right*: a photo of MoS_2 layers grown on a substrate treated with solution of reduced graphene oxide. (b) A schematic representation of the two-step annealing procedure for the growth of MoS_2 thin layers on insulating base substrates. Precursor $(NH_4)_2MoS_4$ is dip coated on base sapphire substrates and base SiO_2/Si substrates, followed by annealing under sulfur gas. Synthesized MoS_2 thin films can be transferred onto arbitrary base substrates. (**c**) A schematic illustration of a CVD-synthesized MoS_2 thin-film transistor, constructed with an ion gel as gate dielectric materials on a SiO_2/Si base substrate. (**d**) The transistor transfer characteristics of the MoS_2 thin-film transistors. V_D corresponds to the drain voltage, and V_G corresponds to the gate voltage. (**e**) Temperature dependence of V_D at the gate voltages of 2.0 V (*red*), 1.2 V (*blue*), and 0.1 V (*green*). A metal/insulator transition was observed in a MoS_2 thin-film transistor. The figures are reprinted with permission from Refs. [163] (Copyright © 2012 Wiley) [173] and [106] (Copyright © 2012 American Chemical Society)

transport under deformation. Although ion gel dielectric layers are very suitable to molybdenum disulfide films, several disadvantages of electrochemical gating TFTs remain. In these molybdenum disulfide thin-film transistors, when we increase the gate voltage to >4 V, which is higher than the electrochemical window of ionic liquids, a significant gate leakage current (>100 nA) is measured. This gate current suggests an electrochemical reaction between the ionic liquid and molybdenum disulfide film, which is a critical disadvantage for future devices. To avoid or reduce these redox reactions, ionic liquids with a wide electrochemical window are strongly required.

In addition to excellent conducting properties, CVD-grown molybdenum disulfide films can be easily transferred onto other arbitrary substrates, enabling TFT fabrications on unconventional substrates, such as flexible plastic and stretchable rubber substrates [106, 107]. A simple and scalable sulfurization method was currently developed for the large-area wafer-scale fabrication of molybdenum disulfide two-dimensional films [178–180]. Highly uniform films were prepared through the direct sulfurization of MoO_3 films evaporated on cm-scale sapphire substrates and were transferable to SiO_2/Si substrates after conducting a PMMA-assisted solution process [178]. In addition to the direct bottom-up approaches on bare surfaces, molybdenum disulfide films can be grown on graphene surfaces [181]. Demonstration of molybdenum disulfide/graphene hetero-structures indicates that other hexagonally structured samples are also able to serve as growth substrates. The vertical hetero-structured surface of the atomically thin two-dimensional films could potentially support hybrid electronics and novel optical properties, such as charge transfer, exciton generation, and high-performance TFTs, due to the absence of dangling bonds. As a result of this scalability, CVD-grown polycrystalline molybdenum disulfide films are suitable for practical applications in large-area, integrated circuits, flexible electronics, and optoelectronic devices [106, 107, 182, 183].

7.3.3 Flexible Molybdenum Disulfide Thin-Film Transistors

Two of the most desirable properties for flexible applications are flexibility and transparency. From this point of view, two-dimensional layered semiconductors are one of the promising candidates. Particularly, graphene is a widely explored atomically thin material, and many demonstrations have been performed regarding the usage of graphene for flexible and transparent TFTs [184–186]. Although the extremely huge carrier mobility of graphene ($\sim 10^5$ $cm^2/(V \cdot s)$ at room temperature) allows its usage in high-frequency applications, its metallic gapless electronic structure limits its application in logic devices [187]. As the result, researchers have currently renewed their interest in the discovery of new two-dimensional analogue samples with excellent mechanical, electronic, and optical properties. Atomically thin molybdenum disulfide film is a particularly intriguing post-graphene material for flexible applications. The mechanical strength of molybdenum disulfide monolayer film is 30 times higher than the strength of steel [102–104]. Furthermore, the robustness of molybdenum disulfide allows it to endure deformation up to 11 % before breaking because of the stiff Mo–S chemical bonds [103]. The tunable bandgaps of molybdenum disulfide thin film can also manage higher current amplification, and currently, tremendous effort has been devoted to the fabrication of flexible TFTs [106, 158, 188–191]. A sub-nm thickness of two-dimensional molybdenum disulfide films affords flexibility and transparency. The rigidity of the bulk materials causes the sample to be fundamentally difficult to bend and results in cracking of crystal structure; however, pliable atomically thin two-dimensional samples can be mechanically flexed. Due to the advantages of these electronic and flexible properties, we have performed highly flexible molybdenum disulfide thin-film transistors on flexible plastic substrates (Fig. 7.14a) [106]. Again, ion gels are adopted as gate dielectric materials, and as a result, the prepared material combines both flexibility and a huge specific capacitance [175–177]. Thin-film transistors were demonstrated on flexible polyimide substrates (thickness ~12.5 μm) and were placed on a home-built bending apparatus to test their carrier transport properties under mechanical bending (Fig. 7.14b). Figure 7.14c shows the transistor transfer characteristics of a flexible molybdenum disulfide film transistor under a curvature radius of 75 μm; the device also performed obvious recovery of conducting characteristics. The curvature radius-dependence of source–drain current and electron carrier mobility (Fig. 7.14d) suggests that the transport properties reveal no degradation under a curvature radius of 0.75 μm. Hence, this thin-film transistor is one of the most bendable TFTs available today in two-dimensional atomically thin films. Moreover, the excellent flexibility is understood by the flexibility of the ion gel films and the thin polyimide substrates, decreasing the effective strains on the molybdenum disulfide films (<1 %).

Yoon and coworkers soon demonstrated flexible and transparent molybdenum disulfide TFTs that can withstand tension and compression [188]. Figure 7.15a represents the process used for the preparation of flexible and transparent TFTs based on molybdenum disulfide films and graphene. Because patterned graphene was used as the electrode, the prepared TFTs revealed high transparency (an optical transmittance ~74 %) and an excellent stability against tension and compression (Fig. 7.15b). Although the samples in these demonstrations realized excellent flexibility, the reported FET mobility on the flexible plastic substrates was less than 5 $cm^2/(V \cdot s)$; thus, further improvements and optimization are strongly required. To improve the TFT performance, Chang et al. reported high-performance, flexible molybdenum disulfide TFTs with high-κ dielectric layers [189]. The effective local screening effect and suppression of Coulomb scattering enhanced the charge carrier mobility up to 30 $cm^2/(V \cdot s)$; the I_{on}/I_{off} was an excess of 10^7, and the subthreshold swing was decreased to 82 mV/dec. A strategy to transfer the molybdenum disulfide TFTs has already been established. This method can fabricate atomic layer-deposited (ALD) dielectric-based thin-film transistors on any arbitrary substrate, enabling device preparation that is both easy and reliable [190]. More currently, Lee and coworkers performed new hetero-structured,

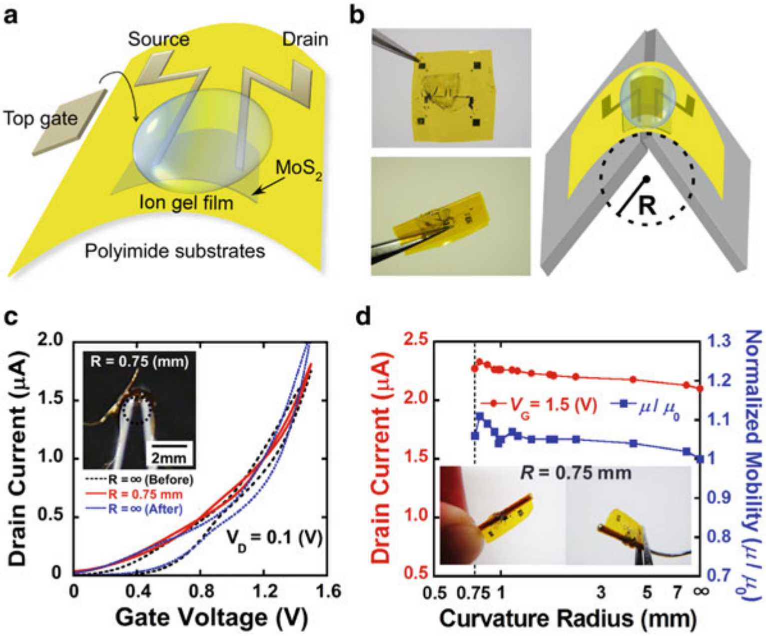

Fig. 7.14 (**a**) A schematic illustration of a MoS_2 thin-film transistor fabricated on a flexible substrate. (**b**) *Left*: a photo of a MoS_2 thin-film transistor on a 12.5-μm-thick flexible polyimide base substrate. *Right*: a schematic representation of measurements under bending. (**c**) Transistor transfer characteristics of a MoS_2 thin-film transistor. The *red*, *black-dotted*, and *blue-dotted lines* indicate the transistor transfer curve for a curvature radius = 0.75 mm and the transistor transfer curves before and after the bending experiments, respectively. The *inset* shows a photo of the measurement under bending when the device is set to a curvature radius = 750 μm. (**d**) Drain current dependence at V_G of 1.5 V (*red*) and the carrier mobility on the curvature radius. The carrier mobility is normalized by the results without bending (*flat*, *blue*). The *inset* shows photos of the MoS_2 thin-film transistor rolled to a curvature radius = 750 μm. The figures are reprinted with permission from Ref. [106] (Copyright © 2012 American Chemical Society)

flexible molybdenum disulfide TFTs [191]. The flexible and transparent molybdenum disulfide TFTs were stacked on hexagonal BN (hBN)–graphene hetero-structures, as revealed in Fig. 7.15c. Compared to typical dielectric materials, such as SiO_2, hBN is beneficial for charge carrier transport in association with atomically flat surfaces that are free of charge traps and dangling bonds. When hBN was used as gate dielectric materials and graphene was utilized for the electrodes, these hetero-structured molybdenum disulfide TFTs performed the highest carrier mobility (~45 $cm^2/(V \cdot s)$ on flexible plastic substrates. These results suggest that two-dimensional atomically thin-film-based hetero-structure TFTs are promising for high-performance flexible and transparent applications. Furthermore, these hetero-structured TFTs allow for new functional devices. For example, vertically stacked graphene–molybdenum disulfide hybrid structures currently enabled vertically integrated CMOS inverters [192], memory devices [193, 194], and photodetectors [195, 196]. The development of multi-hetero-structures of two-dimensional

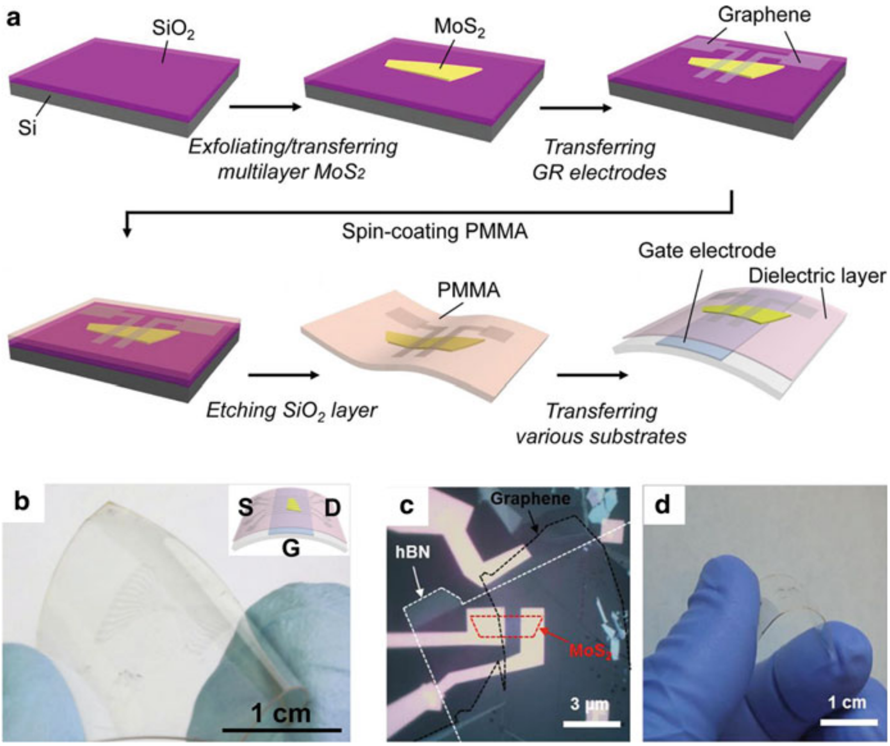

Fig. 7.15 (**a**) A schematic illustration of the fabrication and transfer process used for multilayered MoS_2 thin-film transistors on a flexible plastic substrate. (**b**) An optical image of highly flexible and transparent MoS_2 thin-film transistors on a plastic PET substrate. The *inset* shows a representation of the device structure. (**c**) A photograph of a flexible hetero-structured MoS_2–hBN–graphene (MBG) device. (**d**) A photograph of a MBG device on the plastic PEN substrate, showing its flexibility and transparency. The figures are reprinted with permission from Refs. [188] (Copyright © 2013 Wiley) and [191] (Copyright © 2013 American Chemical Society)

atomically thin films will lead to significant roles for these samples in new functional applications involving flexible and transparent applications.

7.3.4 Stretchable Molybdenum Disulfide Thin-Film Transistors

Beyond flexible applications, the subsequent generation of electronics will involve ubiquitous ambient electronic systems, such as wearable devices and electronic sensing skins. The development of deformable devices, such as transistors, logic circuits, and sensors, is one of the key steps toward the realization of these goals [25, 197–204]. Particularly, mechanically flexible and stretchable transistors are the most essential components of flexible and stretchable applications. The major challenge in this research field is the significant requirement for semiconductors that can remain robust despite mechanical strain. Typical semiconducting materials, including inorganic and organic semiconductors, lack robustness and stretchability; as a result, the strains experienced by these semiconductors must remain at <1 % to avoid fracturing and cracking. Therefore, current researches toward the demonstration of stretchable electronics have explored very unique methods. These researches have focused on the design of devices that can release the substantial strain on semiconducting materials [25, 204]. One commonly used approach in the preparation of stretchable devices is the fabrication of isolated rigid areas on a stretchable elastic substrate [197–199]. These rigid areas are undeformable, such that the TFTs prepared on these protected areas can avoid deformation when the whole substrate is stretched. Another effective method is the engineering of wavy structures in device components [200–202]. Accordion-like structural configurations can relax against applied tensile strain, allowing induced strains to be applied to semiconducting materials within the limit of 1 % strain. Following these unique strategies, graphene has been involved in highly simple and desirable geometries for stretchable applications [160, 205, 206]. Due to its atomically thin thickness and very large Young's modulus [207], graphene can be intentionally formed into ripples or accordion-like wavy structures on a sample surface during the transferring process [160, 205, 206]. Ripple relaxation allows the graphene thin films to stretch to values in excess of 20 % [160, 205], while graphene TFTs prepared on stretchable rubber substrates can perform at a mechanical strain of 5 % [206]. The beneficial properties of atomically thin two-dimensional materials indicate that these samples represent advantageous candidates for usage in stretchable applications. Simply, the same strategy can be applied to molybdenum disulfide atomically thin films, which are more suitable for TFTs because of their large bandgap. The development of CVD growth and the transferring method for molybdenum disulfide films has enabled the demonstration of molybdenum disulfide TFTs on stretchable elastic substrates [173, 178]. Although atomically thin molybdenum disulfide film is a likely material for usage in stretchable applications, further investigation of the intrinsic effect of strain within the molybdenum disulfide crystal structure on electronic properties is essential for device fabrication. Currently, some groups have demonstrated variations in the electronic properties of monolayer and bilayer molybdenum disulfide based on first-principle calculations [208–212]. These researches predicted that the bandgap of molybdenum disulfide films decreases with increasing applied strain and that a semiconductor–metal transition can be induced at a strain of 10 %. To investigate these theoretical predictions, He et al. and Conley et al. collected the photoluminescence and absorption spectrum under strain in the molybdenum disulfide monolayer [213, 214]. These two researches clarified the influence of uniaxial tensile strain in the range from 0 to 2 %. Consequently, a strain-induced bandgap closing was observed, in agreement with first-principle simulations. Moreover, from Raman spectra under induced strains, phonon softening of the doubly degenerate E^1_{2g} mode, followed by energy splitting into two modes with strain in excess of 1 %, breaks the original lattice symmetry

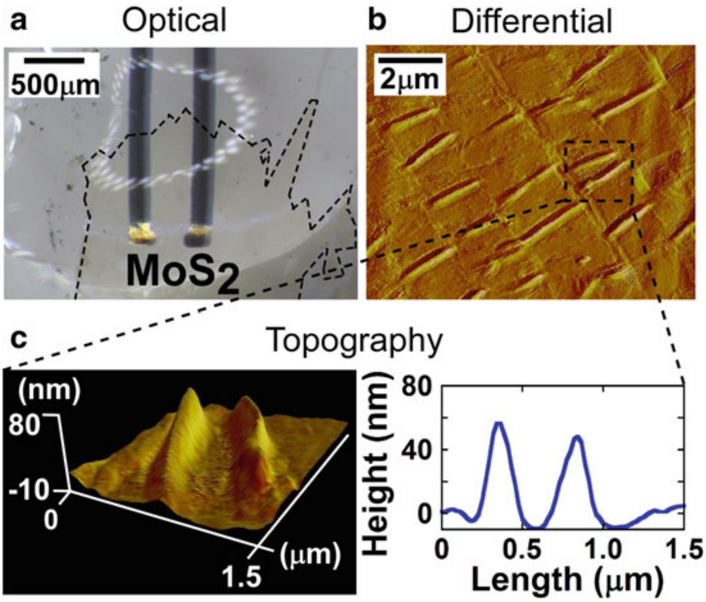

Fig. 7.16 (**a**) A photograph of the transistor channel region of a MoS_2 thin-film transistor mounted on stretchable PDMS substrates. (**b**) A differential atomic force microscopic image, recorded on the surface of MoS_2 films and transferred onto stretchable PDMS. (**c**) Topography (*left*) and height profile (*right*) of the ripple structure on MoS_2 film surfaces, recorded by AFM observations. The figures are reprinted with permission from Ref. [107] (Copyright © 2013 AIP Publishing LLC)

[214–216]. These observations of electronic structure modulation indicate the possible strain engineering and the tuning of optical and electronic properties, with the potential of resulting in novel physical phenomena, pressure-sensing devices, and controllable photonic devices. Stable operation without the degradation or transformation of the electronic properties under strain is a critical requirement for stretchable applications. Therefore, we demonstrated wavy structures of CVD-grown molybdenum disulfide films directly on stretchable PDMS substrates, analogous to graphene [107]. Figure 7.16 reveals an AFM image of the molybdenum disulfide films created with ripples through a transferring procedure from as-grown rigid sapphire substrates to swellable PDMS substrates. These wavy structures of ripples likely assist the molybdenum disulfide films in increasing their expandability because of the strain relaxation allowed against mechanical stretching.

Based on these material and device strategies employed for stretchable applications, as revealed in Fig. 7.17a, we fabricated molybdenum disulfide thin-film transistors on stretchable PDMS substrates using elastic ion gel gate dielectric materials. Figure 7.17b shows the transistor transfer curves under four different tensile strains, performing that the variation in the drain current was very small during stretching to values of ≤ 4 %. Moreover, the charge carrier mobility and

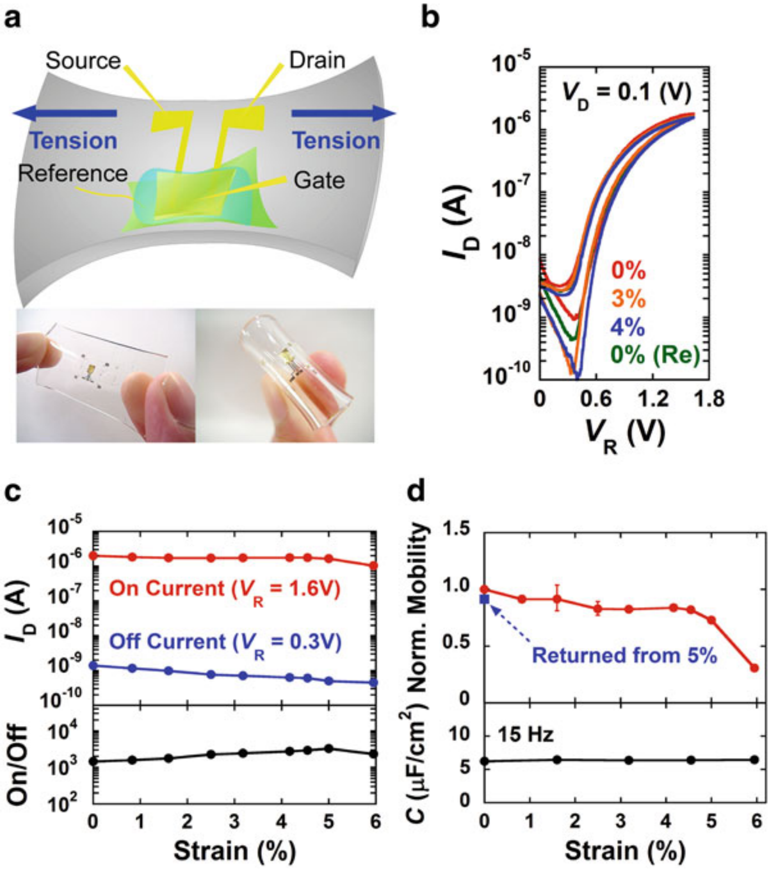

Fig. 7.17 (**a**) A schematic representation and photographs of MoS_2 thin-film transistors under uniaxial stretching. (**b**) Transistor transfer characteristics of MoS_2 thin-film transistors. The *red*, *orange*, *blue*, and *green lines* indicate the transistor transfer curves for strains of 0, 3, and 4 % and after stretching, respectively. (**c**) *Top*: strain dependence of the drain current as a function of reference voltages (V_R) of 1.6 V (*red*) and 0.3 V (*blue*). *Bottom*: strain dependence of the on/off current ratio (*black*). (**d**) *Top*: electron mobility at various strains (*red*). *Bottom*: specific capacitance of an ion-gel/MoS_2 interface at 15 Hz (*bottom*, *black*) at various strains. The mobility is normalized by the results obtained in the absence of an applied tension. The *blue square* in the *top panel* indicates the normalized mobility after stretching at 5 % strain. The figures are reprinted with permission from Ref. [107] (Copyright © 2013 AIP Publishing LLC)

on/off current ratio of these TFTs were approximately constant, even at ≤5 % strain, indicating the stretchability of CVD-grown molybdenum disulfide transistors (Fig. 7.17c, d). Although a significant carrier mobility reduction was observed at strain values in excess of 5 % (Fig. 7.17d), the strain relaxation in the domain boundaries may originate this degradation, as suggested in the case of graphene films [206]. These results provide the potential for stretchable applications based on molybdenum disulfide films. We anticipate that further improvements can be demonstrated to obtain superb stretchability, such as the application of pre-strain procedure to stretchable PDMS substrates before the film transferring process, which would result in larger elastic ripples. Furthermore, the identical strategy and procedure can also be applied to other two-dimensional TMDC films, such as $MoSe_2$ [217], WS_2 [218], and WSe_2 [219]. The material variety of TMDCs provides various transistor polarities, including n- and p-type and ambipolar transport, enabling new electronic and optical applications as a result of combining these films. The outstanding properties of two-dimensional TMDCs provide significant potential for next-generation flexible and stretchable applications.

7.3.5 Summary of TMDC Films and Future Outlook

We have highlighted current studies on the fabrication of thin-film transistors using new two-dimensional molybdenum disulfide thin films for use in flexible and stretchable electronics. The rapid developments of sample preparation techniques, ranging from mechanical exfoliation to scalable CVD, have allowed the demonstration of high-performance molybdenum disulfide TFTs and have expanded the device applications on unconventional substrates. Although molybdenum disulfide TFTs built on flexible plastic and stretchable rubber substrates have superior flexibility and stretchability, further improvements in terms of large-area integration, device performance (such as mobility and switching speed), and operational durability are strongly required. Improving the air stability of the device is also crucial for future practical application. Printing and patterning methods for highly crystalline uniform films will provide the low-temperature, low-cost, and environmentally friendly device fabrication. A variety of two-dimensional atomically thin TMDC films have inspired growing interest in this sample with respect to the exploration of novel complementary functional devices. The application potential of 2 two-dimensional atomically thin TMDC films for flexible and stretchable electronics is vast, ranging from electronics to optoelectronics.

7.4 Conclusions

As described in the overview, nanomaterials are a potentially suitable material for printed flexible and stretchable electronics because the induced strain under R is simply proportional to t. Therefore, SWCNT and TMDC monolayer nanomaterials are possible candidates for next-generation electronics. Importantly, as we explained in this chapter, these materials are excellent active materials for high-performance transistors, and their printing technique is also applicable.

Acknowledgements J.P. acknowledges the Leading Graduate Program in Science and Engineering, Waseda University, from MEXT, Japan, and was supported by Research Fellowship for

Young Scientists, Japan Society for the Promotion of Science (JSPS). T.T. was partially supported by the Funding Program for the Next Generation of World-Leading Researchers and Grants-in-Aid from MEXT (26107533 "Science of Atomic Layers," 26102012 "π-System Figuration" and 25000003 "Specially Promoted Research").

References

1. M.S. Dresselhaus, G. Dresselhaus, P. Avouris (eds.), *Carbon Nanotubes – Synthesis, Structure, Properties, and Applications* (Springer, New York, 2001)
2. A. Javey, J. Kong (eds.), *Carbon Nanotube Electronics* (Springer, New York, 2009)
3. J. Wildoer, L. Venema, A. Rinzler, R. Smalley, C. Dekker, Nature **391**, 59–62 (1998)
4. T. Odom, J. Huang, P. Kim, C. Lieber, Nature **391**, 62–64 (1998)
5. A. Javey, J. Guo, Q. Wang, M. Lundstrom, H. Dai, Nature **424**, 654–657 (2003)
6. T. Durkop, S.A. Getty, E. Cobas, M.S. Fuhrer, Nano Lett. **4**, 35–39 (2004)
7. X. Zhou, J.Y. Park, S. Huang, J. Liu, P.L. McEuen, Phys. Rev. Lett. **95**, 146805 (2005)
8. S. Tans, A. Verschueren, C. Dekker, Nature **393**, 49–52 (1998)
9. R. Martel, T. Schmidt, H.R. Shea, T. Hertel, P. Avouris, Appl. Phys. Lett. **73**, 2447–2449 (1998)
10. A. Javey, J. Guo, D. Farmer, Q. Wang, D. Wang, R. Gordon, M. Lundstrom, H. Dai, Nano Lett. **4**, 447–450 (2004)
11. A. Javey, J. Guo, D. Farmer, Q. Wang, E. Yenilmez, R. Gordon, M. Lundstrom, H. Dai, Nano Lett. **4**, 1319–1322 (2004)
12. A.D. Franklin, M. Luisier, S.-J. Han, G. Tulevski, C.M. Breslin, L. Gignac, M.S. Lundstrom, W. Haensch, Nano Lett. **12**, 758–762 (2012)
13. A. Bachtold, P. Hadley, T. Nakanishi, C. Dekker, Science **294**, 1317–1320 (2001)
14. V. Derycke, R. Martel, J. Appenzeller, P. Avouris, Nano Lett. **1**, 453–456 (2001)
15. A. Javey, Q. Wang, A. Ural, Y. Li, H. Dai, Nano Lett. **2**, 929–932 (2002)
16. Z. Chen, J. Appenzeller, Y. Lin, J.S. Oakley, A.G. Rinzler, J. Tang, S.J. Wind, P.M. Solomon, P. Avouris, Science **311**, 1735 (2006)
17. L. Ding, Z. Zhang, S. Liang, T. Pei, S. Wang, Y. Li, W. Zhou, J. Liu, L.-M. Peng, Nat. Commun. **3**, 1 (2012)
18. R.A. Street (ed.), *Technology and Applications of Amorphous Silicon* (Springer, New York, 2000)
19. S. Uchikoga, MRS Bull. **27**, 881–886 (2002)
20. A.J. Snell, K.D. Mackenzie, W.E. Spear, P.G. LeComber, A.J. Hughes, Appl. Phys. A Solid Surf. **24**, 357–362 (1981)
21. C.D. Dimitrakopoulos, D.J. Mascaro, IBM J. Res. Dev. **45**, 11–27 (2001)
22. S.R. Forrest, Nature **428**, 911–918 (2004)
23. G.H. Gelinck, H. Edzer, A. Huitema, E. Van Veenendaal, E. Cantatore, L. Schrijnemakers, J.B.P.H. Van Der Putten, T.C.T. Geuns, M. Beenhakkers, J.B. Giesbers, B.-H. Hiusman, E.J. Meijer, E.M. Benito, F.J. Touwslager, A.W. Marsman, B.J.E. Van Rens, D.M. De Leeuw, Nat. Mater. **3**, 106–110 (2004)
24. T. Sekitani, U. Zschieschang, H. Klauk, T. Someya, Nat. Mater. **9**, 1015–1022 (2010)
25. T. Sekitani, T. Someya, Adv. Mater. **22**, 2228–2246 (2010)
26. A. Ismach, L. Segev, E. Wachtel, E. Joselevich, Angew. Chem. Int. Ed. **43**, 6140–6143 (2004)
27. A. Ismach, D. Kantorovich, E. Joselevich, J. Am, Chem. Soc. **127**, 11554–11555 (2005)
28. S. Han, X. Liu, C. Zhou, J. Am, Chem. Soc. **127**, 5294–5295 (2005)
29. C. Kocabas, S. Hur, A. Gaur, M. Meitl, M. Shim, J.A. Rogers, Small **1**, 1110–1116 (2005)
30. L. Ding, D. Yuan, J. Liu, J. Am, Chem. Soc. **130**, 5428–5429 (2008)

31. N. Patil, A. Lin, E.R. Myers, K. Ryu, A. Badmaev, C. Zhou, H.-S.P. Wong, S. Mitra, IEEE Trans. Nanotechnol. **8**, 498–504 (2009)
32. L. Ding, A. Tselev, J. Wang, D. Yuan, H. Chu, T.P. McNicholas, Y. Li, J. Liu, Nano Lett. **9**, 800–805 (2009)
33. S.W. Hong, T. Banks, J.A. Rogers, Adv. Mater. **22**, 1826–1830 (2010)
34. C. Wang, K.M. Ryu, L. Gomez, A. Badmaev, J. Zhang, X. Lin, Y. Che, C. Zhou, Nano Res. **3**, 831–842 (2010)
35. X. Liu, S. Han, C. Zhou, Nano Lett. **6**, 34–39 (2006)
36. S.J. Kang, C. Kocabas, T. Ozel, M. Shim, N. Pimparkar, M.A. Alam, S.V. Rotkin, J.A. Rogers, Nat. Nanotechnol. **2**, 230–236 (2007)
37. S.J. Kang, C. Kocabas, H.S. Kim, Q. Cao, M.A. Meitl, D.Y. Khang, J. Rogers, Nano Lett. **7**, 3343–3348 (2007)
38. L. Jiao, B. Fan, X. Xian, Z. Wu, J. Zhang, Z. Liu, J. Am, Chem. Soc. **130**, 12612–12613 (2008)
39. C. Wang, K. Ryu, A. Badmaev, N. Patil, A. Lin, S. Mitra, H.-S.P. Wong, C. Zhou, Appl. Phys. Lett. **93**, 033101 (2008)
40. K. Ryu, A. Badmaev, C. Wang, A. Lin, N. Patil, L. Gomez, A. Kumar, S. Mitra, H.-S.P. Wong, C. Zhou, Nano Lett. **9**, 189–197 (2009)
41. F. Ishikawa, H. Chang, K. Ryu, P. Chen, A. Badmaev, L. De Arco Gomez, G. Shen, C. Zhou, ACS Nano **3**, 73–79 (2009)
42. A. Lin, N. Patil, K. Ryu, A. Badmaev, L. De Arco Gomez, C. Zhou, S. Mitra, H.-S.P. Wong, IEEE Trans. Nanotechnol. **8**, 4–9 (2009)
43. P.G. Collins, M.S. Arnold, P. Avouris, Science **292**, 706–709 (2001)
44. G. Hong, B. Zhang, B. Peng, J. Zhang, W.M. Choi, J.-Y. Choi, J.M. Kim, Z. Liu, J. Am, Chem. Soc. **131**, 14642–14643 (2009)
45. Y. Che, C. Wang, J. Liu, B. Liu, X. Lin, J. Parker, C. Beasley, H.-S.P. Wong, C. Zhou, ACS Nano **6**, 7454–7462 (2012)
46. Q. Cao, J.A. Rogers, Nano Res. **1**, 259–272 (2008)
47. Q. Cao, J.A. Rogers, Adv. Mater. **21**, 29–53 (2009)
48. N. Rouhi, D. Jain, P.J. Burke, ACS Nano **5**, 8471–8487 (2011)
49. C. Kocabas, N. Pimparkar, O. Yesilyurt, S.J. Kang, M.A. Alam, J.A. Rogers, Nano Lett. **7**, 1195–1202 (2007)
50. N. Pimparkar, C. Kocabas, S.J. Kang, J. Rogers, M.A. Alam, IEEE Electron Device Lett. **28**, 593–595 (2007)
51. Q. Cao, H.S. Kim, N. Pimparkar, J.P. Kulkarni, C. Wang, M. Shim, K. Roy, M.A. Alam, J.A. Rogers, Nature **454**, 495–500 (2008)
52. E.S. Snow, J.P. Novak, P.M. Campbell, D. Park, Appl. Phys. Lett. **82**, 2145–2147 (2003)
53. D. Sun, M.Y. Timmermans, Y. Tian, A.G. Nasibulin, E.I. Kauppinen, S. Kishimoto, T. Mizutani, Y. Ohno, Nat. Nanotechnol. **6**, 156–161 (2011)
54. M. Engel, J.P. Small, M. Steiner, M. Freitag, A.A. Green, M.C. Hersam, P. Avouris, ACS Nano **2**, 2445–2452 (2008)
55. M.A. Meitl, Y.X. Zhou, A. Gaur, S. Jeon, M.L. Usrey, M.S. Strano, J.A. Rogers, Nano Lett. **4**, 1643–1647 (2004)
56. M.C. LeMieux, M. Roberts, S. Barman, Y.W. Jin, J.M. Kim, Z. Bao, Science **321**, 101–104 (2008)
57. M. Vosgueritchain, M.C. LeMieux, D. Dodge, Z. Bao, ACS Nano **4**, 6137–6145 (2010)
58. E.S. Snow, P.M. Campbell, M.G. Ancona, J.P. Novak, Appl. Phys. Lett. **86**, 033105 (2005)
59. C. Wang, J. Zhang, K. Ryu, A. Badmaev, L. Gomez, C. Zhou, Nano Lett. **9**, 4285–4291 (2009)
60. C. Wang, J. Zhang, C. Zhou, ACS Nano **4**, 7123–7132 (2010)
61. N. Rouhi, D. Jain, K. Zand, P.J. Burke, Adv. Mater. **23**, 94–99 (2011)
62. T. Takahashi, K. Takei, A.G. Gillies, R.S. Fearing, A. Javey, Nano Lett. **11**, 5408–5413 (2011)

63. C. Wang, J.-C. Chien, K. Takei, T. Takahashi, J. Nah, A.M. Niknejad, A. Javey, Nano Lett. **12**, 1527–1533 (2012)
64. M. Ha, Y. Xia, A.A. Green, W. Zhang, M.J. Renn, C.H. Kim, M.C. Hersam, C.D. Frisbie, ACS Nano **4**, 4388–4395 (2010)
65. P. Chen, Y. Fu, R. Aminirad, C. Wang, J. Zhang, K. Wang, K. Galatsis, C. Zhou, Nano Lett. **11**, 5301–5308 (2011)
66. M. Jung, J. Kim, J. Noh, N. Lim, C. Lim, G. Lee, J. Kim, H. Kang, K. Jung, A.D. Leonard, J.M. Tour, G. Cho, IEEE Trans. Electron Devices **57**, 571–580 (2010)
67. J. Noh, M. Jung, K. Jung, G. Lee, J. Kim, S. Lim, D. Kim, Y. Choi, Y. Kim, V. Subramanian, G. Cho, IEEE Electron Device Lett. **32**, 638–640 (2011)
68. J. Noh, S. Kim, K. Jung, J. Kim, S. Cho, G. Cho, IEEE Electron Device Lett. **32**, 1555–1557 (2011)
69. T. Takenobu, T. Takahashi, T. Kanbara, K. Tsukagoshi, Y. Aoyagi, Y. Iwasa, Appl. Phys. Lett. **88**, 033511 (2006)
70. T. Fukao, S. Nakamura, H. Kataura, M. Shiraishi, Jpn. J. Appl. Phys. **45**, 6524 (2006)
71. S. Fujii, T. Tanaka, S. Nishiyama, H. Kataura, Phys. Status Solidi B **248**, 2692 (2011)
72. D. Fu, H. Okimoto, C.W. Lee, T. Takenobu, Y. Iwasa, H. Kataura, L.-J. Li, Adv. Mater. **22**, 4867 (2010)
73. C.W. Lee, C.H. Weng, L. Wei, Y. Chen, M.B. Chan-Park, C.H. Tsai, K.C. Leou, C.H.P. Poa, J.L. Wang, L.J. Li, J. Phys. Chem. C **112**, 12089 (2008)
74. P. Beecher, P. Servati, A. Rozhin, A. Colli, V. Scardaci, S. Pisana, T. Hasan, A.J. Flewitt, J. Robertson, G.W. Hsieh, F.M. Li, A. Nathan, A.C. Ferrari, W.I. Milne, J. Appl. Phys. **102**, 043710 (2007)
75. T. Takenobu, N. Miura, S.Y. Lu, H. Okimoto, T. Asano, M. Shiraishi, Y. Iwasa, Appl. Phys. Express **2**, 025005 (2009)
76. H. Okimoto, T. Takenobu, K. Yanagi, Y. Miyata, H. Shimotani, H. Kataura, Y. Iwasa, Adv. Mater. **22**, 3981 (2010)
77. H. Okimoto, T. Takenobu, K. Yanagi, H. Shimotani, Y. Miyata, H. Kataura, Y. Iwasa, Jpn. J. Appl. Phys. **49**, 02BD09 (2010)
78. A.M. Rao, P.C. Eklund, S. Bandow, A. Thess, R.E. Smalley, Nature **388**, 257 (1997)
79. T. Takenobu, T. Takano, M. Shiraishi, Y. Murakami, M. Ata, H. Kataura, Y. Achiba, Y. Iwasa, Nat. Mater. **2**, 683 (2003)
80. S. Kazaoui, N. Minami, R. Jacquemin, H. Kataura, Y. Achiba, Phys. Rev. B **60**, 13339 (1999)
81. T. Takenobu, T. Kanbara, N. Akima, T. Takahashi, M. Shiraishi, K. Tsukagoshi, H. Kataura, Y. Aoyagi, Y. Iwasa, Adv. Mater. **17**, 2430 (2005)
82. T. Takenobu, T. Takahashi, N. Akima, M. Shiraishi, H. Kataura, Y. Iwasa, J. Nanosci. Nanotechnol. **7**, 3533 (2007)
83. M. Shim, A. Javey, N.W.S. Kam, H.J. Dai, J. Am. Chem. Soc. **123**, 11512 (2001)
84. Y. Zhou, A. Gaur, S.H. Hur, C. Kocabas, M.A. Meitl, M. Shim, J.A. Rogers, Nano Lett. **4**, 2031 (2004)
85. R. Nouchi, H. Tomita, A. Ogura, H. Kataura, M. Shiraishi, Appl. Phys. Lett. **92**, 253507 (2008)
86. S. Matsuzaki, Y. Nobusa, K. Yanagi, H. Kataura, T. Takenobu, Appl. Phys. Express **4**, 105101 (2011)
87. Y. Takagi, Y. Nobusa, S. Gocho, H. Kudou, K. Yanagi, H. Kataura, T. Takenobu Appl, Phys. Lett. **102**, 143107 (2013)
88. Y. Nobusa, Y. Yomogida, S. Matsuzaki, K. Yanagi, H. Kataura, T. Takenobu, Appl. Phys. Lett. **99**, 183106 (2011)
89. Y. Nobusa, Y. Takagi, S. Gocho, S. Matsuzaki, K. Yanagi, T. Takenobu, Jpn. J. Appl. Phys. **51**, 06FD15 (2012)
90. X. Xu, W. Yao, D. Xiao, T.F. Heinz, Nat. Phys. **10**, 343–350 (2014)
91. K.S. Novoselov, A.K. Geim, S.V. Morozov, D. Jiang, Y. Zhang, S.V. Dubonos, I.V. Grigorieva, A.A. Firsov, Science **306**, 666–669 (2004)

92. K.S. Novoselov, D. Jiang, F. Schedin, T.J. Booth, V.V. Khotkevich, S.V. Morozov, A.K. Geim, Proc. Natl. Acad. Sci. U. S. A. **102**, 10451–10453 (2005)
93. V. Podzorov, M.E. Gershenson, C. Kloc, R. Zeis, E. Bucher, Appl. Phys. Lett. **84**, 3301 (2004)
94. Q.H. Wang, K. Kalantar-Zadeh, A. Kis, J.N. Coleman, M.S. Strano, Nat. Nanotechnol. **7**, 699–712 (2012)
95. B. Radisavljevic, A. Radenovic, J. Brivio, V. Giacometti, A. Kis, Nat. Nanotechnol. **6**, 147–150 (2011)
96. Y. Yoon, K. Ganapathi, S. Salahuddin, Nano Lett. **11**, 3768–3773 (2011)
97. S. Ghatak, A.N. Pal, A. Ghosh, ACS Nano **5**, 7707–7712 (2011)
98. H. Liu, P.D. Ye, IEEE Electron Device Lett. **33**, 546–548 (2012)
99. A. Splendiani, L. Sun, Y. Zhang, T. Li, J. Kim, C.-Y. Chim, G. Galli, F. Wang, Nano Lett. **10**, 1271–1275 (2010)
100. K.F. Mak, C. Lee, J. Hone, J. Shan, T.F. Heinz, Phys. Rev. Lett. **105**, 136805 (2010)
101. A. Ramasubramaniam, D. Naveh, E. Towe, Phys. Rev. B **84**, 205325 (2011)
102. J. Brivio, D.T.L. Alexander, A. Kis, Nano Lett. **11**, 5148–5153 (2011)
103. S. Bertolazzi, J. Brivio, A. Kis, ACS Nano **5**, 9703–9709 (2011)
104. A. Castellanos-Gomez, M. Poot, G.A. Steele, H.S.J. van der Zant, N. Agrait, G. Rubio-Bollinger, Adv. Mater. **24**, 772–775 (2012)
105. M. Chhowalla, H.S. Shin, G. Eda, L.-J. Li, K.P. Loh, H. Zhang, Nat. Chem. **5**, 263–275 (2013)
106. J. Pu, Y. Yomogida, K.-K. Liu, L.-J. Li, Y. Iwasa, T. Takenobu, Nano Lett. **12**, 4013–4017 (2012)
107. J. Pu, Y. Zhang, Y. Wada, J.T.-W. Wang, L.-J. Li, Y. Iwasa, T. Takenobu, Appl. Phys. Lett. **103**, 023505 (2013)
108. C. Lee, H. Yan, L.E. Brus, T.F. Heinz, J. Hone, S. Ryu, ACS Nano **4**, 2695–2700 (2010)
109. A. Molina-Sanchez, L. Wirtz, Phys. Rev. B **84**, 155413 (2011)
110. H. Li, Q. Zhang, C.C.R. Yap, B.K. Tay, T.H.T. Edwin, A. Olivier, D. Baillargeat, Adv. Funct. Mater. **22**, 1385–1390 (2012)
111. B. Chakraborty, A. Bera, D.V.S. Muthu, S. Bhowmick, U.V. Waghmare, A.K. Sood, Phys. Rev. B **85**, 161403 (2012)
112. S.-L. Li, K. Wakabayashi, Y. Xu, S. Nakaharai, K. Komatsu, W.-W. Li, Y.-F. Lin, A. - Aparecido-Ferreira, K. Tsukagoshi, Nano Lett. **13**, 3546–3552 (2013)
113. Z.Y. Zhu, Y.C. Cheng, U. Schwingenschlogl, Phys. Rev. B **84**, 153402 (2011)
114. D. Xiao, G.-B. Liu, W. Feng, X. Xu, W. Yao, Phys. Rev. Lett. **108**, 196802 (2012)
115. A. Molina-Sanchez, D. Sangalli, K. Hummer, A. Marini, L. Wirtz, Phys. Rev. B **88**, 045412 (2013)
116. A. Kormanyos, V. Zolyomi, N.D. Drummond, P. Rakyta, G. Burkard, V.I. Fal'ko, Phys. Rev. B **88**, 045416 (2013)
117. T. Cao, G. Wang, W. Han, H. Ye, C. Zhu, J. Shi, Q. Niu, P. Tan, E. Wang, B. Liu, J. Feng, Nat. Commun. **3**, 1 (2012)
118. H. Zeng, J. Dai, W. Yao, D. Xiao, X. Cui, Nat. Nanotechnol. **7**, 490–493 (2012)
119. K.F. Mak, K. He, J. Shan, T.F. Heinz, Nat. Nanotechnol. **7**, 494–498 (2012)
120. S. Kim, A. Konar, W.-S. Hwang, J.H. Lee, J. Lee, J. Yang, C. Jung, H. Kim, J.-B. Yoo, J.-Y. Choi, Y.W. Jin, S.Y. Lee, D. Jena, W. Choi, K. Kim, Nat. Commun. **3**, 1 (2012)
121. B. Radisavljevic, M.B. Whitwick, A. Kis, ACS Nano **5**, 9934–9938 (2011)
122. H. Wang, L. Yu, Y.-H. Lee, Y. Shi, A. Hsu, M.L. Chin, L.-J. Li, M. Dubey, J. Kong, T. Palacios, Nano Lett. **12**, 4674–4680 (2012)
123. H. Qin, L. Pan, Z. Yao, J. Li, Y. Shi, Appl. Phys. Lett. **100**, 123104 (2012)
124. H. Liu, A.T. Neal, P.D. Ye, ACS Nano **6**, 8563–8569 (2012)
125. S. Das, H.-Y. Chen, A.V. Penumatcha, J. Appenzeller, Nano Lett. **13**, 100–105 (2013)
126. M.-W. Lin, L. Liu, Q. Lan, X. Tan, K.S. Dhindsa, P. Zeng, V.M. Naik, M.M.-C. Cheng, Z. Zhou, J. Phys. D. Appl. Phys. **45**, 345102 (2012)

127. H. Nam, S. Wi, H. Rokni, M. Chen, G. Priessnitz, W. Lu, X. Liang, ACS Nano **7**, 5870–5881 (2013)
128. D. Jariwala, V.K. Sangwan, D.J. Late, J.E. Johns, V.P. Dravid, T.J. Marks, L.J. Lauhon, M.C. Hersam, Appl. Phys. Lett. **102**, 173107 (2013)
129. B. Radisavljevic, A. Kis, Nat. Mater. **12**, 815–820 (2013)
130. B.W.H. Baugher, H.O.H. Churchill, Y. Yang, P. Jarillo-Herrero, Nano Lett. **13**, 4212–4216 (2013)
131. Y. Zhang, J. Ye, Y. Matsuhashi, Y. Iwasa, Nano Lett. **12**, 1136–1140 (2012)
132. M.M. Perera, M.-W. Lin, H.-J. Chuang, B.P. Chamlagain, C. Wang, X. Tan, M.M.-C. Cheng, D. Tomanek, Z. Zhou, ACS Nano **7**, 4449–4458 (2013)
133. Y.J. Zhang, J.T. Ye, Y. Yomogida, T. Takenobu, Y. Iwasa, Nano Lett. **13**, 3023–3028 (2013)
134. H. Shimotani, H. Asanuma, J. Takeya, Y. Iwasa, Appl. Phys. Lett. **89**, 203501 (2006)
135. J.T. Ye, S. Inoue, K. Kobayashi, Y. Kasahara, H.T. Yuan, H. Shimotani, Y. Iwasa, Nat. Mater. **9**, 125–128 (2010)
136. K. Taniguchi, A. Matsumoto, H. Shimotani, H. Takagi, Appl. Phys. Lett. **101**, 042603 (2012)
137. J.T. Ye, Y.J. Zhang, R. Akashi, M.S. Bahramy, R. Arita, Y. Iwasa, Science **338**, 1193–1196 (2012)
138. W. Bao, X. Cai, D. Kim, K. Sridhara, M.S. Fuhrer, Appl. Phys. Lett. **102**, 042104 (2013)
139. Z. Yin, H. Li, H. Li, L. Jiang, Y. Shi, Y. Sun, G. Lu, Q. Zhang, X. Chen, H. Zhang, ACS Nano **6**, 74–80 (2012)
140. W. Choi, M.Y. Cho, A. Konar, J.H. Lee, G.-B. Cha, S.C. Hong, S. Kim, J. Kim, D. Jena, J. Joo, S. Kim, Adv. Mater. **24**, 5832–5836 (2012)
141. H.S. Lee, S.-W. Min, Y.-G. Chang, M.K. Park, T. Nam, H. Kim, J.H. Kim, S. Ryu, S. Im, Nano Lett. **12**, 3695–3700 (2012)
142. M. Fontana, T. Deppe, A.K. Boyd, M. Rinzan, A.Y. Liu, M. Paranjape, P. Barbara, Sci. Rep. **3**, 1634 (2013)
143. O. Lopez-Sanchez, D. Lembke, M. Kayci, A. Radenovic, A. Kis, Nat. Nanotechnol. **8**, 497–501 (2013)
144. R.S. Sundaram, M. Engel, A. Lombardo, R. Krupke, A.C. Ferrari, P. Avouris, M. Steiner, Nano Lett. **13**, 1416–1421 (2013)
145. H. Li, Z. Yin, Q. He, H. Li, X. Huang, G. Lu, D.W.H. Fam, A.I.Y. Tok, Q. Zhang, H. Zhang, Small **8**, 63–67 (2012)
146. F.K. Perkins, A.L. Friedman, E. Cobas, P.M. Campbell, G.G. Jernigan, B.T. Jonker, Nano Lett. **13**, 668–673 (2013)
147. D.J. Late, Y.-K. Huang, B. Liu, J. Acharya, S.N. Shirodkar, J. Luo, A. Yan, D. Charles, U.V. Waghmare, V.P. Dravid, C.N.R. Rao, ACS Nano **7**, 4879–4891 (2013)
148. M. Buscema, M. Barkelid, V. Zwiller, H.S.J. van der Zant, G.A. Steele, A. Castellanos-Gomez, Nano Lett. **13**, 358–363 (2013)
149. H.S.S.R. Matte, A. Gomathi, A.K. Manna, D.J. Late, R. Datta, S.K. Pati, C.N.R. Rao, Angew. Chem. Int. Ed. **49**, 4059–4062 (2010)
150. J.N. Coleman, M. Lotya, A. O'Neill, S.D. Bergin, P.J. King, U. Khan, K. Young, A. Gaucher, S. De, R.J. Smith, I.V. Shvets, S.K. Arora, G. Stanton, H.-Y. Kim, K. Lee, G.T. Kim, G.S. Duesberg, T. Hallam, J.J. Boland, J.J. Wang, J.F. Donegan, J.C. Grunlan, G. Moriarty, A. Shmeliov, R.J. Nicholls, J.M. Perkins, E.M. Grieveson, K. Theuwissen, D.W. McComb, P.D. Nellist, V. Nicolosi, Science **331**, 568–571 (2011)
151. K. Lee, H.-Y. Kim, M. Lotya, J.N. Coleman, G.-T. Kim, G.S. Duesberg, Adv. Mater. **23**, 4178–4182 (2011)
152. K.-G. Zhou, N.-N. Mao, H.-X. Wang, Y. Peng, H.-L. Zhang, Angew. Chem. Int. Ed. **50**, 10839–10842 (2011)
153. V. Nicolosi, M. Chhowalla, M.G. Kanatzidis, M.S. Strano, J.N. Coleman, Science **340**, 1226419 (2013)
154. Z. Zeng, Z. Yin, X. Huang, H. Li, Q. He, G. Lu, F. Boey, H. Zhang, Angew. Chem. Int. Ed. **50**, 11093–11097 (2011)

155. Z. Zeng, T. Sun, J. Zhu, X. Huang, Z. Yin, G. Lu, Z. Fan, Q. Yan, H.H. Hng, H. Zhang, Angew. Chem. Int. Ed. **51**, 9052–9056 (2012)
156. G. Eda, H. Yamaguchi, D. Voiry, T. Fujita, M. Chen, M. Chhowalla, Nano Lett. **11**, 5111–5116 (2011)
157. L.A. King, W. Zhao, M. Chhowalla, D.J. Riley, G. Eda, J. Mater, Chem. A **1**, 8935–8941 (2013)
158. Q. He, Z. Zeng, Z. Yin, H. Li, S. Wu, X. Huang, H. Zhang, Small **8**, 2994–2999 (2012)
159. M.A. Ibrahem, T.-W. Lan, J.K. Huang, Y.-Y. Chen, K.-H. Wei, L.-J. Li, C.W. Chu, RSC Adv **3**, 13193–13202 (2013)
160. K.S. Kim, Y. Zhao, H. Jang, S.Y. Lee, J.M. Kim, K.S. Kim, J.-H. Ahn, P. Kim, J.-Y. Choi, B.H. Hong, Nature **457**, 706–710 (2009)
161. X. Li, W. Cai, J. An, S. Kim, J. Nah, D. Yang, R. Piner, A. Velamakanni, I. Jung, E. Tutuc, S.K. Banerjee, L. Colombo, R.S. Ruoff, Science **324**, 1312–1314 (2009)
162. Y. Zhan, Z. Liu, S. Najmaei, P.M. Ajayan, J. Lou, Small **8**, 966–971 (2012)
163. Y.-H. Lee, X.-Q. Zhang, W. Zhang, M.-T. Chang, C.-T. Lin, K.-D. Chang, Y.-C. Yu, J.T.-W. Wang, C.-S. Chang, L.-J. Li, T.-W. Lin, Adv. Mater. **24**, 2320–2325 (2012)
164. A.M. van der Zande, P.Y. Huang, D.A. Chenet, T.C. Berkelbach, Y. You, G.-H. Lee, T.F. Heinz, D.R. Reichman, D.A. Muller, J.C. Hone, Nat. Mater. **12**, 554–561 (2013)
165. S. Balendhran, J.Z. Ou, M. Bhaskaran, S. Sriram, S. Ippolito, Z. Vasic, E. Kats, S. Bhargava, S. Zhuiykov, K. Kalantar-zadeh, Nanoscale **4**, 461–466 (2012)
166. Q. Ji, Y. Zhang, T. Gao, Y. Zhang, D. Ma, M. Liu, Y. Chen, X. Qiao, P.-H. Tan, M. Kan, J. Feng, Q. Sun, Z. Liu, Nano Lett. **13**, 3870–3877 (2013)
167. Y. Yu, C. Li, Y. Liu, L. Su, Y. Zhang, L. Cao, Sci. Rep. **3**, 1 (2013)
168. X. Wang, H. Feng, Y. Wu, L. Jiao, J. Am, Chem. Soc. **135**, 5304–5307 (2013)
169. W. Wu, D. De, S.-C. Chang, Y. Wang, H. Peng, J. Bao, S.-S. Pei, Appl. Phys. Lett. **102**, 142106 (2013)
170. M. Amani, M.L. Chin, A.G. Birdwell, T.P. O'Regan, S. Najmaei, Z. Liu, P.M. Ajayan, J. Lou, M. Dubey, Appl. Phys. Lett. **102**, 193107 (2013)
171. H. Liu, M. Si, S. Najmaei, A.T. Neal, Y. Du, P.M. Ajayan, J. Lou, P.D. Ye, Nano Lett. **13**, 2640–2646 (2013)
172. W. Zhu, T. Low, Y.-H. Lee, H. Wang, D.B. Farmer, J. Kong, F. Xia, P. Avouris, Nat. Commun. **5**, 1 (2013)
173. K.-K. Liu, W. Zhang, Y.-H. Lee, Y.-C. Lin, M.-T. Chang, C.-Y. Su, C.-S. Chang, H. Li, Y. Shi, H. Zhang, C.-S. Lai, L.-J. Li, Nano Lett. **12**, 1538–1544 (2012)
174. Md.A.B.H. Susan, T. Kaneko, A. Noda and M. Watanabe, J. Am. Chem. Soc., 127, 4976–4983 (2005)
175. J. Lee, M.J. Panzer, Y. He, T.P. Lodge, C.D. Frisbie, J. Am, Chem. Soc. **129**, 4532–4533 (2007)
176. J.H. Cho, J. Lee, Y. Xia, B. Kim, Y. He, M.J. Renn, T.P. Lodge, C.D. Frisbie, Nat. Mater. **7**, 900–906 (2008)
177. Y. Yomogida, J. Pu, H. Shimotani, S. Ono, S. Hotta, Y. Iwasa, T. Takenobu, Adv. Mater. **24**, 4392–4397 (2012)
178. Y.-C. Lin, W. Zhang, J.-K. Huang, K.-K. Liu, Y.-H. Lee, C.-T. Liang, C.-W. Chu, L.-J. Li, Nanoscale **4**, 6637–6641 (2012)
179. Y. Lee, J. Lee, H. Bark, I.-K. Oh, G.H. Ryu, Z. Lee, H. Kim, J.H. Cho, J.-H. Ahn, C. Lee, Nanoscale **6**, 2821–2826 (2014)
180. J. Yang, D. Voiry, S.J. Ahn, D. Kang, A.Y. Kim, M. Chhowalla, H.S. Shin, Angew. Chem. Int. Ed. **52**, 13751–13754 (2013)
181. Y. Shi, W. Zhou, A.-Y. Lu, W. Fang, Y.-H. Lee, A.L. Hsu, S.M. Kim, K.K. Kim, H.Y. Yang, L.-J. Li, J.-C. Idrobo, J. Kong, Nano Lett. **12**, 2784–2791 (2012)
182. D.-S. Tsai, K.-K. Liu, D.-H. Lien, M.-L. Tsai, C.-F. Kang, C.-A. Lin, L.-J. Li, J.-H. He, ACS Nano **7**, 3905–3911 (2013)

183. W. Zhang, J.-K. Huang, C.-H. Chen, Y.-H. Chang, Y.-J. Cheng, L.-J. Li, Adv. Mater. **25**, 3456–3461 (2013)
184. Y. Lee, S. Bae, H. Jang, S. Jang, S.-E. Zhu, S.H. Sim, Y.I. Song, B.H. Hong, J.-H. Ahn, Nano Lett. **10**, 490–493 (2010)
185. B.J. Kim, H. Jang, S.-K. Lee, B.H. Hong, J.-H. Ahn, J.H. Cho, Nano Lett. **10**, 3464–3466 (2010)
186. S.-K. Lee, H.Y. Jang, S. Jang, E. Choi, B.H. Hong, J. Lee, S. Park, J.-H. Ahn, Nano Lett. **12**, 3472–3476 (2012)
187. A.S. Mayorov, R.V. Gorbachev, S.V. Morozov, L. Britnell, R. Jalil, L.A. Ponomarenko, P. Blake, K.S. Novoselov, K. Watanabe, T. Taniguchi, A.K. Geim, Nano Lett. **11**, 2396–2399 (2011)
188. J. Yoon, W. Park, G.-Y. Bae, Y. Kim, H.S. Jang, Y. Hyun, S.K. Lim, Y.H. Kahng, W.-K. Hong, B.H. Lee, H.C. Ko, Small **9**, 3295–3300 (2013)
189. H.-Y. Chang, S. Yang, J. Lee, L. Tao, W.-S. Hwang, D. Jena, N. Lu, D. Akinwande, ACS Nano **7**, 5446–5452 (2013)
190. G.A. Salvatore, N. Munzenrieder, C. Barraud, L. Petti, C. Zysset, L. Buthe, K. Ensslin, G. Troster, ACS Nano **10**, 8809–8815 (2013)
191. G.-H. Lee, Y.-J. Yu, X. Cui, N. Petrone, C.-H. Lee, M.S. Choi, D.-Y. Lee, C. Lee, W.J. Yoo, K. Watanabe, T. Taniguchi, C. Nuckolls, P. Kim, J. Hone, ACS Nano **7**, 7931–7936 (2013)
192. W.J. Yu, Z. Li, H. Zhou, Y. Chen, Y. Wang, Y. Huang, X. Duan, Nat. Mater. **12**, 246–252 (2013)
193. S. Bertolazzi, D. Krasnozhon, A. Kis, ACS Nano **7**, 3246–3252 (2013)
194. K. Roy, M. Padmanabhan, S. Goswami, T.P. Sai, G. Ramalingam, S. Raghavan, A. Ghosh, Nat. Nanotechnol. **8**, 826–830 (2013)
195. L. Britnell, R.M. Ribeiro, A. Eckmann, R. Jalil, B.D. Belle, A. Mishchenko, Y.-J. Kim, R.V. Gorbachev, T. Georgiou, S.V. Morozov, A.N. Grigorenko, A.K. Geim, C. Casiraghi, A.H.C. Neto, K.S. Novoselov, Science **340**, 1311–1314 (2013)
196. W.J. Yu, Y. Liu, H. Zhou, A. Yin, Z. Li, Y. Huang, X. Duan, Nat. Nanotechnol. (2013). doi:10.1038/NNANO.2013.219
197. T. Someya, T. Sekitani, S. Iba, Y. Kato, H. Kawaguchi, T. Sakurai, Proc. Natl. Acad. Sci. U. S. A. **101**, 9966–9970 (2004)
198. T. Sekitani, Y. Noguchi, K. Hata, T. Fukushima, T. Aida, T. Someya, Science **321**, 1468–1472 (2008)
199. I.M. Graz, D.P.J. Cotton, A. Robinson, S.P. Lacour, Appl. Phys. Lett. **98**, 124101 (2011)
200. D.-Y. Khang, H. Jiang, Y. Huang, J.A. Rogers, Science **311**, 208–212 (2006)
201. D.-H. Kim, J.-H. Ahn, W.M. Choi, H.-S. Kim, T.-H. Kim, J. Song, Y.Y. Huang, Z. Liu, C. Lu, J.A. Rogers, Science **320**, 507–511 (2008)
202. K. Park, D.-K. Lee, B.-S. Kim, H. Jeon, N.-E. Lee, D. Whang, H.-J. Lee, Y.J. Kim, J.-H. Ahn, Adv. Funct. Mater. **20**, 3577 (2010)
203. D.J. Lipomi, M. Vosgueritchian, B.C.-K. Tee, S.L. Hellstrom, J.A. Lee, C.H. Fox, Z. Bao, Nat. Nanotechnol. **6**, 788–792 (2011)
204. J.A. Rogers, T. Someya, Y. Huang, Science **327**, 1603–1607 (2010)
205. Y. Wang, R. Yang, Z. Shi, L. Zhang, D. Shi, E. Wang, G. Zhang, ACS Nano **5**, 3645–3650 (2011)
206. S.-K. Lee, B.J. Kim, H. Jang, S.C. Yoon, C. Lee, B.H. Hong, J.A. Rogers, J.-H. Cho, J.H. Ahn, Nano Lett. **11**, 4642–4646 (2011)
207. C. Lee, X. Wei, J.W. Kysar, J. Hone, Science **321**, 385–388 (2008)
208. E. Scalise, M. Houssa, G. Pourtois, V. Afanas'ev, A. Stesmans, Nano Res. **5**, 43–48 (2012)
209. Q. Yue, J. Kang, Z. Shao, X. Zhang, S. Chang, G. Wang, S. Qin, J. Li, Phys. Lett. A **376**, 1166–1170 (2012)
210. T. Li, Phys. Rev. B **85**, 235407 (2012)
211. S. Bhattacharyya, A.K. Singh, Phys. Rev. B **86**, 075454 (2012)
212. P. Lu, X. Wu, W. Guo, X.C. Zeng, Phys. Chem. Chem. Phys. **14**, 13035–13040 (2012)

213. K. He, C. Poole, K.F. Mak, J. Shan, Nano Lett. **13**, 2931–2936 (2013)
214. H.J. Conley, B. Wang, J.I. Ziegler, R.F. Haglund Jr., S.T. Pantelides, K.I. Bolotin, Nano Lett. **13**, 3626–3630 (2013)
215. C. Rice, R.J. Young, R. Zan, U. Bangert, D. Wolverson, T. Georgiou, R. Jalil, K.S. Novoselov, Phys. Rev. B **87**, 081307 (2013)
216. Y. Wang, C. Cong, C. Qiu, T. Yu, Small **9**, 2857–2861 (2013)
217. J.C. Shaw, H. Zhou, Y. Chen, N.O. Weiss, Y. Liu, Y. Huang, X. Duan, Nano Res. (2014). doi:10.1007/s12274-014-0417-z
218. Y. Zhang, Y. Zhang, Q. Ji, J. Ju, H. Yuan, J. Shi, T. Gao, D. Ma, M. Liu, Y. Chen, X. Song, H.Y. Hwang, Y. Cui, Z. Liu, ACS Nano **7**, 8963–8971 (2013)
219. J.K. Huang, J. Pu, C.L. Hsu, M.H. Chiu, Z.Y. Juang, Y.H. Chang, W.H. Chang, Y. Iwasa, T. Takenobu, L.J. Li, ACS Nano **8**, 923–930 (2014)

Chapter 8
Solution-Processed Organic Light-Emitting Devices

Takayuki Chiba, Yong-Jin Pu, and Junji Kido

Abstract Recent progresses on materials and device structures for solution-processed organic light-emitting devices (OLEDs) are discussed. Several solution-processable materials such as fluorescent oligomer, phosphorescent dendrimer, lithium complex, zinc oxide, and polyvinylpyridine are designed and synthesized for achieving multilayer structure. The successful fabrication of solution-processed white phosphorescent OLEDs and tandem OLEDs will pave the way toward printable, low-cost, and large-area solid-state lighting application.

Keywords Solution-processed OLED • Solution-processable material • Multilayer structure • Tandem OLED

8.1 Introduction

Solution processes such as spin coating, inkjet printing, slot-die coating, or spray coating for organic light-emitting devices (OLEDs) are fascinating due to their potential advantages for a production of large-area devices at low cost, although vacuum evaporation (dry) processes are much ahead of the solution processes from the mass production point of view. One of the key solutions to improve the performance of the devices is stacking of a number of successive layers of different functional materials. This multilayer structure allows for the separation of the charge-injecting, charge-transporting, and light-emitting functions to different layers, which leads to a dramatic increase in efficiency and lifetime. In the second section, we discuss our recent studies on fluorescent oligomers [1], phosphorescent dendrimers [2, 3], electron injection materials [4], and polymer binders [5] for solution-processed OLEDs. In the third section, we focus on solution-processed multilayer phosphorescent OLEDs using small molecules. On the basis of estimates from a solvent resistance test of small host molecules, we demonstrate that covalent dimerization or trimerization instead of polymer material can afford conventional

---

T. Chiba • Y.-J. Pu (✉) • J. Kido (✉)
Department of Organic Device Engineering, Research Center for Organic Electronics,
Yamagata University, 4-3-16 Johnan, Yonezawa 992-8510, Japan
e-mail: pu@yz.yamagata-u.ac.jp; kid@yz.yamagata-u.ac.jp

S. Ogawa (ed.), *Organic Electronics Materials and Devices*,
DOI 10.1007/978-4-431-55654-1_8

small host molecules sufficient resistance to alcohols used for processing upper layers. This allows us to construct multilayer OLEDs through subsequent solution-processing steps, achieving record-high power efficiencies of 34 lm W^{-1} at 100 cd m^{-2} for solution-processed white phosphorescent OLEDs [6]. In the fourth section, we discuss the fabrication of a tandem OLED comprising two light-emitting units (LEUs) and a charge generation layer (CGL) between the indium tin oxide (ITO) anode and aluminum (Al) cathode using solution-based processes to simultaneously improve the luminance and device stability. A hybrid process of spin coating and thermal evaporation was utilized for the fabrication [7]. Each LEU with the configuration of first LEUs was fabricated using the spin coating method. Ultrathin (1 nm) Al is deposited as the electron injection layer (EIL) in the first unit, and molybdenum oxide is subsequently deposited as the CGL by thermal evaporation. Tandem OLEDs using hybrid processes showed almost twice the current efficiency of each light-emitting unit (LEU). Additionally, fully solution-processed tandem OLEDs consisting of two LEUs and a CGL between the anode and cathode is fabricated. A zinc oxide (ZnO) and polyethyleneimine-ethoxylated (PEIE) nanoparticle bilayer is used as the EIL in the first LEU and phosphomolybdic acid hydrate (PMA) as the electron acceptor of the CGL. Appropriate choice of solvents during spin coating of each layer ensures that a nine-layered structure is readily fabricated using only solution-based processes [8]. The determined driving voltage and efficiency of the fabricated tandem OLED are the sums of values of the individual LEUs.

8.2 Solution-Processable Materials

8.2.1 Fluorescent Oligomer

The π-conjugated polymers have been extensively studied as solution-processable emitting materials for the field of OLEDs since 1990 [9]. Precise control of molecular weight, end-group structure, and regioregular structure of the conjugated polymers for OLED has been established, but it is not possible to purify structural defects in a polymer chain itself thoroughly. However, monodisperse conjugated oligomers are able to have no structural defects and a better purity from conventional purification methods such as column chromatography, recrystallization, and sublimation. Four novel fluorescent dyes, bis(difluorenyl)amino-substituted carbazole **1**, pyrene **2**, perylene **3**, and benzothiadiazole **4** as solution-processable light-emitting oligomer (Fig. 8.1a), are synthesized by palladium-catalyzed cross-coupling reaction. They are soluble in common organic solvents and can show a high glass transition temperature (T_g) and a good film-forming ability. The energy levels are related to the electronic properties of the central core; the electron-donating carbazole compound showed the lowest ionization potential, and the electron-withdrawing benzothiadiazole compound showed the largest electron affinity.

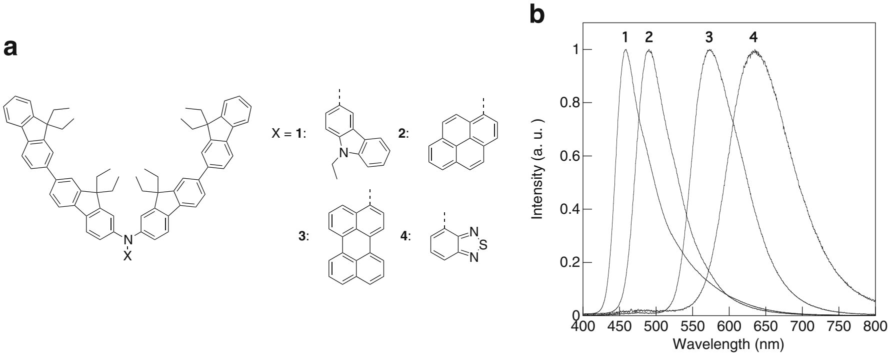

Fig. 8.1 **(a)** Solution-processable fluorescent compounds: bis(difluorenyl)amino-substituted carbazole **1**, pyrene **2**, perylene **3**, and benzothiadiazole **4**. (**b**) EL spectra of the devices with dye 1-4

Emitting color can be easily controlled by a kind of central dyes, and outer fluorene oligomers can sterically prevent excimer formation between the emitting cores in a neat film. All compounds were purified from column chromatography and then thoroughly purified with a train sublimation for OLED application. These sublimable properties are one of the advantages compared with the π-conjugated polymers from the purity point of view, because it is difficult to separate low molecular impurities having similar polarity to the target compounds by column chromatography. In practice, such impurities are regarded as detrimental for device stability. OLEDs with the configuration as ITO/ poly(3,4-ethylenedioxythiophene):poly (styrenesulfonate) (PEDOT: PSS) (40 nm)/**1-4** (50 nm)/ bis(2-methyl-8-quinolinolato) (biphenyl-4-olato)aluminum (BAlq) (50 nm)/LiF (0.5 nm)/Al (100 nm) were fabricated. PEDOT: PSS and the emitting layer were deposited by spin coating. BAlq and LiF/Al layers were deposited by evaporation under vacuum successively. Electroluminescence (EL) spectra of the compounds are well congruous with their photoluminescence (PL) spectrum of the film as shown in Fig. 8.1b, which showed the emission color derived from the central dye (**1**: sky blue, **2**: blue green, **3**: yellow, and **4**: deep red) The outer oligofluorene groups did not affect the emission color because they have a wider energy gap than that of the central dye. The π-conjugations of the fluorene groups and the central dye do not seem to be fully delocalized. Photoluminescence quantum efficiency (PLQE) of the films is determined by using an integrating sphere system under nitrogen atmosphere. PLED of the compounds **1-3** exhibited higher than that of tris(8-quinolinolato) aluminum (Alq_3) film (22 %), which was determined under the same conditions. Multicolor emissions from conjugated oligomer dyes having well-defined structures were achieved in their OLED fabricated from solution processes.

8.2.2 *Phosphorescence Dendrimer*

The combination of the solution process and the phosphorescent compounds can be an ideal choice to achieve low fabrication cost and high efficiency in OLEDs. For the solution process, substitution of functional dendrons on the complex is one of the approaches to solubilize it, and P. L. Burn group has done a lot of pioneering work on the dendrimer OLEDs [10, 11]. The dendron is bulky in volume, so that it can prevent intermolecular interaction between the emitting complexes, resulting in reduction of concentration quenching and high PLQE [12, 13]. From the OLED application point of view, those dendrons have to have enough high charge-transporting ability for low driving voltage[14] and have a larger triplet energy (T_1) level than that of the core complex not to quench the triplet exciton of the complex [15, 16]. In phosphorescent OLEDs, *m*-carbazolylbenzene (mCP) is one of the well-known and widely used host materials, because its T_1 level is high enough (3.0 eV) to confine the phosphorescent emission of the iridium complex, and has bipolar charge-transporting ability [17, 18]. 3,5-(*N*,*N*-di(4-(*n*-butyl)phenyl)amine) (DPA) is also used as hole transport substituent group. We designed and synthesized **(mCP)$_6$Ir** and **(DAP)$_6$Ir** (Fig. 8.2). The phosphorescent iridium complex, **(mCP)$_3$Ir**, attached three mCP dendrons having alkyl groups and high efficiencies of the OLEDs using that complex. In **(mCP)$_3$Ir**, mCP dendrons are attached on each phenyl ring of tris(2-phenylpyridinato)iridium(III) (Ir(ppy)$_3$), and **(mCP)$_3$Ir** is a facial isomer, so that the three mCP dendrons are attached spacially on the same side in the complex and surround only half a side of Ir(ppy)$_3$ as shown in Fig. 8.3a. The fully surrounded Ir(ppy)$_3$ by six host dendrons, **(mCP)$_6$Ir** is shown in Fig. 8.3b. Both of the complexes showed higher PLQE in a neat film than that of half-surrounded **(mCP)$_3$Ir** and **(AP)$_3$Ir**, supporting well the results reported in the literature. PLQEs of the complexes in the neat film are important parameters to estimate the shielding effect of the surrounding dendrons to Ir(ppy)$_3$. PLQEs of the toluene solution and the films were measured by using an integrating sphere system under 331 nm excitation. In a diluted solution, all complexes showed higher PLQE than 70 %, which are comparable to 85 % of unsubstituted Ir(ppy)$_3$.

This result demonstrated that these surrounding dendrons are optically inert and do not affect the emission efficiency of Ir(ppy)$_3$ core. The fully surrounded complexes, **(mCP)$_6$Ir** and **(DAP)$_6$Ir**, showed high PLQE even in a neat film, which is

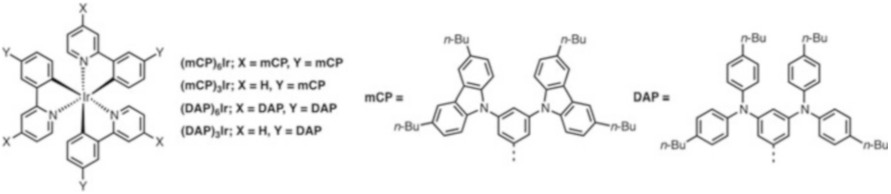

Fig. 8.2 Chemical structures of the dendronized iridium complex (Reprinted from Ref. [3]. Copyright 2012, with permission from Elsevier)

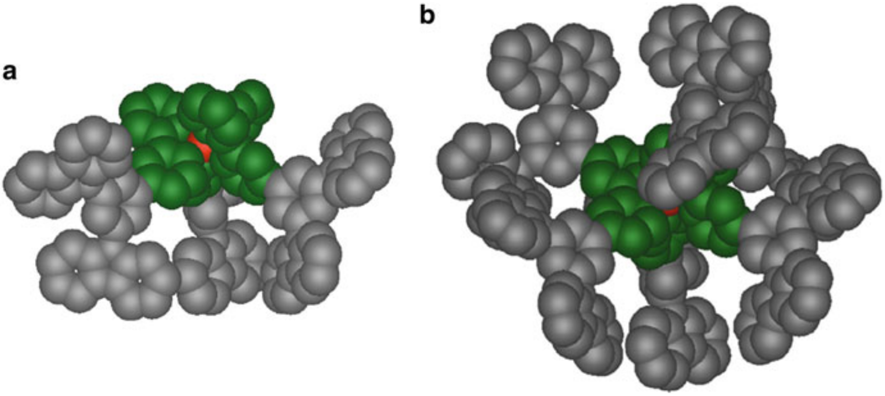

Fig. 8.3 The optimized structures of: (**a**) half-surrounded $(mCP)_3Ir$ and (**b**) fully-surrounded $(mCP)_6Ir$ by PM6 calculation. The butyl groups were replaced to hydrogen in calculation (Reprinted from Ref. [3]. Copyright 2012, with permission from Elsevier)

comparable to PLQE in a dilute solution. On the other hand, the half-surrounded complexes, **$(mCP)_3Ir$** and **$(DAP)_3Ir$**, showed much lower PLQE in a neat film than that in a dilute solution. These complexes are facial isomers; therefore, in **$(mCP)_3Ir$** and **$(DAP)_3Ir$**, some spaces around pyridyl groups of $Ir(ppy)_3$ core are opened, and their three-dimensional structure is like a hemisphere, resulting in only partial suppression of concentration quenching in a neat film of an iridium complex. However, in **$(mCP)_6Ir$** and **$(DAP)_6Ir$**, the bulky host dendrons fully surrounded $Ir(ppy)_3$ and effectively prevented the intermolecular interaction between Ir $(ppy)_3$s. There are still small amounts of reduction of PLQEs from a solution to a neat film, due to the concentration quenching even in the fully substituted complexes. The substituted host dendrons are not large enough to completely suppress the interaction between the core complexes. Adachi et al. reported that an average distance between iridium complexes in a doped film critically influenced PLQE [19]. Förster-type energy transfer between $Ir(ppy)_3$ cores through an overlap of the emission and the absorption causes a decrease of neat film PLQE. If the average distance between iridium complexes is shorter than a Förster radius, a strong quenching occurs. The stronger quenching of **$(mCP)_3Ir$** in the neat film than that of **$(mCP)_6Ir$** is due to the shorter average distance between the cores derived from a smaller number of bulky host dendrons of **$(mCP)_3Ir$** than that of **$(mCP)_6Ir$**. Substitutions of more branched and larger dendrons to the core complexes are desirable to achieve the complete suppression of concentration quenching. Solution-processed OLEDs with **$(mCP)_6Ir$** exhibited high efficiencies, 19 lm W^{-1}, 32 cd A^{-1}, and 12 % of external quantum efficiency (EQE) at 100 cd m^{-2}, and 11 lm W^{-1}, 25 cd A^{-1}, 9.1 % at 1000 cd m^{-2}. The energy levels of the surrounding dendrons intensely affected the charge injection into the emitting layer and the device performance.

8.2.3 Electron Injection Materials

Polymer light-emitting devices (PLEDs) employ low-work-function metals, such as cesium, barium, or calcium, as an electron injection layer (EIL) and a cathode to enhance the electron injection to the emitting layer. However, these metals and the cathode are highly reactive with atmospheric oxygen and moisture, which results in degradation of the device. To avoid these problems, stable alkali metal fluorides, such as LiF or CsF, are commonly used in the EIL of dry-processed OLEDs. Cs_2CO_3 has been reported to be an effective EIL material in solution-processed OLEDs because it is soluble in alcohol solvents and can be coated from solution. The solution-processed Cs_2CO_3 EIL exhibits a high electron injection ability that is comparable to that of alkali metals [20, 21]. However, Cs_2CO_3 still has some disadvantages: it is hygroscopic and unstable in air, and it requires an ultrathin thickness because it is an insulating material. A strong chemical reduction is known to occur between Cs_2CO_3 and the thermally evaporated Al cathode.

Lithium phenolate complexes could be used to form an excellent EIL, and the device performance was much less sensitive to the thickness of the coating of these complexes because of their high electron-transporting ability compared with insulating Cs_2CO_3 [22, 23]. The lithium phenolate complexes also have stability against oxidation and are less hygroscopic. We reported the efficient solution processing of an EIL based on the lithium quinolate complexes (Liq) that are dissolved into alcohol; in this EIL, a low driving voltage and improved stability of the PLEDs is achieved. Liq has high solubility in polar solvents, such as alcohols, and it has a smooth surface morphology. Therefore, Liq can be spin coated onto the emitting polymer; the device prepared with spin-coated Liq as an EIL exhibited a lower turn-on voltage and had a higher efficiency than the devices prepared with spin-coated Cs_2CO_3 or with thermally evaporated calcium.

On the other hand, ZnO nanoparticles have recently been reported to be air-stable electron injection materials in PLEDs [24, 25]. To improve the electron injection ability of the solution-processed EIL that had a thickness of more than 10 nm, we utilized ZnO nanoparticles as a host for Liq or Cs_2CO_3 (Fig. 8.4a). ZnO can enhance the electron injection characteristics through the addition of alkali metal salts [26, 27]. The ZnO nanoparticles, which were synthesized from a zinc acetate precursor [28], were well dispersed into 2-ethoxyethanol at a concentration of 10 mg ml^{-1}.

The average diameter of the ZnO nanoparticles was estimated using transmission electron microscopy (TEM) and dynamic light scattering (DLS) and was approximately 10 nm, with the particles being monodispersed. The mixture of ZnO nanoparticles and Liq formed a thick film with a homogeneous and smooth surface, indicating that Liq is well dispersed around the ZnO nanoparticles. The combination of ZnO and Liq significantly reduced the driving voltage and improved the power efficiency compared to only ZnO or ZnO:Cs_2CO_3 (Fig. 8.4b). This inorganic–organic hybrid EIL is an effective approach for

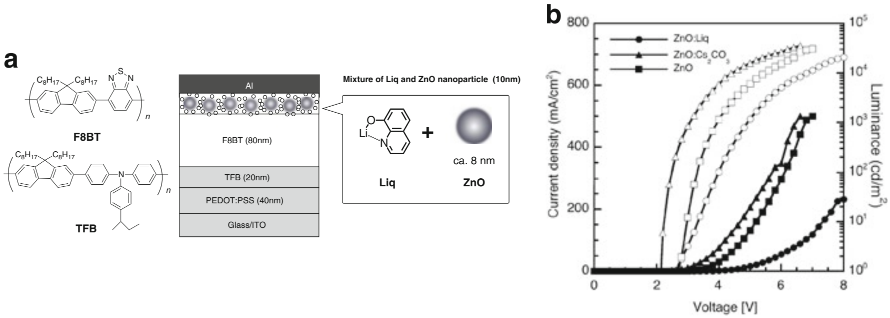

Fig. 8.4 (**a**) The chemical structure of Liq and the structure of the device. (**b**) Current density-voltage (*solid symbol*) and luminance-voltage (*open symbol*) characteristics (Reprinted with the permission from Ref. [4]. Copyright 2011 American Chemical Society)

enhancing the efficiency and the stability of PLEDs, and the thickness can be sufficiently thick for reproducible large-scale devices.

8.2.4 Polymer Binder

The thickness of EILs comprised of compounds such as Liq and Cs_2CO_3 must be ultrathin (<2 nm) to achieve efficient electron injection characteristics due to their poor electron transport properties. However, precise thickness control in the range of a few nanometers is practically impossible for large-scale devices using solution processes such as spin coating and blade coating. In this context, only relatively thick EIL films (10–20 nm) can be mass produced for large PLEDs using solution processing. Herein, we report the use of a mixture of poly(vinylphenylpyridine) and Liq for solution-processable efficient, thick electron injection layers. Vinyl polymers with high solubilities in alcoholic solvents and good film-forming abilities, such as poly(4-vinylpyridine) (PV4Py) and poly[4-(4-vinylphenyl)pyridine] (PVPh4Py) (Fig. 8.5a), were used as binders for Liq, and the effects of the π-conjugation of the polymers on the electron transport and injection characteristics were investigated. The influence of the position of the nitrogen in the pyridine rings was also investigated using poly[2-(4-vinylphenyl)pyridine] (PVPh2Py) and poly [3-(4-vinylphenyl)pyridine] (PVPh3Py).

In the UV–vis absorption spectra, the PVPhPys exhibited smaller energy gaps than that of PV4Py, because the additional phenyl group participates in extended π-conjugation compared with only the pyridine group (Fig. 8.5b). Among the PVPhPys, PVPh2Py exhibited a bathochromically shifted absorption peak compared to those of PVPh3Py and PVPh4Py. The greater π-conjugation of PVPh2Py is probably due to the greater planarity of the structure of 2-phenylpyridine, which results because of the absence of a hydrogen at the ortho position and the consequent reduced steric hindrance. The influence of the concentration of Liq in a

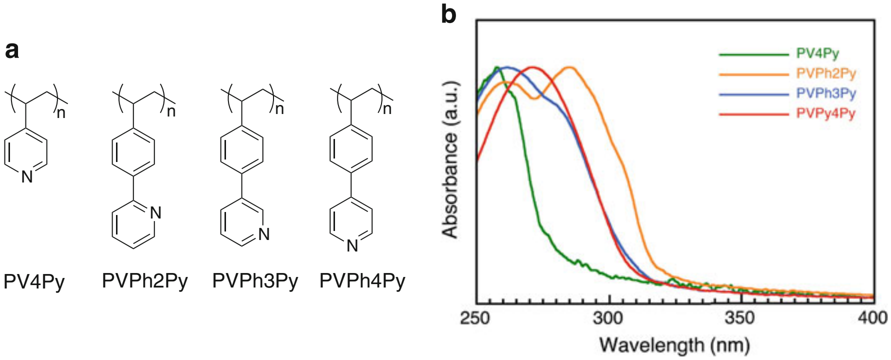

Fig. 8.5 (**a**) Chemical structures and (**b**) UV-vis absorption spectra of the poly(vinylpyridine) compounds

PVPh4Py:Liq mixture in the performance of the *ultrathin* layers of approximately 1.6 nm was investigated. In addition to devices prepared with EIL layers comprised of PVPh4Py with 10, 30, 50, or 70 wt%, two control devices were fabricated using *ultrathin* layers of only Liq and PVPh4Py.

The observed EL spectra of various devices are identical to the emission from F8BT, and no emission was observed from TFB or Liq. This result indicated that the holes and the electrons were confined within the F8BT and that the recombination of the charges occurred only in the F8BT. The device with 100 wt% PVPh4Py exhibited a high turn-on driving voltage of 3.0 V and driving voltages of 5.6 and 8.4 V at 100 and 1000 cd m^{-2}, respectively. The EQE of 0.6 % observed at 1000 cd m^{-2} for the devices with the 100 wt% PVPh4Py layer were lower than those of the device with PVPh4Py doped with Liq. This result suggested that PVPh4Py itself has a poor electron injection property due to its shallow LUMO level of 1.9 eV. However, the device performance dramatically improved when Liq was added to the PVPh4Py. The driving voltage of the devices with PVPh4Py:Liq decreased with increasing Liq concentration from 10 to 70 wt% due to increased electron injection into the F8BT from the Al cathode. The external quantum efficiencies were 4.9–6.9 %. These driving voltages and efficiencies were nearly equivalent to those of the device with the *ultrathin* EIL layer comprised of 100 wt% Liq. In the device with 10 wt% Liq, balanced charge ratio resulted in the highest power efficiency of 23 lm W^{-1} and an EQE of 6.9 % at 1000 cd m^{-2}. Notably, this power efficiency is the highest value reported in the literatures to date for devices with F8BT as the emissive layer (EML) [29, 30]. These results indicate that while PVPh4Py itself is not effective as an EIL, mixing it with Liq does not deteriorate the electron injection properties of Liq and improves the driving voltages and efficiencies of the devices.

The performance of devices with EILs of different thicknesses comprised of the mixtures of PVPh4Py and Liq was investigated. The three types of EILs with thicknesses of 1.6, 8.6, and 16 nm were deposited from solutions with different Liq concentrations using different spin-coating speeds. As the EILs' thickness was

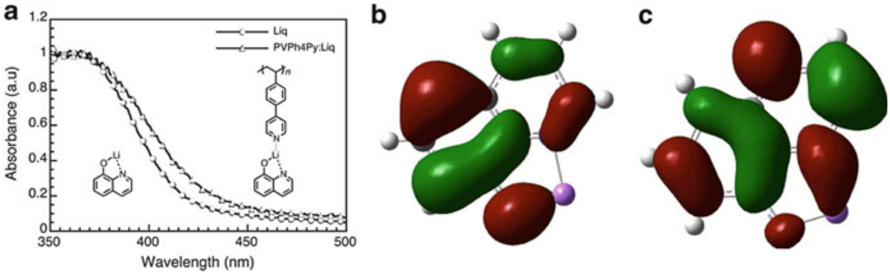

Fig. 8.6 (**a**) UV-vis absorption spectra films of Liq alone and Liq with PVPh4Py film. (**b**) HOMO and (**c**) LUMO of Liq with structures optimized in the grand states by DFT calculation (Reproduced from Ref. [5] by permission of Jon Wiley & Sons Ltd)

increased from 1.6 nm to 16 nm, the driving voltages increased and the EQEs decreased. However, the increase in the voltage and the decrease in the EQE were suppressed in the EILs comprised of PVPh4Py and Liq compared to those for the EIL comprised of 100 wt% Liq. The device with a 50 wt% mixed EIL exhibited the least dependence on the layer thickness, and the lowest driving voltage and the highest EQE for all of the devices was observed for an EIL with thickness of 16 nm. The high driving voltage and low efficiency of the device with the *thick* Liq layer is attributed to the poor electron transport properties of Liq itself. Conversely, mixing PVPh4Py with Liq could improve the electron transport properties of the EIL, and the driving voltage remained low, even for a *thick* EIL. Figure 8.6a shows that the UV absorption edge of the film prepared from the mixture of Liq and PVPh4Py with 50 wt% Liq was red shifted by 15 nm, corresponding to 0.11 eV, compared to that of the pure Liq film. Conversely, both the HOMO levels of Liq and the mixture of 50 wt% Liq and PVPh4Py were the same at 5.5 eV, as determined via photoelectron yield spectroscopy. Consequently, the mixture of Liq and PVPh4Py had a smaller energy gap than that of Liq due to the lower LUMO level of the mixture than that of Liq. Therefore, to understand the distribution of the HOMO and LUMO level in Liq, DFT calculations were conducted. The HOMO is not located on the Li atom (Fig. 8.6b), but the LUMO is associated with the Li atom (Fig. 8.6c). These results suggest that the interactions between the Li atom of Liq and the pyridine ring of PVPh4Py affected the LUMO level. The reduced dependence of EIL performance on the layer thickness will be advantageous for the large-area coating processes, because it is difficult using solution processing to form uniform thin films with an accuracy of a few nanometers.

The position of the nitrogen in the pyridine rings had slight influence on the electron injection properties in the *ultrathin* layers (Fig. 8.7a). Conversely, in the devices with *thin* EILs (approximately 8.6 nm), the position of the nitrogen in the pyridine rings of the polymers had a greater influence on the driving voltage and efficiency. The driving voltage increased in the order PVPh4Py < PVPh3Py < PVPh2Py, Alternatively, the EQE increased in the order PVPh2Py < PVPh3Py < PVPh4Py (Fig. 8.7b). These results suggest that the position of the nitrogen in the pyridine rings significantly affects the electron transport properties of the

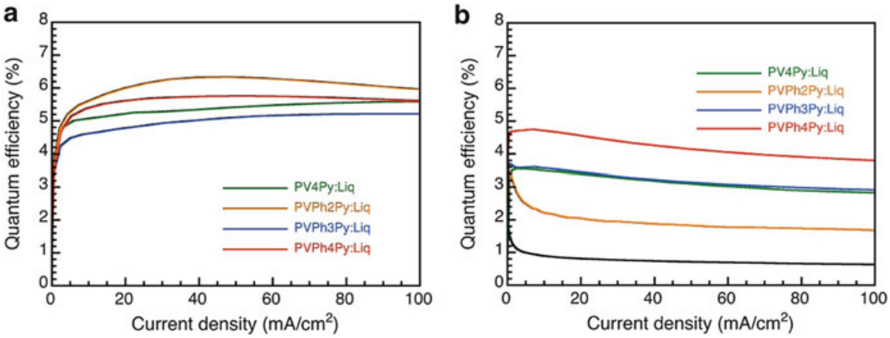

Fig. 8.7 External quantum efficiency–current density characteristics of PLEDs performance with (**a**) *ultrathin* EILs and (**b**) *thin* EILs using PV4Py, PVPh2Py, PVPh3Py and PVPh4Py doped with 50 wt% Liq, respectively, and 100 wt% Liq

polymers, rather than the electron injection properties. Sasabe et al. previously reported that the electron mobility of a series of oligo phenylpyridine derivatives was strongly affected by the position of the nitrogen in the pyridine rings due to C-H$\cdots$N hydrogen bonding interactions [31]. The glass transition temperatures (T_g) were determined *via* differential scanning calorimetry (DSC). The T_g of PVPh4Py was observed at 185 °C, which is higher than that of PV4Py (146 °C) due to the more rigid structure of the phenylpyridine. The T_g of PVPh4Py was also higher than those of PVPh2Py (162 °C) and PVPh3Ph (140 °C), suggesting that the location of the nitrogen at the 4-position of the PVPh4Py enables stronger intermolecular hydrogen bonding interactions than those in PVPh3Py and PVPh2Py. The denser packing of PVPh4Py that results from the stronger hydrogen bonding interactions probably leads to the enhanced electron transport properties observed for the *thick* films.

8.3 Solution-Processed Multilayer Small-Molecule OLEDs

8.3.1 Solubility of Small-Molecule Materials

Small-molecule-based OLEDs typically consist of four or more multiple layers of different materials in precise optoelectrical design. Such multilayer structures allow for the separation of the charge-injecting, charge-transporting, and light-emitting functions to the different layers, thus leading to a marked increase in efficiency and lifetime [32–34]. Although stepwise vacuum evaporation easily achieves the required multilayer structures of small molecules at the expense of high manufacturing cost, it is more challenging in the case of solution processing, because depositing one layer would dissolve the layer beneath it. To achieve the multilayer structures by solution processing, research efforts have focused on π-conjugated polymers that afford a robust hydrophobic layer, on which a hydrophilic layer can be deposited from orthogonal solvents, such as water or water/alcohol mixture [35]. In situ cross-linking reactions have also been explored to afford covalently bound structures that are highly resistant to processing solvents [36–38]. Despite their high mechanical robustness and compatibility with subsequent solution processing, polymers are plagued by limited reproducibility in the device performance because of batch-to-batch variations with respect to molecular weight, polydispersity, regioregularity, and purity. Moreover, their efficiencies are still far below the fluorescent tubes [39]. The highest reported power efficiency of white polymer LEDs is 25 lm W^{-1} thus far [40, 41]. On the other hand, small molecules are very attractive because they have a well-defined molecular structure that offers more reproducibility of synthesis procedures and better understanding of molecular structure–device performance relationships. However, their thin-film assemblies, most of which are amorphous in nature, are easily broken up, even by the orthogonal solvents, because small molecules typically attach to each other only by weak intermolecular forces such as van der Waals, H-bonding, and π–π stacking interactions. Consequently, the highest reported efficiency of solution-processed small-molecule OLEDs still relies on a vacuum-evaporated electron-transporting layer (ETL), which is not practical for low-cost mass production of scalable devices [42]. Herein, we demonstrate highly efficient small-molecule OLEDs in which quadruple organic layers, including a molecular-emitting layer (EML) and ETL, are fully solution processed. The key feature of the devices is the use of newly developed small host molecules in the EML, which are sufficiently resistant to the orthogonal solvents such as alcohols, used for processing upper ETLs, thus allowing us to construct the multilayer structure through subsequent solution-processing steps. While a robust host polymer is typically required to realize the multilayer structure, we simply modified conventional host molecules by covalent dimerization or trimerization to afford sufficient resistance to alcohols. With this approach, record-high efficiencies have been achieved for solution-processed blue, green, and white OLEDs.

Through experiments with 17 host molecules over a wide range of molecular weight from 243 to 1146 (Fig. 8.8), we found that their resistance to alcohols remarkably increasing molecular weight. Figure 8.8b shows the normalized remaining thickness of molecular thin films after rinsing with a variety of alcohols as a function of molecular weight, as measured by ultraviolet–visible absorption spectroscopy. From the best-fit cumulative distribution function, we determined that the threshold molecular weights for achieving 95 % remaining thickness were 775, 811, 849, and 767 for methanol, ethanol, 1-propanol, and 2-propanol, respectively. This result demonstrates that even conventional host molecules can be compatible with the subsequent solution process simply by covalent dimerization or trimerization to exceed the threshold molecular weights, eliminating the need for polymeric counterparts. In addition, this figure covers a wide variety of building blocks, including arene, carbazole, triphenylamine, fluorene, benzothiophene, and

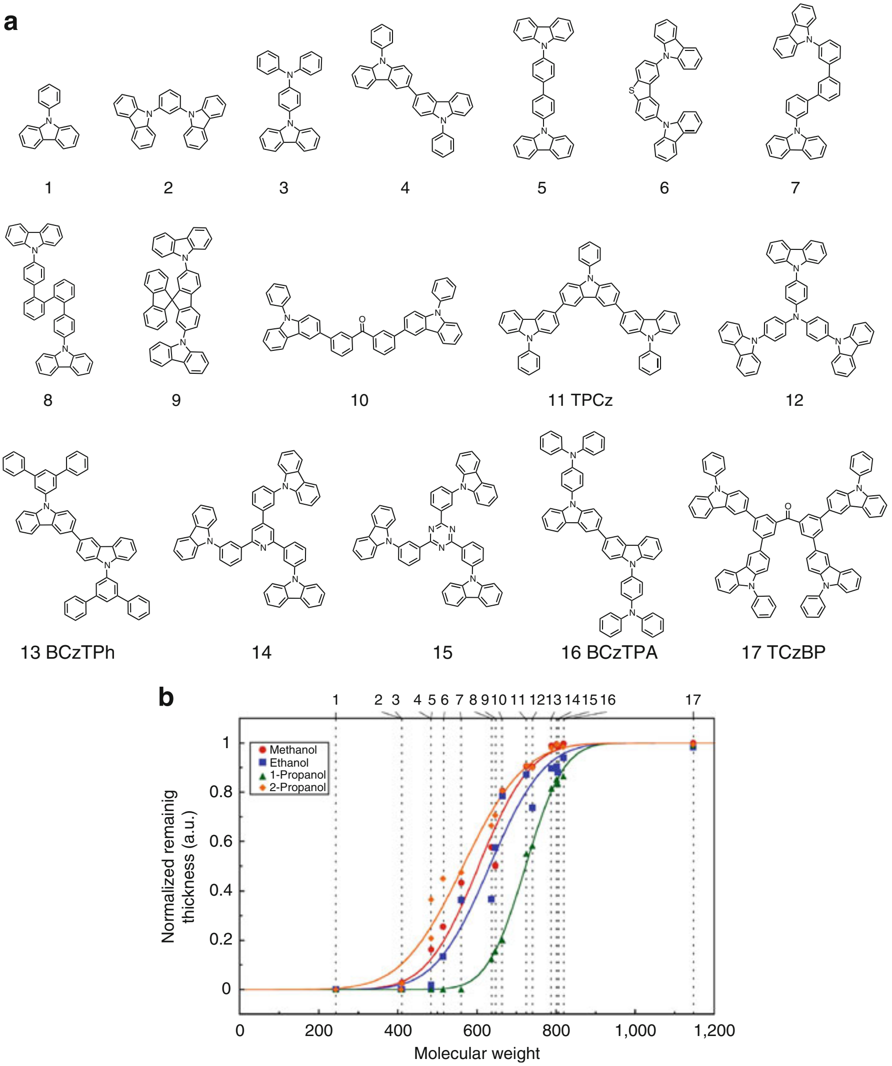

Fig. 8.8 Solvent resistance of molecular thin films. (**a**) Molecular structures of the host molecules arranged in order of increasing molecular weight. (**b**) Plots of normalized remaining thickness of the molecular thin films after rinsing with a variety of alcohols as a function of molecular weight. The solid lines represent the best fit to the cumulative distribution function (Reprinted by permission from Macmillan Publishers: Ref. [6], copyright 1993)

even polar moieties such as benzophenone, pyridine, and triazine, making this approach broadly applicable. We also note that our approach enables subsequent solution processing onto the EML without having to use water, which is detrimental to device efficiency and stability [43–45].

8.3.2 Green and Blue Phosphorescent OLEDs

On the basis of the above estimates, we elected to use two host molecules for green phosphorescent OLEDs: 3,3′:6′,3″-ter(9-phenyl-9H-carbazole) (TPCz) and 3,3′,6,6′-tetrakis(9-phenyl-9H-carbazol-3-yl) benzophenone (TCzBP). The schematic energy diagram of the host molecules is shown in Fig. 8.8b. When mixing the two host molecules in an EML, holes should preferentially reside in the shallow highest occupied molecular orbital of TPCz and electrons in the deep lowest unoccupied molecular orbital of TCzBP. Consequently, we can accurately optimize charge balance in the device by varying the ratio of the two host molecules to achieve high efficiency. By using the two molecules as hosts for $Ir(ppy)_3$, we fabricated green phosphorescent OLEDs, in which quadruple organic layers were fully solution processed. The device configuration was ITO (130 nm)/ PEDOT:PSS (30 nm)/TFB (20 nm)/host:12 wt% Ir(ppy)3 (30 nm)/ 2,2′,2″-(1,3,5-benzinetriyl) tris(1-phenyl-1-H-benzimidazole) (TPBi) (50 nm)/ Liq (1 nm)/Al (100 nm) (Fig. 8.9a). In these devices, TPBi was elected as an ETL because of its sufficient solubility in methanol, enabling the subsequent solution processing on the molecular EML. The most common host polymer poly(*N*-vinylcarbazole) (PVK) was also used for comparison. By mixing a 1:1 ratio of TPCz and TCzBP, we achieved a power efficiency of 52 lm W^{-1} at 100 cd m^{-2}. Indeed, the peak power efficiency reached an extremely high value of 96 lm W^{-1}. The corresponding external quantum efficiency (EQE) was 23 %, which remained as high as 22 % and 20 % at 100 cd m^{-2} and 1,000 cd m^{-2}, respectively. We also note that there is no perceivable change in luminance as a function of viewing angle (Lambertian factor: 1.03), eliminating the possibility of overestimating the efficiencies.

Despite the impressive efficiencies of the green phosphorescent OLEDs, our initial attempt at using standard blue phosphorescent emitter bis(2-(4,6-difluorophenyl)pyridine) (picolinate)iridium(III) (FIrpic) resulted in poor efficiencies. In the blue OLEDs, 4,4′-(3,3′-bi(9H-carbazole)-9,9′-diyl)bis(2,6-diphenyl) benzene (BCzTPh) and 4,4′-(3,3′-bi(9H-carbazole)-9,9′-diyl)bis(*N*,*N*-diphenyl)aniline (BCzTPA) were employed as host molecules, and 2-propanol- soluble 1,3-bis (3-(diphenylphosphoryl)phenyl)benzene (BPOPB) was used as an ETL. The device configuration was ITO (130 nm)/PEDOT:PSS (30 nm)/TFB (20 nm)/host:12 wt% FIrpic (30 nm)/BPOPB (45 nm)/Liq (1 nm)/Al (100 nm) (Fig. 8.9a). While these host molecules have a sufficiently high T_1 level for efficient exothermic energy transfer to the phosphorescent blue emitter, the resulting device exhibited considerable emission from the host molecules at around 420 nm and with a low power efficiency of 6.5 lm W^{-1} at 100 cd m^{-2}. Alternatively, with three-coordinated tris (2-(4,6-difluorophenyl)pyridine)iridium(III) ($Ir(Fppy)_3$), the device efficiencies significantly increased to 36 lm W^{-1} for power efficiency and 20 % for EQE at 100 cd m^{-2}. It is intriguing to note that $Ir(Fppy)_3$ performs five times as well as FIrpic in power efficiency, although these two blue emitters possess almost identical optoelectrical properties. In these devices, the majority of excitons would be generated near the EML/ETL interface because of the relatively large injection

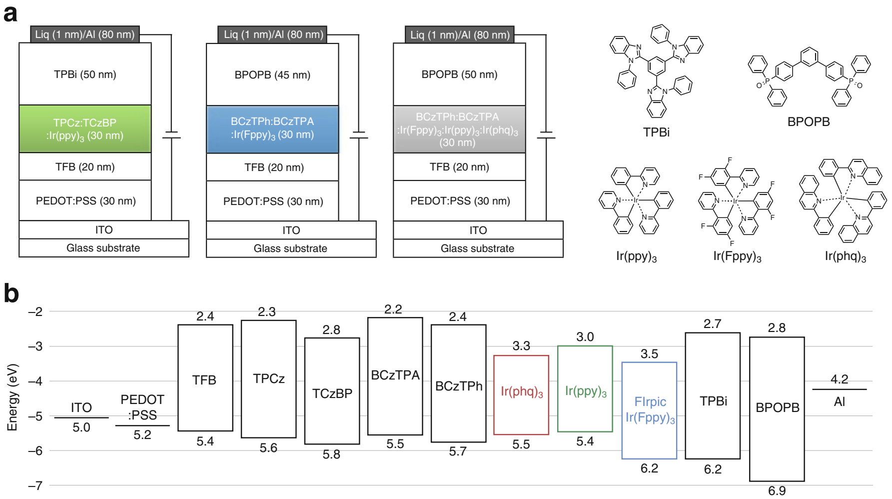

Fig. 8.9 Device structure of the solution-processed OLEDs. (**a**) Schematic of the optimized device and molecular structures of the materials used. (**b**) Schematic energy-level diagram of the materials Reprinted by permission from Macmillan Publishers: Ref. [6], copyright 1993)

barrier between them (Fig. 8.9b) and would subsequently be harvested by the doped blue phosphorescent emitter. In addition, we have previously reported that the direct electron-trapping process of a blue phosphorescent emitter played a major role in efficient electron injection at the EML/ETL interface in evaporated OLEDs [46]. We thus hypothesized that polar picolinate ligand-containing FIrpic would dissolve away from the EML surface upon the subsequent solution processing of the ETL from the 2-propanol solution, resulting in the unwanted host emission and poor device efficiencies.

To verify the hypothesis, we performed depth-profiling measurements of the devices by time-of-flight secondary ion mass spectrometry (TOF-SIMS). These measurements involved Ar_{2500}^{+} gas cluster ion beam etching starting [47] from the ETL surfaces to the underlying substrates. This direction of etching allows for collecting the composition of the EMLs without alternating their original position at the EML/ETL interfaces (peak fronts), while etching and primary ion beams cause peak tailing. Figure 8.10 displays the TOF-SIMS depth profiles of the solution-processed devices with the different blue phosphorescent emitters, FIrpic and Ir (Fppy)$_3$, in comparison with reference devices with a vacuum-evaporated ETL, for which a well-defined interface is expected to exist between the EML and ETL. We focused on $[C_{22}H_{12}F_4IrN_2]^+$ ions with $m/z = 573$ as signatures both of FIrpic and Ir (Fppy)$_3$ to obtain sufficient intensity in the dilute emitters embedded in the host matrix. We also monitored the corresponding molecular ions for the other molecules. The depth resolution was 11.5 nm under our experimental conditions. One observed from the TOF-SIMS depth profiles that the composition at the solution-processed EML/ETL interface was significantly varied between the FIrpic and Ir

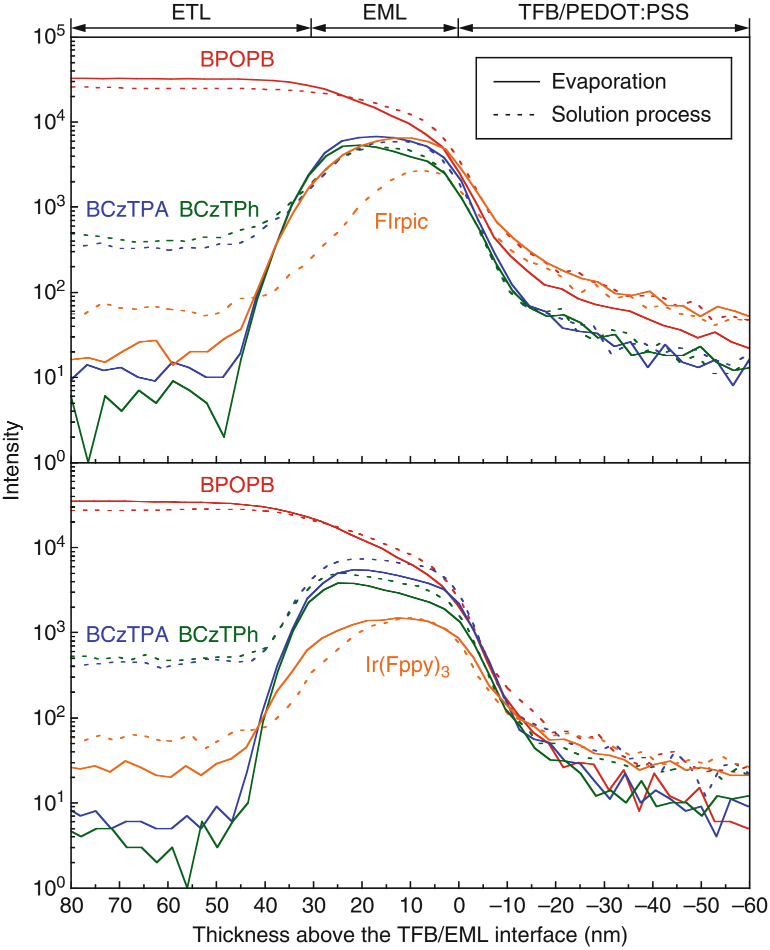

Fig. 8.10 TOF-SIMS depth profiles of the blue OLEDs with different emitters (top: FIrpic and bottom: Ir(Fppy)$_3$). The dashed lines represent depth profiles of the devices using solution-processed BPOPB. The solid lines represent data for reference devices using evaporated BPOPB (Reprinted by permission from Macmillan Publishers: Ref. [6], copyright 1993)

(Fppy)$_3$ system. Ir(Fppy)$_3$ showed a slight reduction in intensity in the interface region of roughly 10–20 nm for the solution-processed device, whereas a noticeable reduction in FIrpic intensity occurred almost over the entire EML, particularly at the EML/ETL interface. The corresponding reduction in the concentration of the blue emitters was also quantitatively observed by high-performance liquid chromatography analysis; the reduction in concentration of emitters was 48 % and 8 % for FIrpic and Ir(Fppy)$_3$, respectively, upon rinsing with pure 2-propanol. These results indicate that almost half of the FIrpic molecules dissolved from the EML while depositing the ETL and the host molecules were compositionally rich in the resulting interface. On the other hand, the Ir(Fppy)$_3$ molecules existed over the entire EML, including the interface even after the deposition of the ETL. The improved device efficiencies upon introduction of Ir(Fppy)$_3$ therefore arise from the efficient electron injection at the EML/ETL interface through the direct electron-trapping process of Ir(Fppy)$_3$. We also note that a very small amount of the EML composition migrated and uniformly distributed into the solution-processed ETL.

8.3.3 White Phosphorescent OLEDs

We fabricated solution-processed multilayer white OLEDs by incorporating green-emitting Ir(ppy)$_3$ (0.2 wt%) and red-emitting tris(2-phenyl-1-quinoline)iridium(III) (Ir(phq)$_3$) (0.7 wt%) into the blue EML. Although the EL spectra of white OLEDs typically depend on current density (in other words, luminance) [20, 48, 49], the resulting solution-processed white OLED surprisingly showed no perceived change in the EL spectra under varying current density. The corresponding color shift in the Commission internationale de l'éclairage (CIE) coordinates was as small as $\Delta x, y = 0.002$, 0.002 between 100 and 1,000 cd m^{-2}. For comparison, the evaporated ETL exhibited relatively strong green and red emissions and a gradual blue shift in the CIE coordinates of $\Delta x, y = 0.054$, 0.002 between 100 and 1,000 cd m^{-2}.

The stable EL spectra can be explained if the green and red emitters were partially washed away from the EML surface upon the solution processing of the ETL, causing electron trapping and recombination preferentially on the blue emitter at the EML/ETL interface. This would provide uniform exciton distribution among the three emitters, and thus the stable EL spectra, because the only exciton generation path left for the green and red emitters is energy transfer from the blue emitter staying at the EML/ETL interface. This hypothesis was confirmed with PL spectroscopy, showing that the red and green emissions of the EML decreased upon rinsing with pure 2-propanol. Similar stable EL spectra have also been observed in evaporated OLEDs, in which the blue emitter is placed at the recombination interface and spatially separated from other emitters as in this case.

Remarkably, we achieved a high power efficiency of 34 lm W^{-1} and an EQE of 21 % at 100 cd m^{-2} for a white emission with a color rendering index (CRI) of 70 and CIE coordinates of 0.43, 0.43 without the use of any outcoupling enhancement. The peak power efficiency and EQE reached 45 lm W^{-1} and 22 %, respectively. To the best of our knowledge, these efficiencies are considerably higher than the highest efficiencies ever reported for white polymer LEDs. In addition, when outcoupling all the photons trapped in the glass substrate, these efficiencies increase by a factor of 1.96 as confirmed by using an index-matched hemisphere lens. As a result, the maximum achievable power efficiency and EQE are expected to be 88 lm W^{-1} and 41 %, respectively. We also note that the solution-processed device showed lower driving voltages and higher efficiencies compared with the corresponding device with an evaporated ETL. The superior performance with a solution-processed ETL was also observed in the green phosphorescent OLEDs using TPBi as an ETL.

8.4 Solution-Processed Tandem OLEDs

8.4.1 Solution-Evaporation Hybrid Tandem OLEDs

Whereas the luminance of OLEDs increases with the current density, high currents promote the degradation of the organic materials [50]. To simultaneously improve the luminance and device stability, Kido et al. developed tandem OLEDs, comprising several stacked LEUs interconnected by CGLs [51]. In general, tandem OLED fabricated by evaporation can have more than ten layers between the anode and the cathode [52–58]. Whereas stepwise vacuum evaporation-based processes can generate multilayered structures, such structures are a challenge to solution-processing techniques because solution-based coating of one layer can dissolve the layer beneath it. Electron injection from CGL into the first LEU is a key factor impacting the characteristics of tandem OLEDs. In vacuum-processed devices, an alkali metal [52, 54, 55] or a bilayer of alkali metal halide and Al [58] effectively enhances electron injection and is used in the EIL of the first LEU. The CGL is composed of electron-accepting materials such as MoO_3, [55] V_2O_5, [54] and WO_3, [59] and electron-donating materials such as arylamine derivatives. It is important to match the Fermi level of electron-accepting materials and the HOMO level of electron-donating materials. However, such metals, metal halides, and metal oxides are not readily solution processable because of their poor solubility in organic solvents.

A hybrid process of spin coating and thermal evaporation was utilized for the tandem OLEDs' fabrication. Each LEU with the configuration of PEDOT:PSS/LE-polymer/EIL was fabricated by spin coating. Ultrathin Al was deposited as the EIL in the first unit, and MoO_3 was subsequently deposited as the CGL by thermal evaporation. Low-work-function metals cannot be used as the EIL for solution-based processing of tandem devices because of their high reactivity with organic solvents, which results in severe degradation of the device. Cs_2CO_3-doped ZnO nanoparticles were used as an EIL on the LE polymer to improve the electron injection from the cathode.

The surface morphology of a spin-coated metal oxide nanoparticle layer appears to be rough, with many gaps due to agglutination of nanoparticles. Consequently, the thin layer of metal oxide nanoparticles cannot protect the first LEU organic layer from the spin-coating solvent of the second LEU organic layer. Thus, we chose PV4Py as a binder to improve the film morphology of the ZnO:Cs_2CO_3 mixture and facilitate the formation of a uniform and dense film to prevent the solvent from soaking into the first LEU. The thermally evaporated MoO_3 layer is insoluble in organic solvents, such as toluene, p-xylene, and dichlorobenzene. Thus, an electron-donating layer can be spin coated on top of the MoO3 layer. Poly

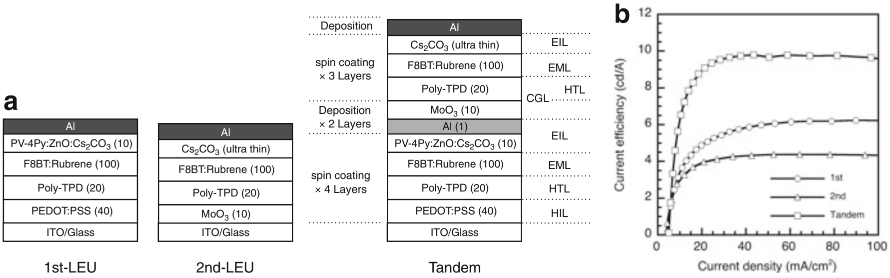

Fig. 8.11 (**a**) Device structure of the 1st-LEU, 2nd-LEU, and tandem OLED. (**b**) Current efficiency–current density characteristics of the 1st-LEU, 2nd-LEU, and tandem OLED (Reproduced from Ref. [7] by permission of The Royal Society of Chemistry)

(4-butylphenyl-diphenyl-amine) (poly-TPD) was used as an electron-donating and hole-transporting layer and was spin coated onto the MoO_3 layer using a dichlorobenzene solution. This combination of MoO_3 and poly-TPD as a prospective CGL may be successful because bilayers of MoO_3 and arylamine derivatives, such as NPD or TPD, can work as an efficient CGL in tandem OLEDs [55]. Poly-TPD is insoluble in toluene and p-xylene; therefore, an LE polymer such as F8BT can be spin coated onto the poly-TPD layer using a p-xylene solution without dissolving the bottom layer. The efficient solution-based processing of EILs in the CGL containing MoO_3/poly-TPD bilayers was employed for the construction of a tandem device as shown in Fig. 8.11a.

At high luminance values of 1000 cd m^{-2}, first LEU and second LEU exhibited efficiencies of 6 cd A^{-1} and 4 cd A^{-1}, respectively (Fig. 8.11b). The efficiency of second LEU was lower than that of the first LEU due to the decrease in the charge balance and the increase in the driving voltage for MoO_3 as an HIL. Nevertheless, the current efficiency of the tandem device increased to 10 cd A^{-1}, which is the sum of the efficiency of the two single devices. The LUMO level of poly-TPD was 2.3 eV, which was just shallow enough to block electrons from the second LEU to the first LEU [60]. The conduction band (CB) of ZnO was 7.4 eV, which was deep enough to block holes from the first LEU to the second LEU. Thus, the emissions are attributed to the recombination of charges that were generated in the CGL without current leakage. These results demonstrate that MoO_3/poly-TPD can function as an effective CGL.

8.4.2 *Fully Solution-Processed Tandem OLEDs*

Recently, solution-processed tandem OLEDs were reported by Colsmann and coworkers [61] with an inverted structure of polymer OLEDs. To the best of our knowledge, there is no report on the tandem OLEDs having the regular configuration of ITO anode and Al cathode. Figure 8.12 shows tandem OLED structure

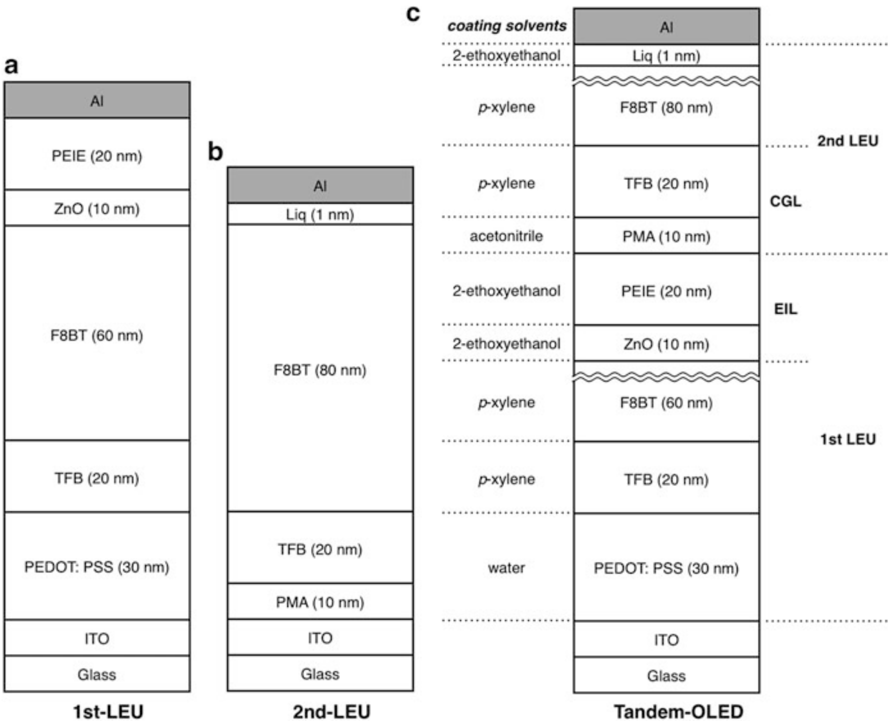

Fig. 8.12 Layered sequence of individual LEUs and the tandem OLED (Reproduced from Ref. [8] by permission of John Wiley & Sons Ltd)

comprising two LEUs (first LEU and second LEU) and a CGL between the anode and the cathode using only solution-based processes. The driving voltage and efficiency of the fabricated tandem OLED are the sums of corresponding values of the component LEUs. These results demonstrate that the solution-processed CGL successfully generated electrons and holes and that the generated electrons and holes were injected into first LEU and second LEU, respectively, when a voltage was applied, resulting in charge recombinations in each LEU. Recently, PEIE and ZnO nanoparticles have been reported as efficient electron-collecting layers between a semiconducting organic layer and a cathode in organic photovoltaics (OPV) [62, 63] and electron injection layers between a cathode and the semiconducting organic layer in OLEDs [64–66]. These properties emerge from their ability to reduce the work function of the cathode. PEIE along with ZnO nanoparticles in the EIL of first LEU and F8BT as the emitting polymer were used. The PEIE and ZnO nanoparticles can be coated as EILs onto the F8BT layer from 2-ethoxyethanol solution and dispersion, respectively. Furthermore, it is required that these EILs not be soluble in the solvent used for coating subsequent layers, which include layers of *p*-type electron-accepting and hole-transporting materials in second LEU, consisting of the CGL. The solvent used for coating the electron acceptor cannot be water or alcohol, both of which dissolve PEIE.

Therefore, we chose phosphomolybdic acid hydrate $(MoO_3)_{12} \cdot H_3PO_4 \cdot (H_2O)_x$ (PMA) [67] as the electron acceptor of the CGL and acetonitrile as the solvent; PMA is soluble in acetonitrile, whereas PEIE, ZnO, and F8BT are not. Furthermore, TFB is chosen as the HTL of second LEU. For coating, a solution of TFB is prepared in *p*-xylene because *p*-xylene does not dissolve PMA, PEIE, or ZnO. However, F8BT is soluble in *p*-xylene; therefore, we carefully monitored the tendency of ZnO and/or PEIE layers to resist the dissolution of underlying F8BT in *p*-xylene using AFM surface images and the intensity of UV–Vis absorption after rinsing with the solvent (Fig. 8.13). Rinsing PEIE-coated F8BT with *p*-xylene reduces the thickness of the underlying F8BT layer, as indicated by the reduction in the intensity of UV–Vis absorption (Fig. 8.13a). The loss of F8BT is attributed to the nonuniform deposition of the PEIE layer (from its solution in 2-ethoxyethanol) on the F8BT layer due to the large difference in the surface energies of the compounds. Consequently, the roughness of the PEIE (0.67 nm) allows *p*-xylene to readily permeate into the F8BT layer. Similar dissolution of the F8BT underlayer on rinsing ZnO-coated F8BT is observed (Fig. 8.13b). It is likely that the roughness of the ZnO layer (2.19 nm) permits *p*-xylene to permeate the layer and dissolve F8BT. It must be noted here that both ZnO and PEIE are not soluble in *p*-xylene. To ensure the formation of a uniform layer of PEIE, we first deposited a layer of ZnO nanoparticles onto F8BT using a dispersion of the same in 2-ethoxyethanol. Once the ZnO layer is dried, it is not able to be redispersed into 2-ethoxyethanol. Subsequently, PEIE (in 2-ethoxyethanol) is uniformly coated onto the ZnO layer. The surface roughness of the F8BT/ZnO/PEIE layer (30 nm) is much smaller than that observed for F8BT/ZnO or F8BT/PEIE. Absence of any change in the intensity of UV–Vis absorption on rinsing F8BT/ZnO/PEIE with *p*-xylene (Fig. 8.13c) clearly demonstrates that a uniformly coated PEIE layer can prevent *p*-xylene. When compared with the device containing EIL composed only of ZnO, the driving voltage of first LEU device is lower and the efficiency is higher, demonstrating the superior electron injection property of the ZnO/PEIE bilayer. The second LEU device (Fig. 8.12b), fabricated with the electron acceptor PMA as HIL, showed a similar low driving voltage, indicating that holes and electrons were generated at the interface of electron acceptor PMA and electron donor TFB, and these two layers worked properly as solution-processed CGL. These devices corresponding to the first LEU and the second LEU were combined to fabricate a solution-processed tandem OLED (Fig. 8.12c), which consists of nine layers except electrodes.

The insolubility of each layer in the solvent used for coating the subsequent layer is carefully monitored, allowing for the successful stacking of the nine layers on the ITO substrate by a series of solution processes. Finally, Al is deposited in vacuum, and solution processing of the electrodes remains a formidable challenge. The driving voltage of the tandem OLED is nearly equal to the sum of the driving voltages of individual LEU devices at low current density. The driving voltage of the tandem OLED increases gradually. In tandem OLEDs, the two LEUs are connected in series; therefore, the current in each LEU must be the same, whereas

a Glass/F8BT/PEIE

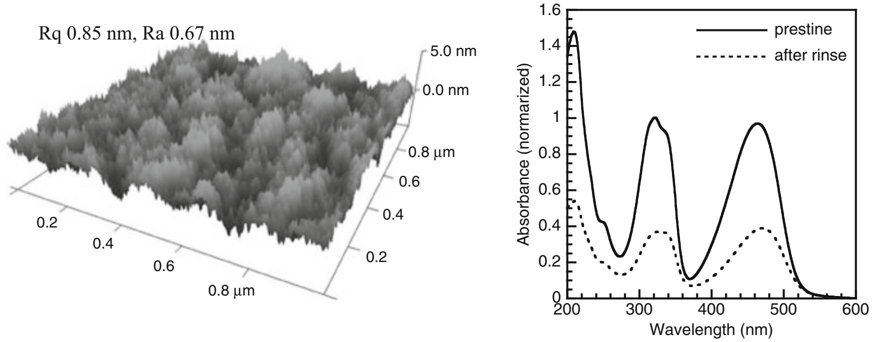

b Glass/F8BT/ZnO

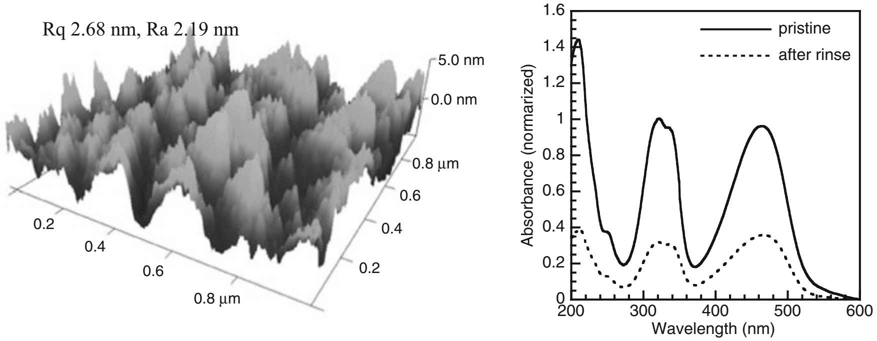

c Glass/F8BT/ZnO/PEIE

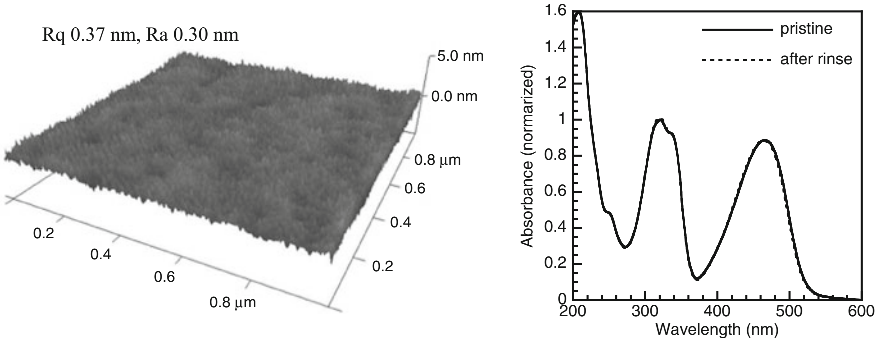

Fig. 8.13 AFM images of the films, and UV–Vis absorption spectra of the pristine and *p*-xylene-rinsed films: (**a**) Glass/F8BT (80 nm)/PEIE (20 nm), (**b**) Glass/F8BT (80 nm)/ZnO (10 nm), and (**c**) Glass/F8BT (80 nm)/ZnO (10 nm)/PEIE (20 nm). The *Rq* is square surface roughness and the *Ra* is average surface roughness (Reproduced from Ref. [8] by permission of John Wiley & Sons Ltd)

the voltage must be the sum of the voltages applied across each LEU. This additive driving voltage in the tandem OLED demonstrates that the interfaces in the device do not offer large resistance to increase voltage, and in particular, the electrons

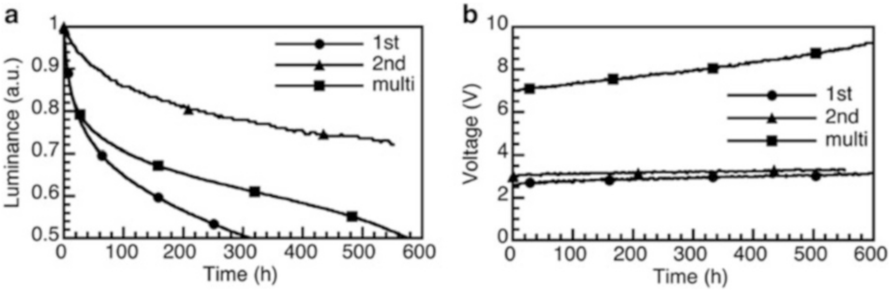

Fig. 8.14 Lifetime of the devices at the same current density (7.5 mA cm^{-2}). Initial luminances were 800 cdm^{-2} for the 1st-LEU, 300 cdm^{-2} for the 2nd-LEU and 1200 cdm^{-2} for the tandem OLED (Reproduced from Ref. [8] by permission of John Wiley & Sons Ltd)

accepted by PMA from TFB in the CGL are smoothly injected into the F8BT of first LEU through the electron-injecting ZnO/PEIE bilayers. Investigation into the stability of the device at the same current density (Fig. 8.14) shows that the absolute value of the device lifetime is strongly dependent on the nature of the materials used. However, a distinct difference between the single LEU device and the tandem OLED is observed. The tandem OLED and first LEU show similar degradation tendencies in terms of the drop in luminance with increasing voltage, although the luminance of the tandem OLED is twofold higher than that of first LEU. This observation shows that the solution-based process used for stacking the two LEUs does contribute to device instability; the advantage of the tandem OLED manifests in the form of high luminance for the lifetime of the device. The stability of second LEU extends to periods much longer than that observed in case of the tandem OLED or first LEU. The luminance of second LEU, however, is much lower than that of the tandem OLED due to lower efficiency. One clear reason for the longer lifetime of second LEU is the absence of the PEDOT:PSS layer, recognized widely as being unstable. Another possible reason can be the ZnO/PEIE bilayer, which is found in the tandem OLED and the other individual LEUs, in common, that show relatively short lifetimes.

8.5 Summary

In summary, solution-processed OLEDs have promising results of large area processing and low fabrication cost for lighting application. Several approaches have been studied to achieve efficiencies of solution-processed OLEDs. In this chapter, we discussed our recent works: 1) solution-processable materials and 2) solution-processed multilayer structure. Fluorescent oligomers and phosphorescent dendrimers are synthesized as solution-processable light-emitting dyes having well-defined structures. Liq, Cs_2CO_3, and ZnO nanoparticles are also studied as a solution-processed electron injection material. In addition, series of (vinylphenyl) pyridine-based polymer binders, PVPh2Py, PVPh3Py, and PVPh4Py, are synthesized for thick layers that can be mass produced for large-area coating using solution processing. In the solution-processed multilayer white phosphorescent OLEDs using small molecules, we achieved high power efficiencies of 34 lm W^{-1} at 100 cd m^{-2} with stable electroluminescence spectra under varying current density. In addition, a tandem OLED consisting of two LEUs and a CGL between the anode and the cathode is fabricated using only solution-based processes. Appropriate choice of solvents during spin coating of each layer ensures that a nine-layered structure is readily fabricated using only solution-based processes. The determined driving voltage and efficiency of the fabricated tandem OLED are the sums of values of the individual LEUs. These results indicate that the CGL formed by the solution-based process successfully generates electrons and holes under applied voltage. The formed electrons are efficiently injected into the first LEU through the ZnO/PEIE bilayer, and the holes are injected into the second LEU. The successful fabrication of solution-processed white phosphorescent OLEDs and tandem OLEDs will pave the way toward printable, low-cost, and large-area white light sources.

References

1. Y.-J. Pu, M. Higashidate, K. Nakayama, J. Kido, J. Mater. Chem. **18**, 4183 (2008)
2. N. Iguchi, Y.-J. Pu, K. Nakayama, M. Yokoyama, J. Kido, Org. Electron. **10**, 465 (2009)
3. Y.-J. Pu, N. Iguchi, N. Aizawa, H. Sasabe, K. Nakayama, J. Kido, Org. Electron. **12**, 2103 (2011)
4. T. Chiba, Y.-J. Pu, M. Hirasawa, A. Masuhara, H. Sasabe, J. Kido, ACS Appl. Mater. Interfaces **4**, 6104 (2012)
5. T. Chiba, Y.-J. Pu, S. Takahashi, H. Sasabe, J. Kido, Adv. Funct. Mater. **24**, 6038 (2014)
6. N. Aizawa, Y.-J. Pu, M. Watanabe, T. Chiba, K. Ideta, N. Toyota, M. Igarashi, Y. Suzuri, H. Sasabe, J. Kido, Nat. Commun. **5**, 5756 (2014)
7. T. Chiba, Y.-J. Pu, H. Sasabe, J. Kido, Y. Yang, J. Mater. Chem. **22**, 22769 (2012)
8. Y.-J. Pu, T. Chiba, K. Ideta, S. Takahashi, N. Aizawa, T. Hikichi, J. Kido, Adv. Mater. **27**, 1327 (2015)
9. J.H. Burroughes, D.D.C. Bradley, A.R. Brown, R.N. Marks, K. Mackay, R.H. Friend, P.L. Burn, A.B. Holmes, Nature **347**, 539 (1990)
10. P.L. Burn, S.C. Lo, I.D.W. Samuel, Adv. Mater. **19**, 1675 (2007)
11. S.C. Lo, P.L. Burn, Chem. Rev. **107**, 1097 (2007)
12. T. Sato, D.-L. Jiang, T. Aida, J. Am. Chem. Soc. **121**, 10658 (1999)
13. A.W. Freeman, S.C. Koene, P.R. Malenfant, M.E. Thompson, J.M. Fréchet, J. Am. Chem. Soc. **122**, 12385 (2000)
14. S. Gambino, S.G. Stevenson, K.A. Knights, P.L. Burn, I.D. Samuel, Adv. Funct. Mater. **19**, 317 (2009)
15. S.-C. Lo, R.E. Harding, C.P. Shipley, S.G. Stevenson, P.L. Burn, I.D. Samuel, J. Am. Chem. Soc. **131**, 16681 (2009)
16. J.J. Kim, Y. You, Y.-S. Park, J.-J. Kim, S.Y. Park, J. Mater. Chem. **19**, 8347 (2009)
17. V. Adamovich, J. Brooks, A. Tamayo, A.M. Alexander, P.I. Djurovich, B.W. D'Andrade, C. Adachi, S.R. Forrest, M.E. Thompson, New J. Chem. **26**, 1171 (2002)
18. B.W. DAndrade, S.R. Forrest, J. Appl. Phys. **94**, 3101 (2003)

19. Y. Kawamura, J. Brooks, J.J. Brown, H. Sasabe, C. Adachi, Phys. Rev. Lett. **96**, 017404 (2006)
20. J. Huang, G. Li, E. Wu, Q. Xu, Y. Yang, Adv. Mater. **18**, 114 (2006)
21. J. Huang, Z. Xu, Y. Yang, Adv. Funct. Mater. **17**, 1966 (2007)
22. J. Endo, T. Matsumoto, J. Kido, Jpn. J. Appl. Phys. **41**, L800 (2002)
23. Y.-J. Pu, M. Miyamoto, K. Nakayama, T. Oyama, Y. Masaaki, J. Kido, Org. Electron. **10**, 228 (2009)
24. D. Kabra, M.H. Song, B. Wenger, R.H. Friend, H.J. Snaith, Adv. Mater. **20**, 3447 (2008)
25. H.J. Bolink, E. Coronado, J. Orozco, M. Sessolo, Adv. Mater. **21**, 79 (2009)
26. H.J. Bolink, H. Brine, E. Coronado, M. Sessolo, Adv. Mater. **22**, 2198 (2010)
27. D. Kabra, L.P. Lu, M.H. Song, H.J. Snaith, R.H. Friend, Adv. Mater. **22**, 3194 (2010)
28. B. Sun, H. Sirringhaus, Nano Lett. **5**, 2408 (2005)
29. L.P. Lu, D. Kabra, R.H. Friend, Adv. Funct. Mater. **22**, 4165 (2012)
30. B.R. Lee, E.D. Jung, J.S. Park, Y.S. Nam, S.H. Min, B.S. Kim, K.M. Lee, J.R. Jeong, R.H. Friend, J.S. Kim, S.O. Kim, M.H. Song, Nat. Commun. **5**, 4840 (2014)
31. H. Sasabe, D. Tanaka, D. Yokoyama, T. Chiba, Y.-J. Pu, K.-i. Nakayama, M. Yokoyama, J. Kido, Adv. Funct. Mater. **21**, 336 (2011)
32. C.W. Tang, S.A. Vanslyke, Appl. Phys. Lett. **51**, 913 (1987)
33. J. Kido, M. Kimura, K. Nagai, Science **267**, 1332 (1995)
34. S. Reineke, F. Lindner, G. Schwartz, N. Seidler, K. Walzer, B. Lussem, K. Leo, Nature **459**, 234 (2009)
35. P.K.H. Ho, J.S. Kim, J.H. Burroughes, H. Becker, S.F.Y. Li, T.M. Brown, F. Cacialli, R.H. Friend, Nature **404**, 481 (2000)
36. X.H. Yang, D.C. Muller, D. Neher, K. Meerholz, Adv. Mater. **18**, 948 (2006)
37. R.Q. Png, P.J. Chia, J.C. Tang, B. Liu, S. Sivaramakrishnan, M. Zhou, S.H. Khong, H.S.O. Chan, J.H. Burroughes, L.L. Chua, R.H. Friend, P.K.H. Ho, Nat. Mater. **9**, 152 (2010)
38. N. Aizawa, Y.-J. Pu, T. Chiba, S. Kawata, H. Sasabe, J. Kido, Adv. Mater. **26**, 7543 (2014)
39. S. Reineke, M. Thomschke, B. Lussem, K. Leo, Rev. Mod. Phys. **85**, 1245 (2013)
40. B.C. Krummacher, V.E. Choong, M.K. Mathai, S.A. Choulis, F. So, F. Jermann, T. Fiedler, M. Zachau, Appl. Phys. Lett. **88**, 113506 (2006)
41. F. Huang, P.I. Shih, C.F. Shu, Y. Chi, A.K.Y. Jen, Adv. Mater. **21**, 361 (2009)
42. B.H. Zhang, G.P. Tan, C.S. Lam, B. Yao, C.L. Ho, L.H. Liu, Z.Y. Xie, W.Y. Wong, J.Q. Ding, L.X. Wang, Adv. Mater. **24**, 1873 (2012)
43. T. Ikeda, H. Murata, Y. Kinoshita, J. Shike, Y. Ikeda, M. Kitano, Chem. Phys. Lett. **426**, 111 (2006)
44. H. Yamamoto, J. Brooks, M.S. Weaver, J.J. Brown, T. Murakami, H. Murata, Appl. Phys. Lett. **99**, 33301 (2011)
45. H.T. Nicolai, M. Kuik, G.A.H. Wetzelaer, B. de Boer, C. Campbell, C. Risko, J.L. Bredas, P.W.M. Blom, Nat. Mater. **11**, 882 (2012)
46. H. Sasabe, N. Toyota, H. Nakanishi, T. Ishizaka, Y.J. Pu, J. Kido, Adv. Mater. **24**, 3212 (2012)
47. I. Yamada, J. Matsuo, N. Toyoda, Nucl. Inst. Methods Phys. Res. B **206**, 820 (2003)
48. J.H. Zou, H. Wu, C.S. Lam, C.D. Wang, J. Zhu, C.M. Zhong, S.J. Hu, C.L. Ho, G.J. Zhou, H.B. Wu, W.C.H. Choy, J.B. Peng, Y. Cao, W.Y. Wong, Adv. Mater. **23**, 2976 (2011)
49. S.Y. Shao, J.Q. Ding, L.X. Wang, X.B. Jing, F.S. Wang, J. Am. Chem. Soc. **134**, 20290 (2012)
50. R. Meerheim, K. Walzer, M. Pfeiffer, K. Leo, Appl. Phys. Lett. **89**, 61111 (2006)
51. T.N.T. Matsumoto, J. Endo, K. Mori, N. Kawamura, A. Yokoi, J. Kido, *SID 03 Digest, 979*, 2003
52. L.S. Liao, K.P. Klubek, C.W. Tang, Appl. Phys. Lett. **84**, 167 (2004)
53. T. Tsutsui, M. Terai, Appl. Phys. Lett. **84**, 440 (2004)
54. F.W. Guo, D.G. Ma, Appl. Phys. Lett. **87**, 173510 (2005)
55. H. Kanno, R.J. Holmes, Y. Sun, S. Kena-Cohen, S.R. Forrest, Adv. Mater. **18**, 339 (2006)
56. M.Y. Chan, S.L. Lai, K.M. Lau, M.K. Fung, C.S. Lee, S.T. Lee, Adv. Funct. Mater. **17**, 2509 (2007)

57. T.W. Lee, T. Noh, B.K. Choi, M.S. Kim, D.W. Shin, J. Kido, Appl. Phys. Lett. **92**, 43301 (2008)
58. T. Chiba, Y.-J. Pu, R. Miyazaki, K. Nakayama, H. Sasabe, J. Kido, Org. Electron. **12**, 710 (2011)
59. M.H. Ho, T.M. Chen, P.C. Yeh, S.W. Hwang, C.H. Chen, Appl. Phys. Lett. **91**, 233507 (2007)
60. G. Sarasqueta, K.R. Choudhury, J. Subbiah, F. So, Adv. Funct. Mater. **21**, 167 (2011)
61. S. Hofle, A. Schienle, C. Bernhard, M. Bruns, U. Lemmer, A. Colsmann, Adv. Mater. **26**, 5155 (2014)
62. Y. Zhou, C. Fuentes-Hernandez, J. Shim, J. Meyer, A.J. Giordano, H. Li, P. Winget, T. Papadopoulos, H. Cheun, J. Kim, M. Fenoll, A. Dindar, W. Haske, E. Najafabadi, T.M. Khan, H. Sojoudi, S. Barlow, S. Graham, J.L. Bredas, S.R. Marder, A. Kahn, B. Kippelen, Science **336**, 327 (2012)
63. A.K. Kyaw, D.H. Wang, V. Gupta, J. Zhang, S. Chand, G.C. Bazan, A.J. Heeger, Adv. Mater. **25**, 2397 (2013)
64. T. Xiong, F. Wang, X. Qiao, D. Ma, Appl. Phys. Lett. **93**, 123310 (2008)
65. Y.H. Kim, T.H. Han, H. Cho, S.Y. Min, C.L. Lee, T.W. Lee, Adv. Funct. Mater. **24**, 3808 (2014)
66. S. Hofle, A. Schienle, M. Bruns, U. Lemmer, A. Colsmann, Adv. Mater. **26**, 2750 (2014)
67. Y. Zhu, Z. Yuan, W. Cui, Z. Wu, Q. Sun, S. Wang, Z. Kang, B. Sun, J. Mater. Chem. A **2**, 1436 (2014)

Chapter 9
Microfluidic Organic Light-Emitting Devices Using Liquid Organic Semiconductors

Takashi Kasahara and Jun Mizuno

Abstract Since a first liquid organic light-emitting diode (liquid OLED) was proposed by Xu and Adachi in 2009, liquid organic semiconductors have been considered to be promising materials for novel electronic device applications. Although the luminescent characteristics of liquid OLEDs have been improved over the past few years, from the viewpoint of device structure, there are technical challenges associated with multicolor light emissions on a single device. In general, liquid OLEDs are simply fabricated by sandwiching a liquid emitter between two electrode-patterned glass substrates, and the thickness of the emitting layer is controlled with single-μm-thick spacer materials. Therefore, the development of integration method for multiple liquid OLEDs on a single device is an important step toward next-generation liquid-based displays. This chapter provides a brief overview of the authors' own recent researches on the microfluidic OLEDs which are novel liquid OLEDs combined with microfluidic technology. The following topics are discussed in this chapter: research background, fabrication methodologies for single-μm-thick electro-microfluidic devices using a novel exposure method and a heterogeneous bonding technique through the use of self-assembled monolayers, and demonstration of multicolor microfluidic OLEDs with the pyrene-based liquid organic semiconductors. The proposed microfluidic OLEDs are believed to open a new possibility for future liquid-based electronic devices.

Keywords Microfluidic OLEDs • Liquid organic semiconductor • Electro-microfluidic • Flexible microfluidic • Flexible OLEDs

---

T. Kasahara
Department of Nanoscience and Nanoengineering, Waseda University, 3-4-1 Okubo,
Shinjuku, Tokyo, 169-8555, Japan

J. Mizuno (✉)
Research Organization for Nano and Life Innovation, Waseda University,
513 Wasedatsurumakicho, Shinjuku, Tokyo 162-0041, Japan
e-mail: mizuno@waseda.jp

S. Ogawa (ed.), *Organic Electronics Materials and Devices*,
DOI 10.1007/978-4-431-55654-1_9

9.1 Introduction of Microfluidic OLEDs

Organic light-emitting diodes (OLEDs) have attracted attention for use in next-generation flat-panel displays and lighting applications [1–5] since Tang and VanSlyke reported the first thin-film OLED in 1987 [6]. It is because OLEDs offer advanced features including self-emission, wide view angle, and reduced weight. Furthermore, in the fields of analytical chemistry, the use of OLEDs has been reported as excitation sources for the detection of the analytes in the microfluidic devices [7–11]. Today, the basic structures of OLEDs are composed of 100-nm-thick functional solid-state organic semiconductor layers sandwiched between two electrodes. In order to realize the patterned multicolor emitting layers on a single panel, several research groups have reported on the fabrication methodologies such as the vacuum deposition through a shadow mask [12], screen printing [13, 14], gravure printing [15, 16], and ink-jet printing [17, 18].

On the other hand, in the last decade, the liquid-based light-emitting devices such as electrochemiluminescence (ECL) cells [19–30] and liquid OLEDs [31–35] have been expected to open new type of display applications. These devices also have given a self-emission under the appropriate voltage. In general, both ECL cells and liquid OLEDs are simply fabricated by sandwiching a liquid emitter between two electrode-patterned glass substrates without the need for vacuum processes. The thickness of the emitting layers is controlled by approximately a few micrometers to several hundred micrometers using spacer materials such as glass beads [19] and insulating films [24, 25]. The emitting layer of traditional ECL cells typically consists of solid-state organic semiconductor materials dissolved in several organic solvents, while in the case of liquid OLEDs, novel liquid organic semiconductors are used as the emitting layer.

ECL is a light-emitting phenomenon generated by electrochemical reactions, and the studies on mechanisms of ECL phenomena have been reported since the mid-1960s [36–38]. In 1964, Hercules showed the light emissions of several aromatic hydrocarbon materials such as anthracene, chrysene, perylene, coronene, 5,6,11,12-tetraphenyltetracene (rubrene), decacyclene, and 1,2:5,6-dibenzanthracene [36]. In 1965, Santhanam and Bard investigated the ECL mechanisms of 9,10-diphenylanthracene (DPA) dissolved in dimethylformamide [37]. In the early studies on ECL, emission mechanisms are reported to be generated by the ion annihilation, i.e., the reaction between radical anions and cations generated cathode and anode surfaces, respectively [38]. Over the past few decades, ECL phenomena have become one of the powerful tools in analytical chemistry. Today, many ECL-based detection methods have been developed, including immunoassay [39], liquid chromatography [40], capillary electrophoresis [41], and flow injection analysis [42]. On the other hand, ECL phenomena have attracted attention for applications in self-luminous display devices [24], and several studies have been reported for enhancing the ECL performance [19–30]. Chang et al. (1999) developed polymer-based ECL cells [19]. They used a poly[9,9-bis(3,6-dioxaheptyl)-fluorene-2,7-diyl] (BDOH-PF) dissolved in dichlorobenzene solution. The device exhibited the luminance of around 100 cd/m^2 at 20 Vdc. Nishimura et al. (2001) developed an ion conductive assistant dopant (ICAD) system for enhancing ECL intensity of rubrene [20]. 1,2-Diphenoxyethane as the ICAD was dissolved in the mixed solvent of acetonitrile and 1,2-dichlorobenzene. The maximum luminance of 183 cd/m^2 was obtained at 8 Vdc from the ECL cell with an ICAD. This luminance value is 600 times higher than ECL cell without an ICAD (0.3 cd/m^2). In 2010, Nobeshima et al. developed an AC-driven ECL cell having quick response and high-efficiency characteristics [21]. They prepared the ECL solutions consisting of 10-mM $Ru(bpy)_3(PF6)_2$ as emitting material and 100-mM tetrabutylammonium perchlorate (TBAP) as electrolyte dissolved in propylene carbonate solution. In that work, the fabricated ECL cell exhibited fast turn-on response of 4 ms in the AC-driven at 200 Hz, which was much faster than that of 1.5 s in the case of DC method. In addition, ECL intensity was improved with AC-driven ECL cells, and the maximum current efficiency reached 0.59 cd/A.

Liquid OLEDs are novel light-emitting devices consisting of the liquid organic semiconductor-based emitting layer. Liquid organic semiconductors have the unique property of being in a liquid phase at room temperature [31–35, 43, 44]. Therefore, unlike the ECL cells having an organic solvent, the emitting layers of liquid OLEDs are not vaporized during constant voltage application. In addition, liquid organic semiconductors are considered to be promising materials not only for OLEDs but also for novel organic electronic device applications such as organic dye lasers [45] and memory devices [46]. In 2009, Adachi's group at Kyushu University presented the first demonstration of a liquid OLED with a carbazole-based liquid organic semiconductor (9-2-ethylhexylcarbazole (EHCz)) [31]. In that work, they used EHCz as the liquid host, and 1 wt% rubrene was doped into EHCz as a guest emitter. This liquid OLED has a simple device structure of a single liquid-emitting layer (rubrene-doped EHCz) sandwiched between indium tin oxide (ITO) anode and cathode. In addition, poly(3,4-ethylenedioxythiophene)/poly (styrenesulfonate) (PEDOT:PSS) was spin coated on an ITO anode as a hole injection layer, while Cs_2CO_3 was formed on an ITO cathode as an electron injection layer. This first liquid OLED successfully exhibited an electroluminescence (EL) emission with a peak wavelength of 555 nm from rubrene, and the highest luminance of 0.35 cd/m^2 was obtained. In 2011, Hirata et al. reported improvement in liquid OLED performance via introduction of electrolyte and a hole-blocking layer [32]. Tetrabutylammonium hexafluorophosphate (TBAHFP) was doped into the host EHCz as the electrolyte, while a titanium dioxide (TiO_2) layer was formed on an ITO cathode as a hole-blocking layer. The maximum luminance of nearly 100 cd/m^2 was realized by the liquid OLED with the structure of ITO anode/PEDOT:PSS/liquid-emitting layer/TiO_2/ITO cathode. This suggests that anions and cations of TBAHFP were moved toward the anode and cathode surfaces, respectively, when a voltage was applied to the liquid OLED. Therefore, the electric dipole layers were formed at the interfaces between the liquid-emitting layer and electrodes, which reduced the injection barrier and facilitated the carrier injection from the electrodes into the liquid-emitting layer. Furthermore, the TiO_2 layer prevented the hole leakage into the cathode, and consequently, the carrier balance was improved. Shim et al. (2012) proposed a novel refreshable liquid OLED having a mesh-structured aluminum cathode and a backside reservoir structure [35]. The performances of the liquid OLEDs have also been improved. However, at present, few liquid organic semiconductors are available for the emitting layer in liquid OLEDs. Therefore, the development of liquid organic semiconductor-based multicolor emitting layers is also a serious challenge toward next-generation display applications.

Although the luminescence characteristics of both the ECL cells and liquid OLEDs have been significantly improved over the past few years, from the viewpoint of device structure, there are technical challenges associated with multicolor light emissions on a single device. It is because only a single liquid-emitting layer has been sandwiched between two electrodes with spacer materials. Therefore, the development of integration methods for multiple liquid OLEDs (or ECL cells) on a single device is an important step for functional multicolor liquid-based light-emitting applications.

In the last few decades, microfluidic devices have been developed for a wide range of chemical and biological applications such as point-of-care diagnostics [47, 48], cell culturing [49], drug discovery [50, 51], and organic synthesis [52] due to their potential platforms for delivering and mixing small amounts of samples on a single device [53]. In general, the miniaturized components such as microchannels, microchambers, and micropumps are fabricated via microelectromechanical systems (MEMS) technologies, including deposition, photolithography, and etching processes. Furthermore, several studies have been reported on incorporation of electrodes into microchannels toward next-generation microfluidic devices [54, 55]. Therefore, MEMS and microfluidic technologies are considered to be potential candidates for novel functional liquid-based display devices.

This chapter aims to give an overview of the recent progress in novel multicolor microfluidic OLEDs which are the functional liquid OLEDs combined with an electro-microfluidic device technology. In the subsequent sections of this chapter, the authors describe a new fabrication methodology of single-μm-thick electro-microfluidic device in order to integrate multiple liquid OLEDs (or ECL cells) on a single device [56–59]. In addition, the characteristics of the microfluidic OLED are presented with novel liquid organic semiconductor-based multicolor emitting layers.

9.2 Fabrication Technology for Microfluidic OLEDs

A design of a prototype microfluidic OLED is shown in Fig. 9.1a. The prototype microfluidic OLED consists of three single-μm-thick SU-8 microchannels sandwiched between the ITO on a glass substrate (anode substrate) and the polyethylene naphthalate (PEN) film with the amine-terminated self-assembled monolayer (SAM)-coated ITO (cathode substrate) [56–58]. A 3 × 3 matrix of light-emitting pixels is formed in a single electro-microfluidic device. The widths of the microchannels are designed to be 1000, 1250, and 1500 μm for ensuring smooth flow of the liquid organic semiconductors. Inlets and outlets are located on the cathode

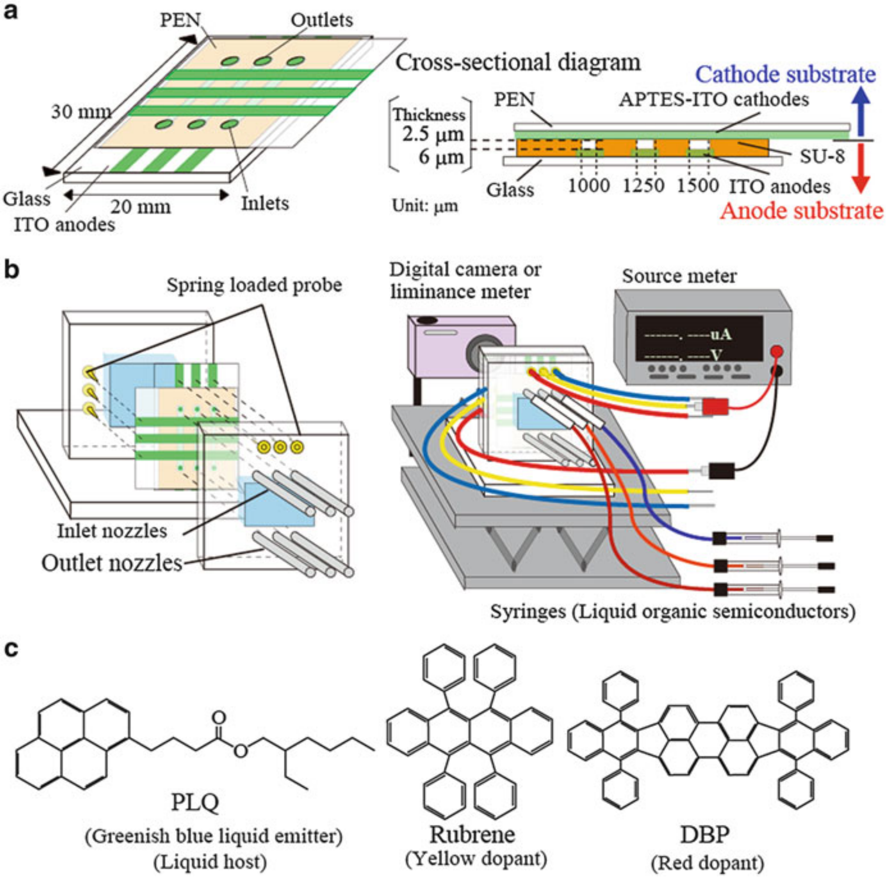

Fig. 9.1 (**a**) Design of the prototype microfluidic OLED. Single-μm-thick SU-8-based microchannels are sandwiched between an ITO anode and cathode. (**b**) Experimental setup of the microfluidic OLED. (**c**) Chemical structures of the employed materials. PLQ is used as both a greenish-blue liquid emitter and a liquid host, while rubrene and DBP are used as yellow and red guest emitters, respectively

substrate. In order to obtain a stable characterization, the evaluation system was designed, as shown in Fig. 9.1b. The microfluidic OLED was clamped between two acrylic plates. The inlet nozzles are connected to one side of the acrylic plates. Thus, in this microfluidic OLED, the liquid-emitting layers can be formed on demand by injecting liquid organic semiconductors from the inlet nozzles into the microchannels with syringes. The used emitters are individually collected from outlet nozzles. The spring-loaded probes embedded in the plates are utilized for the electrical connection of the anode and cathode electrodes to the source meter (Keithley Instruments, Inc., Model 2400). EL emissions and luminance from the microfluidic OLED are monitored with digital camera and luminance meter (Konica Minolta LS-110), respectively.

In this section, three kinds of liquid organic semiconductor-based emitting layers are introduced to evaluate the performance of the microfluidic OLED. The chemical structures of the employed materials are illustrated in Fig. 9.1c. A novel pyrene-based liquid organic semiconductor (1-pyrenebutyric acid 2-ethylhexyl ester (PLQ)) (Nissan Chemical Industries, Ltd.) was used as both a greenish-blue liquid emitter and a liquid host for solid-state fluorescent guest dopants [58]. According to energy levels of PLQ reported by Hirata et al. (2012), its highest occupied molecular orbital (HOMO) and lowest unoccupied molecular orbital (LUMO) levels are located at 5.8 and 2.6 eV, respectively [33]. Here, rubrene and tetraphenyldibenzoperiflanthene (DBP), which have been utilized in the emitting layer of the solid-state OLEDs [60–65], were selected as the yellow and red guest emitters, respectively. For doping guest emitter into the host PLQ, first, both the PLQ and guest emitter were dissolved in dichloromethane (CH_2Cl_2) solution. Then, for evaporating CH_2Cl_2, the sample solutions were placed in a vacuum oven at 80 °C for 5 h. Furthermore, in accordance with the studies of Hirata et al. [32, 33] and Shim et al. [35], 0.25 wt% tributylmethylphosphonium bis(trifluoromethanesulfonyl)imide (TMP-TFSI) as electrolyte was also introduced into the prepared emitters [56, 58, 59].

The fabrication process of the prototype microfluidic OLED is illustrated in Fig. 9.2. The anode and cathode substrates were separately fabricated via photolithography and wet etching. Then, according to the heterogeneous bonding technique developed by Tang and Lee (2010) [66], the anode and cathode substrates were bonded through the use of amine- and epoxy-terminated SAMs to form single-μm-thick microchannel structures. Epoxy-terminated SAM of 3-glycidyloxypropyltrimethoxysilane (GOPTS, 98 wt%) and amine-terminated SAM of 3-aminopropyltriethoxysilane (APTES, 98 wt%) were used for the anode and cathode substrates, respectively.

On the anode substrate part, an ITO-coated glass substrate was used, and the surface was ultrasonic cleaned with acetone and isopropyl alcohol (IPA) for 10 and 5 min, respectively, prior to use (Fig. 9.2a). The ITO anodes were patterned by standard photolithography with positive photoresist, followed by wet etching with an aqua regia solution of $HCl:HNO_3$ in the ratio of 5:1 (Fig. 9.2b). Negative photoresist SU-8 3005 (MicroChem Co.) was spin coated on the patterned ITO-coated glass substrate and then soft baked at 100 °C for 10 min. For forming open microchannel structures on the ITO anodes, UV exposure was carried out through a photomask. The postexposure bakes were performed at 65 °C for 2 min, and then at 95 °C for 5 min on a hot plate. The substrate was subsequently developed by the SU-8 developer (MicroChem Co.) at room temperature, followed by rinsing with IPA. Finally, the hard baking was performed at 180 °C for 30 min (Fig. 9.2c). For forming GOPTS-SAM only on the SU-8 layer, the ITO surfaces in the microchannels were covered with a sacrificial layer of positive resist (Tokyo Ohka Kogyo Co., TSMR-V90) (Fig. 9.2d). This process plays an important role to fabricate shallow microchannels because the chemical reaction between APTES- and GOPTS-SAMs can be prevented in the microchannels during the bonding process [56]. On the cathode substrate part, the ITO-coated PEN film substrate was used (Fig. 9.2e), and the pattern of ITO cathodes was formed on a PEN film using the same process as the ITO anodes (Fig. 9.2f). The inlet and outlet were mechanically punched out using a sharpened needle of 1 mm in diameter

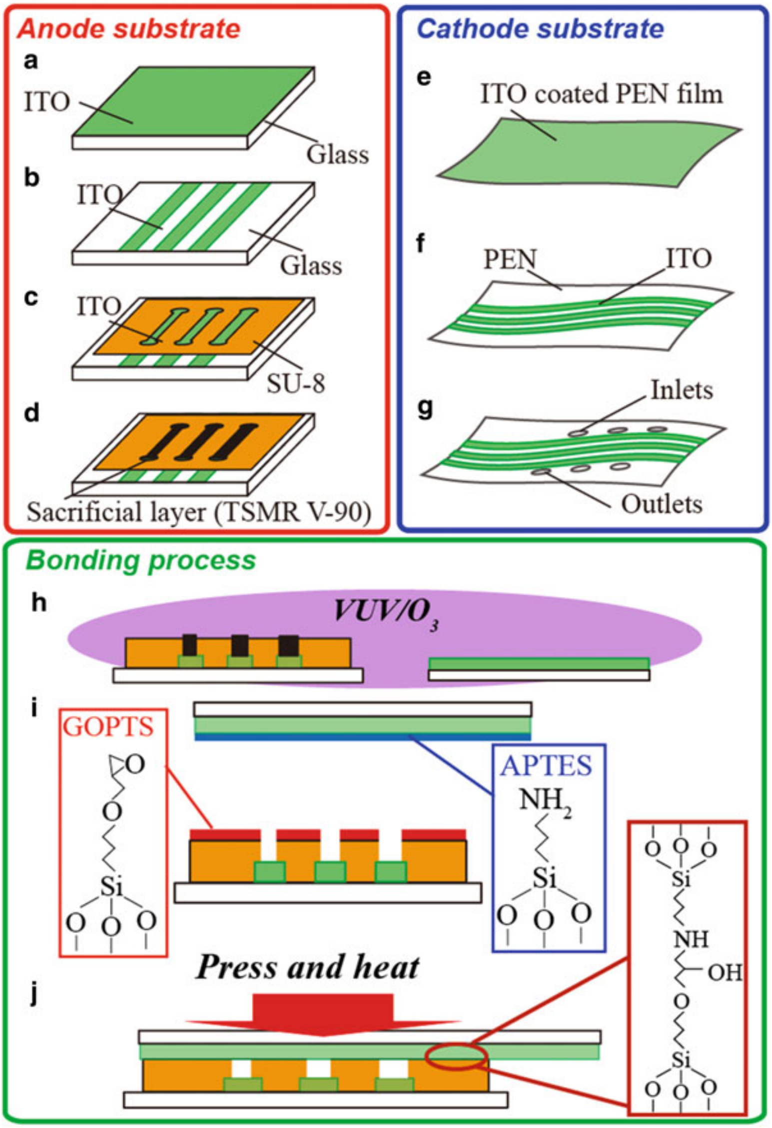

Fig. 9.2 Fabrication process of the microfluidic OLED. (**a**) ITO-coated glass and (**e**) ITO-coated PEN were used as the anode and cathode substrates. (**b**) Anode and (**f**) cathode electrodes were fabricated by photolithography and wet-etching. (**c**) SU-8 microchannels were formed on the anodes, and (**d**) ITO surfaces were covered with a sacrificial layer of positive resist. (**g**) Inlet and outlet were mechanically punched out. (**h**) Anode and cathode substrates were pre-treated by VUV/O_3. (**i**) Anode and cathode substrates were modified with GOPTS- and APTES-SAMs, respectively. (**j**) Two substrates were bonded under contact pressure of 1.5 MPa at 140 °C for 5 min

(Fig. 9.2g). For the bonding process, first, the anode and cathode substrates were pretreated by vacuum ultraviolet irradiation in the presence of oxygen gas (VUV/O_3) for 10 min using a Xe_2* excimer lamp source (Ushio Inc., UER20-172) for enhancing hydrophilic properties of the SU-8, PEN, and ITO cathode surfaces (Fig. 9.2h). In the recent years, VUV/O_3 treatments have widely been utilized for surface modification and cleaning of several materials, including gold [67, 68], wood-based carbon material [69], polyethylene terephthalate (PET) [70], and polymethyl methacrylate (PMMA) [71]. The VUV/O_3-treated anode and cathode substrates were subsequently immersed in 1 % (v/v) GOPTS and 5 % (v/v) APTES solutions prepared in water, respectively, for 20 min. The anode substrate was subsequently rinsed with acetone, followed by IPA and DI water to remove both the sacrificial resist and any unbound GOPTS-SAM, while the cathode substrate was rinsed with ethanol and DI water (Fig. 9.2i). Finally, the anode and cathode substrates were bonded under contact pressure of 1.5 MPa at 140 °C for 5 min to form amine-epoxy bonds using a bonding machine (SUSS MicroTec AG., SB6e) (Fig. 9.2j).

9.3 Luminescent Characteristics of Prototype Microfluidic OLEDs

As shown in Fig. 9.3a, a pyrene-based liquid organic semiconductor (PLQ), which was employed as both a greenish-blue liquid emitter and a liquid host, was found to have a strong UV absorption feature [58]. Under 365-nm LED irradiation, PLQ exhibits a greenish-blue photoluminescence (PL) emission having a maximum PL wavelength of 500 nm. Furthermore, it can be clearly seen that the PL spectrum of PLQ has spectral overlaps with the absorption spectra of 50-μM rubrene and 6.25-μM DBP dissolved in CH_2Cl_2 solution. This indicates that Förster energy transfer can take place effectively from the host PLQ to guest emitters, which is similar to the solid-state OLEDs based on the guest-host system [72]. The photographed image of the prepared liquid emitters is displayed in the inset of Fig. 9.3b. The guest emitter-doped PLQ was found to be maintained in the liquid phase. Fig. 9.3b shows the PL spectra of the PLQ, 2 wt% rubrene-doped PLQ, and 0.4 wt% DBP-doped PLQ. For PL spectrum measurements, the 365-nm LED light was used as the excitation light for the selective excitation of only the host PLQ. Although small contributions from PLQ (around 500 nm) were observed in the PL spectra, the maximum PL wavelengths of the rubrene-doped PLQ and DBP-doped PLQ were confirmed to be at 557 and 609 nm, respectively. This result indicates that Förster energy transfer occurred from the host PLQ to guest rubrene and DBP, respectively.

Before demonstrating microfluidic OLEDs, EL emissions of the prepared liquid organic semiconductors were confirmed using simple-structured liquid OLED cells, as shown in Fig. 9.4. This OLED consists of two ITO-coated glass substrates (anode and cathode substrates) with single-μm-thick SU-8 spacer. The spacer was patterned on the anode substrate by photolithography. The emitting layers were simply fabricated, as follows: The prepared liquid emitter was manually dropped on the

Fig. 9.3 (**a**) Absorption spectra of PLQ, rubrene, and DBP and PL spectrum of PLQ. (**b**) PL spectra of PLQ, rubrene-doped PLQ, and DBP-doped PLQ under 365-nm LED irradiation and photographic image of the prepared liquid emitters (*inset*)

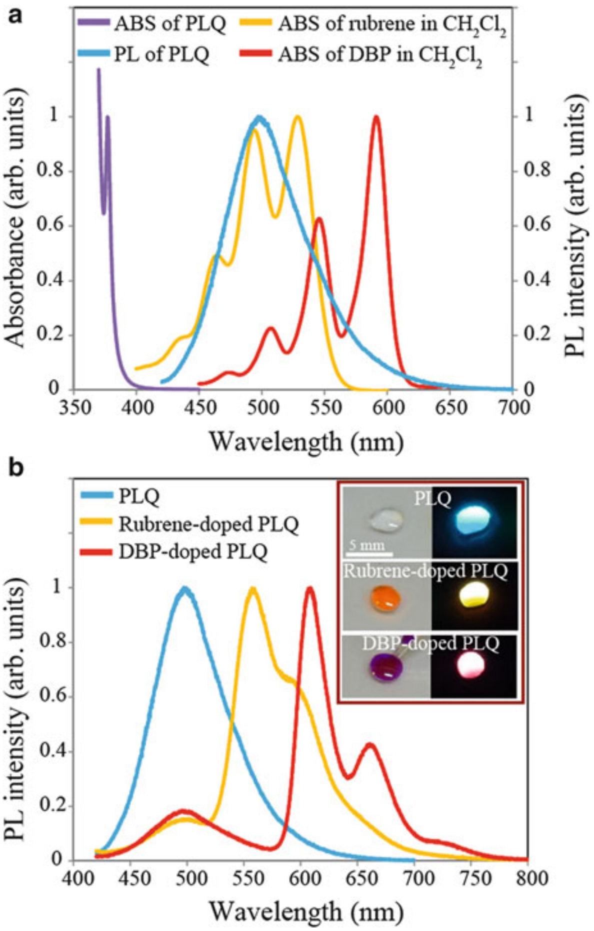

light-emitting area of the anode substrate and subsequently covered with the cathode substrate. Finally, the substrates were clipped tightly to form single-µm-thick emitting layer sandwiched between two ITO electrodes. It can be clearly seen that the fabricated liquid OLED cells with PLQ, rubrene-doped PLQ, and DBP-doped PLQ exhibited greenish-blue, yellow, and red EL emissions without significant *Mura* defects, respectively. This result indicates that a uniform electric field was formed between the ITO anode and cathode under the applied voltage, and subsequently, holes and electrons were injected into the emitting layer. Therefore, excitons were formed by radiative recombination of holes and electrons. As a result, although EL emissions can be simply realized by simple-structured liquid OLED cells, it is difficult to obtain the patterned liquid emitters and multicolor EL emissions on a single device. Therefore, the development of patterning methods for small amounts of liquid emitters is an important step toward next-generation liquid-based display applications.

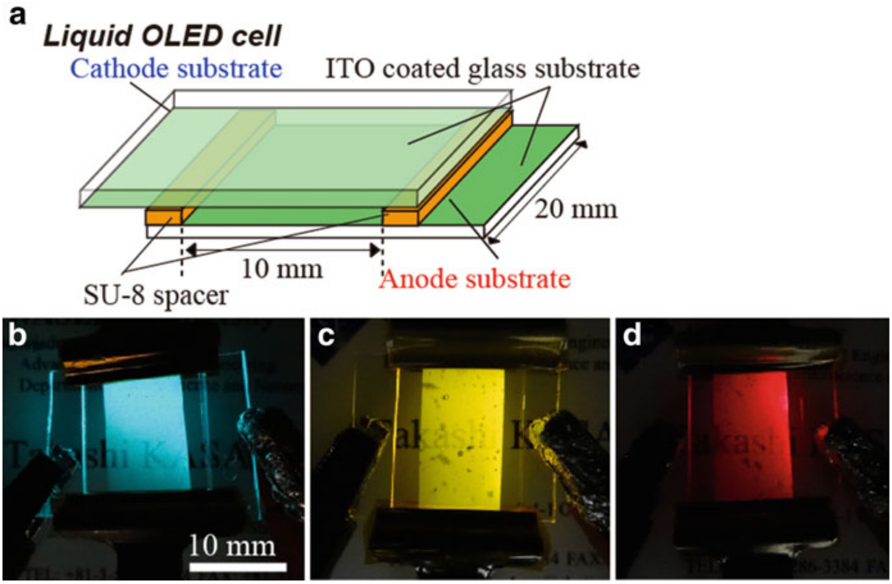

Fig. 9.4 (**a**) Design of simple-structured liquid OLED cells. Photograph images of EL emissions. (**b**) PLQ, (**c**) rubrene-doped rubrene, and (**d**) DBP-doped rubrene

A photographed image of the fabricated 6-μm-thick microfluidic OLED and its experimental setup are shown in Fig. 9.5. It was found that no obvious defects are observed in the microchannels fabricated via selective GOPTS-SAM formation process [56]. This suggests that the chemical reaction between ITO anode and cathode substrate was prevented during bonding process, and consequently, single-μm-thick gap structures for liquid emitters were successfully fabricated. In addition, although ITO cathodes were patterned on a PEN film, no significant voids were observed at the bonded interfaces between the PEN film and SU-8 as well as between the ITO cathodes and SU-8 layer. This is probably due to the use of a flexible PEN film as the lid substrate. As shown in the image of an experimental setup, the fabricated microfluidic OLED was clamped between two acrylic plates, and then the selected liquid organic semiconductors were injected from inlet nozzles using syringes to form liquid-emitting layers.

N1s and Si2p X-ray photoelectron spectroscopy (XPS) spectra of the untreated and APTES-treated ITO cathodes were shown in Fig. 9.6a. These spectra were obtained with JEOL Ltd., JPS-9100TR [58]. Nitrogen and silicon peaks were detected from the APTES-SAM-treated ITO. This result indicates that the ITO surface was successfully modified with APTES-SAM. In contrast, the anode surface in the microfluidic OLED is almost the same as the untreated ITO because sacrificial layer of TSMR-V90 was removed with acetone (also see Fig. 9.2) [58]. The energy-level diagram of the fabricated microfluidic OLED with PLQ is shown in Fig. 9.6b. In this device, PLQ (or guest emitter-doped PLQ) is sandwiched between the ITO anode and APTES-modified ITO cathode. The work functions of

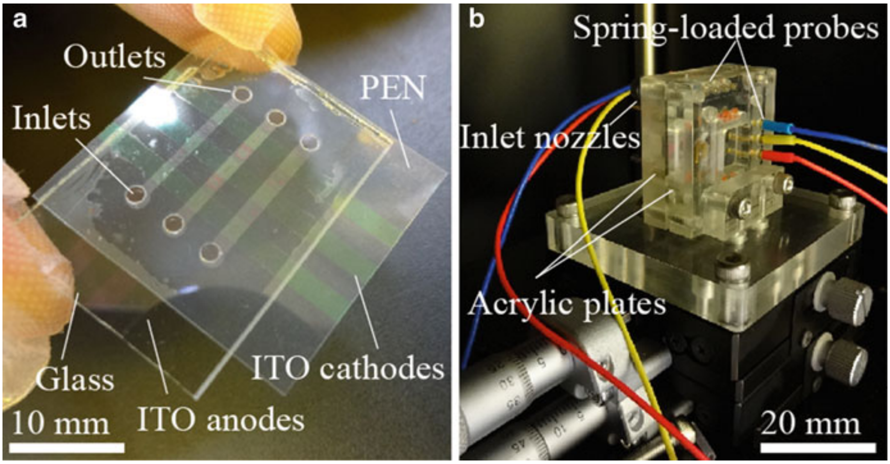

Fig. 9.5 (**a**) Fabricated microfluidic OLEDs. No significant voids were confirmed both in the microchannels and at the bonded interfaces. (**b**) Experimental setup for the fabricated microfluidic OLED. The liquid organic semiconductors were injected from inlet nozzles to form the emitting layers

the anode and cathode are found to be 4.77 eV and 4.55 eV, respectively. These values were measured with a photoemission yield spectroscopy in air (Riken Keiki Co., Ltd., AC-2). It can be clearly seen that APTES-modified ITO has a low work function in comparison with the untreated ITO (4.9 eV) [58]. In the last few years, the use of APTES-modified ITO as electrodes has been reported in other research fields such as organic solar cells (OSCs) [73, 74] and electrochemical biosensors [75]. In accordance with the study of Song et al. (2013), the work function of ITO is decreased by APTES-SAM treatment because the amine groups in the APTES-SAM are electron donating in nature [73]. Thus, the work function value of the ITO cathode used in the microfluidic OLEDs is in agreement with other works.

Figure 9.7 shows the demonstration of the fabricated 6-μm-thick microfluidic OLED with PLQ. In this device, only PLQ was injected into three microchannels. As shown in the image of PL emissions under 365-nm UV-lamp irradiation, PLQ was passed through the microchannels, and consequently, the emitting layers were formed in the microfluidic OLED without leakage at the bonded interface [56]. It can be seen that the microfluidic OLED successfully exhibited greenish-blue EL emissions under stopped-flow condition when 70 V was applied. This result suggests that single-μm-thick gap structures for the liquid-emitting layers were preserved under the voltage applications. In addition, holes and electrons were injected into the PLQ from ITO anode and APTES-modified ITO cathode, and consequently, EL emissions were generated by the radiative recombination of holes and electrons. Target light-emitting pixels were found to be controlled simply by passive matrix addressing.

As shown in Fig. 9.8, 6-μm-thick microfluidic OLED with PLQ, rubrene-doped PLQ, and DBP-doped PLQ successfully exhibited greenish-blue, yellow, and red

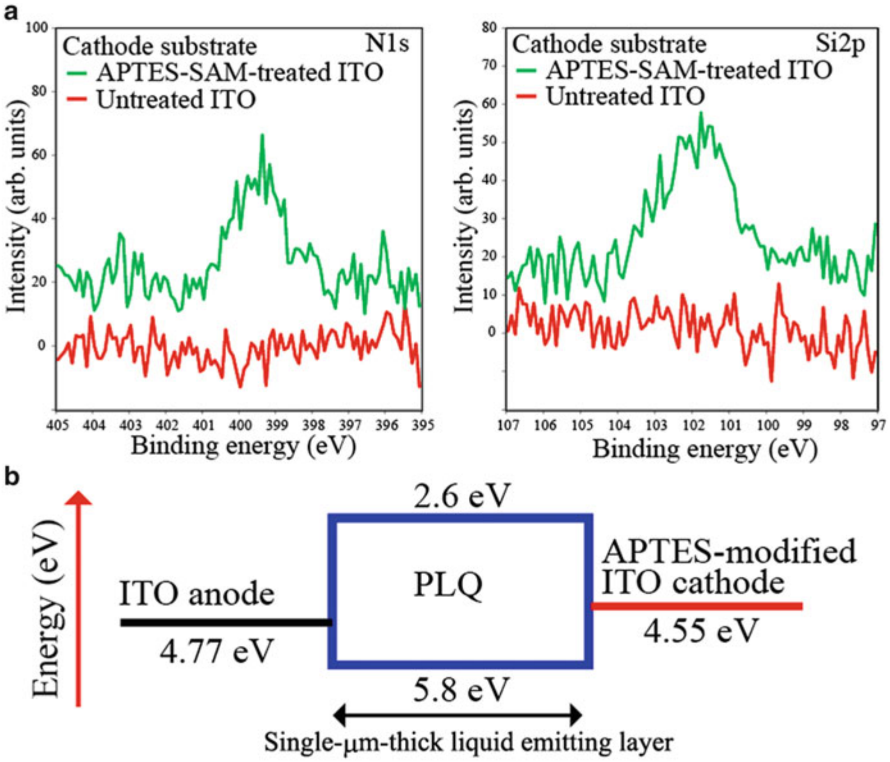

Fig. 9.6 (**a**) N1s and Si2p XPS spectra of the untreated and APTES-SAM-treated ITO cathodes. ITO surface was found to be modified by APTES-SAM. (**b**) Energy-level diagram of the microfluidic OLED with PLQ

EL demonstrations under applied voltage of 80 V. In the proposed microfluidic OLED, several liquid-emitting layers can be formed on demand by simply injecting the selected liquid emitters into the microchannels without the need for a high vacuum process. Similar to the microfluidic OLED with only PLQ, target pixels can be controlled by passive matrix addressing. This result indicates that PLQ can be useful for both a greenish-blue emitter and a liquid host. From Fig. 9.9, it was found that the obtained maximum EL wavelengths of PLQ, rubrene-doped PLQ, and DBP-doped PLQ are identical to their PL spectra (see also Fig. 9.3). This suggests that the excitons were mostly formed in the guest emitters. In addition, no significant contributions from PLQ (500 nm) were observed in the EL spectra of guest-doped PLQ. Thus, the exciton formation mechanisms of the guest-doped PLQ are partially different between PL and EL emissions. In accordance with the energy-level diagram reported by Griffith and Forrest (2014), LUMO levels of rubrene and DBP are located at 3.1 and 3.5 eV, respectively, while their HOMO levels are approximately 5.4 eV [76]. The HOMO and LUMO levels of rubrene and DBP are found to be inside the HOMO-LUMO gap of the host PLQ (see also Fig. 9.6).

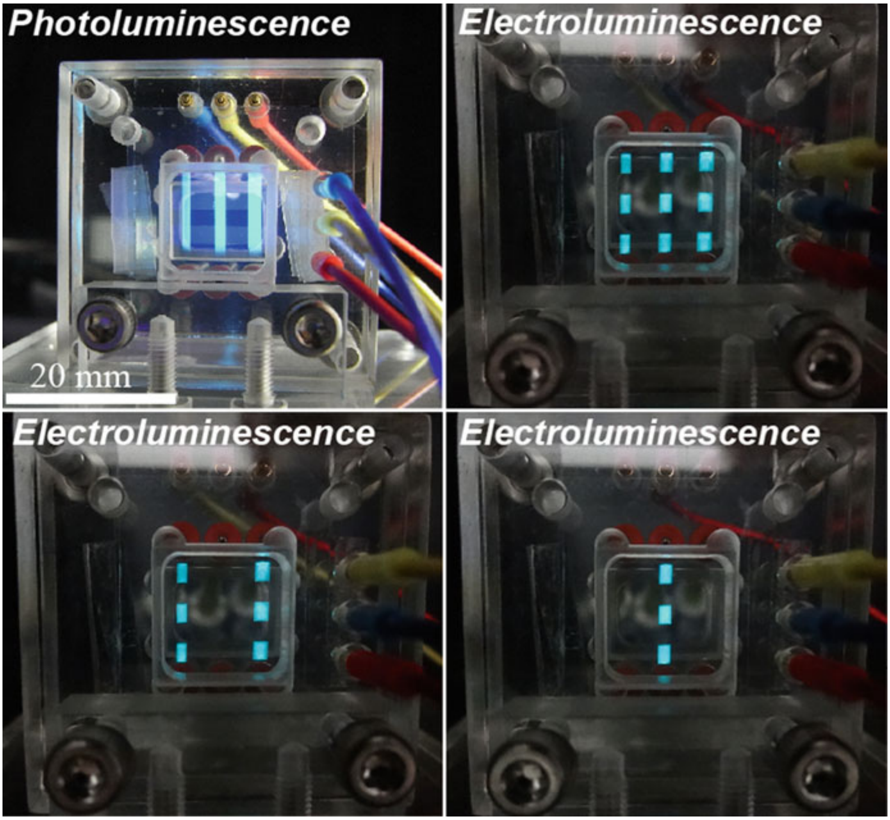

Fig. 9.7 PL and EL emissions from the microfluidic OLED with PLQ. The emitting layers were found to be formed in the microfluidic OLED without leakage at the bonded interface. EL emissions were successfully obtained at the light-emitting pixels

Therefore, another possible mechanism may be direct carrier recombination on guest emitters. The electrons and holes injected into liquid emitters can be presumed to be trapped by guest emitters, and therefore, excitons were generated by direct recombination on guest emitters. These emission mechanisms are often discussed in host-guest systems of the solid-state OLEDs [72, 77] and the liquid OLEDs [31].

The current density-voltage (*J*-*V*) and luminance-voltage (*L*-*V*) characteristics of the 2.5-μm- and 6-μm-thick microfluidic OLEDs with PLQ are shown in Fig. 9.10. It is found that the current density and luminance increase significantly with decreasing microchannel thickness. Furthermore, the turn-on voltage, which was defined at luminance of above 0.01 cd/m^2, decreased with decreasing thickness. The 2.5-μm-thick microfluidic OLEDs exhibited the highest current density of 10.6 mA/cm^2 and luminance of 26.0 cd/m^2 under the applied voltages of 61 V, and its turn-on voltage value was 13 V. This result indicates that the bulk resistance

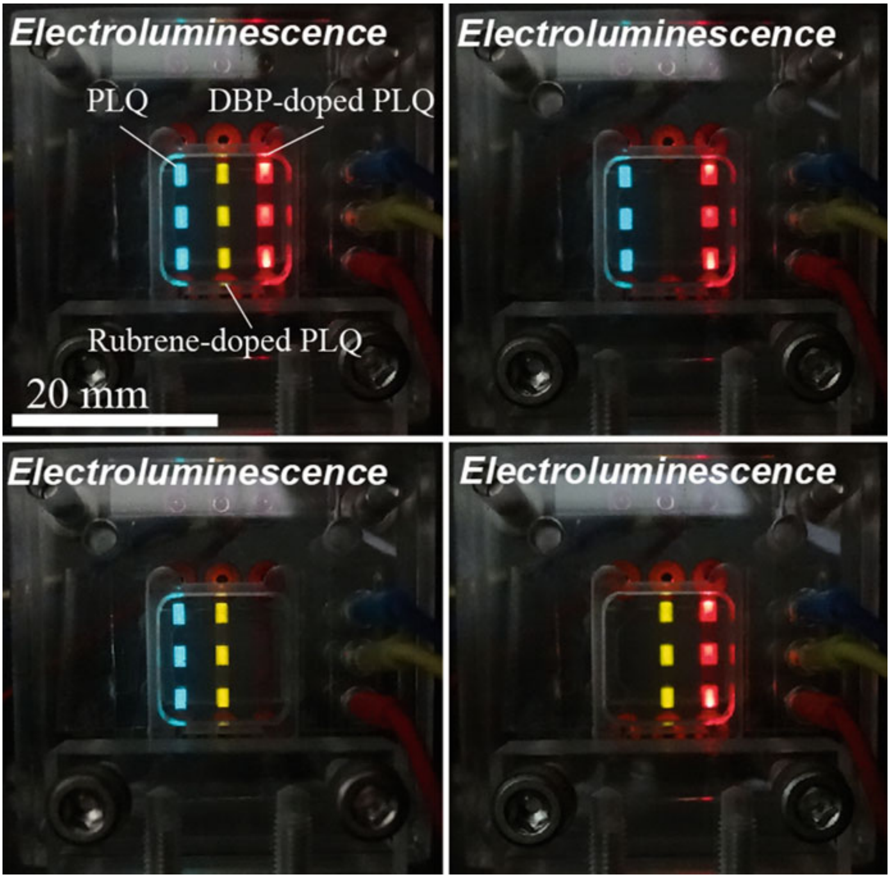

Fig. 9.8 On-demand multicolor EL emissions from the microfluidic OLED with PLQ, rubrene-doped PLQ, and DBP-doped PLQ. The liquid emitting layers can be formed on demand by simply injecting the selected liquid emitters into the microchannels

of PLQ decreased with decreasing microchannel thickness. In comparison with conventional solid-state OLEDs, the obtained luminance is still in a research stage. Therefore, for the improvement of the microfluidic OLED performance, the fabrication methodology for the submicron-thick electro-microchannels has to be developed. In addition, highly efficient microfluidic OLEDs are expected to be realized by using appropriate electrodes and by inserting several functional layers such as electron injection layer and hole-blocking layer. In the prototype microfluidic OLEDs, there are large energy barriers between the HOMO of PLQ (5.8 eV) and the ITO anode (4.77 eV) and between the LUMO of PLQ (2.6 eV) and the APTES-modified ITO cathode (4.55 eV).

Images shown in Fig. 9.11 are the demonstration of the luminance recovery characteristics of the microfluidic OLED with PLQ. It can be clearly seen that luminance decreased with increasing operating time under the applied voltage of

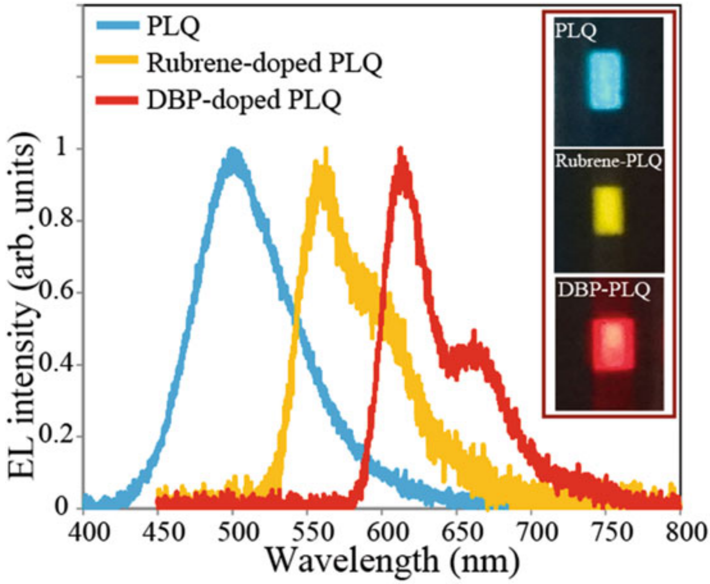

Fig. 9.9 EL spectra of PLQ, rubrene-doped PLQ, and DBP-doped PLQ from 6-μm-thick microfluidic OLED. Excitons were confirmed to be formed in the guest molecules

70 V (Fig. 9.11a). This result indicates that the emitting layer was decomposed during the carrier injection and transportation. Subsequently, fresh PLQ was reinjected manually from the inlet nozzles into the target microchannel using a syringe under no-voltage conditions (Fig. 9.11b). When the constant voltage of 70 V was applied again, the recovery of the EL emission was observed at the top edge of the light-emitting pixel (Fig. 9.11c). This recovery is due to replacement of the decomposed PLQ with fresh one. Furthermore, after this process was repeated multiple times, EL was generated from the whole light-emitting pixels. This refreshable luminance feature may be applied to future long-life liquid-based light-emitting devices.

9.4 Flexible Microfluidic OLED Technology

In Sect. 9.2, the fabrication methodology for the electro-microfluidic device (microfluidic OLED) on a glass substrate was proposed to integrate multiple liquid OLEDs. The use of liquid emitters as the emitting layers is expected to provide a new possibility for crack-free and flexible organic electronic devices. However, from a standpoint of conventional glass-based liquid OLEDs and microfluidic OLEDs, it is difficult to obtain flexible liquid-emitting layers. Thus, the development of the flexible liquid-emitting layers that enable to keep single-μm-thick gap structures under the repeated bending is important. This section provides the

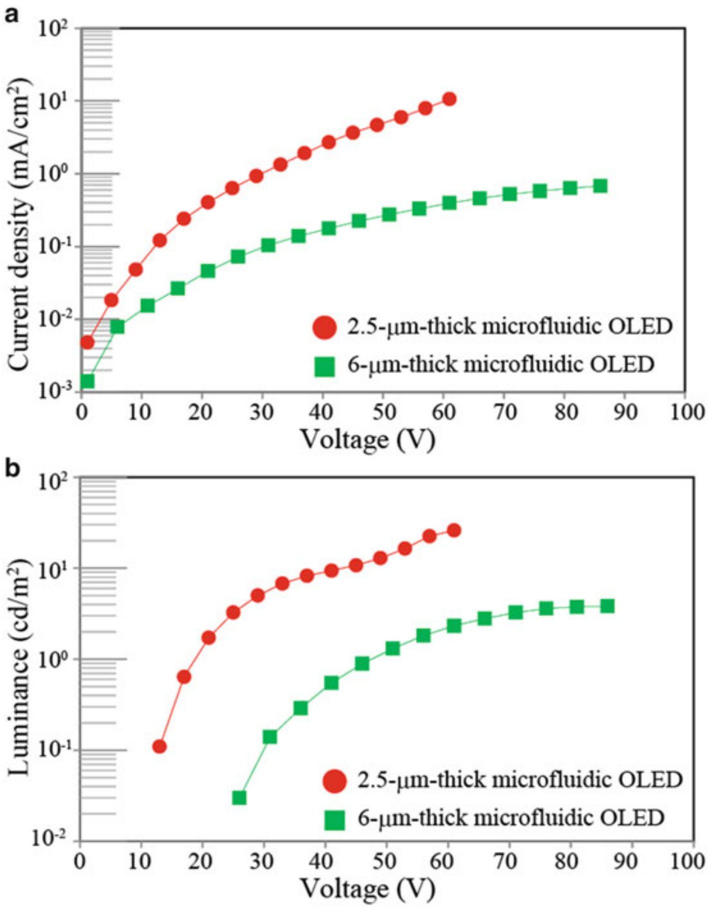

Fig. 9.10 (**a**) *J-V* and (**b**) *L-V* characteristics of the 2.5-μm-thick and 6-μm-thick microfluidic OLEDs with PLQ

fabrication methodology for the flexible microfluidic OLEDs using a novel belt-transfer exposure technique [59].

The design of a flexible microfluidic OLED is illustrated in Fig. 9.12. SU-8-based microchannels are sandwiched between an ITO anode and APTES-modified ITO cathode, and an 8 × 8 matrix of light-emitting pixels is formed in the flexible microfluidic device [59]. Here, in order to obtain flexible microchannel structures, the ITO-coated polyethylene terephthalate (PET) films were utilized as both anode and cathode substrates. The microchannel widths are designed to be 250, 500, 750, and 1000 μm, while thickness is 4.5 μm. The dimension of the flexible microfluidic OLED was 102 mm × 102 mm. PLQ is also used as greenish-blue liquid emitter and injected from inlets, which are located in the cathode substrate, into the microchannels.

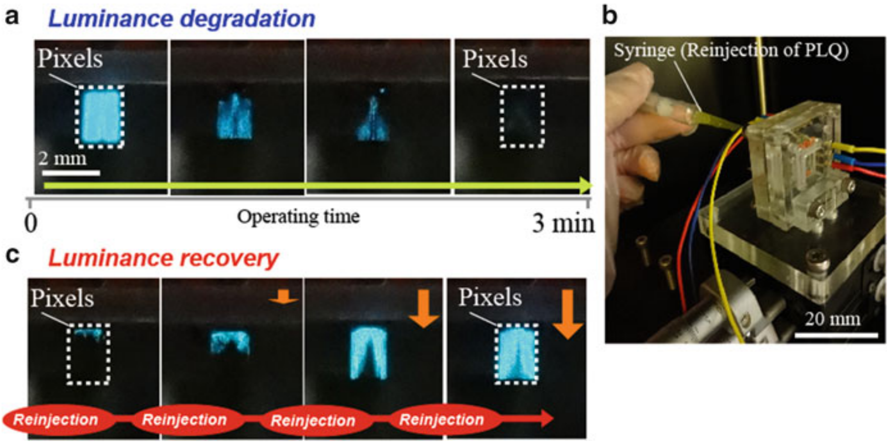

Fig. 9.11 Images of (**a**) luminance degradation, (**b**) reinjection of PLQ, and (**c**) luminance recovery. Recovery of the EL emission was confirmed at the top edge of the light-emitting pixel by reinjection of PLQ into the microchannels

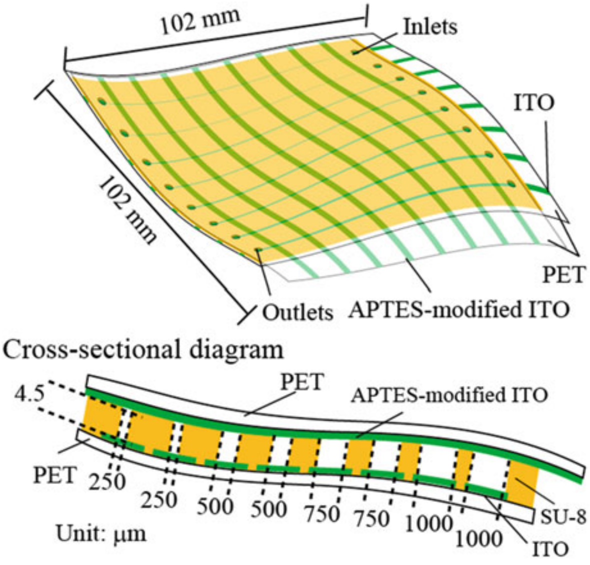

Fig. 9.12 Design of the flexible microfluidic OLED. Single-μm-thick microchannels sandwiched between two transparent electrodes are preserved in both flat and curved states

Fabrication process of the SU-8 microchannels is shown in Fig. 9.13. A screen printing technique and wet etching are used for patterning ITO electrodes on both anode and cathode substrates. First, the etching-resist ink (Taiyo Ink Mfg. Co., Ltd, X-87) was screen printed on the ITO-coated PET films (Fig. 9.13b). A hand printing machine (Newlong Seimitsu Kogyo Co., Ltd, HP-320) was utilized in this process. The anode and cathode patterns were subsequently formed by wet etching with a dilute aqua regia (Fig. 9.13c). The resist ink on the substrates was removed with

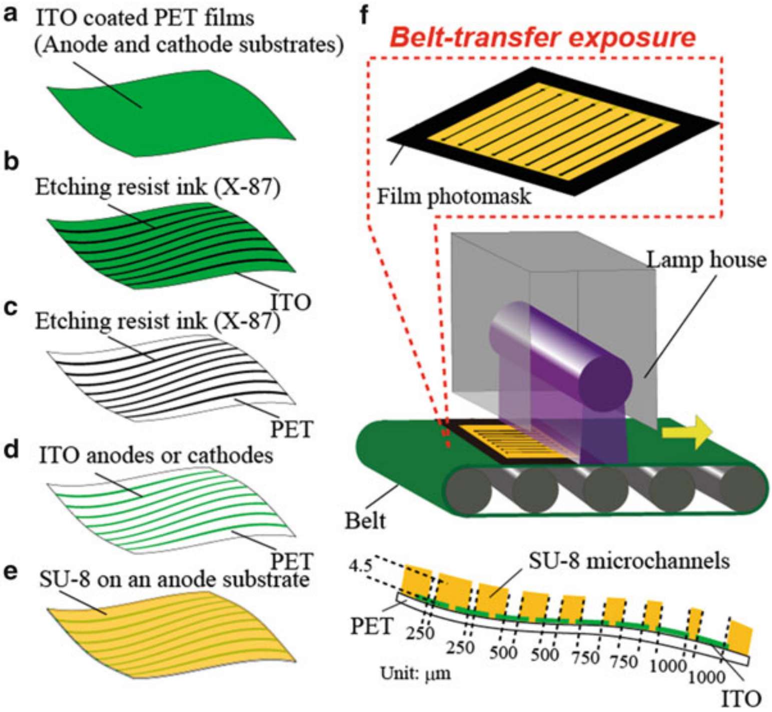

Fig. 9.13 Fabrication process of flexible microfluidic OLEDs. (**a**) ITO-coated PET films were used as the anode and cathode substrates. (**b**) Screen printing technique and (**c**) wet-etching are used for patterning electrodes. (**d**) Resist ink was removed with acetone, and (**e**) SU-8 was spin-coated on the anode substrate. (**f**) Belt-transfer exposure technique was applied to form flexible SU-8 microchannels

acetone, and then the substrates were cleaned with IPA (Fig. 9.13d). The inlets and outlets for liquid emitters were formed on the cathode substrate. On the anode substrate part, the ITO-patterned PET surface was pretreated with O_2 plasma (SUSS MicroTec AG., PL8) for enhancing the hydrophilic property, and then SU-8 3005 was spin coated (Fig. 9.13e). The SU-8-coated substrate was subsequently manually aligned with a film photomask having the light interception pattern of the microchannels (Fig. 9.13f). Here, a novel belt-transfer exposure technique was applied to form SU-8 microchannels, as shown in Fig. 9.13f. The exposure equipment (Japan Technology System Co., JU-C1500), which enables rapid exposure to large-area substrates, was utilized in this process [78]. The SU-8 was exposed to UV lamp having wavelength between 260 and 420 nm through the film photomask at the belt-transfer speed of 11.6 m/min and then developed by the SU-8 developer. For fabricating flexible microchannels sandwiched between two electrodes, the anode and cathode substrates were bonded using a heterogeneous bonding method through the use of APTES- and GOPTS-SAMs (see also Fig. 9.2). Finally, PLQ was injected into the microchannels for forming flexible emitting layers.

From the scanning electron microscope (SEM) image of the fabricated SU-8 microchannels on the anode substrate (Fig. 9.14a), no significant exposure failure

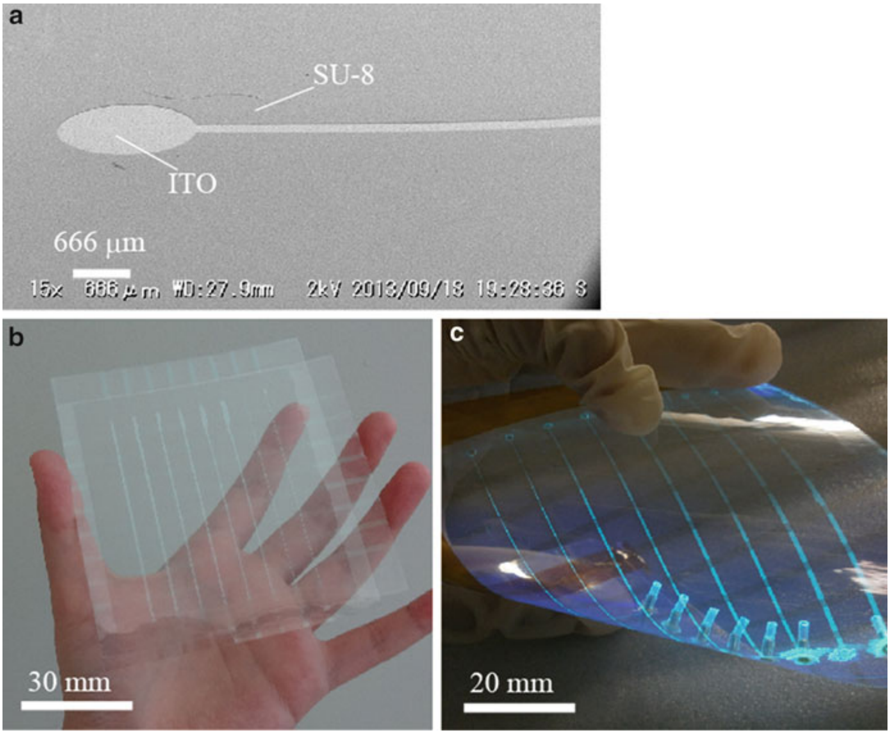

Fig. 9.14 (**a**) SEM image of the fabricated SU-8 microchannels on a PET film. (**b**) Fabricated flexible microfluidic OLED without infection of PLQ. (**c**) Photographic images of PL emissions from the microfluidic OLED with PLQ under 365-nm UV-lamp irradiation

was observed. This indicates that only the SU-8 layer beneath light-permission area of the film photomask was irradiated by the UV lamp of the belt-transfer exposure equipment. Thus, a newly proposed belt-transfer exposure technique is applicable for patterning the miniaturized components such as microchannels and microchambers on large-area flexible substrates. Photographic images of the fabricated flexible electro-microfluidic device without and with injection of PLQ are shown in Fig. 9.14b, c. It can be seen that the fabricated OLED has a flexible microchannel structures and can be rolled up. As shown in the image of PL emissions of PLQ under 365-nm UV-lamp irradiation, no significant bonding defects were confirmed in the microchannels and at the bonded interfaces. Furthermore, all the microchannels were successfully filled with PLQ without leakage. Therefore, flexible liquid-emitting layers were formed in the flexible electro-microfluidic device.

An image shown in Fig. 9.15a is the demonstration of the flexible microfluidic OLED in the curved state. It can be seen that EL emissions were successfully obtained at the light-emitting pixels. The *J*-*V* characteristics in straight and curved state (radius of 3 cm) are also shown in Fig. 9.15b. The fabricated microfluidic

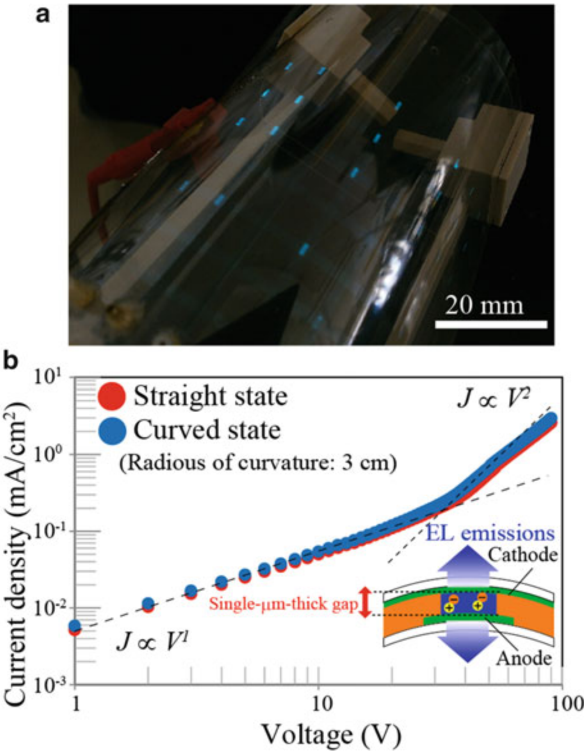

Fig. 9.15 (**a**) EL emissions from the flexible microfluidic OLED in the curved state (radius curvature of 3 cm). (**b**) *J*-*V* characteristics in straight and curved states

OLED was found to exhibit almost same *J*-*V* curves in both states. This result indicates that the single-μm-thick microchannel structures were preserved in the curved state. Therefore, holes and electrons were injected into PLQ from the ITO anode and the APTES-modified ITO cathode, respectively, to generate EL emissions. In addition, the current density increased proportionally with increasing voltage up to 40 V ($J \propto V^1$). When the voltage higher than 40 V was applied to the OLEDs, the current density increased steeply to be proportional to the square of the voltage. It may be suspected that this phenomenon is due to the space-charge-limited current (SCLC). Hirata et al. (2011) studied liquid OLEDs with other liquid organic semiconductor (EHCz) and reported the SCLC behavior [32]. Based on this study, it can be concluded that the proposed flexible microfluidic OLED operated successfully and is expected to be a highly promising technology toward future unique display applications.

9.5 Conclusions

In this chapter, multicolor microfluidic OLEDs were proposed by combining liquid OLEDs with microfluidic technology toward next-generation liquid-based display applications. Novel fabrication methodologies for single-μm-thick electro-microfluidic devices were developed with belt-transfer exposure and heterogeneous bonding technique through the use of amine- and epoxy-terminated SAMs. The patterned liquid organic semiconductor-based emitting layers were confirmed, and then the glass-based microfluidic OLED successfully exhibited single- and multicolor EL emissions. Furthermore, EL emissions were obtained from the flexible microfluidic OLED in curved state. In comparison with conventional solid-state OLEDs, the proposed microfluidic OLEDs have unique features such as on-demand emitting layer formation and refreshable emissions. This on-demand emission feature may be applicable as the excitation source for portable microfluidic point-of-care chip [79]. Furthermore, the fabricated electro-microfluidic devices can exhibit not only EL emission of liquid organic semiconductors but also ECL emissions [58]. In the past few decades, microfluidic devices have been developed for a wide range of chemical and biological applications because of their advantages such as delivering and mixing small amounts of samples on a chip. Thus, novel liquid emitters may be prepared by using the Y-shaped electro-microfluidic mixing device [80]. The authors expect that the proposed microfluidic technology can open a new possibility for future liquid-based electronic device applications.

Acknowledgements This work was supported in part by the Funding Program for World-Leading Innovative R&D on Science and Technology (FIRST) and the International Institute for Carbon Neutral Energy Research (WPI-I2CNER) sponsored by the Japan Ministry of Education, Culture, Sports Science and Technology (MEXT) and Grants-in-Aid for Scientific Basic Research (S) No. 23226010 and for Scientific Basic Research (B) No. 25289241. The authors thank MEXT Nanotechnology Platform Support Project of Waseda University. The authors would like to acknowledge Prof. Chihaya Adachi (Kyushu University), Prof. Shuichi Shoji (Waseda University), Dr. Tomohiko Edura (Kyushu University), Dr. Shigeyuki Matsunami (Kyushu University), Prof. Toshihiko Imato (Kyushu University), Dr. Ryoichi Ishimatsu (Kyushu University), Dr. Juro Oshima (Nissan Chemical Industries, Ltd.), Mr. Osamu Uesugi (Nissan Chemical Industries, Ltd.), and Ms. Miho Tsuwaki (Waseda University) for valuable discussion and insightful suggestions.

References

1. C.D. Müller, A. Falcou, N. Reckefuss, M. Rojahn, V. Wiederhirn, P. Rudati, H. Frohne, O. Nuyken, H. Becker, K. Meerholz, Multi-colour organic light-emitting displays by solution processing. Nature **421**, 829–833 (2003)
2. H. Aziz, Z.D. Popovic, N.-X. Hu, A.-M. Hor, G. Xu, Degradation mechanism of small molecule-based organic light-emitting devices. Science **283**, 1900–1902 (1999)
3. L. Xiao, Z. Chen, B. Qu, J. Luo, S. Kong, Q. Gong, J. Kido, Recent progresses on materials for electrophosphorescent organic light-emitting devices. Adv. Mater. **23**, 926–952 (2011)
4. S. Reineke, F. Lindner, G. Schwartz, N. Seidler, K. Walzer, B. Lüssem, K. Leo, White organic light-emitting diodes with fluorescent tube efficiency. Nature **459**, 234–238 (2009)
5. B.W. D'Andrade, S.R. Forrest, White organic light-emitting devices for solid-state lighting. Adv. Mater. **16**, 1585–1595 (2004)
6. C.W. Tang, S.A. VanSlyke, Organic electroluminescent diodes. Appl. Phys. Lett. **51**, 913–915 (1987)

7. A. Pais, A. Banerjee, D. Klotzkin, I. Papautsky, High-sensitivity, disposable lab-on-a-chip with thin-film organic electronics for fluorescence detection. Lab Chip **8**, 794–800 (2008)
8. A. Marcello, D. Sblattero, C. Cioarec, P. Maiuri, P. Melpignano, A deep-blue OLED-based biochip for protein microarray fluorescence detection. Biosens. Bioelectron. **46**, 44–47 (2013)
9. B. Yao, G. Luo, L. Wang, Y. Gao, G. Lei, K. Ren, L. Chen, Y. Wang, Y. Hu, Y. Qiu, A microfluidic device using a green organic light emitting diode as an integrated excitation source. Lab Chip **5**, 1041–1047 (2005)
10. F. Lefèvre, A. Chalifour, L. Yu, V. Chodavarapu, P. Juneau, R. Izquierdo, Algal fluorescence sensor integrated into a microfluidic chip for water pollutant detection. Lab Chip **12**, 787–793 (2012)
11. R. Liu, R. Ishimatsu, M. Yahiro, C. Adachi, K. Nakano, T. Imato, Photometric flow injection determination of phosphate on a PDMS microchip using an optical detection system assembled with an organic light emitting diode and an organic photodiode. Talanta **132**, 96–105 (2014)
12. Z. Shen, P.E. Burrows, V. Bulović, S.R. Forrest, M.E. Thompson, Three-color, tunable, organic light-emitting devices. Science **276**, 2009–2011 (1997)
13. D.A. Pardo, G.E. Jabbour, N. Peyghambarian, Application of screen printing in the fabrication of organic light-emitting devices. Adv. Mater. **12**, 1249–1252 (2000)
14. K. Mori, T. Ning, M. Ichikawa, T. Koyama, Y. Taniguchi, Organic light-emitting devices patterned by screen-printing. Jpn. J. Appl. Phys. **39**, L942–L944 (2000)
15. P. Kopola, M. Tuomikoski, R. Suhonen, A. Maaninen, Gravure printed organic light emitting diodes for lighting applications. Thin Solid Films **517**, 5757–5762 (2009)
16. S. Tekoglu, G. Hernandez-Sosa, E. Kluge, U. Lemmer, N. Mechau, Gravure printed flexible small-molecule organic light emitting diodes. Org. Electron. **14**, 3493–3499 (2013)
17. T.R. Hebner, C.C. Wu, D. Marcy, M.H. Lu, J.C. Sturm, Ink-jet printing of doped polymers for organic light emitting devices. Appl. Phys. Lett. **72**, 519–521 (1998)
18. Z. Ding, R. Xing, Q. Fu, D. Ma, Y. Han, Patterning of pinhole free small molecular organic light-emitting films by ink-jet printing. Org. Electron. **12**, 703–709 (2011)
19. S.-C. Chang, Y. Yang, Q. Pei, Polymer solution light-emitting devices. Appl. Phys. Lett. **74**, 2081–2083 (1999)
20. K. Nishimura, Y. Hamada, T. Tsujioka, S. Matsuta, K. Shibata, T. Fuyuki, Solution electrochemiluminescent cell with a high luminance using an ion conductive assistant dopant. Jpn. J Appl. Phys. **40**, L1323–L1326 (2001)
21. T. Nobeshima, T. Morimoto, K. Nakamura, N. Kobayashi, Advantage of an AC-driven electrochemiluminescent cell containing a $Ru(bpy)_3{}^{2+}$ complex for quick response and high efficiency. J. Mater. Chem. **20**, 10630–10633 (2010)
22. N. Itoh, Electrochemical light-emitting gel. Materials **3**, 3729–3739 (2010)
23. H.C. Moon, T.P. Lodge, C.D. Frisbie, Solution-processable electrochemiluminescent ion gels for flexible, low-voltage, emissive displays on plastic. J. Am. Chem. Soc. **136**, 3705–3712 (2014)
24. T. Daimon, E. Nihei, Fabrication of organic electrochemiluminescence devices with π-conjugated polymer materials. J Mater. Chem. C. **1**, 2826–2833 (2013)
25. T. Daimon, E. Nihei, Fabrication of a poly(3-octylthiophene-2,5-diyl) electrochemiluminescence device assisted by perylene. Materials **6**, 1704–1717 (2013)
26. M. Honma, T. Hirouchi, T. Nose, Light-emitting liquid-crystal cells with polarization switching function: electrochemiluminescent method. J. Appl. Phys. **106**, 014507 (2009)
27. M. Honma, T. Horiuchi, K. Watanabe, T. Nose, Influence of hole injection layer and work function of cathode on the performance of light-emitting liquid crystal cells with fluorescent dye-doped nematic liquid crystal. Jpn. J. Appl. Phys. **53**, 112102 (2014)
28. T. Kado, M. Takenouchi, S. Okamoto, W. Takashima, K. Kaneto, S. Hayase, Enhanced electrochemiluminescence by use of nanoporous TiO_2 electrodes: electrochemiluminescence devices operated with alternating current. Jpn. J. Appl. Phys. **44**, 8161–8164 (2005)

29. S. Sato, T. Ishikawa, K. Yagyu, H. Taniguchi, Emission enhancing characteristics in electrochemiluminescence devices by 9,10-diphenylanthracene dye-highly scattering TiO_2 solid-nanoparticle mixture. Appl. Phys. B **98**, 523–527 (2010)
30. R. Okumura, S. Takamatsu, E Iwase, K Matsumoto, I Shimoyama, Solution electrochemiluminescent microfluidic cell for flexible and stretchable display. *Proceedings of IEEE International Conference on Micro Electro Mechanical System*, Sorrento, 947–950 (2009)
31. D. Xu, C. Adachi, Organic light-emitting diode with liquid emitting layer. Appl. Phys. Lett. **95**, 053304 (2009)
32. S. Hirata, K. Kubota, H.H. Jung, O. Hirata, K. Goushi, M. Yahiro, C. Adachi, Improvement of electroluminescence performance of organic light-emitting diodes with a liquid-emitting layer by introduction of electrolyte and a hole-blocking layer. Adv. Mater. **23**, 889–893 (2011)
33. S. Hirata, H.J. Heo, Y. Shibano, O. Hirata, M. Yahiro, C. Adachi, Improved device lifetime of organic light emitting diodes with an electrochemically stable π-conjugated liquid host in the liquid emitting layer. Jpn. J. Appl. Phys. **51**, 041604 (2012)
34. K. Kubota, S. Hirata, Y. Shibano, O. Hirata, M. Yahiro, C. Adachi, Liquid carbazole substituted with a poly(ethylene oxide) group and its application for liquid organic light-emitting diodes. Chem. Lett. **41**, 934–936 (2012)
35. C.-H. Shim, S. Hirata, J. Oshima, T. Edura, R. Hattori, C. Adachi, Uniform and refreshable liquid electroluminescent device with a back side reservoir. Appl. Phys. Lett. **101**, 113302 (2012)
36. D.M. Hercules, Chemiluminescence resulting from electrochemically generated species. Science **145**, 808–809 (1964)
37. K.S.V. Santhanam, A.J. Bard, Chemiluminescence of electrogenerated 9,10-diphenylanthracene anion radical. J. Am. Chem. Soc. **87**, 139–140 (1965)
38. W. Miao, Electrogenerated chemiluminescence and its biorelated applications. Chem. Rev. **108**, 2506–2553 (2008)
39. H. Niu, R. Yuan, Y. Chai, L. Mao, Y. Yuan, Y. Zhuo, S. Yuan, X. Yang, Electrochemiluminescence of peroxydisulfate enhanced by l-cysteine film for sensitive immunoassay. Biosens. Bioelectron. **26**, 3175–3180 (2011)
40. O.M. Steijger, D.A. Kamminga, A. Brummelhuis, H. Lingeman, Liquid chromatography with luminol-based electrochemiluminescence detection: determination of histamine. J. Chromatogr. A **799**, 57–66 (1998)
41. J. Li, Q. Yan, Y. Gao, H. Ju, Electrogenerated chemiluminescence detection of amino acids based on precolumn derivatization coupled with capillary electrophoresis separation. Anal. Chem. **78**, 2694–2699 (2006)
42. C.A. Marquette, L.J. Blum, Luminol electrochemiluminescence-based fibre optic biosensors for flow injection analysis of glucose and lactate in natural samples. Anal. Chim. Acta **381**, 1–10 (1999)
43. B.A. Kamino, B. Mills, C. Reali, M.J. Gretton, M.A. Brook, T.P. Bender, Liquid triarylamines: the scope and limitations of Piers-Rubinsztajn conditions for obtaining triarylamine-siloxane hybrid materials. J. Org. Chem. **77**, 1663–1674 (2012)
44. B.A. Kamino, T.P. Bender, R.A. Klenkle, Hole mobility of a liquid organic semiconductor. J. Phys. Chem. Lett. **3**, 1002–1006 (2012)
45. E.Y. Choi, L. Mager, T.T. Cham, K.D. Dorkenoo, A. Fort, J.W. Wu, A. Barsella, J.-C. Ribierre, Solvent-free fluidic organic dye lasers. Opt. Express **21**, 11368–11375 (2013)
46. J.-C. Ribierre, T. Aoyama, T. Muto, P. André, Hybrid organic–inorganic liquid bistable memory devices. Org. Electron. **12**, 1800–1805 (2011)
47. J. Mai, V.V. Abhyankar, M.E. Piccini, J.P. Olano, R. Willson, A.V. Hatch, Rapid detection of trace bacteria in biofluids using porous monoliths in microchannels. Biosens. Bioelectron. **54**, 435–441 (2014)
48. Y. Li, X. Yan, X. Feng, J. Wang, W. Du, Y. Wang, P. Chen, L. Xiong, B.-F. Liu, Agarose-based microfluidic device for point-of-care concentration and detection of pathogen. Anal. Chem. **86**, 10653–10659 (2014)

49. P.J. Hung, P.J. Lee, P. Sabounchi, R. Lin, L.P. Lee, Continuous perfusion microfluidic cell culture array for high-throughput cell-based assays. Biotechnol. Bioeng. **89**, 1–8 (2005)
50. L.Y. Wu, D.D. Carlo, L.P. Lee, Microfluidic self-assembly of tumor spheroids for anticancer drug discovery. Biomed. Microdevices **10**, 197–202 (2008)
51. J. Pihl, M. Karlsson, D.T. Chiu, Microfluidic technologies in drug discovery. Drug Discov. Today **10**, 1377–1383 (2005)
52. J. Ji, Y. Zhao, L. Guo, B. Liu, C. Ji, P. Yang, Interfacial organic synthesis in a simple droplet-based microfluidic system. Lab Chip **12**, 1373–1377 (2012)
53. V. Srinivasan, V.K. Pamula, R.B. Fair, An integrated digital microfluidic lab-on-a-chip for clinical diagnostics on human physiological fluids. Lab Chip **4**, 310–315 (2004)
54. A. Pavesi, F. Piraino, G.B. Fiore, K.M. Farino, M. Moretti, M. Rasponi, How to embed three-dimensional flexible electrodes in microfluidic devices for cell culture applications. Lab Chip **11**, 1593–1595 (2011)
55. C. Priest, P.J. Gruner, E.J. Szill, S.A. Al-Bataineh, J.W. Bradley, J. Ralston, D.A. Steele, R.D. Short, Microplasma patterning of bonded microchannels using high-precision injected electrodes. Lab Chip **11**, 541–544 (2011)
56. T. Kasahara, S. Matsunami, T. Edura, J. Oshima, C. Adachi, S. Shoji, J. Mizuno, Fabrication and performance evaluation of microfluidic organic light emitting diode. Sens. Actuators A **195**, 219–223 (2013)
57. T. Kasahara, S. Matsunami, T. Edura, R. Ishimatsu, J. Oshima, M. Tsuwaki, T. Imato, S. Shoji, C. Adachi, J. Mizuno, Multi-color microfluidic electrochemiluminescence cells. Sens. Actuators A **214**, 225–229 (2014)
58. T. Kasahara, S. Matsunami, T. Edura, R. Ishimatsu, J. Oshima, M. Tsuwaki, T. Imato, S. Shoji, C. Adachi, J. Mizuno, Multi-color microfluidic organic light-emitting diodes based on on-demand emitting layers of pyrene-based liquid organic semiconductors with fluorescent guest dopants. Sens. Actuators B **207**, 481–489 (2015)
59. M. Tsuwaki, T. Kasahara, T. Edura, S. Matsunami, J. Oshima, S. Shoji, C. Adachi, J. Mizuno, Fabrication and characterization of large-area flexible microfluidic organic light-emitting diode with liquid organic semiconductor. Sens. Actuators A **216**, 231–236 (2014)
60. H. Murata, C.D. Merritt, Z.H. Kafafi, Emission mechanism in rubrene-doped molecular organic light-emitting diodes: direct carrier recombination at luminescent centers. IEEE J. Sel. Top. Quantum Electron. **4**, 119–124 (1998)
61. C.-B. Moon, W. Song, M. Meng, N.H. Kim, J.-A. Yoon, W.Y. Kim, R. Wood, P. Mascher, Luminescence of Rubrene and DCJTB molecules in organic light-emitting devices. J. Lumin. **146**, 314–320 (2014)
62. K. Okumoto, H. Kanno, Y. Hamada, H. Takahashi, K. Shibata, High efficiency red organic light-emitting devices using tetraphenyldibenzoperiflanthene-doped rubrene as an emitting layer. Appl. Phys. Lett. **89**, 013502 (2006)
63. K. Okumoto, H. Kanno, Y. Hamada, H. Takahashi, K. Shibata, Organic light-emitting devices using polyacene derivatives as a hole-transporting layer. J. Appl. Phys. **100**, 044507 (2006)
64. Y. Zhang, S.R. Forrest, Triplets contribute to both an increase and loss in fluorescent yield in organic light emitting diodes. Phys. Rev. Lett. **108**, 267404 (2012)
65. H. Nakanotani, T. Higuchi, T. Furukawa, K. Masui, K. Morimoto, M. Numata, H. Tanaka, Y. Sagara, T. Yasuda, C. Adachi, High-efficiency organic light-emitting diodes with fluorescent emitters. Nat. Commun. **5**, 4016 (2014)
66. L. Tang, N.Y. Lee, A facile route for irreversible bonding of plastic-PDMS hybrid microdevices at room temperature. Lab Chip **10**, 1274–1280 (2010)
67. K. Sakuma, J. Mizuno, N. Nagai, N. Unami, S. Shoji, Effects of vacuum ultraviolet surface treatment on the bonding interconnections for flip chip and 3-D integration. IEEE Trans. Electron. Packag. Manuf. **33**, 212–220 (2010)
68. N. Unami, K. Sakuma, J. Mizuno, S. Shoji, Effects of excimer irradiation treatment on thermocompression Au-Au bonding. Jpn. J. Appl. Phys. **49**, 06GN12 (2010)

69. T. Funabashi, J. Mizuno, M. Sato, M. Kitajima, M. Matsuura, S. Shoji, Film of lignocellulosic carbon material for self-supporting electrodes in electric double-layer capacitors. APL Mater. **1**, 032104 (2013)
70. T. Kasahara, S. Shoji, J. Mizuno, Surface modification of polyethylene terephthalate (PET) by 172-nm excimer lamp. Trans. Jpn. Inst. Electron. Packag. **5**, 47–54 (2012)
71. H. Shinohara, T. Kasahara, S. Shoji, J. Mizuno, Studies on low-temperature direct bonding of VUV/O_3-, VUV- and O_2 plasma-pre- treated poly-methylmethacrylate. J. Micromech. Microeng. **21**, 085028 (2011)
72. M.A. Wolak, B.-B. Jang, L.C. Palilis, Z.H. Kafafi, Functionalized pentacene derivatives for use as red emitters in organic light-emitting diodes. J. Phys. Chem. B **108**, 5492–5499 (2004)
73. M. Song, J.-W. Kang, D.-H. Kim, J.-D. Kwon, S.-G. Park, S. Nam, S. Jo, S.Y. Ryu, C.S. Kim, Self-assembled monolayer as an interfacial modification material for highly efficient and air-stable inverted organic solar cells. Appl. Phys. Lett. **102**, 143303 (2013)
74. K.A. Luck, T.A. Shastry, S. Loser, G. Ogien, T.J. Marks, M.C. Hersam, Improved uniformity in high-performance organic photovoltaics enabled by (3-aminopropyl)triethoxysilane cathode functionalization. Phys. Chem. Chem. Phys. **15**, 20966–20972 (2013)
75. H. Tang, W. Zhang, P. Geng, Q. Wang, L. Jin, Z. Wu, M. Lou, A new amperometric method for rapid detection of Escherichia coli density using a self-assembled monolayer-based bienzyme biosensor. Anal. Chim. Acta **562**, 190–196 (2006)
76. O.L. Griffith, S.R. Forrest, Exciton management in organic photovoltaic multidonor energy cascades. Nano Lett. **14**, 2353–2358 (2014)
77. L.C. Picciolo, H. Murata, Z.H. Kafafi, Organic light-emitting devices with saturated red emission using 6,13-diphenylpentacene. Appl. Phys. Lett. **78**, 2378–2380 (2001)
78. J. Mizuno, L. Li, Y. Kawaguchi, K. Tsunozaki, H. Shinohara, S. Shoji, Anti-sticking curing of fluorinated polymers for improvement of mold releasability. J. Photopolym. Sci. Technol. **24**, 89–93 (2011)
79. M. Tsuwaki, J. Mizuno, T. Kasahara, T. Edura, E. Kunisawa, R. Ishimatsu, S. Matsunami, T. Imato, C. Adachi, S. Shoji, Microfluidic electrochemiluminescence (ECL) integrated flow cell for portable fluorescence detection. *Proceedings of IEEE Int. Conf. Micro Electro Mechanical Systems*, San Francisco, 108–111 (2014)
80. T. Kasahara, J. Mizuno, S. Matsunami, T. Edura, M. Tsuwaki, J. Oshima, C. Adachi, S. Shoji, Variable multi-color microfluidic organic light emitting device based on mixing of electrochemiluminescence solutions. *Proceedings of International Solid-State Sensors, Actuators and Microsystems Conference (TRANSDUCERS)*, Barcelona, 2596–2560 (2013)